University of Nottingham
UK | CHINA | MALAYSIA

Monitoring Sand Dune Movement using Remote Sensing

By

Ahmed Mutasim Abdalla Mahmoud

BSc, MSc

Thesis submitted to the University of Nottingham

for the degree of Doctor of Philosophy

Nottingham Geospatial Institute, Department of Civil Engineering

University of Nottingham, UK

April 2022

DECLARATION

During this research study, three journal articles and one media article were published:

1. 'The Use of SAR Offset Tracking for Detecting Sand Dune Movement in Sudan', which formed the basis of chapter 4.
   Mahmoud, A.M.A.; Novellino, A.; Hussain, E.; Marsh, S.; Psimoulis, P.; Smith, M. The Use of SAR Offset Tracking for Detecting Sand Dune Movement in Sudan. Remote Sens. 2020, 12, 3410. https://doi.org/10.3390/rs12203410.

2. **'**Monitoring the Dynamics of Formby Sand Dunes Using Airborne LiDAR DTMs**'.**
   Mahmoud, A.M.A.; Hussain, E.; Novellino, A.; Psimoulis, P.; Marsh, S. Monitoring the Dynamics of Formby Sand Dunes Using Airborne LiDAR DTMs. *Remote Sens.* 2021, *13*, 4665. https://doi.org/10.3390/rs13224665.

3. **'**A Field Survey of Formby Coastal Dunes using TLS and GNSS**'.**
   Mahmoud, A.M.A.; A Field Survey of Formby Coastal Dunes using TLS and GNSS, SENSED-the RSPSoc Newsletter, July 2021.

   - Articles 2 and 3 formed the basis of chapter 5.

4. **Mahmoud, A.M.A.;** Sudan's 'Forgotten' Pyramids Risk being Buried by Shifting Sand Dunes (Media Article), The Conversation, June 2021.

I acknowledge that all the processing and written content of the articles was done by me, and I led the analysis under the supervision and contribution of the supervisors.

ACKNOWLEDGEMENT

This PhD research is a collaboration between the University of Nottingham and the British Geological Survey (BGS).

Firstly, I would like to express my sincere gratitude to my principal supervisor Prof. Stuart Marsh who has been an excellent supervisor providing endless support, guidance and encouragement throughout my PhD study period.

I would like also to thank Dr. Panos Pasimuiouls and Dr. Martin Smith for their exceptional supervision role.

I would like to thank my supervisors from the British Geological Survey, Dr. Alessandro Novellino and Dr. Ekbal Hussain for their excellent support and supervision.

I wish to extend my appreciation to Sean Ince (Senior Engineering Technical Supervisor) and Norma Oldfield (Engineering Survey Technician) from the Nottingham Geospatial Institute (NGI) for their tremendous support and participation in Formby field work study.

I would like to thank the University of Nottingham and the Ministry of Higher Education and Scientific Research of the Republic of Sudan for awarding me this PhD studentship. Moreover, I would like to extend my thanks to the BGS University Funding Initiative (BUFI) for awarding me a partial funded PhD studentship, (S448).

The financial assistance provided by the Faculty of Engineering of the University of Nottingham, during the COVID-19 pandemic is greatly appreciated.

My words cannot express my gratitude to my parents, family and friends for their endless support and encouragement throughout my learning journey.

ABSTRACT

Deserts are arid and semi-arid regions with low rainfall and sparse vegetation, which makes them suitable hosts for the formation of sand dunes. Deserts cover an area of more than one-fifth of the Earth's total land cover. Despite the fact that some of these desert dunes have been monitored for many years, the size and volume of sand dunes as a whole are not adequately monitored and updated, due to both the difficulty of using traditional methods of measurement and the continuous movement of the sand dunes. Many attempts have been made to quantify desert areas around the world, but quantifying desert dunes requires a thorough investigation that considers the different sand dunes' behaviour, as well as the impact of influencing factors such as wind, vegetation, topography, and sand supply on the dune movement. This must also involve analysing the dune activity both horizontally and vertically.

The movement of sand dunes is considered one of the major environmental issues in arid and semi-arid regions, that threatens livelihoods and rural communities by causing them to be submerged in sand. It also contributes to the degradation of land, causing poverty and food insecurity. Sand movement can be experienced on different scales: individual dune movement, dune field changes or in the form of dust storms. The key to mitigating these risks is to understand the movement of the dunes.

Sand dunes can also be found in coastal areas, where sediments are carried into the shores by sea tides and winds. Coastal dunes play an important role in coastal erosion risk management, where they act as a dynamic natural sea defence. In addition, they provide habitats that enrich coastal biodiversity and add resilience to the ecosystem. The world's sandy beaches are undergoing significant changes, with 24% eroding and 28% accumulating material, while the remaining 48% are stable.

Therefore, a comprehensive understanding of dune activity is urgently needed. This requires more accurate measurement techniques that match the frequency of observation to the rapid dynamic movement of the sand dunes.

There are two main sets of techniques for monitoring sand dunes: conventional techniques, such as sand traps, Global Navigation Satellite System (GNSS) and Terrestrial Laser scanner (TLS); and remote sensing techniques such as optical, Synthetic Aperture Radar (SAR) and Airborne Light Detection and Ranging (LiDAR). The conventional techniques provide vital information about sand dunes, such as the sand particle size, which can be detected by sand traps, in addition to highly accurate ground truth data collected by GNSS, total station and levels that can be used for validating the monitoring results detected by the remote sensing techniques.

However, these conventional techniques have significant limitations related to time consuming data collection processes and the complexity of monitoring large, inaccessible sand areas. Additionally, they only provide an approximation of the dune movement, as the data are collected for discrete dune locations rather than the dune field as a whole. Moreover, with few repeated surveys, conventional techniques are limited to detecting the movement that occurs within days or hours due to the rapid movement of the sand dunes. This can be overcome by applying time series analysis using remote sensing techniques, providing continuous observations of the dunes over periods of years that are contiguous over very large areas.

Therefore, the aim of this research is to investigate the capabilities of various novel remote sensing techniques (i.e. optical multi-spectral satellite sensors, SAR techniques, airborne LiDAR) for detecting and monitoring sand dune movement and its impact on urban areas, crop fields, forests, water bodies and archaeological sites, to determine the most vulnerable areas to sand dune movement. As part of this study, the impact of the influencing factors that control the movement of the dunes, such as wind speed/direction, vegetation, topography and sand supply, is also considered. This aim is fulfilled by four objectives: (1) develop an automated framework that uses Google Earth Engine and machine learning classifiers applied on multi-temporal satellite images to detect the areal changes in sand dunes, in addition to computing the displacement and direction of movement for individual sand dunes; (2) investigate the capabilities of the SAR Offset Tracking technique for detecting horizontal sand dune movement; (3) investigate the use of multi-temporal Airborne LiDAR DTMs for monitoring the dynamic activity of the coastal sand dunes; (4) investigating the capabilities of Differential Interferometric Synthetic Aperture Radar (DInSAR) for detecting the vertical deformation of sand dunes. This was carried out in two study areas: a desert sand dune area in Northern Sudan, and a coastal sandy beach near Formby in the Northwest of England.

This research highlighted the capabilities of the novel remote sensing techniques in addition to defining the limitations of using the more traditional land surveying techniques for monitoring sand dunes. Moreover, it has been found that detecting the deformation of individual dunes could be provided from moderate spatial resolution images, but the higher resolution of the images, the better the footprints of the individual dunes. Additionally, using digital terrain models time series data demonstrated high capability in monitoring sand dunes both horizontally and vertically, providing rates of horizontal and vertical dune motion in addition to the volumetric changes of the dunes.

Based on that analysis, a strategy has been developed for monitoring sand dune movement, that consists of three main implementation stages: (1) the detection of sand dunes using different surveying techniques, measuring the changes and movement of the dunes; (2) a monitoring stage, where time series analysis is applied to distinguish patterns in the dune movement, in addition to identifying the impact of the sand movement influencing factors (i.e. wind, vegetation, topography, …etc.) and its relationship to the sand movement behaviour; and (3) a prediction stage of sand movement, based on previously detected dune behaviour and the influencing factors from the monitoring results. This strategy could have wide applicability and could also be modified to study other environmental challenges, such as glaciers.

TABLE of CONTENTS

LIST of FIGURES

LIST of TABLES

LIST of ACRONYMS

API	Application Programming Interface
ASF	Alaska Satellite Facility
COSI_Corr	Co-registration of Optically Sensed Images and Correlation
DEM	Digital Elevation Model
DInSAR	Differential Interferometric Synthetic Aperture Radar
DoD	DTM of Difference
DTM	Digital Terrain Model
ECMWF	Medium-Range Weather Forecast
ERS	European Remote Sensing
ESA	European Space Agency
GCP	Ground Control Point
GEE	Google Earth Engine
GIS	Geographic Information System
GNSS	Global Navigation Satellite System
GPS	Global Positioning System
GRD	Ground Range Detected
HH	Horizontal-Horizontal Polarization
HV	Horizontal-Vertical Polarization
IMU	Inertial Measuring Unit
InSAR	Interferometric Synthetic Aperture Radar
IW	Interferometric Wide
LiDAR	Light Detection and Ranging
LOS	Line-of-Sight
MODIS	Moderate Resolution Imaging Spectroradiometer
NASA	National Aeronautics and Space Administration
NDVI	Normalized Difference Vegetation Index
PCA	Principal Component Analysis
PSTP	Pairs of Source and Target Points
RADAR	Radio Detection And Ranging
RF	Random Forest
RTK	Real-Time Kinematic
SAR	Synthetic Aperture Radar
SET	Sand Encroachment Tool
SLC	Single Look Complex
SVM	Support Vector Machine
TLS	Terrestrial Laser Scanner
TOPSAR	Terrain Observation with Progressive Scans SAR
TS	Total Station
UAV	Unmanned Aerial Vehicle
UNESCO	United Nations Educational, Scientific and Cultural Organization
USGS	United States Geological Survey
UTM	Universal Transverse Mercator
VIS	Visual Inertial System
VV	Vertical-Vertical Polarization
WGS84	World Geodetic System 1984

1 CHAPTER 1: INTRODUCTION

1.1 Background

Dunes are an accumulation of fine particles of sand stimulated by wind (Huggett, 2007), where the sand particles are carried by the wind speed force until it strikes an obstacle such as bushes, rocks, fences…etc.; and start accumulating, forming the dunes. While recent experiments suggest that dunes can be also formed in sand sheets landscape without any obstacles (Ping et al. 2014).

For many decades desert dunes have been under the microscope of earth observation scientists. Previous studies focused on three main aspects: (1) describing dune formation and patterns to distinguish the different types of dunes; (2) analysing dune sediment by investigating the grain size and sorting characteristics to reveal how dunes are accumulated; and (3) investigating dune dynamics and processes to understand the aeolian process and sand transport rates (Lancaster, 1995).

Sand movement has a significant impact on arid and semi-arid regions threatening the livelihoods of rural communities (Shepherd et al. 2016). On the other hand, sand dunes play a vital role in protecting coastal shorelines (Nordstrom et al. 1990). This makes sand movement a pressing environmental issue. Therefore, understanding the geomorphological activity of the dunes has been the focus of this research.

1.1.1 Desert Sand Dunes

Deserts are arid and semi-arid regions with low rainfall and sparse vegetation (Goudie and Seely, 2011), which makes them suitable host for the formation of sand dunes. Deserts cover an area of more than one-fifth of the Earth's total land cover (Abdelaziz Bouteflika et al. 2016).

In 1989, the locations of major sand accumulation areas known as sand seas or ergs were mapped; these were considered to be the dust sources, (Figure 1.1). Geomorphologists agree that sand seas must cover an area of at least 125 km^2 while smaller areas are classified as dune fields (Pye and Tsoar, 2008). Sand seas are mainly distributed in the eastern hemisphere forming sandy deserts in the Sahara, Arabia, central Asia, Australia and southern Africa covering about 15 to 30 per cent of the arid land cover class in these arid zones (Lancaster, 1995).

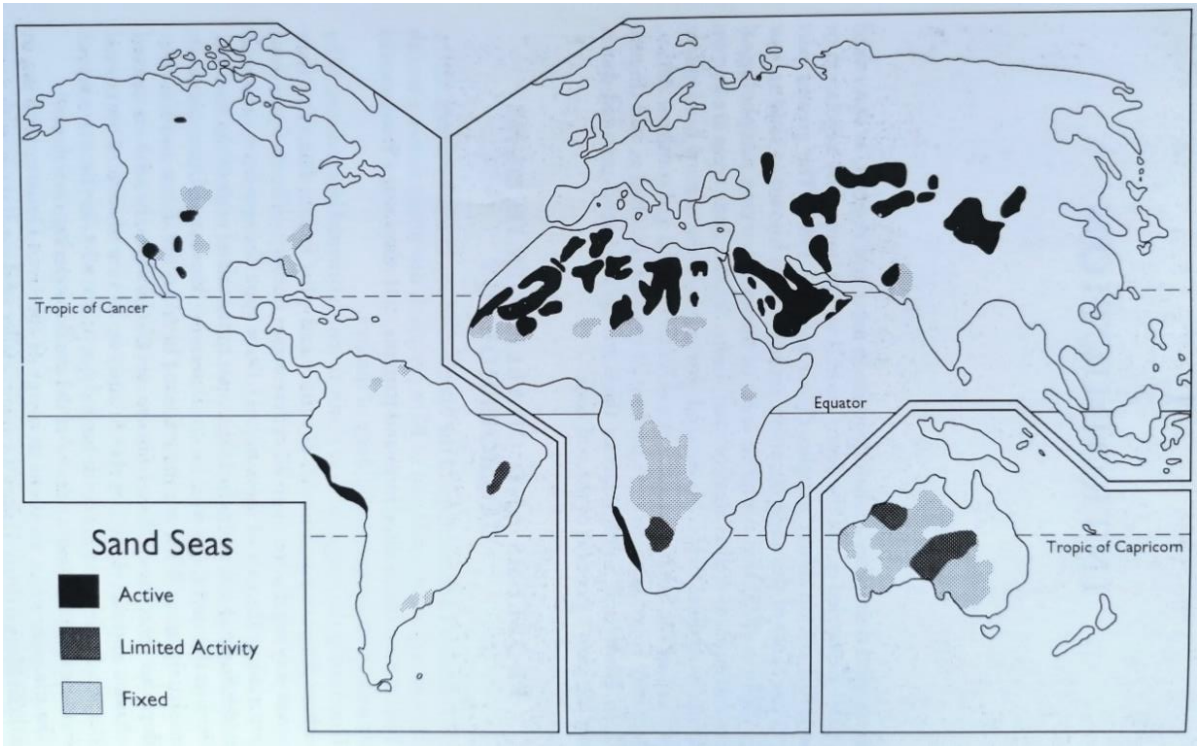

Figure 1.1. Location of major sand seas and dune fields, (after Thomas 1989) (Lancaster, 1995).

In order for sand seas and dune fields to form, there must be a large supply of sand and sufficient wind energy to carry the sand or redistribute it in situ, in addition to suitable topographic and climatic conditions which enable the accumulation of a large thickness of sand over a long period of time (Pye and Tsoar, 2008).

The geological records and age structure of the present sand dunes only show that the sand deposits are dated to no more than 100,000 years. Stratigraphic and radiocarbon dating evidence indicates that the current forms of sand dunes date back to the Pleistocene or the late Holocene (Pye and Tsoar, 2008). However, (Vermeesch et al. 2010) showed that sand dunes have resided in the Namib Sand Sea for at least one million years.

Several of the largest sand seas in the northern hemisphere can be found in the subtropical desert belt of North Africa and the Arabian subcontinent into Iran and Pakistan, or in the mid-latitude desert basins of Central Asia (Pye and Tsoar, 2008). Table 1.1 shows the major world ergs with an area sized larger than 12,000 km^2.

Table 1.1. Ergs in the world with an area larger than 12,000 km2. (After Wilson 1973), (Pye and Tsoar, 2008).

No	Name	Area (km2)	Activity	No	Name	Area (km2)	Activity
	North Africa				**Arabia**		
1	Great Sand Sea	105,000	Active erg	26	Rub al Khali	560,000	Active erg
2	Sudanese Qoz	240,000	Fixed erg	27	Al Dahana	51,000	Active erg
3	Erg Rebiana	65,000	Active erg	28	Al Jafura	57,000	Active erg
4	Erg Calanscio	62,000	Active erg	29	Ramlat Wahibah	16,000	Active erg
5	Edeyen Murzuq	61,000	Active erg	30	Ramlat Sabatayn	14,000	Active erg
6	Edeyen Ubari	62,000	Active erg	31	Al Nefud	72,000	Active erg
7	Issaouane-N-Irarrarcn	38,500	Active erg	32	Nafud complex'	25,000	Active erg
8	Erg Oriental	192,000	Active erg		**Asia**		
9	Erg Occidental	103,000	Active erg	33	Thal Desert	18,000	Fixed erg
10	Erg Iguidi	68,000	Active erg	34	Thar Desert	214,000	Fixed erg
11	Erg Chech-Adrar	319,000	Active erg	35	Ryn Peski	24,000	Active erg
12	North Mauretanian Erg	85,000	Active erg	36	Peski Kara-kum	38,000	Active erg
13	South Mauretanian Erg	65,000	Fixed erg	37	Peski Kyzyl-kum	276,000	Active erg
14	Trarza and Cayor Erg	57,000	Fixed erg	38	Peski Priaralskye	56,000	Active erg
15	Ouarane, Aouker, Akle, etc.	206,000	Active/Fixed erg	39	Peski Muyunkum	38,000	Active erg
16	El Mreye	63,000	Active erg	40	Peski Sary Isnikotrav	65,000	Active erg
17	Erg Tombuctou	66,000	Active erg	41	Peski Dzosotin	47,000	Active erg
18	Erg Azouad	69,000	Fixed erg	42	Takla Makan	247,000	Active erg
19	Erg Gourma	43,000	Fixed erg	43	East Takla Makan	14,000	Active erg
20	West Azouak	35,000	Fixed erg	44	South Ala Shan	65,000	Active erg
21	East Azouak	34,000	Active/Fixed erg	45	North Ala Shan	44,000	Active erg
22	Erg Bilma-Tenere	155,000	Active erg	46	South-east Ala Shan	14,000	Active erg
23	Erg Foch	13,000	Active erg	47	East Ala Shan	12,000	Active erg

24	Erg Djourab	45,000	Active erg	48	West Ala Shan	27,000	Active erg
25	Erg Kanem	294,00	Fixed erg	49	Ordos	17,000	Active erg
	Australia			50	Peski Lop Nor'	18,000	Active erg
51	Victoria Desert	300,000	Fixed erg				
52	Great Sandy-Gibson Desert	630,000	Fixed erg				
53	Simpson Desert	300,000	Active/Fixed erg				
54	Northern Desert'	81,000	Fixed erg				
	South Africa						
55	Namib Desert	32,000	Active erg				
56	Kalahari Desert	N/A	Fixed erg				

Despite the fact that some of these desert dunes have been monitored for many years, the size and volume of sand dunes as a whole are not adequately monitored and updated, due to the difficulty of using traditional methods of measurement and the continuous movement of the sand dunes. Many attempts have been made to measure desert areas around the world but measuring desert dunes requires a thorough investigation that considers the different sand dune behaviour as well as the impact of influencing factors such as wind, vegetation, topography, and sand supply on the dune movement. This must also involve analysing the dune activity both horizontally and vertically.

1.1.2 Coastal Sand Dunes

Sand dunes can be also found in coastal areas (Nordstrom et al. 1990), where sediments are carried into the shores by sea tides and winds. Coastal dunes play an important role in coastal erosion risk management (Nordstrom et al. 1990), where they act as a dynamic natural sea defence (van de Graaff, 1986, Van der Meulen and Van der Maarel, 1989, Nordstrom et al. 1990, Pye et al. 2007, Pye and Tsoar, 2008, Provoost et al. 2011). In addition, they provide habitats that enrich coastal biodiversity and add resilience to the ecosystem (Pye et al. 2007). Figure 1.2 shows sand dunes on the coast of Formby, northwest England.

Figure 1.2. Coastal sand dunes on the coast of Formby, northwest England.

The morphology of the coastal dunes depends mainly on four factors: (1) the beach morphology and shoreline dynamics, which affect the sand supply; (2) the wind characteristics, speed and direction variability; (3) the vegetation cover along the coastal area; and (4) human activities, such as planting trees, installing fences etc. (Nordstrom et al. 1990).

The world's major dune coastlines are located along the Atlantic coasts of northwest Europe, the Pacific northwest of North America, southwest Australia and southwest Africa (Nordstrom et al. 1990). The Namibian sand sea in southwest Africa is the most famous sandy coast in the world. It has been nominated by UNESCO as a world heritage site (Seely, 2012). Figure 1.3 shows the sand dunes of the Namibian sand sea.

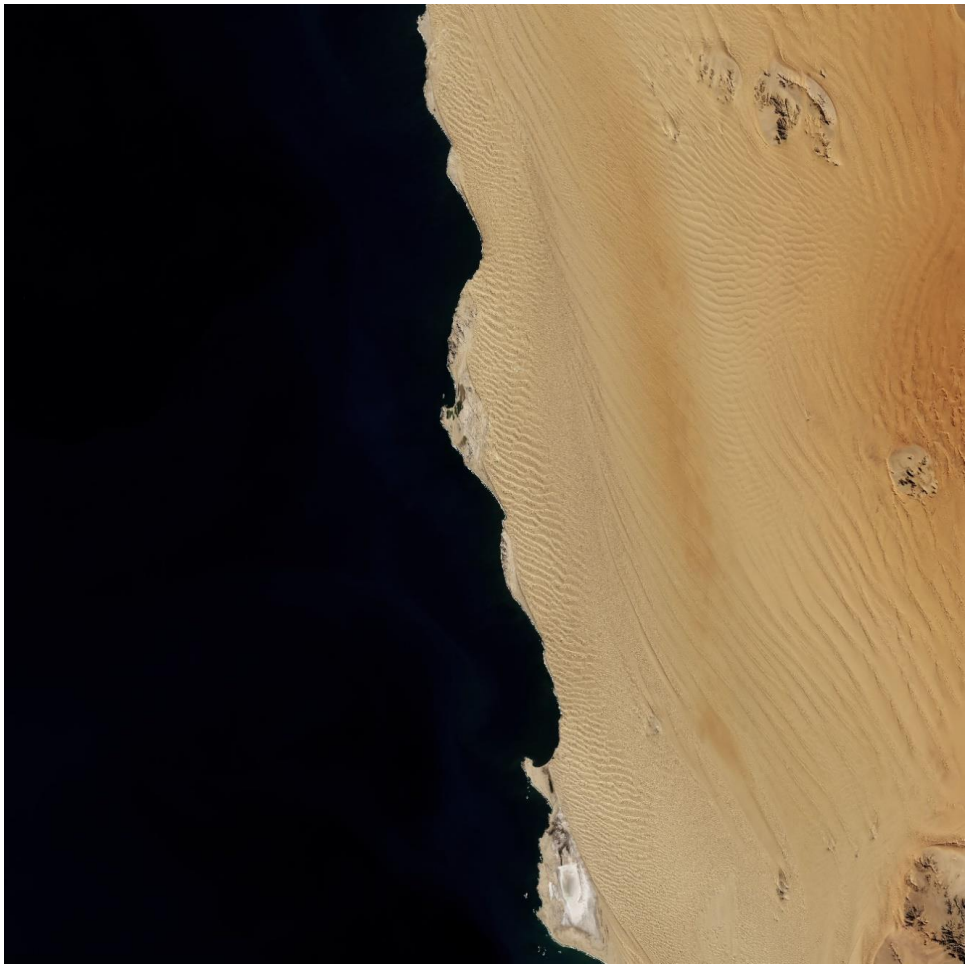

Figure 1.3. Landsat 8 satellite image captured on the 5th of July 2018 showing coastal desert dunes of the Namibian sand sea near Namib Naukluft National Park, (https://earthobservatory.nasa.gov/images/92695/between-the-ripples-of-the-namib-sand-sea).

The world's sandy beaches are undergoing significant changes in coastal areas, with 24% eroding and 28% accumulating material, while the remaining 48% are stable (Luijendijk et al. 2018). Due to that, sand preservation projects have been initiated by local authorities where vegetation and fences are utilized to stabilize and reinforce the dunes (Pye et al. 2007).

There are also projects that involve creating artificial sandy beaches as part of so-called sandscape projects. For instance, in the UK, a recent project was developed in North Norfolk after a devastating impact from a sea surge in 2013 caused significant damage to the infrastructure in the area: https://www.north-norfolk.gov.uk/sandscaping. The project was established in 2019 and involved importing 1.8 million cubic metres of sand from the seabed and depositing it onto the coast. This project intends to increase the level of protection of the coast defences and cliffs by reducing the energy of the sea waves. Such a project will need to be monitored consistently to determine its impact and stay on top of the potential risks.

In general, climate change poses the main threat to coastal communities and natural habitats by causing severe storms and sea level rise (Zsamboky et al. 2011) making understanding coastal dunes activity an essential task. This must be addressed from a geomorphological perspective to understand the formation of the dunes.

1.2 Research Problem: Sand movement

Sand movement is one of the main environmental hazards in the arid and semi-arid regions defined in section 1.1. It threatens the livelihoods of rural communities. The invasion of urban areas (including buildings and roads), agricultural fields, water bodies, and archaeological sites is a prevalent problem caused by dunes' movement. Figure 1.4 shows the encroachment of sand towards the archaeological site of the royal cemetery of Meroe in Sudan. Figure 1.5 shows the invasion of sand dunes on houses in the same area, which resulted in the displacement of local communities (Shepherd et al. 2016). Figure 1.6 illustrates the migration of dunes across a newly constructed road (Shepherd et al. 2016).

Figure 1.4. Sand encroachment toward archaeological sites in Sudan (Royal Cemetery of Meroe).

Figure 1.5. Sand encroachment displaced entire communities in the River Nile state, Sudan.

Figure 1.6. Migration of dunes across a newly constructed road (Photo credit: David Thomas).

Moreover, the phenomenon has some serious health implications that are generated as a result of the frequent dust storms causing, for example, shortness of breath and air pollution (Aghababaeian et al. 2021). The movement of sand also contributes to the degradation of land in arid and semi-arid regions (Feng et al. 2019), causing poverty and food insecurity, and contributing to major conflicts over food and water resources.

Considering all these reasons, it is vital to understand how sand dunes behave and respond to changing weather conditions. However, monitoring the movement of the dunes in deserts and coastal areas is a challenging task. For instance, conventional monitoring techniques such as sand traps and land surveying techniques (e.g. levelling, GNSS and terrestrial laser scanners) have several limitations, including a time consuming data collection process and the fact that many of them obtain only low spatial resolution data. This becomes more challenging if repeated surveys are required when covering larger dune areas, especially in remote areas.

To overcome these challenges, this research suggests utilizing the latest advancement in remote sensing technologies to develop novel techniques for the estimation and monitoring of sand dune movement. This will provide more accurate and frequent detection of the dunes for large dune systems of all types described above.

1.3 Research Aim and Objectives

1.3.1 Aim

This research investigates the capabilities of various novel remote sensing techniques (i.e. optical multi-spectral satellite sensors, Synthetic Aperture Radar (SAR) techniques, airborne LiDAR) for detecting and monitoring sand dune movement and its impact on urban areas, crop fields, forests, water bodies and archaeological sites, to determine the most vulnerable areas to sand dune movement. As part of this study, the impact of the influencing factors that control the movement of the dunes, such as wind speed/direction, vegetation, topography and sand supply will also be considered.

In particular, this will involve the development of automated frameworks that use multi-temporal optical and Airborne LiDAR data sets to monitor the movement of sand dunes. Other techniques such as SAR pixel offset, which have not been previously applied to this problem will also be investigated, as well as the use of DInSAR to detect the vertical deformation of sand dunes.

1.3.2 Objectives

1. Develop an automated framework that uses machine learning classifiers applied on multi-temporal optical satellite images to detect the changes in sand dunes land cover and use it to compute the displacement and direction of individual sand dune movement identified from multi-temporal optical satellite images.
2. Investigate the capabilities of the SAR Offset Tracking technique for detecting horizontal sand dune movement.
3. Develop a framework that uses multi-temporal Airborne LiDAR DTMs for monitoring the dynamic activity of sand dunes.
4. Investigate the capabilities of Differential Interferometric Synthetic Aperture Radar (DInSAR) for detecting the vertical deformation of sand dunes.

Having established the vertical and horizontal movement dynamics of the dunes, we will be able to understand the relationship between the different influencing factors and the rate of dune movement, the influence of vertical changes on the horizontal movement of the dunes and ultimately define the limitations of using classical land survey techniques and how they can be improved by modern satellite-based surveying.

1.4 Chapters Summary

Following this introductory chapter, **Chapter 2** provides a thorough literature review on the geomorphology of sand dunes describing the formation of the dunes, distinguishing different types of dunes, identifying factors that control dune movement, in addition to providing a reflection on previous research experiences on the use of land surveying and various remote sensing techniques for monitoring the dynamics of the dunes.

Chapter 3 addresses objective 1 by presenting a developed automated framework that uses Google Earth Engine and machine learning classifiers applied on multi-temporal Sentinel 2 L2A satellite images to detect the changes in sand dunes, in addition to computing the displacement and direction of movement for individual sand dunes. Two machine learning classifiers were used in this study, the random forest and the support vector machine to monitor the horizontal movement of sand dunes in Northern Sudan between December 2018 to December 2021. It also demonstrates the use of the individual dune detection tool for detecting individual dune displacement and direction of movement.

Chapter 4 investigates the use of SAR offset tracking for detecting the horizontal sand dune movement to meet objective 2. High-resolution images from the Sentinel-1 satellite were used for the generation of displacement maps. This technique showed high competency in monitoring the movement of sand dunes, in addition to identifying areas exposed to large sand drifting as a risk mapping technique.

Chapter 5 is aimed at objective 3 and investigates the use of multi-temporal Airborne LiDAR DTMs for monitoring the dynamic activity of the coastal sand dunes. A framework was developed to determine how much sand volume has been lost or deposited in a dune system as well as determining the rate of change in the elevation of the dunes, taking Formby sand dunes as a case study.

Chapter 6 provides a discussion on the uses of different remote sensing techniques and the limitation of each technique. It also provides a reflection on the limitations of land surveying techniques while addressing its benefits. In the context of objective 4, a framework of DInSAR is initially investigated for detecting sand dune movement from short temporal SAR images. This chapter also provides a detailed strategy for monitoring sand dunes.

Chapter 7 provides a conclusion on the uses of remote sensing techniques for detecting and monitoring sand dunes in deserts and coastal areas. It summarises the findings of the study and makes recommendations for future work in the field of dune monitoring.

2 CHAPTER 2: LITERATURE REVIEW: REFLECTION ON DUNE MONITORING AND MODELLING TECHNIQUES

2.1 Geomorphology of Sand Dunes

Studying the geomorphology of sand dunes has been an interest for researchers for many decades (Bagnold, 1941, Nordstrom et al. 1990, Lancaster, 1995, Huggett, 2007, Livingstone et al. 2007, Pye and Tsoar, 2009). In this section of the thesis, an understanding of dune formation processes is developed, presenting the different types of dunes, the factors that influence the dune morphology and the techniques that are used for monitoring and modelling the movement of the dunes.

2.1.1 Dune Formation

Sand dunes can be found in coastal areas, riverbanks and indeed most commonly in deserts (Bagnold, 1941). The aeolian transport plays a fundamental role in the formation of the dunes. This requires an understanding of the characteristics of the earth's surface including determining the sediment texture, vegetation cover, degree of cohesion and crusting, and the dynamics of airflow over the surface (Lancaster, 1995).

Sand particles are transported by wind in three modes: suspension, saltation and creeping (Lancaster, 1995). These modes apply depending on the grain size of the sand particles and the wind speed (Bagnold, 1941). The first, suspension mode, controls the movement of sand particles that have a very small grain size <60-70μm, and this results in sand particles being transported for long distances by turbulent eddies in the wind and kept high up in the atmosphere. The role of the size of particles is considered insignificant in dune dynamics. However, the sand particles deposition by dust is important in many areas (Lancaster, 1995), for example, satellite images capture the migration of sand every year from the Sahara desert across the Atlantic Ocean and its deposition in the Amazon forest (Koren et al. 2006).

The second aeolian transport mode is saltation, which is the dominant process in transporting sand particles. In this process, particles with a size of 60-500μm move downwind in a series of short distance jumps, where particles need a lifting force to make them vibrate and move to get in the airstream and initiate saltation. This force is generated due to the air pressure differences near the surface (Lancaster, 1995). The impact angle (i.e. the angle where the particle interacts with the surface) of a saltation particle increases with the decrease of wind velocity and particle size (Sorensen 1985; Lancaster 1995). Most sand particles travel close to the ground within the lowest part of the atmosphere, close to the ground surface (1-2 cm) (Lancaster, 1995).

The third aeolian transport mode is creeping where the sand particles with a size of >500μm are pushed and rolled along the surface and transported by the influence of saltating grains in surface creep (Lancaster, 1995). Figure 2.1 illustrates the different modes of aeolian transport of sand particles, (Kok et al. 2012).

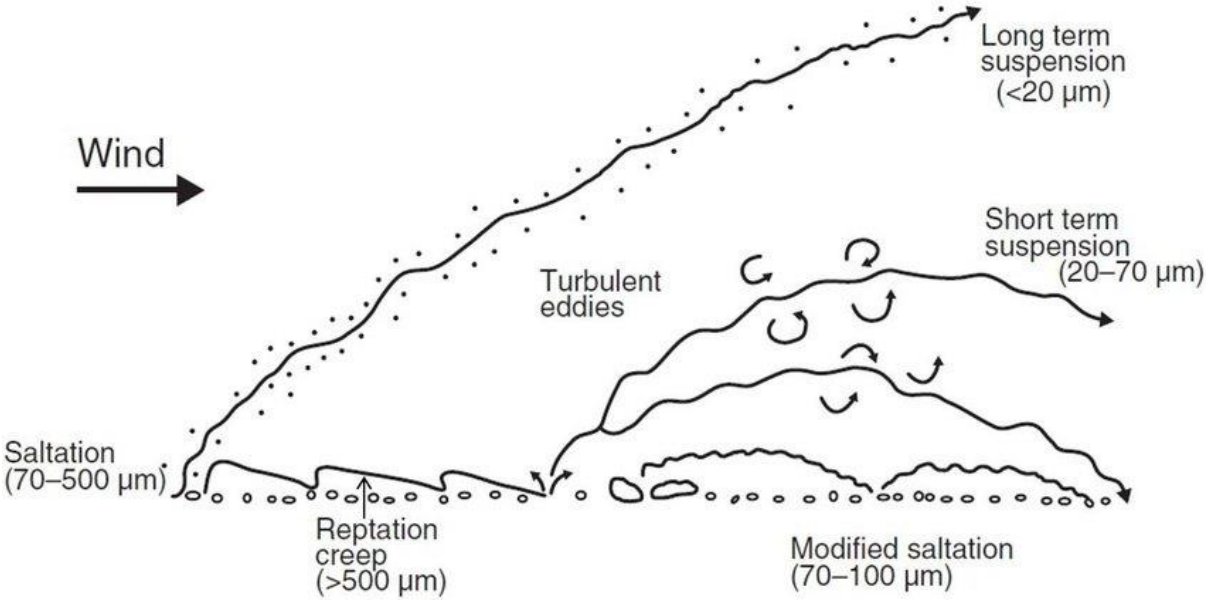

Figure 2.1. Different modes of aeolian transport of sand particles.

The wind's behaviour contributes significantly to the shaping of the desert dunes. An individual dune consists of a stoss side formed based on the dominant direction of wind where sand particles are pushed upwards in the direction of the wind, and a slip face side (lee side) on the downwind direction of the wind, with two horns at the end which represent the width of the dune (Durán et al. 2011, Bagnold, 1941). Figure 2.2 illustrate the components of an individual barchan dune, stoss side, lee side and horns.

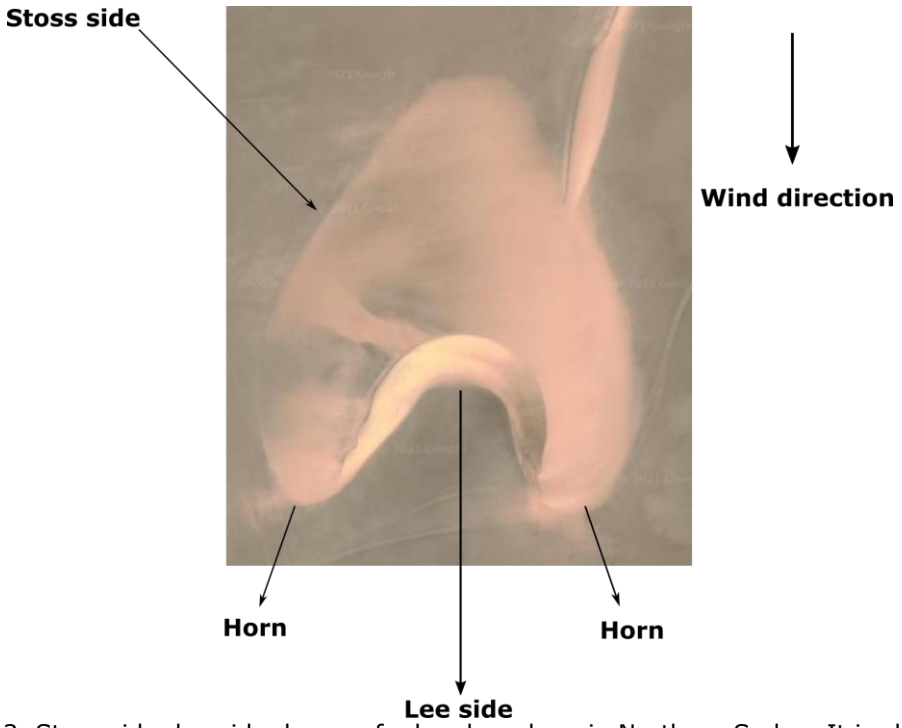

Figure 2.2. Stoss side, lee side, horns of a barchan dune in Northern Sudan. It is showing a barchan dune moving south influenced by a southward wind.

The formation of coastal sand dunes also depends on the wind and sand sediment supply (Nordstrom et al. 1990). The sand particles are transported landward in the wind direction and get deposited when the wind velocity decreases or with the increase in the surface slope. This movement continues landward until it is interrupted by vegetation or any other barrier; at that stage sand particles start forming the dunes (Nordstrom et al. 1990). An additional factor that also has an impact on the coastal dune formation process is the changes in sea level and water tides (Nordstrom et al. 1990, Pye and Blott, 2008, King et al. 2019). These sea tide waves move the sand particles along the shore and deposit them on the shorelines, a phenomenon known as longshore sand drifting (Engel et al. 2015).

Sand dunes in coastal areas have several formation stages that rely mainly on time and the amount of sand supply. The fore dunes are the newly formed dunes that are closer to the beach, while the older dunes are formed further inland (Nordstrom et al. 1990, Tsoar, 2001). Figure 2.3 demonstrates the cycle of coastal dune formation.

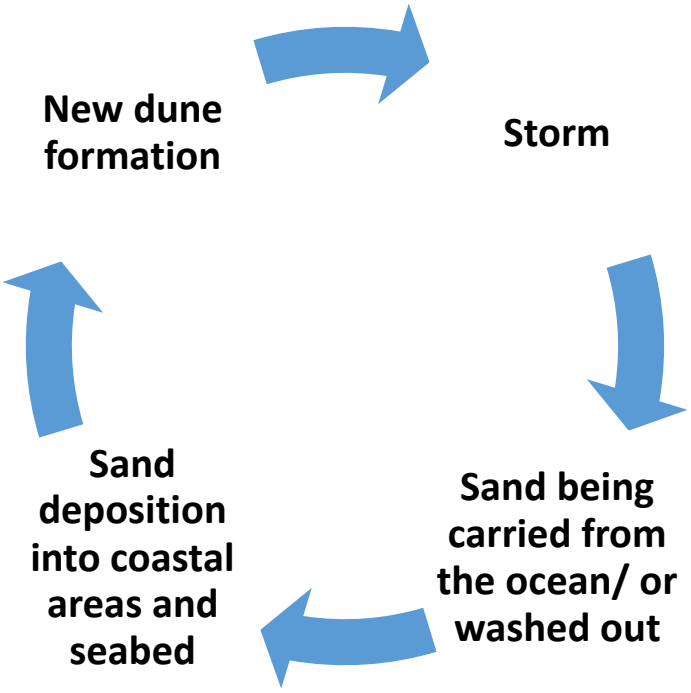

Figure 2.3. A repetitive process cycle of coastal dune formation.

Recent studies that use numerical models and simulations have overturned the previously held theories of dune formation (Courrech du Pont et al. 2014, Lucas et al. 2014, Gao et al. 2015a, Gao et al. 2015b, Lü et al. 2017, Fernandez-Cascales et al. 2018, Hu et al. 2021). According to (Courrech du Pont et al. 2014) a single multidirectional wind regime can cause dunes to form in two distinct directions depending on the availability of sand.

2.1.2 Dune Types

Sand dunes are classified based on two aspects morpho-dynamic and morphological classification (Lancaster, 1995). The morpho-dynamic classification relies on formative wind and sediment supply and its relationship to the dune types, expressly, the classification is based on the dune alignment to the resultant wind direction; shaping different classes of dunes (i.e. transverse, oblique and longitudinal)(Lancaster, 1995), see Figure 2.4.

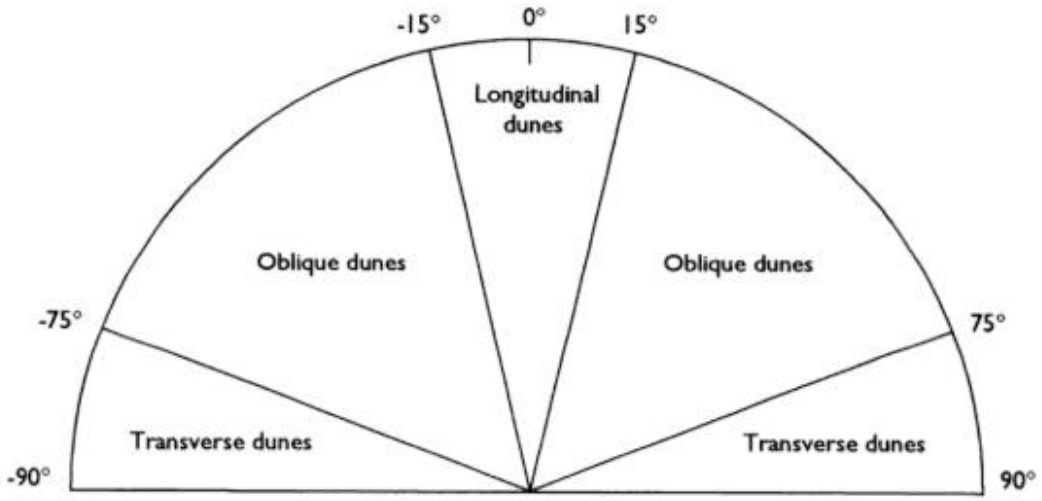

Figure 2.4. Morpho-dynamic classification of dunes based on its relations to wind direction, after (Hunter et al. 1983).

Other researchers also relied on the dune dynamic and classified the dunes based on their mobility and association to sediment flux, and by doing that they distinguished between the erosional types (i.e. parabolic dunes and sand ridges) and the depositional forms (i.e. barchanoid dunes, transverse chains, linear dunes and star dunes) (Lancaster, 1995).

The other aspect of dune classification is the morphological classification and that depends on the external morphology of the dunes. It classifies the dunes into five types based on their shape and the number of slip faces (i.e. crescentic, linear, reversing, star, and parabolic) (McKee et al. 1979; Lancaster, 1995). Crescentic dunes are the dominant type of dunes in the absence of vegetation, while barchan dunes tend to be formed in areas with limited availability of sand and any increase in the amount of sand will result in shaping crescentic dunes or barchanoid ridges (Lancaster, 1995), which are considered the fastest moving type of dunes. When linear dunes are formed in straight lines, exhibit parallelism and a regular spacing shape (Lancaster, 1995), they are considered the most common type of dunes to be found in deserts (Pye and Tsoar, 2009). Figure 2.5 shows the major dune types, (Lancaster, 1995).

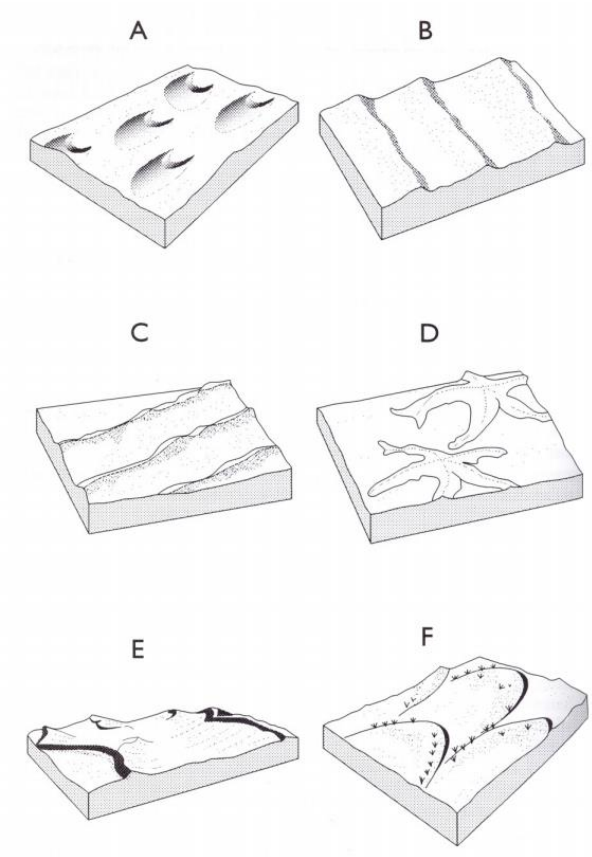

Figure 2.5. Major dune types. A: Barchan; B: Crescentic ridges; C: Linear; D Star; E: Reversing; F: Parabolic, after (McKee 1979a).

The use of different naming conventions for dune types has resulted in some confusion in describing the dunes in different parts of the world (Pye and Tsoar, 2009). Pye and Tsoar, 2009, put together a classification system for the major dune types which divides simple dunes into three categories: (a) dunes that are formed based on topographic obstacles, (b) dunes that are self-accumulated, and (c) dunes that are formed based on vegetation presence (Pye and Tsoar, 2009). Figure 2.6 illustrates the classification of major dune types, (Pye and Tsoar, 2009).

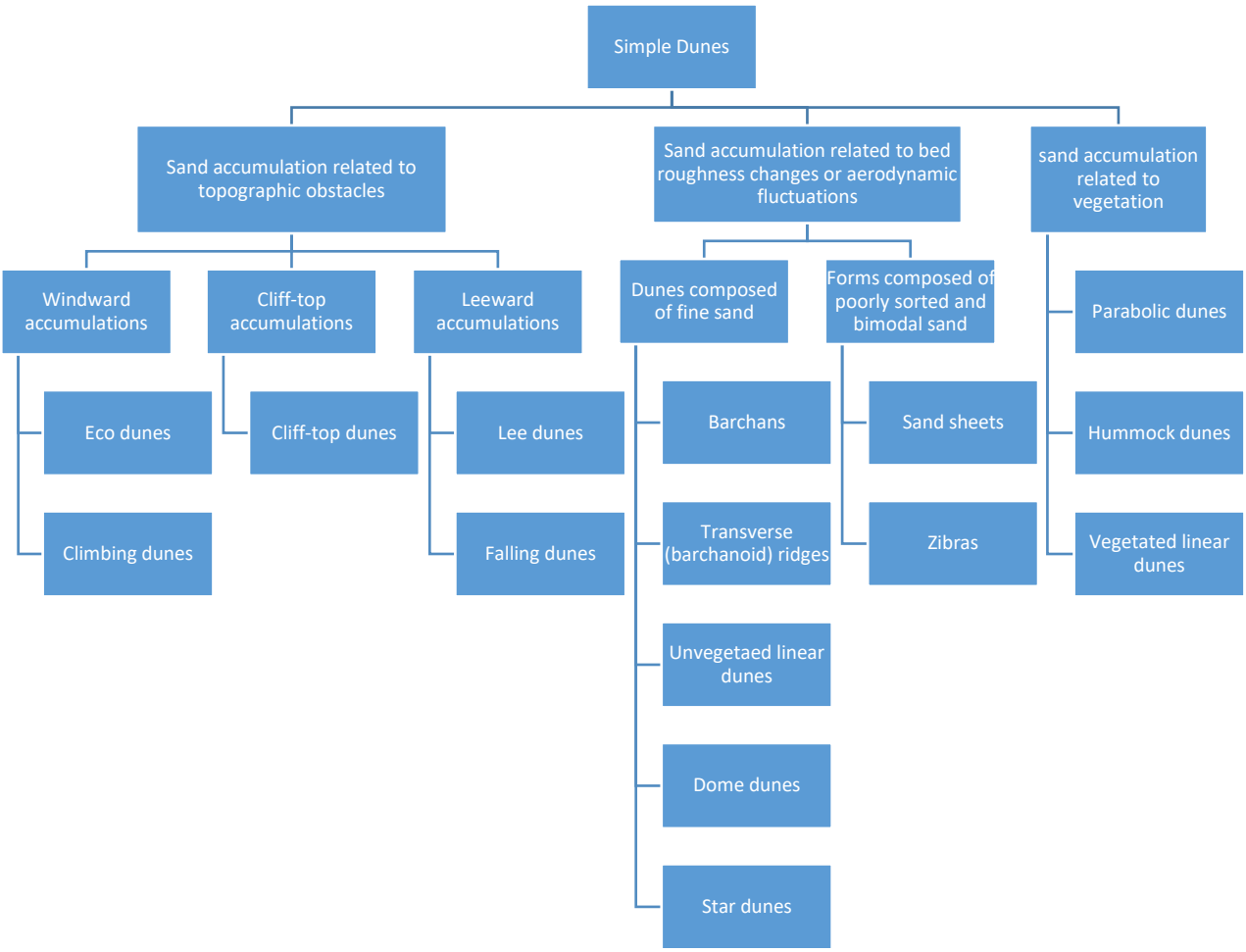

Figure 2.6. Classification of major dune types, (Pye and Tsoar, 2009).

2.1.3 Factors of Dune Morphology

The morphology of sand dunes is determined by the interaction between sand and wind. Therefore, its characteristics have the major influence on the formation of dunes. These characteristics are represented by five main factors (Lancaster, 1995):

1. Variation of wind speed and wind direction, as they play an important role in determining the dune type. The wind speed mainly works as the stirring force that determines the magnitude displacement of the dunes, while the wind direction plays the role of determining the direction in which the sand dune should move; downward wind movement (Kok et al. 2012).
2. Sand supply has a significant impact on dune type (Hersen, 2005, Courrech du Pont et al. 2014, Gao et al. 2015b).
3. Grain size and sorting characteristics of sand have a significant influence on dune size and spacing.
4. Vegetation plays an important role in controlling sand dune movement (Nordstrom et al. 1990, Lancaster, 1995, Pye and Tsoar, 2009).

5. Time is as important as the other factors in the process of dune accretion (Lancaster, 1995).

   The influence of terrain and topography cannot be ignored in dune formation. The topography can be a mountain, a wall of trees or any barrier that changes the behaviour of wind near the surface and controls the movement of sand particles, which results in a deviation in the sand transport direction (Pye and Tsoar, 2009). Figure 2.7 illustrates the main factors of dune morphology.

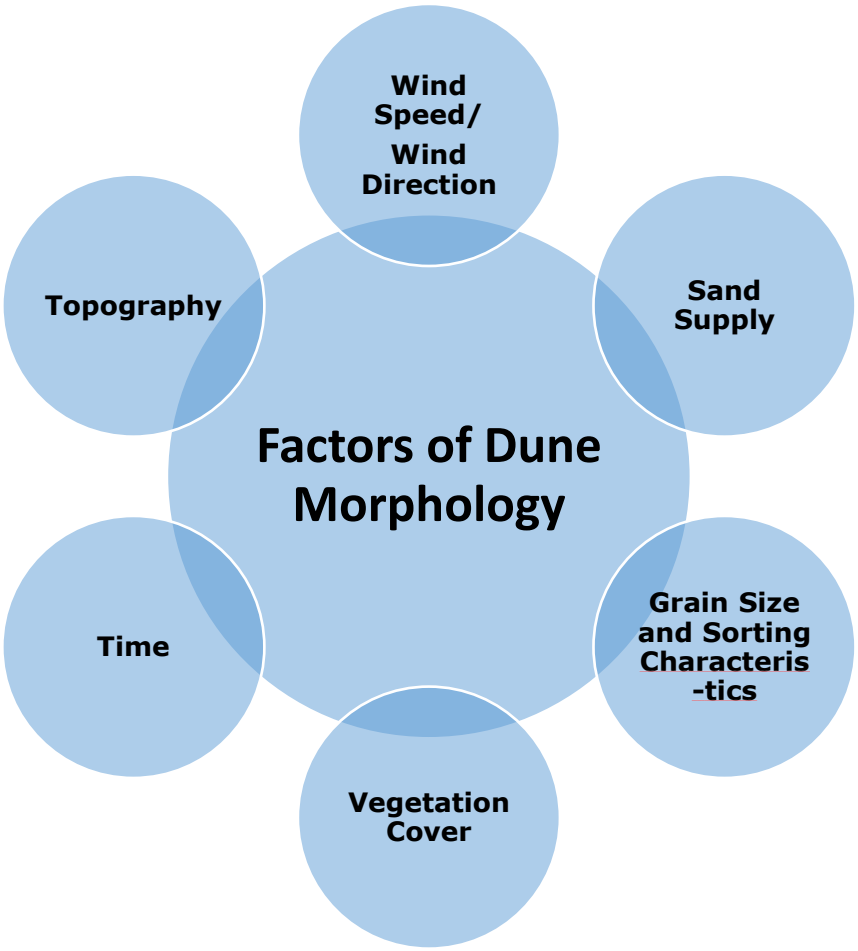

Figure 2.7. Factors of Dune Morphology.

Each one of these factors has a significant impact on the formation and movement of the dunes. The wind is considered the main driving factor in the movement of the dunes (Tsoar, 2001). The wind speed mainly works as the stirring force that determines the magnitude of displacement of the dunes, while the wind direction plays the role of determining the direction in which sand dunes should move, and therefore the dune type (Kok et al. 2012). The same wind regime can result in two different dune orientations based on sand availability (Gao et al. 2015b). Although the impact of wind is significant in the movement of the dunes, dune formation cannot be defined only based on wind behaviour as different dune types can be formed in the same area due to other factors (Zhu et al. 2021).

Studies show that the presence of vegetation cover in sand dune areas works as a slowing mechanism on wind speed and therefore stabilises the movement of sand, resulting in the growth of dunes (Kok et al. 2012, Pye and Tsoar, 2009). Sand dunes with less vegetation migrate actively compared to sand dunes with denser vegetation (Thomas and Tsoar, 1990; Lancaster, 1995). There are multiple, successful examples of the stabilization of sand movement, which involve using different types of vegetation to trap sand and to also to stop it from overwhelming field crops, houses and other landscapes (Levin and Ben-Dor, 2004, Zhang et al. 2004b, Durán and Herrmann, 2006, Alghamdi and Al-Kahtani, 2005, Wiggs et al. 1995, Xu et al. 2015, Hertling and Lubke, 1999, Lubke and Hertling, 2001, Munro et al. 2012).

Although, the impact of each factor in the process of sand movement and dune formation is generally clear, however, it is not possible to separate the impact of each individual factor, as the movement and formation of the dunes is a cumulative result of all these factors.

2.2 Sand Dune Monitoring Techniques

2.2.1 Sand Traps and Empirical Models

Many techniques have been used to monitor and model the changes in sand dunes over the years; each technique has its capabilities and limitations. Sand traps (i.e. horizontal or vertical traps) are one of the conventional techniques that have been used for decades. They are devices that measure, in the field, the sand transport rates by capturing in traps the wind-blown sand grains (Pye and Tsoar, 2009). They measure the intensity of wind erosion and predict potential wind erosion using empirical functional relationships (Woodruff and Siddways, 1965; Pye and Tsoar, 2009). Vertical sand traps are used to measure the horizontal flux of the sand particles while horizontal sand traps are used for measuring the vertical sand flux (Goossens et al. 2000).

A vertical sand trap consists of several stalls that can catch sand particles on different heights and with different grain sizes (Wang and Kraus, 1999). Most aeolian sand transport research involves using vertical sand traps (Rasmussen and Mikkelsen, 1998, Sherman et al. 1998, Goossens et al. 2000, Navarro-Pons et al. 2015, Hilton et al. 2017). These vertical sand traps rely mainly on the wind behaviour in the study area and the sand particles supply as the wind lifts and moves up the sand particles into the vertical traps. These traps can be installed easily and be placed simply at 90 degrees in the direction of the wind. Their efficiency varies due to the changes in wind speed and surface conditions (Wang and Kraus, 1999). Figure 2.8 shows a vertical sand trap used for measuring horizontal sand flux, (Sherman et al. 2014).

Figure 2.8. A vertical sand trap used for measuring horizontal sand flux.

In contrast, a horizontal sand trap is simply a hole dug in the ground that traps all the sand that passes over it (Wang and Kraus, 1999, Goossens et al. 2000, Munro et al. 2012). With blowing wind, sand particles are deposited in the traps and by placing a measuring rod inside the hole and knowing the size of the hole, the amount of sand captured in the hole can be computed and used to assess the volume change and therefore the vertical sand flux. Horizontal sand traps are considered more efficient compared to vertical sand traps as they have a more stable trapping efficiency (Wang and Kraus, 1999). However, one of the disadvantages of horizontal traps is that they cannot be readjusted in case of wind direction variation and also the digging process is hard and time consuming (Wang and Kraus, 1999). Figure 2.9 is an example of a horizontal sand trap used to measure vertical sand flux, (Munro et al. 2012).

Figure 2.9. Horizontal sand trap used for measuring vertical sand flux.

Researchers have developed several empirical formulas to model the transport rate of sand (Lancaster, 1995, Sherman et al. 1998) that use field data acquired by sand traps. Bagnold is the most famous pioneer researcher, who started working early in the 20th century, in the field of monitoring and modelling sand movement using sand traps and empirical models. Most researchers who came after followed him and developed their models on the foundation of Bagnold's models (Bagnold, 1941). Table 2.1 shows different empirical models for the transport of sand dunes by wind.

Table 2.1. Several examples of empirical models used in aeolian sand transport, (modified after Lancaster 1995).

Model	Empirical formulas for sand transport	Description
Bagnold 1941	$q=\sqrt{C\frac{dp}{D}\frac{\rho}{g}u_*^3}$	This equation shows better saltation of sand grains with hard and pebbly surfaces as less momentum is extracted
Kawamura 1951	$q= K\frac{\rho_a}{g}(u_*-u_{*t})(u_*-u_{*t})^2$	Proposed an equation that includes a threshold shear velocity.
Bagnold 1953	$q= \left(1.0.\frac{10^{-4}}{(\log 100z)^3}\right).t.(v-16)$	This equation was modified to overcome the lack of wind shear velocity data

Hsu 1971	$q=1.16.10^{-4}v^3$	This formula has a problem when using wind velocity measurements for estimating the regional sediment transport rates where the shear velocity varies with the surface aerodynamic roughness.
Lettau and Lettau 1978	$q= C\frac{dp}{D}\frac{\rho}{g}u*^2(u_*-u_{*t})$	It does include a threshold shear velocity.
White 1979	$q= 2.61\,u_*^2(1-\frac{u_{*t}}{u_*})(1+\frac{u_{*t}^2}{u_*^2})\rho_a/g$	A universal transport equation that shows good estimates of sand flux

In these formulas, q is the sediment transport rate, (dp/D) is the ratio of the mean size of given sand to that of a 0.25mm sand. C is the sorting coefficient, u_* is the shear velocity, u_{*t} is a threshold shear velocity, K is an empirical coefficient which is a function of the textural characteristics of the sediment, ρ_a is the air density, g is the gravitational acceleration, v is the wind speed and z is the wind measurement height.

There are several limitations of using sand traps and one of the main ones is that sand transport rates measured by sand traps are only considered as an approximation, as the impact of airflow cannot be neglected (Bagnold, 1938a; Pye and Tsoar, 2009). Moreover, the flow of sand grains around the traps can generate vortices, which will lead to localizing the areas of bed erosion or deposition around traps (Pye and Tsoar, 2009), a particular problem in the case of using vertical sand traps (Wang and Kraus, 1999). Another limitation is that during wind storm events these sand traps cannot capture all the passing sand particles due to the high saltation generated effect, which means missing flux data (Goossens et al. 2000).

Bagnold in 1941 shaped the equation of sediment transport mass flux in saltation and creep and defined that the sediment flux increases with the shape of the sand surface where the minimum increment appears with nearly uniform sand, while the sediment flux increases with poorly sorted sands. The maximum increment in the sediment flux tends to occur with pebbly surfaces (Bagnold, 1941). Therefore, sand grains saltate more with rough and pebbly surfaces, as a result of less generated momentum due to the impact of the bed (Bagnold, 1941). This is another limitation of these sand traps, in that they do not measure accurately the impact of vegetation cover and changes in topography on the transport rate of sand.

Despite all these limitations, sand traps can provide vital information about the sand grain size (Sherman et al. 1998, Navarro-Pons et al. 2015), which is essential in understanding its impact on the dynamic dune movement process. However, it is neither accurate enough in measuring the sand transport rate nor cost and time efficient, when it comes to monitoring sand movement over large, inaccessible areas.

Another way of measuring sand flux instantaneously is using the impact responders (Baas, 2004). According to (Davidson-Arnott et al. 2009) there are three main types of instruments for measuring the instantaneous aeolian sand transport rate: (1) instruments that record the acoustic signal generated by the impact of saltating grains on a microphone's screen (Leenders et al. 2005, Ellis et al. 2009); (2) instruments that measures and record the impact of saltating grains on a ring connected to a piezo-electric crystal (Stockton and Gillette, 1990, Stout and Zobeck, 1997, Wiggs et al. 2004, Baas, 2004); and (3) instruments that use load cells or electronic balance to trap sediment and record the weight of sand grains (Jackson, 1996). A significant advantage of most impact responders over traditional sand traps is that the measurable quantities of sand are not required to be captured (Baas, 2004).

2.2.2 Land Surveying Techniques

There are several land surveying techniques that are used for measuring the changes in dunes by repeating surveys (Pye and Tsoar, 2009). These include measuring rods, theodolites, levels, total stations, and RTK-DGPS (Morton et al. 1993, Dornbusch, 2010, Łabuz, 2016). Figure 2.10 shows different land surveying instruments used for monitoring sand dunes changes.

(a) Leica NA720 Automatic Level (b) Leica TS12 Totla Station (c) Leica RTC360 Terrestrial Laser Scanner

(d) Lecia Viva GS 10 GNSS receiver (e) Lecia Viva GS 10 GNSS rover

Figure 2.10. Different land surveying instruments.

Using land-surveying techniques could be more effective for modelling and monitoring small sand dunes, especially in areas with limited visibility of the remote sensing satellite (Hugenholtz et al. 2012). However, the main limitations of using such techniques are that the data collection process is time consuming, and it obtains low-resolution data over large areas, in addition to the complexity of accessible control points or benchmarks. However, the recent development of terrestrial laser scanning devices means that they can now provide an accurate, dense measurement of the dunes (Montreuil et al. 2013, Baddock et al. 2018, Corbí et al. 2018, Terefenko et al. 2019, Xiong et al. 2019). Nonetheless, the process of data collection takes days to cover a small dune field. In other words, this technique is suitable for monitoring the movement of small individual dunes, but it is not considered efficient enough when monitoring large dune fields in desert areas. A practical demonstration of the limitations of the land surveying techniques (i.e. TLS and GNSS) is discussed in section 5.3 in chapter 5. Table 2.2 shows a comparison between different land surveying techniques and their expected accuracy, (Łabuz, 2016).

Table 2.2. Comparison between different land surveying techniques and their expected accuracy, modified after (Łabuz, 2016).

Technique	Data type	Height accuracy range (cm)	Expertise accuracy	Field accuracy. Coverage hour or 1-day research	Points data per measure hour	No. of working people	Cost/day/ device (EURO)
Measuring rods	Points, lines	0.5–1/0.1-1	Low	Line 100 m, plot 10 × 10 m/ 2 h	1–50, scattered or line	1–2	50
Traditional levelling	Points, lines	0.5–1	Medium	Line 250 m long, plot 36 sq.m/h	30–150, line	2–3	200
Total Station (TS)	Points, lines	0.1–0.5	High	100 m line or 10 × 10 plot/h	250–300 Around device	1–2	3,000
DGPS and RTK GPS	Points, lines	0.1–0.5	High / very high	Wide plot 60 × 200 m/ day	200(300) dep. on surface	1–2	5,000-10,000
Terrestrial Laser Scanning (TLS)	Point cloud	<0.01	Very high	c.a. 200 × 200 m/ 0.5 h	2 min/ 30 min	2	14,000

The need for a full understanding of the dune movement is pressing, which requires accurate measuring techniques that take into consideration the frequency of observation and wide coverage of the area of interest. This can more readily be provided using remote sensing techniques.

2.2.3 Optical Remote Sensing Techniques

Remotely sensed images have been commonly used for monitoring and modelling the changes in the earth's surface and related environmental phenomena for decades (Willis, 2015). Optical remote sensing is developed on sensing passive electromagnetic radiations (i.e. visible radiation, infrared and thermal radiations) where the source of radiation is the sun and the sensor is mounted on the satellite. The sensor receives the reflected electromagnetic waves from objects on the earth's surface or in the case of thermal radiation the earth's surface emits thermal energy which is also detected by the sensors (Tempfli et al. 2009, Mather and Koch, 2011, Lillesand et al. 2015). The backscattered waves shape the images with each pixel in that image having a different energy response from different characteristics of the area that it represents. Figure 2.11 illustrates the energy interaction with the atmosphere and the earth's surface, (Tempfli et al. 2009).

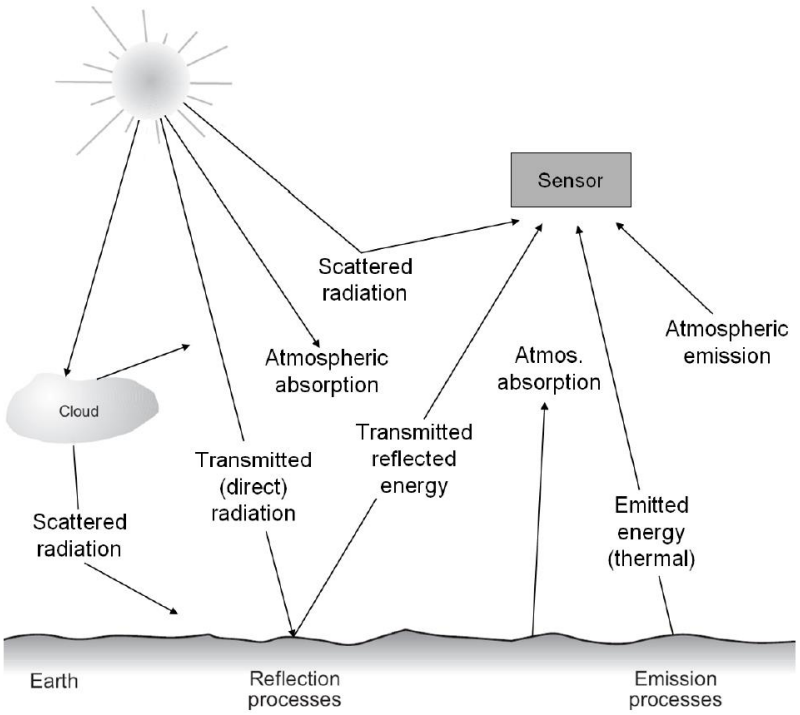

Figure 2.11. Energy Interaction with the Atmosphere and the Earth's Surface.

One of the first legacy satellites that have been used to collect optical images is LandSat, which has been running since 1972 providing a wide range of data for multiple environmental studies (Willis, 2015). Many multispectral satellites were launched into space for various purposes following LandSat. A widely used one is Sentinel 2. It is a space mission launched in 2015 by the European Space Agency (ESA) for monitoring the earth's land surface changes (Phiri et al. 2020). The constellation of Sentinel-2 consists of two polar-orbiting sun-synchronous satellites, providing worldwide coverage of the earth, with a wide swath width of 290km, a spatial resolution of 10m x 10m in the visible and near infra-red bands and a high temporal resolution of 10 days in the equator with one satellite and 5 days with the two satellites (Sentinel 2A and 2B) and less than 6 days in mid-latitudes (Sentinel).

One of the data services that provide free support for various collections of satellite images is Earth Explorer from the United States Geological Survey (USGS) (https://earthexplorer.usgs.gov/). It is a data plug-in where different types of raw remote sensing data can be downloaded, in addition to some processed data such as topographic maps and normalized difference vegetation index (NDVI). Similarly, the Copernicus services hub is the data platform for Sentinel products, where it provides access to all the collected images in addition to the operational details and metadata of the acquisition process (https://scihub.copernicus.eu/). Table 2.3 provide a brief summary of some of the available optical satellites.

Table 2.3. A brief summary of the available optical satellites; after (Willis, 2015).

Satellite	Mission	Revisit Time	Visible and NIR Bands Spatial Resolution (m)	Scene Size	Availability
LandSat	1972-present, Different missions are up to space (LandSat1-5/6), LandSat-9 just been Launched	LandSat 7,8 every 16 days	30m, with a panchromatic band with 15m of spatial resolution	170 km x 185 km	Free access, USGS
SPOT	1986-present	2-3 days, and 1 day for Spot-6/7	Spot 1-4 (10m) Spot 5 (2.5m) Spot-6/7 (1.5m)	60km X 60km, 120kmX 120km,	Licensed Access
MODIS	1999-Present	1-2 days	250m/500m	2,330km x 2,330km	Free access, USGS
IKONOS	1999-2015	Approx. 3 days	Panchromatic 0.80m Multispectral 2.4 m	11.3km x 11.3km	Licensed Access
ASTER	1999	16 days	15m visible NIR, 30m shortwave IR, 90m thermal IR	60 km x 60 km	Free access, USGS
QuickBird	2001-2015	1-3.5 days	Panchromatic 0.61m Multispectral 2.4m	16.8Km X 18Km	Licensed Access

Worldview1	2007	1.7 days	Panchromatic 0.50m	17.6Km x 14Km	Licensed Access
Pleiades	2011	24 Hours	0.70m spatial resolution	20km x 20km	Licensed Access
GeoEye-1	2008	less than three days	Panchromatic 0.46 m Multispectral 1.84 m	15km x15km	Licensed Access
Sentinel 2	2014-present	6 days	10m spatial resolution	Level-1C 100 km x 100km	Free access, EESA
PlanetScope	2018-present	daily	3m	24 km x 8 km	Licensed/ Scientific Access

Many techniques and spatial analysis tools that use optical remote sensing images have been developed for detecting and modelling the changes on the earth's surface and modelling various environmental phenomena (Lu et al. 2004). Some of these techniques are image differencing, image ratioing and principal component analysis (PCA) (Mas, 1999, Singh, 1989), image classification (Ratnayake, 2004, Gómez-Chova et al. 2015, Lu and Weng, 2007) and normalized difference vegetation index (NDVI) (Pettorelli et al. 2005).

These techniques have been applied for monitoring vegetation cover and forest canopy estimation (Hayes and Sader, 2001, Ratnayake, 2004, Nuri et al. 2016, Houborg et al. 2015), land cover changes (Kharazmi et al. 2018, Chang et al. 2018, Regasa et al. 2021, Winkler et al. 2021), digital surface model generation (Barbarella et al. 2017, Nasir et al. 2015, Toutin and Cheng, 2002), flood mapping (Shaker et al. 2008, Opolot, 2013, Mateo-Garcia et al. 2021). Furthermore, some of them have been applied for monitoring and modelling the changes in sand dunes (Gómez et al. 2018).

2.2.3.1 Researchers' experiences in detecting sand movement using optical remote sensing and GIS models

This section is devoted to reflecting on different research experiences where optical remote sensing and GIS techniques have been applied for monitoring and modelling desertification and sand movement. Many studies were undertaken to analyse the capabilities of remote sensing and GIS techniques for the estimation of desert expansion and sand drifting rates; this was commonly achieved by combining these two techniques into one robust monitoring system (Albalawi and Kumar, 2013, Abdelrahim Elhag et al. 2019, El-Hadidy, 2020, Lam et al. 2011, Lan et al. 2013, Abou El-Magd et al. 2013, Potter and Weigand, 2016, Hadeel et al. 2010, Aydda et al. 2020, Pradhan et al. 2018, Ahmady-Birgani et al. 2017).

Most researchers focused on developing different spatial analysis techniques to detect and model land degradation, where the normalized difference vegetation index (NDVI) and image classification are the most commonly used methods (Albalawi and Kumar, 2013, Higginbottom and Symeonakis, 2014, ED Chaves et al. 2020, Yengoh et al. 2015, Hadeel et al. 2010, Lu et al. 2004, Lu and Weng, 2007). The NDVI is computed from the ratio difference of the satellite image's reflection in the red and near-infrared bands (Pettorelli et al. 2005). It distinguishes the variation in health and changes in coverage of vegetated areas. By comparing different NDVI maps for a certain period of time it reveals the level of increase or decrease of the vegetation land cover. This is a preliminary stage to understanding the characteristics of land cover changes in arid and semi-arid areas, as vegetation is one of the main factors for assessing land degradation. Additionally, this index indicates the presence or absence of vegetation in dune field areas, where the presence of vegetation plays a significant role in controlling the movement of the dunes.

(Salih et al. 2017) used two models, the spectral mixture analysis (SMA) and change vector analysis (CVA) methods, for modelling desertification in arid and semi-arid areas in Sudan. Multi-temporal LandSat images were used to analyse the rate of desertification between 1987 and 2014. Those two techniques demonstrated high capabilities in characterizing and mapping desertification in this arid and semi-arid environment.

Although modelling land degradation using spatial analysis techniques showed significant ability in the assessment and monitoring of land degradation, it is essential to develop techniques that are oriented to detect sand dune movement. These techniques must focus on studying the morphometric changes of sand dunes. Quite a large group of researchers have developed examples of this (Hugenholtz et al. 2012, Ahmady-Birgani et al. 2017, Ghadiry et al. 2012, Gómez et al. 2018, Chen et al. 2017, Pradhan et al. 2018, Aydda et al. 2020, Potter and Weigand, 2016, Abou El-Magd et al. 2013, Els, 2017, Lam et al. 2011, El-Hadidy, 2020, del Valle et al. 2008).

(Ghadiry et al. 2012) developed a GIS-based model for an automated sand dune extraction process using remote sensing images, in order to assess the rate of sand movement. Two Spot images captured in 1995 and 2007 were used to detect the movement of sand dunes in the Dakhla oases area. An image subtraction was performed to determine the movement between the two images' dates. This model provided statistical information about the sand dunes migration rate, placing it between 3-9m per year.

In 2012, some researchers tried to understand the relationship between remote sensing technologies and spatial analysis of aeolian sand dunes, to understand the dune activity and its patterns (Hugenholtz et al. 2012). They stated that the recent revolution of remote sensing technologies and numerical modelling software has resulted in powerful techniques for modelling quantities and patterns of sand dunes. Also, that remote sensing and spatial analysis techniques play a vital role in understanding the dune activity. However, there are some challenges that face these techniques when monitoring and quantifying sand movement; such challenges are important when the surface reflectance characteristics are for a partly vegetated dune field.

A sand dune encroachment vulnerability index (SDEVI) was developed to assess the dune encroachment in Nouakchott, Mauritania, relying on remote sensing and GIS techniques (Gómez et al. 2018). This model, Equation (2.1), includes some morphometric and topographic data, such as wind direction (DirFa), wind speed (SpeFa), slope (SloFa), height (HeiFa), vegetation cover (VegFa), land use and soil type (SoiFa), in order to compute the changes of sand cover and identify most vulnerable areas to sand encroachment.

$$SDEVI = SpeFa + DirFa + HeiFa + SloFa + LanFa + VegFa + SoiFa \qquad \text{Equation (2.2)}$$

The study showed that, by using this vulnerability index, areas vulnerable to sand encroachment can be identified and monitored and the decision making process in land management projects can be supported (Gómez et al. 2018).

In 2017, research was undertaken to model the Brittas-Buckroney dunes on the south-eastern coast of Ireland (Chen et al. 2017). This research involved using unmanned aerial vehicle (UAVs) technology to collect high resolution images in order to map the topographical changes and generate vegetation maps of coastal dunes complexes. The stages of map generation included: setting ground control points, flight planning, data collection, data processing and results analysis. Pix4D and ArcGIS software were used for processing and analysing the data and generating topographical maps. This research concluded that UAVs could improve the quality of mapping in coastal areas. However, this conclusion was also constrained by the experienced weather conditions (e.g. wind, rain and low light) along the coast at the time of acquisition.

On a larger scale, high altitude satellites such as MODIS have been used to detect and monitor dust storms (Miller, 2003, Samadi et al. 2014, El-ossta et al. 2013, Qu et al. 2006, Shahraiyni et al. 2015, Butt and Mashat, 2018, Albarakat and Lakshmi, 2019, Li et al. 2010, El-Askary et al. 2002, Boloorani et al. 2014). For instance, the journey of dust plumes initiated from the Sahara Desert in Africa, particularly from northeast of Lake Chad, is observed every year crossing the Atlantic Ocean and deposited in the Amazon Forests (Koren et al. 2006). Over 40 million tunes of sand are deposited providing these forests with essential nutrition such as phosphate (Koren et al. 2006). Figure 2.12 shows a dust storm captured by MODIS and crossing the Atlantic Ocean from West Africa on the 2nd of March 2003, (https://www.nasa.gov/multimedia/imagegallery/image_feature_22.html).

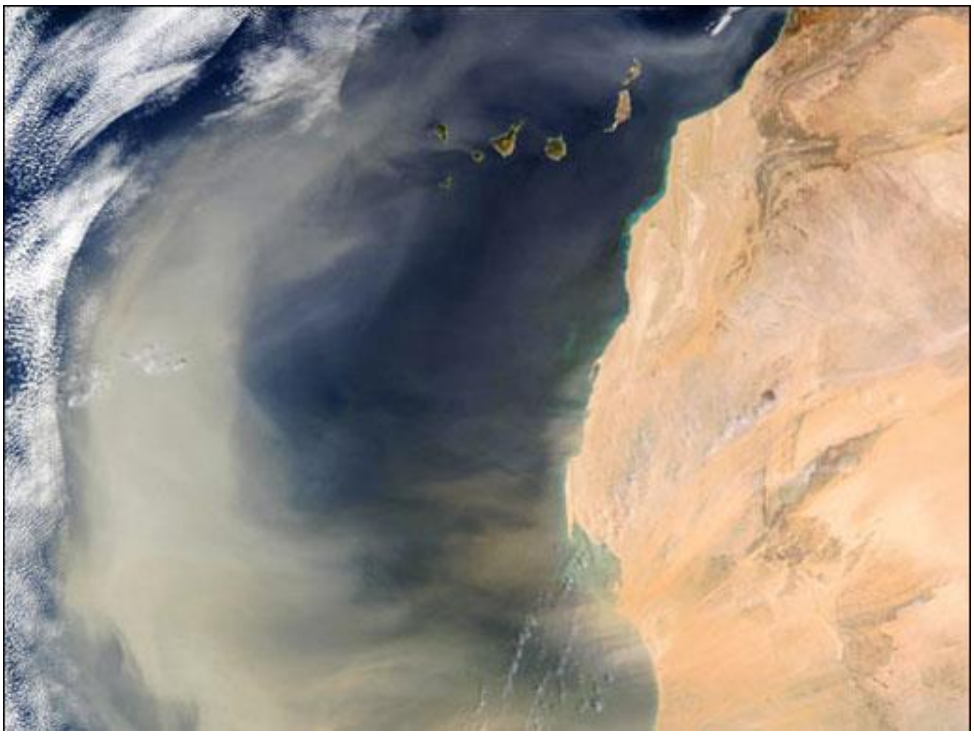

Figure 2.12. A dust storm captured by MODIS crossing the Atlantic Ocean from West Africa on the 2nd of March 2003.

NASA has developed several sensing techniques, such as the High Resolution Imaging Experiment (HiRISE) (McEwen et al. 2007) and Compact reconnaissance imaging spectrometer for Mars (CRISM) (Murchie et al. 2007) on the Mars Reconnaissance Orbiter (MRO) mission (Zurek and Smrekar, 2007). One of the applications of these techniques is monitoring the movement of the dunes on Mars (Silvestro et al. 2010). These techniques demonstrated that the dunes on Mars migrate (Silvestro et al. 2010) and have similar behaviour to the dunes on the Earth (Bridges et al. 2012). Figure 2.13 A HiRISE image showing sand dunes in the Nili Patera area on Mars, (https://mars.nasa.gov/resources/22285/a-dune-field-near-nili-patera/).

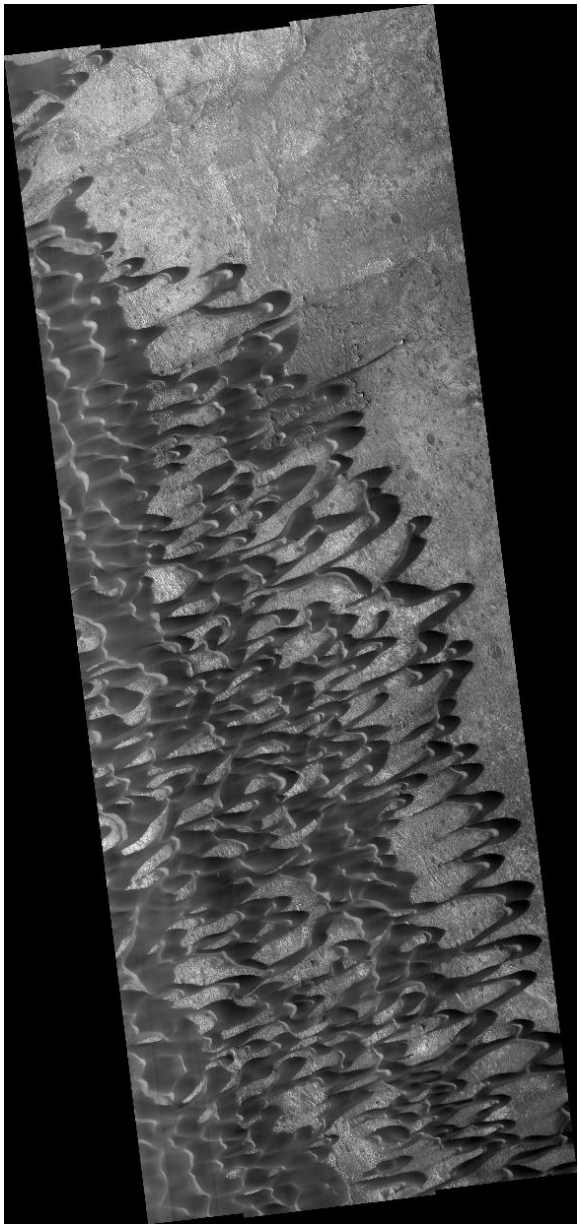

Figure 2.13. A HiRISE image showing sand dunes in the Nili Patera area on Mars, February 05, 2019. Credit: NASA/JPL-Caltech/University of Arizona.

It can be concluded that optical remote sensing techniques are considered one of the best techniques for measuring and monitoring the movement of sand dunes. However, they only provide this for the horizontal component of the dunes, missing the vertical. In addition, there are some problems that remain unsolved, such as the mixed pixel problem (Ettritch et al. 2018), the effects of topography, the image commensurability and model parameterization (Hugenholtz et al. 2012). Medium resolution images might include different distinct features mixed in one pixel, which might result in misclassification of the land cover type (Ettritch et al. 2018). In addition, the high spectral similarity between dune pixels might cause the same issue (Afrasinei et al. 2018).

2.2.3.2 COSI-Corr for Sand Dune Motion Tracking

Co-registration of Optically Sensed Images and Correlation (COSI_Corr) is a technique developed at the California Institute of Technology, (Caltech) (Leprince et al. 2007, Ayoub et al. 2017). This technique suggests an automated processing chain for co-registering and comparing optical satellite images to accurately measure ground deformations. The fundamental process consists of four stages: (1) projecting the image pixels from a satellite image focal plane to a projected ground reference system, (2) performing a resampling on the images based on the calculated projection system in order to generate ortho-rectified images. This is then followed by (3) a stage of optimization of the satellite viewing parameters to a reference frame needed to determine the magnitude of distortions and misregistration due to the uncertainties of the imaging system and the topography between the two ortho-rectified images and to prepare it for the last step (4) the correlation to measure the displacement. The technique requires the ancillary data of the raw images which contain details of the geometry of the satellite at the acquisition time, and also it requires a digital topographic model with a resolution close to the ground resolution of the images needed for the ortho-rectification stage (Leprince et al. 2007).

The first application of COSI-Corr was to detect a seismic rupture in the Himalaya after the M_w 7.6 Kashmir earthquake that took place on the 8th of October 2005 (Avouac et al. 2006). Two ASTER optical images were used, prior to and post the event, to measure surface slip and geometry of the rupture. This provided an early assessment of the damages of the devastating earthquake.

COSI_Corr has been also used to detect the deformation of glaciers and landslides (Leprince et al. 2008, Türk, 2018), sand movement (Vermeesch and Drake, 2008, Necsoiu et al. 2009, Hermas et al. 2012, Vermeesch and Leprince, 2012, Scheidt and Lancaster, 2013, Al-Ghamdi and Hermas, 2015, Sam et al. 2015, Al-Mutiry et al. 2016, Baird et al. 2019) and also for the detection of sand movement in Mars (Bridges et al. 2012).

A common element between all these studies is the long-time interval (months and years). This affects the computed dune migration rate as it disregards the migration of the dunes that occur in between these periods due to the rapid activity of the dunes. For instance, (Vermeesch and Leprince, 2012) applied COSI-Corr to measure the long term migration rate of sand dunes from optical satellite images in Central Sahara to study the dune changes over a period of 45 years. This study was oriented to provide wind information in desert areas based on the migration rates of the dunes where images with a time interval of 3-6 years were used, this is a quite large gap when modelling the movement of sand dunes as no dynamic dune motion that occurs in between these periods will be observed or captured. Therefore, to overcome that, using satellite images with the smallest acquisition time will accommodate the changes that occur at shorter intervals and thus result in a much more accurate estimate of the dune changes.

The COSI-Corr technique faces some challenges in the co-registration of the satellite images due to several factors; limitations in the characteristics of the optical image sensors, variation in the spacecraft altitude during the image collection, and errors in the used digital elevation model in addition to inaccurate resampling of the images. All of these affect the accuracy of the measurement (Leprince et al. 2007). Although COSI-Corr shows high ability in the detection of ground deformation, it only detects this displacement horizontally.

2.2.4 Radar Remote Sensing Techniques (SAR)

With the recent development and increase in the number of orbiting radar satellites, earth observation monitoring techniques have seen a wide development over the last decade. Radar is an active remote sensing technique that uses the microwave bands of the electromagnetic spectrum (e.g. L band, C band and X band) to form images of surfaces (Tempfli et al. 2009). The main advantages of radar sensors are that they can record data day and night and also under various environmental conditions, as the radar waves can penetrate the clouds (Sinha et al. 2015), and that gives a variety of measurement options when it comes to modelling environmental phenomena.

The measurement mechanism of Synthetic Aperture Radar (SAR) depends on the phase differences between the transmitted and backscattered waves from the reflecting objects in sequential images. By knowing the phase difference and the speed of transmission, the movement of objects can be identified in relation to the source of the radiation (Zhou et al. 2009). Figure 2.14 shows a geometric model of SAR system.

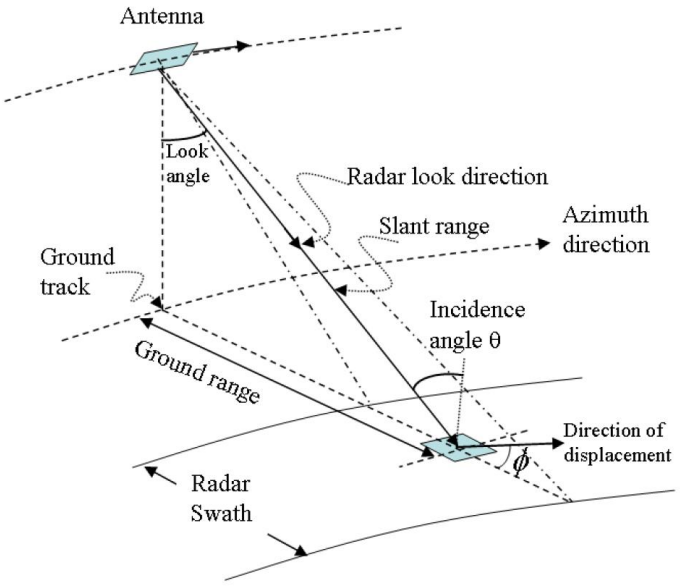

Figure 2.14. A geometric model for SAR system, (Zhou et al. 2009).

SAR images are formed based on the received echoes from each emitted pulse in the azimuth direction, where these echoes are arranged by their transmission and receiving time, generating the slant range resolution. The slant range is the distance between the antenna and the ground pixel. As the radar sensor moves, its antenna location changes and receives different returned pulses from different features. The ground pixel size is determined based on the cross track resolution and the along track resolution (Zhou et al. 2009).

The recorded information on the radar images includes: the amplitude; where it shows the capacity of each ground pixel on the terrain in reflecting an amount of energy; and the phase, which records the history of the signal from emission to its return and known as the single look complex (SLC) (Zhou et al. 2009). Figure 2.15 shows the relationship among the amplitude, phase and wavelength of the radar signal. Equation 2.2 shows the computation of the phase return of a single scatterer, (Zhou et al. 2009).

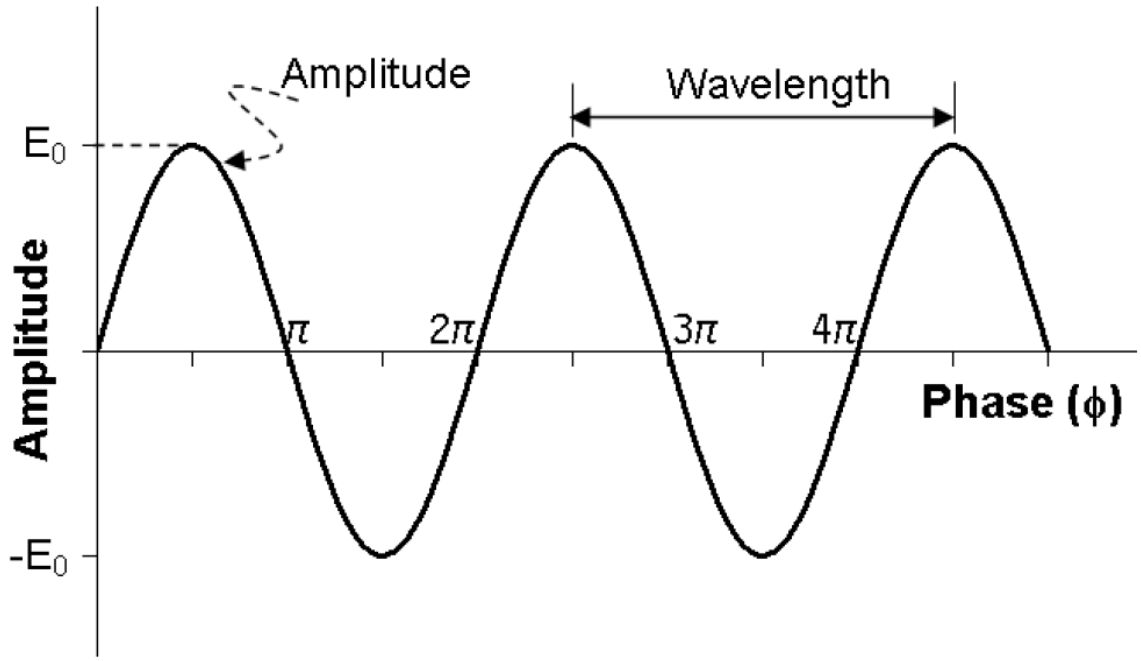

Figure 2.15. Relationship among the amplitude, phase and wavelength of a radar signal.

$$\varphi = 2R_p 2\pi/\lambda + \varphi_{scat} \qquad \text{Equation (2.2)}$$

Where φ is the phase, R_p is the range between radar and the point on the ground, λ is the radar signal wavelength, and φ_{scat} is the scattering phase.

The radar signal can be transmitted and received horizontally or vertically, which is known as the polarization (Tempfli et al. 2009). Different polarizations (i.e. HH, VV, HV or VH) form different radar images, where each type of these images has a specific purpose and use (Blumberg, 1998, Balzter, 2001). Figure 2.16 shows information about the different radar bands that are used for sensing by SAR platforms, (Tempfli et al. 2009).

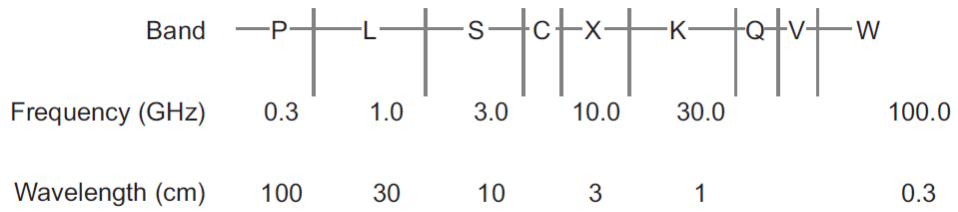

Figure 2.16. Radar bands on the microwave spectrum.

One of the most developed radar techniques is the interferometric synthetic aperture radar technique (InSAR) (Zhou et al. 2009). It uses two images taken from different locations, different incidence angles or at different times to generate differences of phase for each pixel in an image which is known as interferogram (Zhou et al. 2009). Interferograms are used to generate the topography of the landscape, in addition to subsequently estimating its amount of displacement. This displacement is represented in lines of equal phase that appear on the interferogram and are known as fringes. It represent the amount of movement and it is counted from a reference point where the displacement is known to be zero (Zhou et al. 2009). Figure 2.17 shows radar sensor capturing two different InSAR images, (Chang et al. 2011).

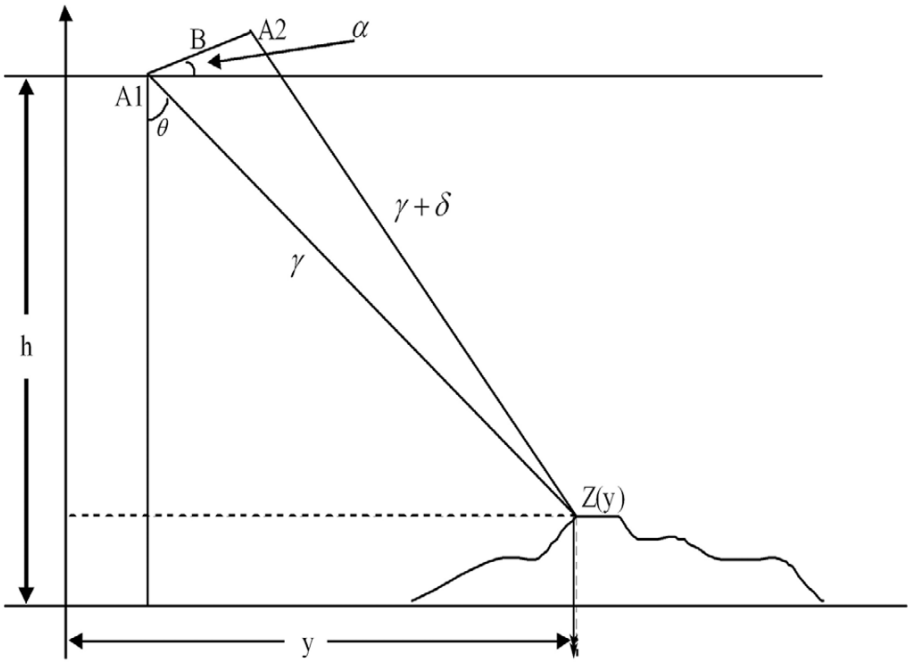

Figure 2.17. A Radar sensor capturing two different InSAR Images.

Where Z(*y*) is the topographical height, *h* is the satellite altitude, *λ* is the wavelength of radar wave, *B* is the baseline length, *θ* is the angle of view, and α is the angle of inclination.

There are some factors that affect InSAR interferograms such as atmospheric conditions $\Delta\varphi_{atm}$ (Tempfli et al. 2009), the distance between the antenna and the ground pixel (Zhou et al. 2009), surface topography (Osmanoğlu et al. 2016), the dielectric properties of the ground surface $\Delta\varphi_{dielectric}$ and the system noise (Zhou et al. 2009). However, there are many techniques that can be applied to remove all these noises and distortions in the data collected by radar sensors, in order to distinguish the amount of deformation. Equation 2.3 shows the form of two registered phase images.

$$\Delta\varphi = \frac{4\pi}{\lambda}\,\Delta D_0 + \frac{4\pi}{\lambda}\frac{H\mathrm{B}_{\perp}}{R\sin\theta} + \frac{4\pi}{\lambda}B_{\parallel} + \Delta\varphi_{atm} + \Delta\varphi_{dielectric} + \Delta\varphi_{pn} + 2n\pi \qquad \text{Equation (3.3)}$$

Where $\Delta\varphi$, is the phase difference between two registered phase images, ΔD_0 is the line-of-sight (LOS) displacement, λ is the wavelength of the SAR system, $\mathrm{B}_{\perp}\ and\ B_{\parallel}$ are the vertical and parallel components of the baseline orbit separation of the SAR image pair, H is the height of a pixel above a reference surface, R is the slant range between the ground pixel and the antenna of the master image, θ is the local incidence angle, $\Delta\varphi_{pn}$ is phase noise, $2n\pi$ is the ambiguity associated with phase wrapping (Zhou et al. 2009).

Several satellite radar missions have been launched into space for the purpose of modelling and monitoring the changes on the earth's surface and for monitoring different environmental phenomena. Table 2.4 shows some information on the available radar satellites (Massonnet and Feigl, 1998, Zhou et al. 2009).

Table 2.4. Information on the available radar satellite missions.

Satellite	Mission	Data Acquisition Interval (days)	Wavelength(cm) Band	Spatial Resolution(m)	Data Availability
ERS1	1991-2000	3,5, 168	5.66cm (C)	along-track ≤ 30 m, cross-track ≤ 26.3 m	Free Access
ERS2	1995-2011	35	5.66cm (C)	along-track ≤ 30 m, cross-track ≤ 26.3 m	Free Access
ENVISAT/ASAR	2002-2012	35	5.63cm (C)	30m x 30m	Free Access
RADARSAT-1	1995-2013	24	5.66cm (C)	9m x (8,9)m	Limited Data Access
SRTM	2000	N/A	5.6cm (C)	30m 90m	Free Access to its

					products (DTM)
JERS-1	1992-1997	44	23.5cm (L)	18m (range) x 18m (azimuth, 3 looks)	Limited Data Access
TerraSAR-X	2007-Present	11	3.125cm (X)	2m x (1.5-3.5)m	Limited Data Access
Sentinel-A1	2014-Present	12	(C)	20 x 5 m	Free Access
Sentinel-B1	2016-Present	12	(C)	20 x 5 m	Free Access
COSMO-skyMed, 1,2,3,4	2007-present	5	(X)	1 x 1 m	Limited Data Access

Several data access services provide a free download of SAR data. Table 2.5 shows available data access services to SAR data.

Table 2.5. Data Access Services of SAR Data

Data Access Service Provider	SAR data
USGS United States Geological Survey	SRTM (i.e. End product DEM)
EOLI-SA	ENVISat and ERS
Copernicus Open Access Hub	Sentinel-1
Alaska Satellite Facility (ASF)	Sentinel-1 Data, ERS1/2, ALOS, JERS-1, RADARSAT-1, AIRSAR, UAVSAR, SIR-C

For the last decades researchers have been using InSAR for modelling the ground surface deformation of the earth (Zhou et al. 2009, Chen et al. 2000), changes in forests canopy (Balzter et al. 2007, Deutscher et al. 2013), estimation of biomass (Sinha et al. 2015), water level changes (Kim et al. 2009), and detecting land subsidence (Tosi et al. 2015, Fan et al. 2011). In addition, the technique has been used for the application of estimating the volume of ice lands (Maghsoudia et al. 2013). InSAR technique has been used significantly to monitor the impact of different geohazard events such as floods (Refice et al. 2014), volcanos (Pedersen and Sigmundsson, 2006), landslides (Tantianuparp et al. 2013) and earthquakes (Massonnet and Feigl, 1998, Suresh and Yarrakula, 2020), where the technique provides an early warning system.

Time series analysis is applied to InSAR data for monitoring and modelling the displacement of a specific phenomenon over a certain period (Osmanoğlu et al. 2016). Many algorithms have been developed for time series analysis of InSAR data, such as the coherent pixels technique (CPT), Delft persistent scatterer interferometry (DePSI), interferometric point target analysis (IPTA), permanent scatterer InSAR (PSInSARTM), persistent scatterer pairs (PSP), quasi persistent scatterers (QPS), small baseline subset (SBAS), stable points network (SPN), SqueeSAR, and Stanford method for persistent scatterers (StaMPS) (Osmanoğlu et al. 2016).

All these algorithms produce a near continuous record of displacement by connecting wrapped phase measurements. In other words, producing an unwrapped phase time series of InSAR phase measurements explains the amount of deformation over a certain period. However, there is no optimal algorithm that can be applied for monitoring the deformation in all cases, which makes the development of algorithms for time series analysis of InSAR data an area of active research.

2.2.4.1 InSAR application in detecting sand dunes movement

In 1998, a NASA report was published to distinguish desert dune forms by polarimetric synthetic aperture radar (SAR) (Blumberg, 1998). The report reflected SAR observations of desert dune fields in North America, Bolivia and Australia where AIRSAR was used and in Namibia using SIR-C/X-SAR. It also reviewed the use of polarimetric and multi-wavelength SAR and reflected on the advantages of the various combinations. The report stated that SAR data are considered very useful for dunes mapping, as it has the ability to control the illumination parameters (i.e. look angle, wavelength and polarization) (Blumberg, 1998). Moreover, the SAR responses to surface roughness make it a useful technique for mapping dunes forms. The report showed that using longer wavelengths (i.e. P-band 68cm and L-band 24cm) has advantages over using shorter wavelengths (i.e. C-band 5.6cm) by providing better contrast. In addition, it stated that the co-polarized channels (i.e. HH and VV) are considered the best for modelling dune forms and differentiating between dune types, while the cross-polarized channels (i.e. HV and VH) could be used for providing information about vegetation which is needed for discriminating between active and inactive dunes (Blumberg, 1998).

InSAR has been used for the application of estimating the volume of sand dunes using very high frequency VHF and Ka radar bands, where they can penetrate the sand soil and provide the underlying terrain topography (Maghsoudia et al. 2013, Nashashibi et al. 2011).

In 2011, a group of researchers used Differential Interferometric Synthetic Aperture Radar (DInSAR) techniques to monitor the desert height changes due to sandstorms in Beijing (Chang et al. 2011). They applied a series of procedures (i.e. image configuration, correction of the earth flattening, phase unwrapping and geocoding) on a pair of descending EnviSat ASAR images acquired on January 20 and October 26 of 2004, to monitor the changes in the Hunshandake Sandy Land. They detected a deformation ranging between -160 to +120 cm with height increase in most of the study area and a few locations with height decrease in other parts. They concluded that DInSAR is an important technique for detecting changes in the height of deserts. Moreover, it can be used as a tool for modelling sandstorm erosion and deposition. The long time interval between the two InSAR images (280 days) has resulted in some distortions.

Other research looked into the use of coherence maps generated by the InSAR technique to analyse the dynamics of sand dunes on the southern coast of Israel (Havivi et al. 2018). High-resolution TerraSAR-X (TSX) radar images of the period between February and July 2012 were used with metrological data (i.e. wind and rainfall records).

They stated that coherence maps show the stability of individual dunes as a function of time. Moreover, they found that dunes' crests are more stable than windward slopes and the degree of stability depends on the distance of dunes from the sea. This study suggests that InSAR decorrelation can be used for sand dunes characterization studies.

An automated procedure was developed to quantify the dune dynamics for isolated barchan dunes using C band InSAR satellite images (Delgado Blasco et al. 2020). The method uses an adaptive parametric thresholding algorithm and geospatial analysis tools to compute the dune movement. This has been applied to monitor the movement of barchan dunes in Mauritania and Egypt. The measured dune migration rate was 2-6 m/year in the NNW-SSE direction and 11-20 m/year NNE-SSW for Egypt and Mauritania dunes fields, respectively. This result has been validated manually using optical imagery from Google earth, where agreement between both results was observed.

(Song et al. 2020) used the InSAR temporal decorrelation model to study dune stability by distinguishing the surface changes in sand dunes over time. They constructed a temporal decorrelation model that combined thermal and spatial decorrelation for dune areas and validated that model using the sand drift potential and precipitation. The evaluation of the model revealed that temporal decorrelation of InSAR can characterise the activity of the dunes.

(Kim et al. 2020) developed an interferometric synthetic aperture radar time series approach to defining the ongoing aeolian erosion in the Gobi Desert. The mapping scheme uses pairs of Sentinel 1 InSAR images to generate phase coherences for a period of time and the means of principle component analysis for the extraction of the topographic persistence, indicative of surface erosions. The technique is suggested for mapping land erosion dust sources/sand seas; therefore, it will contribute to tackling desertification.

(Manzoni et al. 2021) developed a temporal stability index to characterize the level of stability for a target point in the desert. It also provides an assessment mitigation plan for the protection of habitat environments from sand movement impact. The method suggests the synthetic aperture radar (SAR) coherent methods and long-time series SAR images contribute to the sand mitigation measures. In addition, the SAR coherence is considered suitable for the detection and evaluation of sand dune movement.

2.2.5 Airborne LiDAR (Light Detection and Ranging)

Airborne light detection and ranging (LiDAR) or laser scanning is an active remote sensing technique in the application of modelling the surface of the earth (Wehr and Lohr, 1999, Juha Hyyppä, 2009, Jaboyedoff et al. 2012, Gallay, 2013, Maltamo et al. 2014, Okyay et al. 2019). The Airborne LiDAR system consists of a Global Navigation Satellite System (GNSS) receiver and inertial measuring unit (IMU) for the determination of the position and a laser system which emits and receives the transmitted and backscattered light pluses (Wehr and Lohr, 1999). The principle of Airborne LiDAR uses the time of flight between the transmitted and backscattered laser pulses to measure the distance between the LiDAR sensor and the reflecting surface (Wehr and Lohr, 1999). This distance is calculated using the following equation:

$$D = c(\frac{t}{2}) \qquad \text{Equation (2.4)}$$

D is the distance between the sensor transmitter and the reflecting object, c is the speed of light and t is the time of flight between the transmitted and backscattered laser pulses. The terrain topography is computed using the measured distance (D) for each point and the GNSS and IMU data are used to determine the exact location and altitude of the aircraft at the time of exposure. The height of flight determines the width of the scanned area (Gallay, 2013). The airborne LiDAR point clouds can be used to generate digital elevation models (DEM) of the observed surface. This can be achieved by using different filtering approaches to distinguish the LiDAR points into ground and feature points.

The accuracy of Airborne LiDAR data depends mainly on the positioning and orientation accuracies of the GNSS and IMU (Hodgson and Bresnahan, 2004; Gallay, 2013), (Wehr and Lohr, 1999), in addition to the surface reflection, terrain slope, atmospheric conditions

and the density of vegetation cover (Gallay, 2013). This accuracy has increased with the latest advancement in the GNSS and IMU positioning techniques.

This technique can provide data day/night and under different weather conditions (Gallay, 2013). It also has several advantages over the conventional techniques where it maps the earth's surface and provides very dense and accurate three dimensional spatial data generated over a short period of time (Woolard and Colby, 2002). In addition, it has the capability of penetrating small gaps in the canopy, which allows the user to render the topography and morphological changes (Kraus and Pfeifer, 1998, Thomas et al. 2006, Okyay et al. 2019).

Airborne LiDAR data has been used widely for monitoring coastal changes: sediment volumetric changes (Meridith et al. 1999), shorelines (Stockdonf et al. 2002, Caudle et al. 2019), coast morphology (Saye et al. 2005, Middleton et al. 2013, Grünthal et al. 2014, Julge et al. 2014, Le Mauff et al. 2018), and vegetation growth on coastal dunes (Frati et al. 2021). The application of using airborne LiDAR for monitoring coastal areas demonstrated the capabilities of the technique in providing dense and accurate 3D data for large areas along the coast. It has also shown that analysing airborne LiDAR multitemporal data can support the risk assessment for coastal erosion management. This can be delivered in many forms by analysing the changes in the profile of the beach and the dunes alongside the coast, and by providing volumetric changes analysis that show areas with deposition and erosion along the coast.

There are several case studies where Airborne LiDAR has been used for the detection of changes in desert dunes (Solazzo et al. 2018, Dong et al. 2021, Reitz et al. 2010, Baitis et al. 2014). We address in detail a case study that involved the development of an automated method that uses multi-temporal LiDAR DEMs. An automated approach, Pairs of Source and Target Points (PSTP), is developed for the detection of dune migration direction and migration rates using multi-temporal LiDAR data. This approach is implemented in a geographical information system (GIS) environment (Dong, 2015). The PSTP relies on a theoretical foundation that the sand collapsing events initiated by gravity tend to occur in the inclination direction of the slip face of the dunes (Bagnold, 1941; Dong, 2015). Therefore, the PSTP works on detecting the migration direction, migration rates of the dunes from the centrelines of old slip faces (source lines), and the centrelines of the new slip faces (target lines). This is implemented in three major steps to obtain the direction, distance and rate of migration for each targeted point: (1) extracting the slip face centrelines from the LiDAR DEMs; (2) processing the source and target lines where thousands of random points (source points, target points) are generated along the source and target lines; (3) identifying the source and target points, by searching for the nearest source point for each target point and calculating the angels and distances between pairs

of source and target points. Any source point that did not find a target point will be considered unmatched and will be removed from the target feature layer (Dong, 2015). Figure 2.18 illustrates the workflow of the automated measurement of sand dunes using the PSTP approach.

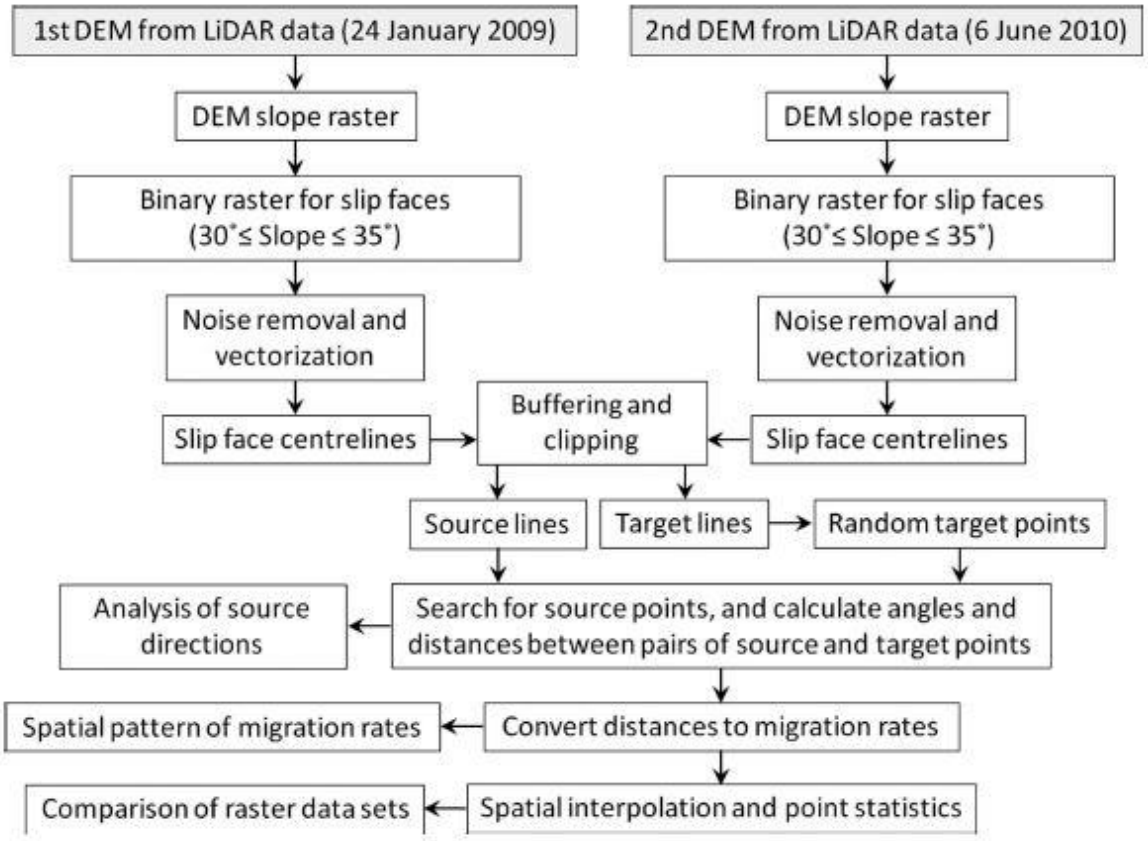

Figure 2.18. Workflow of the automated measurement of sand dunes using PSTP approach, (Dong, 2015).

PSTP is used to detect the migration direction and migration rates of the dunes in the White Sand Dune Field in New Mexico (USA) applied on two LiDAR DEMs with 1m x 1m cell size acquired on the 24th of January 2009 and the 6th of June 2010, a year and a half later. The results show a dominant direction for the dunes migration ranging between 225 degrees to 285 degrees, with a migration rate ranging between 4-7 m/year.

Some challenges can occur when using PSTP which are related to the dune formation and the temporal resolution of the LiDAR DEMs, where source points are mistakenly identified closest to target points. Also, care must be taken when using PSTP for fast moving dunes (Dong, 2015). The PSTP approach has been mainly applied for the detection of migration of desert dunes. Applying this approach to coastal areas would be quite challenging, where the dune system is complex and connected and the identification of the source and target centrelines would be significantly difficult. This is an area of research that is worthy of a thorough investigation.

Some of the limitations of Airborne LiDAR is that it is considered expensive compared to optical and radar sensing techniques, especially when surveying large areas multiple times. This means that the application of using this technology for detecting the movement of sand dunes in desert areas is less effective.

2.3 Conclusion

In conclusion, this chapter provides a comprehensive background on dune morphology and the factors that control the dune movement process. Various remote sensing techniques were investigated from previous research conducted to monitor the movement of sand dunes. This demonstrated the capabilities of each technique in accurately detecting the movement of sand dunes and the advantage of remote sensing techniques over conventional land surveying techniques. It identified significant limitations of the conventional techniques; sand traps and land surveying techniques related to time consuming and data collection process, and the complexity of monitoring large inaccessible sand areas. It also highlighted the capabilities of remote sensing technologies as a supportive tool for risk assessment for environmental projects.

There are a few automated techniques for monitoring sand dunes, therefore the first objective of this research aims to develop an automated framework that uses multi-temporal optical images for monitoring sand dunes. Moreover, the use of pixel offset applied on SAR images has not been used before for monitoring sand dunes, therefore, this research investigates for the first time the capabilities of this technique.

It is observed from the literature that most researchers working on modelling sand encroachment focused their work only on detecting the horizontal component of the dunes (horizontal movement) and they disregarded the fact that sand dunes move in the vertical component as well. Therefore, one of the objectives of this research is to understand the vertical movement of the dunes. In addition, it is also observed that most research use images with a large temporal gap (i.e. months, years) which does not detect the small movement that can occur between these acquisition dates. Thus, in this research, high temporal resolution images were used, to ensure much more accurate detection of the movement of the dunes.

3 CHAPTER 3: MULTI-TEMPORAL OPTICAL SATELLITE IMAGES FOR MONITORING SAND MOVEMENT USING MACHINE LEARNING AND GOOGLE EARTH ENGINE

This chapter investigates the application of optical satellite images for the detection of sand dune movement. It addresses the first objective of the research with a developed framework that applies machine learning classifiers on multi-temporal optical images to detect the horizontal changes in sand dune land cover in northern Sudan. It also shows how to compute the displacement and direction of movement for individual sand dunes. As an optimization step, the developed framework has been semi-automated using Google Earth Engine (GEE) to enable the processing of multi-temporal satellite images in pursuit of this objective.

3.1 Background

3.1.1 Sand Dust Storms in Sudan

Sand dust storms are considered to be the main environmental natural hazard in arid and semi-arid regions (Wang, 2015). The Northern Hemisphere is considered the dominant natural mineral dust source and is known as the 'Afro-Asian Dust Belt' (Kok et al. 2012). A published report by the United Nations Environment Programme (UNEP) stated that there are many places over the world that are considered dust sources, and the coastal region of northeast Sudan is one of them (Shepherd et al. 2016). Moreover, the Saharan desert is considered the major global dust source where major dust events are witnessed in the Northern and Western parts of Africa (Kok et al. 2012, Shepherd et al. 2016), Figure 3.1. This has a significant impact on the land cover dynamics in affected regions; however, the sand dust storm impacts can extend further to affect areas thousands of kilometres away (Shepherd et al. 2016).

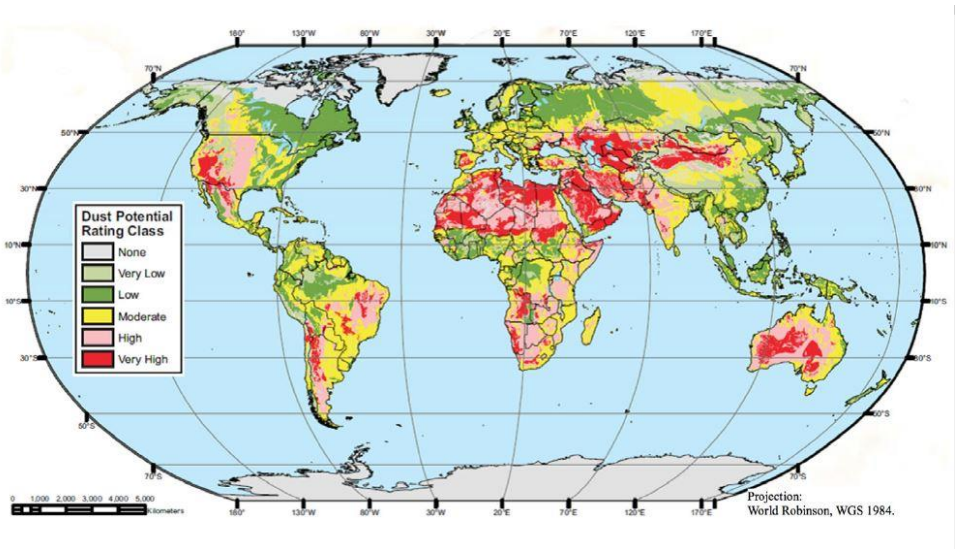

Figure 3.1. Global dust potential map. Source: DTF (2013).

Table 3.1 shows some of the environmental impacts of sand dust deposition (Shepherd et al. 2016).

Table 3.1. Sand dust deposition environmental impacts.

Advantages	Disadvantages
• Work as a fertilizer providing nutrients to ocean surface waters and forests. • Enhances precipitation where it acts as droplet nuclei.	• Escalates drought. • Soil loss and degradation. • Damaging effects on coral reefs. • Economic impacts (crop damages, livestock mortality, and infrastructure damages). • Human health problems.

In northern Sudan, dust storms are locally known as "Haboob". They tend to occur during both winter and autumn seasons, where gusty winds have a significant impact on sand dunes drifting. Sudan faces 17 to 20 sand storms regularly every year (Munro et al. 2012). Figure 3.2 shows a massive dust storm over Sudan captured from space by the Moderate Resolution Imaging Spectroradiometer (MODIS) on the 12th of August 2017, https://modis.gsfc.nasa.gov/gallery/individual.php?db_date=2017-08-17. Figure 3.3 shows a ground view of a dust storm that hit the capital of Sudan, Khartoum, (Britton, 2016).

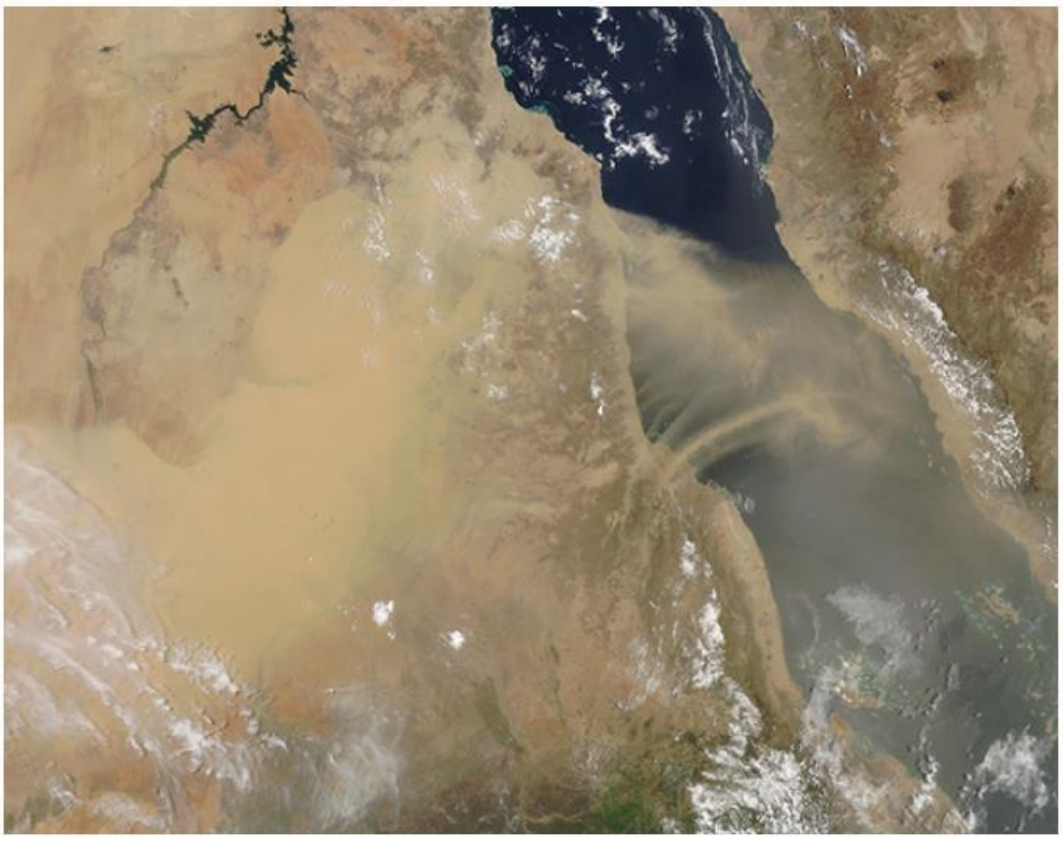

Figure 3.2. Dust Storm over Sudan crossing the Red Sea acquired by MODIS on 12 August 2017.

Figure 3.3. A dust storm hit the capital of Sudan, Khartoum.

Monitoring the impact of dust storms requires an understanding of the movement of the dunes on the ground, detecting the land cover changes and assessing the environmental impacts and factors that control this relationship.

3.1.2 Study Area

The study area is part of the Nubian Desert located in the Northern state of Sudan between latitudes 18◦00’00”-19◦00’00” N and longitudes 30◦30’00”-31◦10’00” E, and it is bordered by the city of Ed Dabba to the south and Dongola city to the North. It covers an area of about 10,180 km^2 with five distinct types of land cover (i.e. sand, vegetation, water, urban and rocks or bare land) where the most dominant land cover types are sand and rocky areas (Figure 3.4). This region receives very low rainfall with precipitation of about 12 mm annually, which explains the significant experienced drought (Zhang et al. 2012). The habitable areas are located on the banks of the River Nile, where the local population depends on agricultural crops and farming as their main source of income (Figure 3.4, c).

This study area was selected because it contains individual sand dunes and integrated sand dune fields. Moreover, it is a representative study area for monitoring sand movement in the arid and semi-arid regions of Sudan, where sand dunes are a dominant land cover type. It also contains agricultural projects, irrigation canals, river banks, and archaeological sites (i.e. Affad, Old Dongola, Kawa), which emphasises the need to investigate the impact of sand movement on rural communities and a variety of infrastructures.

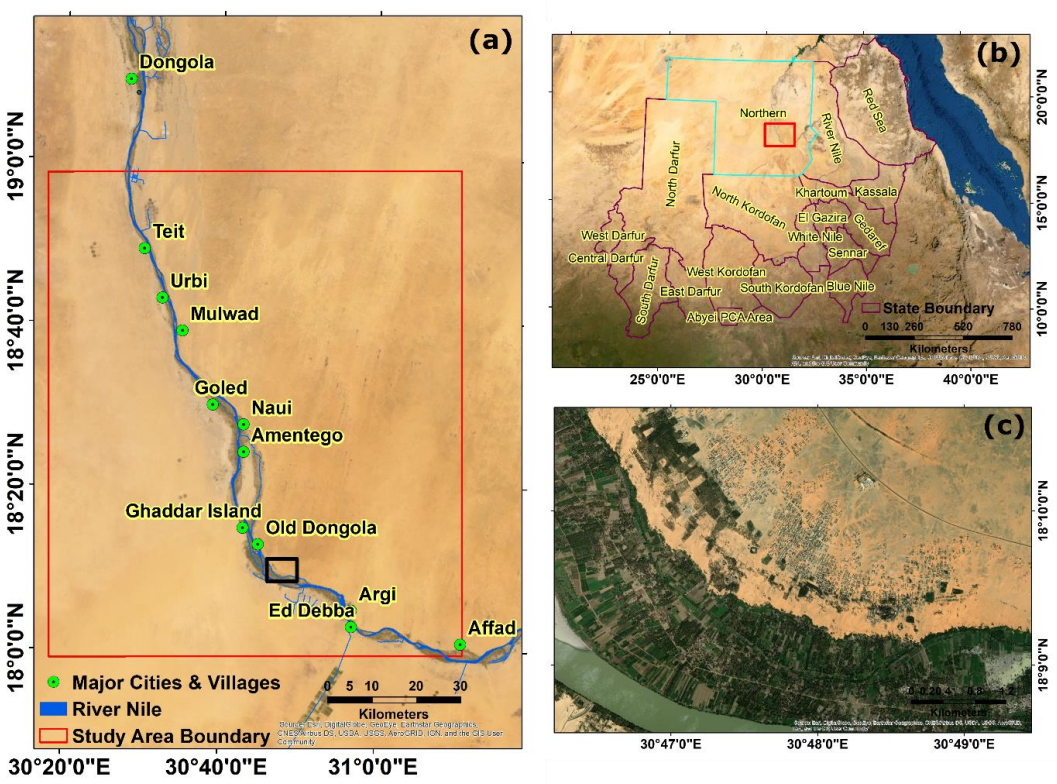

Figure 3.4. Study Area in the Northern state of Sudan. (a) Location of the study area and the main cities and villages scattered along the River Nile banks (b) key map showing Sudan's states and the extent of the study area, (c) a zoomed-in image showing the five distinguished land cover types (sand, vegetation, water, urban and rocky) near Old Dongola city.

3.1.3 Land Cover Change Detection

Due to the significant global climate change impact and human interventions, monitoring land cover changes has become an essential supporting tool for sustainability development and risk assessment for environmental studies. In concept, change detection in remote sensing refers to identifying the changes between sequential image acquisitions covering the same location (Singh, 1989). Change detection studies provide valuable information on the area of change, rate of change, and spatial distribution of change types, in addition to assessing the accuracy of the change detection results (Lu et al. 2004).

The detection of land cover changes has been applied for various environmental and earth observation applications, such as measuring the damage caused by a flood or a hurricane (Klemas, 2015), monitoring forest fires (Langner et al. 2007), agricultural crop assessment (El Hajj et al. 2009), drought management (Karakani et al. 2021), assessing the impact of geohazards (e.g. earthquakes, volcanos, landslides…etc.) (Hervás et al. 2003, Ishihara and Tadono, 2017, Kadavi and Lee, 2018). Hence, detecting changes in land cover is a powerful geospatial tool that can support policy makers to assess and mitigate environmental hazards.

For decades, environmental and earth observation scientists have been developing different remote sensing techniques that use optical satellite images to detect and monitor land cover changes. Examples of these techniques are image differencing, normalized difference vegetation index and image classification applied to sequential images to provide a measurable and statistical description of the changes, Table 3.2, (Lu et al. 2004).

Table 3.2. Most common used change detection techniques (after D. Lu et al. 2004).

Technique	Characteristics	Advantages	Disadvantages
Image differencing	Applies pixel by pixel subtraction between first date image and second date image	Simple implementation, easy interpretation of the results	Providing a change matrix is not applicable
Vegetation index differencing	Produces vegetation index, subtracts the second date from the first date vegetation index	Emphasizes differences in the spectral response of different features and reduces impacts of topographic effects and illumination	Coherence noise
Post classification comparison	Classifies multi-temporal images into thematic maps, followed by a pixel-by-pixel comparison of the classified images	Reduces the impact of atmospheric and environmental differences between multi-temporal images; produces a full matrix of change information	Requires technical expertise to produce a classification product.

In this chapter of the research, the image differencing and image classification methods were used to detect the land cover changes, with a special focus on the machine learning classification methods.

3.1.4 Machine Learning Classification Algorithms

The advancement in computer vision and machine learning algorithms has elevated the capabilities of classification of thematic mapping and provided the potential of achieving much more accurate classification results. The different classification methods are assessed in terms of the accuracy of the classification results, which mainly depends on several factors: the spatial resolution of the images, the sensor type, the size of the training samples and the employed classification approach (Sheykhmousa et al. 2020). In addition, the computational time for the classification process is considered an important factor when selecting a classifier.

The most widely used machine learning algorithms in remote sensing are the supervised classification algorithms; the Random Forest (RF) (Breiman, 2001) and the support vector machine (SVM) (Mountrakis et al. 2011) algorithms, due to their higher interpretability capabilities and lower computational complexity (Sheykhmousa et al. 2020). In this study, a comparison has been made between the random forest classifier and the support vector machine classifier in order to select the optimum classifier to perform supervised classification on multi-temporal satellite images in GEE.

The random forest (RF) classifier is an ensemble classifier, which combines several models, that uses a group of decision trees to predict and distinguish different classes (Breiman, 2001). There are two ensemble learning methods that are applied to build the forest trees, which are boosting and bagging. Boosting methods build sequential models where each model is used to correct the error of the classification in the previous model. However, this model generates a problem of overfitting a dataset with insufficient training samples and may fail to predict reliably (Sheykhmousa et al. 2020). In contrast, the bagging method improves the stability and accuracy of the integrated models and reduces the variance. In comparison to boosting, the bagging approach is considered more robust to the overfitting problem (Sheykhmousa et al. 2020). The random forest classifier was developed based on the bagging approach.

The random forest generates random multiple decision trees by using a subset of the training samples, with two thirds of the training samples being used to train the model decision trees while the rest third is used to cross validate the performance of the random forest model. This allows different training samples to be selected for each individual tree, which results in high variance and low bias and reduces the generalized estimation errors (Breiman, 2001).

The two main parameters in the RF are the number of trees (Ntrees), which is the number of decision trees in the ensembled forest, and the number of variables (Mtry), which is the number of predictors used to split the tree's nodes to grow the decision trees and assign a classification decision (Belgiu and Drăguţ, 2016). Both the number of trees and the number of features are user defined and have an impact on the accuracy of the classification results, although, theoretical and empirical models suggest that the RF model is less sensitive to the number of trees than to the number of predictors (Belgiu and Drăguţ, 2016). The outcome of the unclassified input is generated from the ensembled decision trees majority voting for the most popular class.

The support vector machine (SVM) is a non-parametric statistical classifier that uses training samples to define a hyperplane that separates the dataset into different predefined classes. The hyperplane works as a decision boundary to minimize the misclassification of the datasets (Mountrakis et al. 2011). SVM uses a portion of the training samples that lies closet in the feature space to the optimal decision boundary, known as support vectors, to maximize the separation boundary or margin between the different classes. An iterative process takes place for defining the optimal hyperplane, which minimizes the misclassification error (Mountrakis et al. 2011).

There are three main parameters to define with the SVM: (1) the kernel function that is used to distinguish the non-linear decision boundaries in the original data space into linear ones in a high dimensional space; (2) the kernel regularization parameter (C), which controls the amount of penalty during the optimization of the SVM; and (3) the kernel width (gamma), which is the spread of the kernel (Sheykhmousa et al. 2020).

There are several kernel functions that are used with the SVM, such as the linear kernel, polynomial kernel, and the gaussian radial basis function (RBF) (Huang et al. 2002). The selection of a specific kernel is reflected significantly in the classification results, and this is considered to be one of the major challenges in SVM; deciding which kernel should be used for the intended remote sensing application (Huang et al. 2002, Mountrakis et al. 2011). Figure 3.5 demonstrates a linear support vector machine example with a hyperplane distinguishing two different classes with some misclassified pixels, (Mountrakis et al. 2011).

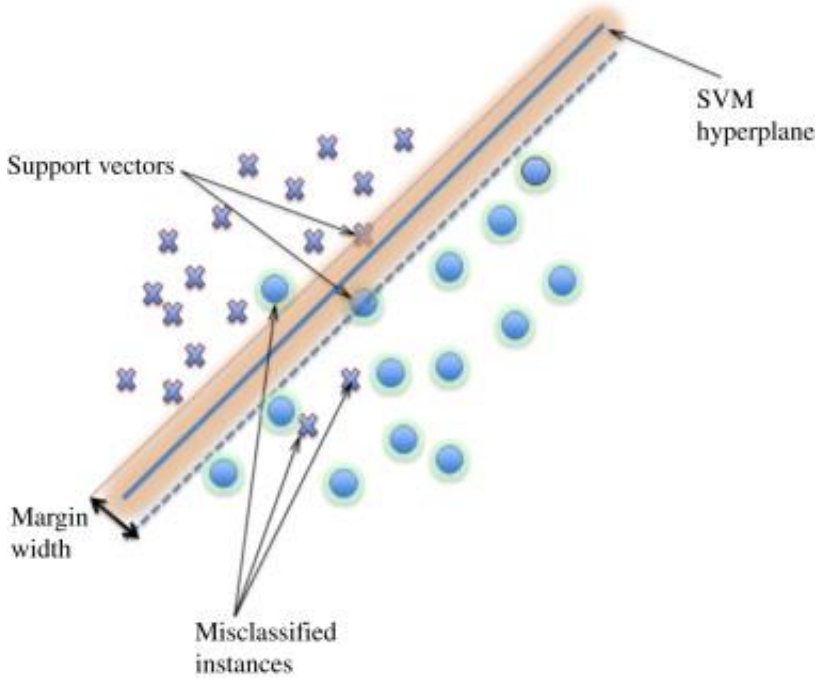

Figure 3.5. Linear support vector machine example. A hyperplane distinguishing two different classes with some misclassified pixels, (Mountrakis et al. 2011).

Table 3.3 highlights the main differences between the random forest and the support vector machine algorithms for the application of image classification, (Huang et al. 2002, Pal, 2005, Mountrakis et al. 2011, Belgiu and Drăguţ, 2016, Sheykhmousa et al. 2020).

Table 3.3. Main characteristics of the Random Forest and the support vector machine classifiers.

Method	Random Forest (RF)	Support Vector Machine (SVM)
Performance	• Robust and stable to noise in the training data. • It is less sensitive to overfitting. • Can handle categorical data and unbalanced data.	• Depends on the suitable kernel function. • Capability in locating optimal separating hyperplanes. • Can tackle the high dimensionality and limited training samples issues. • Does not assume frequency distribution of data.
Classification Accuracy	• Sensitive to outliers in the training data. • Does not overfit.	• Kernel models can be sensitive to overfitting which limits the SVM.
Processing Speed	• Computationally efficient.	• Considered slow when comparing training speeds due to training data size, the kernel parameter setting and the class separability.

3.1.5 Cloud Based Computing Service: Google Earth Engine

Earth observation has historically been limited by the processing power of low-performance computers, however the emergence of cloud-based computing services such as Google Earth Engine (GEE), Sentinel Hub, Open Data Cube (ODC), openEO, JEODPP and pipsCloud (Gomes et al. 2020) has opened up the possibility of processing petabyte-scale remote sensing data.

Google Earth Engine (GEE) is a cloud based computing platform that allows the processing and analysis of large time series satellite imagery and geospatial datasets for the application of earth observation monitoring (Gorelick et al. 2017). The GEE platform, https://earthengine.google.com/, provides access to different types of remote sensing data (e.g. satellite images: Landsat, MODIS, Sentinel 1&2, precipitation data, weather…etc.) and a public data archive that includes historical imagery. It allows users to visualize and perform planetary-scale geospatial analysis on time series datasets more rapidly and accurately, in an interactive environment implemented in the JavaScript code editor or via an application programming interface (API) using JavaScript or Python.

The use of GEE APIs expands researchers' capabilities to develop more effective geospatial tools. Figure 3.6 illustrates the components of the Earth Engine code editor, (https://developers.google.com/earth-engine/guides/playground).

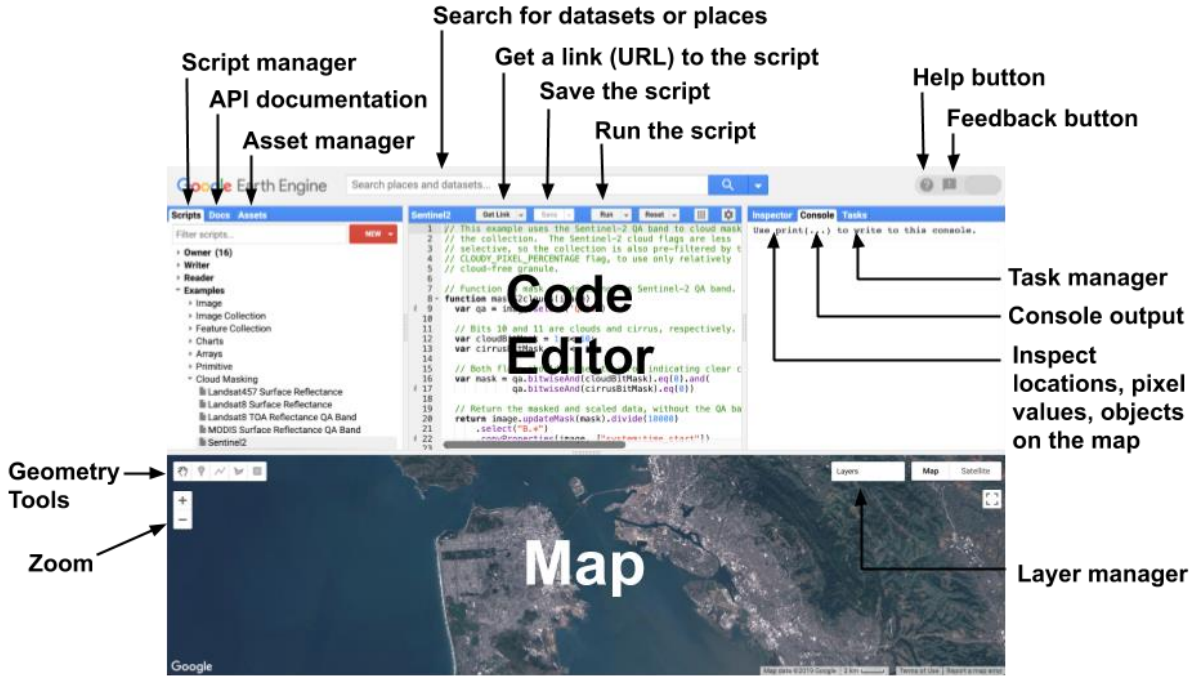

Figure 3.6. Diagram of components of the Earth Engine Code Editor.

In the past few years, many researchers have used GEE for different remote sensing applications such as crop mapping and agricultural monitoring (Amani et al. 2020, Shelestov et al. 2017), drought management (Sazib et al. 2018, Khan and Gilani, 2021), forest mapping (Johansen et al. 2015), flood assessment and management (Liu et al. 2018), coastal monitoring (Vos et al. 2019) and volcanic monitoring (Genzano et al. 2020). Moreover, it has been widely used for the application of land cover analysis. For instance, several workers (Lin et al. 2020, Zurqani et al. 2018, Midekisa et al. 2017, Huang et al. 2017, Arévalo et al. 2020) performed land cover classification and NDVI analysis to detect the long term changes in land cover, in addition to monitoring the degradation of land by processing large amounts of continuous satellite images and spatial datasets.

All these studies demonstrate the capabilities of GEE as a powerful platform for the application of large scale environmental and earth observation studies. In this case study, GEE has been applied to support the automation of an optical satellite image processing framework that uses machine learning to monitor the movement of sand dunes in Northern Sudan.

3.2 Data and Methodology

3.2.1 Data

The Sentinel-2 mission was developed and operated by the European Space Agency with the first satellite in the constellation, Sentinel-2A, launched in 2015, and joined by Sentinel-2B in 2017. These satellites are orbiting the earth in a sun-synchronous orbit providing systematic coverage of all the land and coasts between latitudes 56◦ south and 83◦ north, with a revisit time of 5 days at the equator (Sentinel, 2015). The sensor on board has a multispectral instrument with 13 bands: four visible bands (B1, B2, B3, B4), six infrared bands (B5, B6, B7, B8, B8A B9) and three shortwave bands (B10, B11, B12) used for various applications, such as land cover change detection, crop mapping and marine monitoring...etc. (Sentinel, 2015).

Sentinel-2 image products are provided to users in two different types: Level-1C (Top-Of-Atmosphere (TOA) reflectance) or Level-2A (Bottom of atmosphere (BOA) reflectance) ortho-rectified images in UTM/WGS84. The Sentinel 2 Level-2A (L2A) multi spectral resolution images were used in this case study to perform the image classification and change detection analysis. Sentinel 2 images were chosen because they are free to acquire and have a higher spatial resolution of 10 m compared to LandSat data which has a 30 m spatial resolution. The Sentinel 2 L2A images were processed from the associated Sentinel 2 Level-1C products using the Sen2Cor processor, which was developed by ESA, and by applying scene classification, atmospheric and cirrus corrections (Louis et al. 2016).

As the Level-2A images became systematically available globally from December 2018, hence, the selected study period spans from December 2018 to December 2021, which is three years of sequential time series of Sentinel 2 L2A images. Although, the temporal resolution between the images is 5 days, applying cloud filters to the dataset to select images with low cloud percentage (see section 3.3.2), to reduce miss classification, resulted in collecting 110 images and excluding 110 images with a cloud percentage more than the determined threshold. Table 3.4 shows the Sentinel 2 L2A image bands specifications.

Table 3.4. Sentinel 2 L2A bands specifications.

Name	Description	Resolution	Wavelength for S2A /S2B(nm)
Band 1	Coastal Aerosols	60 meters	443.9nm / 442.3nm
Band 2	Blue	10 meters	496.6nm / 492.1nm
Band 3	Green	10 meters	560nm / 559nm
Band 4	Red	10 meters	664.5nm / 665nm
Band 5	Red Edge 1	20 meters	703.9nm / 703.8nm
Band 6	Red Edge 2	20 meters	740.2nm / 739.1nm
Band 7	Red Edge 3	20 meters	782.5nm / 779.7nm
Band 8	NIR	10 meters	835.1nm/ 833nm
Band 8A	Red Edge 4	20 meters	864.8nm / 864nm
Band 9	Water Vapor	60 meters	945nm / 943.2nm
Band 11	SWIR 1	20 meters	1613.7nm /1610.4nm
Band 12	SWIR 2	20 meters	2202.4nm /2185.7nm

3.2.2 Methodology

3.2.2.1 Sand Encroachment Tool (SET)

A preliminary step to detect the changes in land cover is to use the image differencing by applying it to two sequential images and subtracting the corresponding pixel values to distinguish areas that have seen significant land cover changes. This was applied on band 8, the near Infrared band. However, this does not provide statistics on the displacement and the direction of movement. Therefore, an alternative change detection method, image classification, has been implemented to detect and calculate the changes in sand dunes areas. In this case study, this has been achieved by developing a framework in the ArcGIS model builder called 'Sand Encroachment Tool (SET)'.

The framework (SET) integrates remote sensing and GIS methods that involve different spatial analysis and geo-processing tools to monitor the changes in sand dune land cover, by applying a time series analysis to detect the changes in land cover classification, in addition to determining the displacement and direction of movement of individual dunes. SET uses optical images and depends mainly on the results of the supervised classification.

The detection of sand movement using the SET framework includes two parts, Figure 3.7, and Figure 3.8. The first part focuses on detecting sand cover area changes and generating land cover classification maps that demonstrate the changes over time and the spread of sand areas. The second part of the tool works on detecting the displacement and the direction of movement of specified individual dunes following the classification of sand cover areas stage.

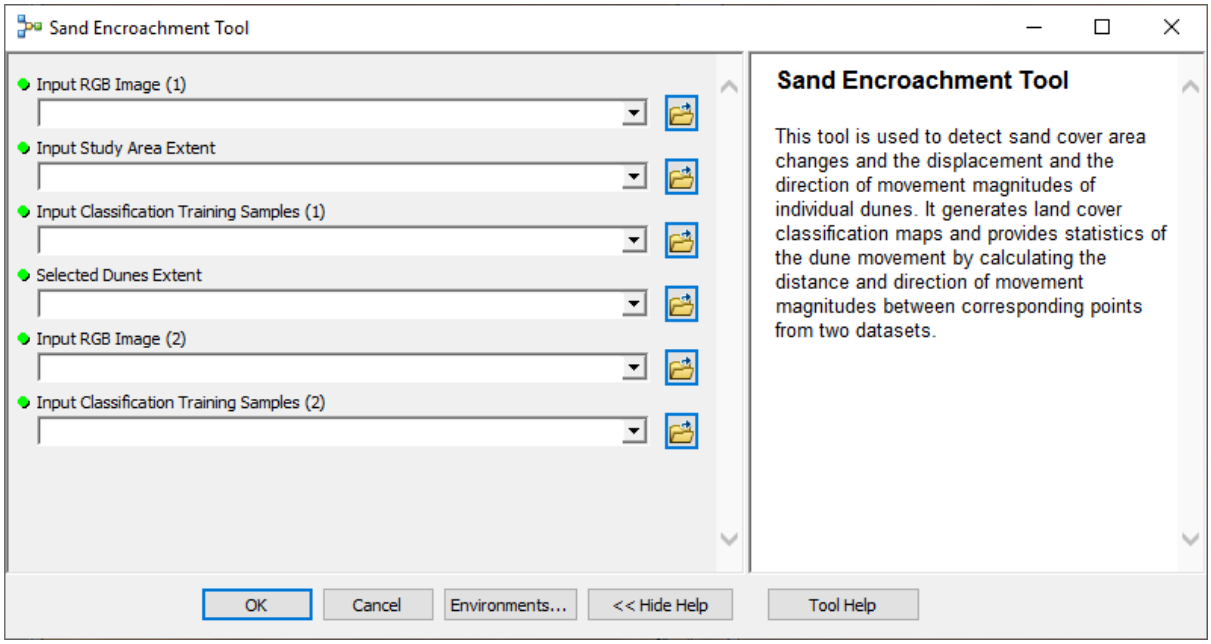

Figure 3.7. Description of the SET tool input parameters.

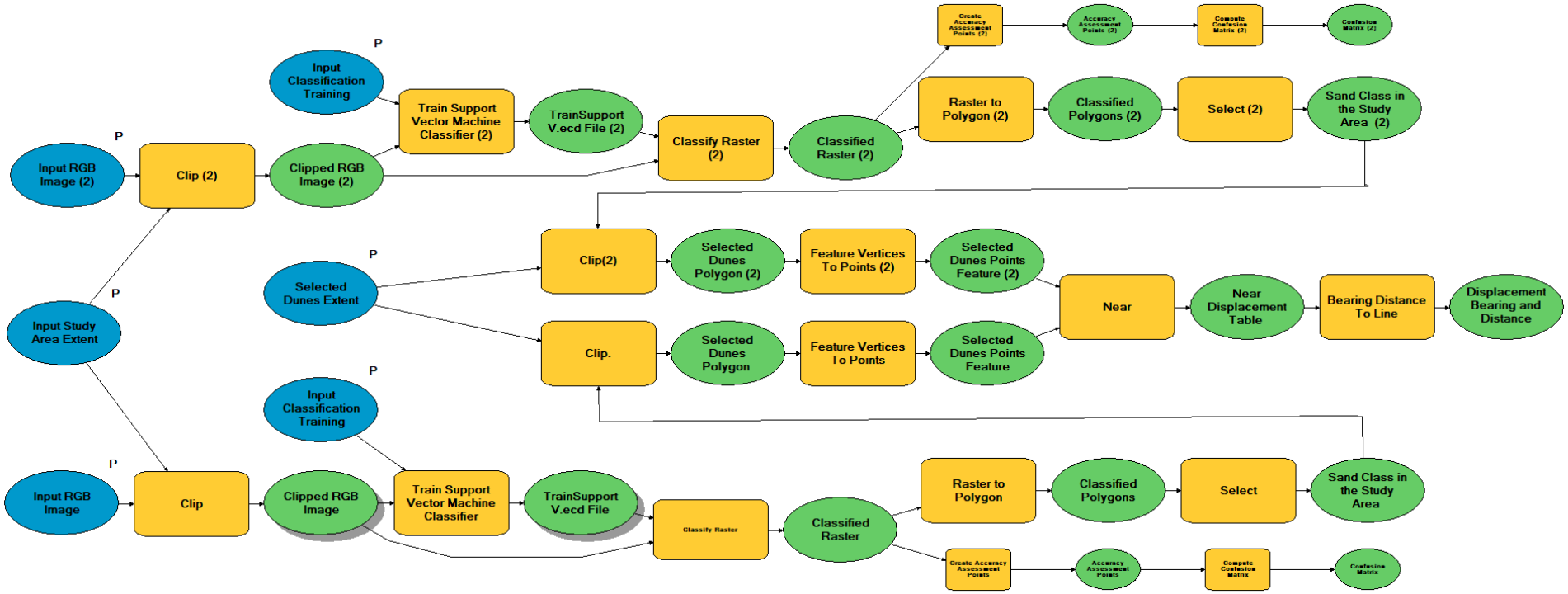

Figure 3.8. SET framework applied in ArcGIS for land cover classification changes and detecting the displacement and direction of the movement of individual dunes.

The first step applied in the framework is to clip the satellite images to the study area boundary, in order to reduce the processing time and to ensure that all of the analysis is applied to the same area extent. Then, the training samples are collected, based on the five main land cover types in the study area (i.e. sand, vegetation, water, urban and rocky). Table 3.5 shows a description of the land cover classes in the study area.

Table 3.5. Description of the land cover classes in the study area

Class	Description
Sand	Sand sheets and sand dune areas
Vegetation	Agricultural areas and farms
Water	River Nile water body
Urban	Houses and built-up areas
Rocky	Rocks and bare lands

The training samples were manually collected from seven Sentinel- 2 images collected in June and December months of the years 2018-2021 based on visual inspection and were validated with the available historical high-resolution images in Google earth from the same period.

The optimum way of obtaining training samples is by collecting ground truth data or collecting it from previously generated Thematic maps. This is not usually applicable, especially in the case of remote monitoring of desert areas; therefore, the training samples were collected by visual inspection.

One hundred training sample points were collected for each class, in addition to 40 test validation points collected to validate the classification results. Figure 3.9 shows the distribution location of the training samples and validation samples over the study area, where each sample point corresponds to a single pixel.

The collected training samples were then used to train the classifier by acquiring the signature of the image pixels that correspond to each training sample, in order to be used to generate classification maps.

In order to select the optimum machine learning classification method, a comparison between the RF and SVM classifiers was conducted. This involved computing the confusion matrix, overall accuracy and the Kappa coefficient for the classification of Sentinel-2 L2A image collected on the 11th of January 2019. The confusion matrix provides an array that contains all the assigned classes in the validation dataset showing the error in the classification (Maxwell et al. 2021).

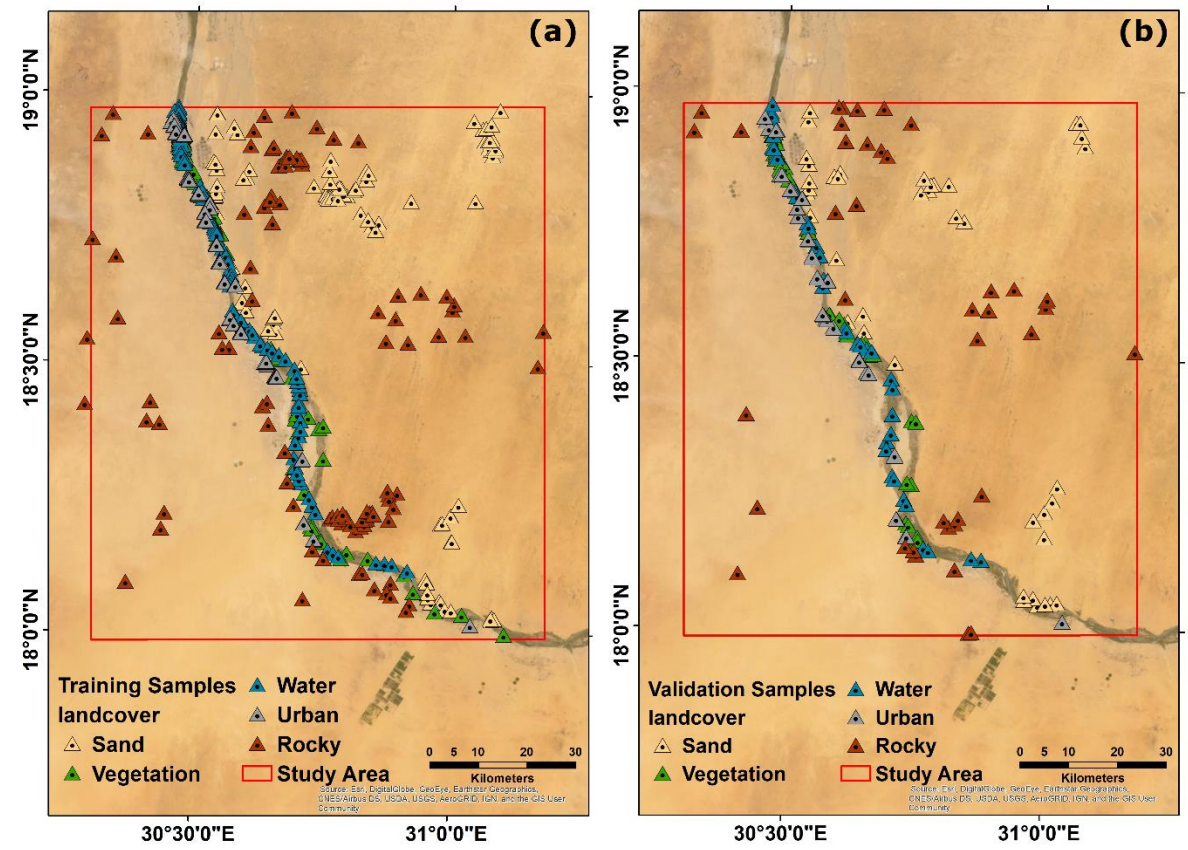

Figure 3.9. Distribution location of the training and validation samples collected over the study area for image classification. (a) Training samples location map (b) Validation samples location map.

The kappa coefficient is another accuracy indicator that is used to assess the agreement between the classification results and the validation samples, Table 3.6, (Landis and Koch, 1977).

Kappa statistic = (observed accuracy – chance accuracy)/ (1- chance accuracy).

Table 3.6. Kappa coefficient values indicator for the agreement between the validation data and the classification results.

Kappa Statistic	Strength of Agreement
<0	No agreement
0.00-0.20	Slight agreement
0.21-0.40	Fair agreement
0.41-0.60	Moderate agreement
0.61-0.80	Substantial agreement
0.81-0.99	Almost perfect agreement

The comparison results demonstrated that the random forest is capable of achieving significantly higher accuracy of classification compared to the SVM when using 100 decision trees and above. Therefore, the Random Forest classifier was used to process the time series analysis to detect the land cover changes.

The classification maps generated using the Random Forest classifier were validated using the test dataset and the confusion matrices and Kappa coefficient were computed to statistically determine the accuracy of the classification.

To determine how significant the sand area has changed over time, the raster classes were converted into polygon feature datasets using the 'Raster to Polygon' tool. Then the sand class was extracted from the classification results, after which the area summation of the sand class in each classified image was calculated. This step is the final step of the first part of SET and focuses on identifying the changes in land cover that have occurred over time.

The second part of SET is oriented to calculate the displacement and direction of movement for individual dunes. This requires selecting individual dunes from the sand class and converting those dunes' polygons into point features using the 'Feature vertices to points' tool. Then the movement of the individual dunes on different dates is determined by calculating the displacement magnitude and the direction of movement using the 'Near analysis' tool.

The 'Near analysis' tool (Figure 3.10) provides a table that contains the displacement magnitude and the near angle between a point from a primary feature (dune) and the closest point on a secondary feature (shifted dune), in addition to the near X and near Y coordinates of the primary points.

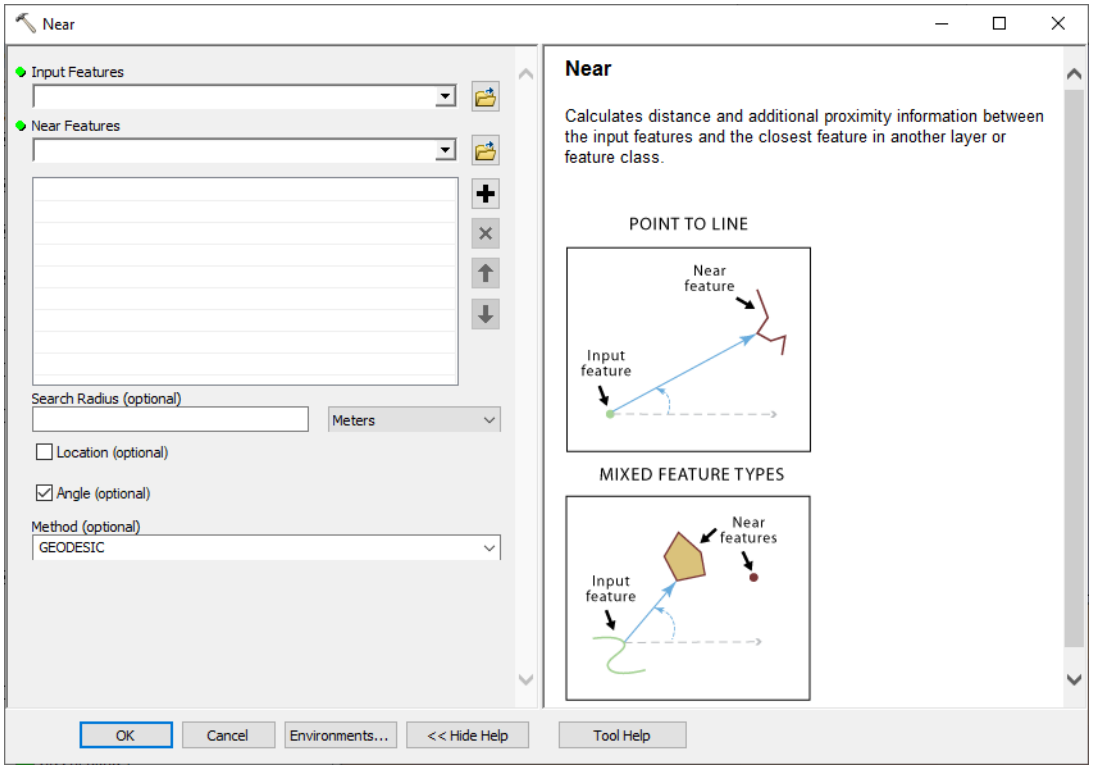

Figure 3.10. Near analysis tool in ArcGIS is used to calculate the displacement between shifting dunes.

The 'Near analysis' tool works on layers of the geodetic coordinate system, therefore, the dune points were converted into the geographical coordinates system. The method used in the Near analysis tool for the calculation of the near distance and the proximity information was geodesic. It provides the near distance in a linear unit (i.e. metres) and the near angle within the range of -180◦ to 180◦, with 0° representing the north, 90° to the east, 180° (or -180°) to the south, and -90° to the west. The near angle was converted into azimuth by adding 180◦ to the near angle field using the field calculator tool to compute the azimuth bearing direction values.

Then the displacement magnitude and azimuth direction are used to generate the bearing distance line that connects the two corresponding points and displays the movement of the dunes using the 'Bearing Distance to Line' tool, Figure 3.11.

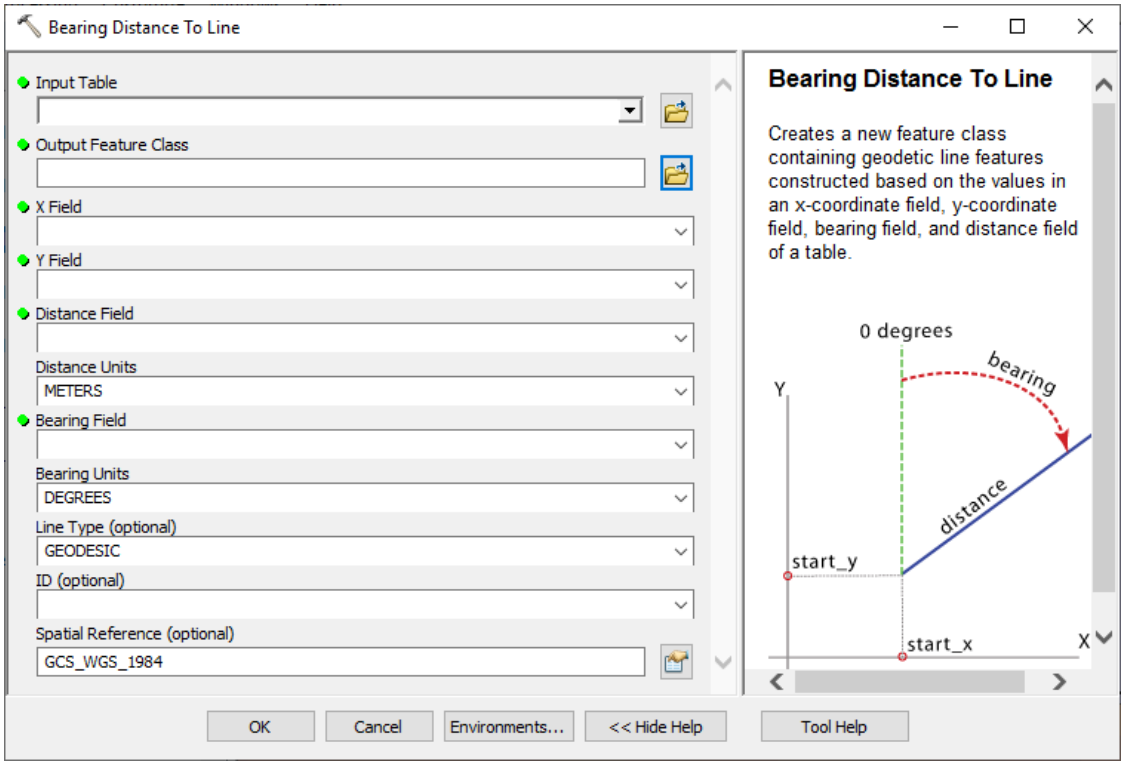

Figure 3.11. The bearing distance to line tool used in ArcGIS to create a line feature that connects the two corresponding points to display the displacement of the dunes.

3.2.2.2 Monitoring sand dune movement using Google Earth Engine

As an automation step, the framework (SET) developed in the ArcGIS model builder has been tailored and implemented in Google Earth Engine (GEE) to allow for the automation process to be applied to large datasets of multi-temporal satellite images (i.e. 3 sequential years of Sentinel-2 image collection). This provided a detailed detection of the changes in land cover in the study area, and the sand dunes particularly.

GEE provided a powerful tool and access to different remote sensing datasets. For this study, the Sentinel-2 L2A was used. The processing was implemented in the GEE code editor that uses JavaScript language, (the written code is provided in the Appendix chapter). Figure 3.12 shows a diagram that illustrates the main processing stages of detecting sand dune movement using GEE.

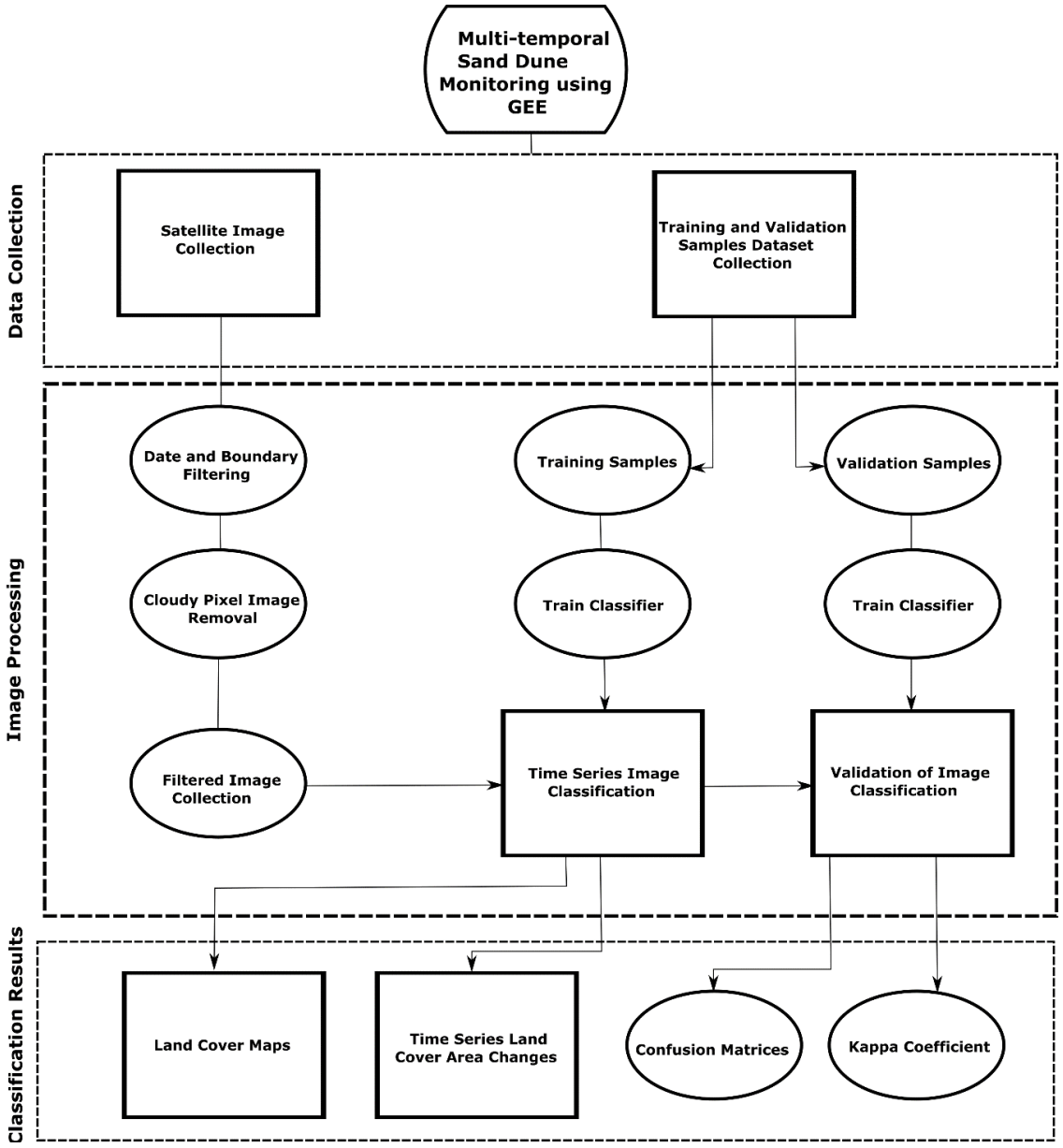

Figure 3.12. Processing framework implemented in GEE for sand dune monitoring.

Different built-in functions in the GEE were used to automate the geospatial processing steps of SET to detect the movement of sand from time series images. The ee.FeatureCollection() was used to import the shapefiles of the study area and applied with the geometry() function to define the study area. The study area shapefile has been used to define the area to download the Sentinel 2 images and also to mask out the images to their extent.

```
// Define the study area
var Study_Area = ee.FeatureCollection('projects/ee-ahmedmahmoud/assets/shapefiles/Study_Area');
Study_Area = Study_Area.geometry();
Map.centerObject(Study_Area);
Map.addLayer(Study_Area, {color: 'yellow'}, 'Study_Area');
```

To access a time series dataset of Sentinel 2 multi-spectral L2A images the ee.ImageCollection() function was used. This function provides access to a stack of satellite images that covers the same area.

The Sentinel 2 images are provided as image tiles and several tiles overlap so that determining a path and row won't work. In other words, overlapped images can be taken on the same day representing the same area, which could cause an issue when analysing a time series. This issue has been resolved in this study by selecting a point (rio) that is only located on one granule, so the accessed images would represent the same granule on different dates when selecting only one image for each day.

To ensure that the collected images are cloud free or have a very low cloud coverage, in order to reduce the radiometric distortion in the land cover classification results, a filter was applied using the .filterMetadata() function to filter out all the images that have cloud percentage more than a threshold of 1%. However, this sometimes results in filtering out too many good images that only contain cloud percentages in parts of the image but not over the study area.

A .map() function has been used to loop on and returning clipped images to the study area using the .clip() function.

```
//Collect the Sentinel 2 Multi spectral instrument L2A images between December 2018 to December 2021
////////////////////////////////////////////////////////////////////////////////////////////////////
var SenImageCollection = ee.ImageCollection("COPERNICUS/S2_SR")
                    .filterBounds(rio)
                    .filterDate('2018-12-01', '2021-12-31')
                    .select('B[1-8]')
                    .filter(ee.Filter.lt('CLOUDY_PIXEL_PERCENTAGE',1))
                    .map(function(image){return image.clip(Study_Area)});
print('SenImageCollection', SenImageCollection);
```

The Map.centerObject() and the Map.addLayer() functions were used to display the output results on an interactive map to inspect all the downloaded image dataset. The Sentinel image collection to In order to get the actual dates format of the images, which was used to plot the time series, the .distinct() function and the .aggregate_array() function were used.

```
// Get the list of the image acquisition dates
////////////////////////////////////////////////////////////////////////////////////////////////////
var ImageDates = SenImageCollection.map(function(image){
    return ee.Feature(null, {'date': image.date().format('YYYY-MM-dd'), 'id': image.id()});
})
.distinct('date')
.aggregate_array('date');
print ('ImageDates', ImageDates);
```

In order to validate that all the collected images complied with the threshold of the 1% of cloud pixel percentage, the .aggregate_stats() function was used. The function provided statistics of the cloud pixel coverage for the image collection, Table 3.7.

Table 3.7. Image collection cloud pixel percentage statistics.

Cloud Coverage Status	Percentage
Maximum	0.983
Mean	0.203
Minimum	0
Standard Deviation	0.277

```
// Statistics of the cloud pixel percentage in the image collection
////////////////////////////////////////////////////////////////////////////////////////////////////
var CloudCoverageStats = SenImageCollection.aggregate_stats('CLOUDY_PIXEL_PERCENTAGE');
print('Cloud Coverage stats:', CloudCoverageStats);
```

The classification of the images was applied on bands (B2, B3, B4 and B8) to clearly distinguish between the land cover classes. The random forest and support vector machine classifiers were used. The classification result was validated using the training samples by computing the confusion matrices and the kappa coefficient.

```
//Train the Random Forest classifier and classify the image collection
////////////////////////////////////////////////////////////////////////////////////////////////////
var bands = ['B2', 'B3', 'B4', 'B8'];
function RFclassification(image){
  var classification_training_samples = image.select(bands).sampleRegions({collection:training_samples,
    properties: ['landcover'],
    scale: 10
});
var RFtrained_classifier = ee.Classifier.smileRandomForest(100).train(classification_training_samples, 'landcover', bands);
var RFclassified_image = image.select(bands).classify(RFtrained_classifier);
return RFclassified_image;
}
var RFclassified_imageCollection = SenImageCollection.map(RFclassification);
print('RFclassified_imageCollection', RFclassified_imageCollection);
var RFclassified_imageCollectionlist = RFclassified_imageCollection.toList(RFclassified_imageCollection.size());
print('RFclassified_imageCollectionlist', RFclassified_imageCollectionlist);
```

The ee.Image.pixelArea() function was used to calculate the area of each pixel of the classified image. The reducedRegion () function was then applied to calculate the total area of the specific class.

The GEE processing code is provided in the appendix chapter, and it contains a step-by-step processing guide for monitoring sand dunes using machine learning classifiers in GEE.

3.3 Results and Discussion

3.3.1 Sand Area Extent Changes

Image difference analysis was carried out between two Sentinel 2 images collected on the 10th of July 2019 and the 15th of February 2020 to distinguish land cover changes in the study area. The image difference results show significant changes in the vegetation areas as a result of vegetation growth, and in the water channel due to the sediment deposition and erosion. Moreover, the sand dune areas have seen significant differences, which indicates a continuous movement of the dunes.

This process is a preliminary stage to develop a general overview of what sort of changes or movement is expected in this region. Figure 3.13 illustrates the image difference between the 10th of July 2019 and the 15th of February 2020 applied on band 8 (Near Infrared band).

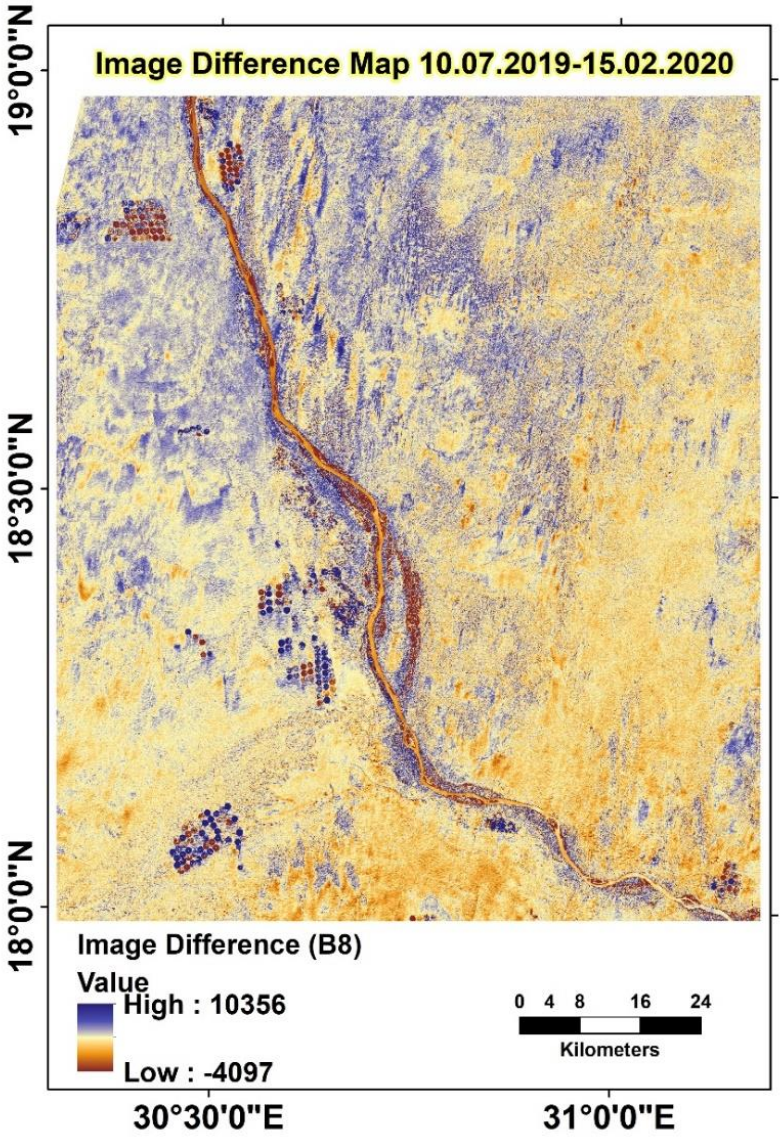

Figure 3.13. Image difference map between 10 July 2019 and 15 February 2020 computed from band 8 NIR.

The image classification has been carried out in Google Earth Engine on a time series of images to detect the land cover changes in the study area between December 2018 and December 2021. An initial step was performed to validate the accuracy of the classification from the random forest and the support vector machine classifiers to select the optimum classifier. The validation was performed on an image collected on the 11th of January 2019.

Several classification experiments were preformed using the random forest classifier to select the ideal parameters. A different number of trees (10, 50, 100, 150, 200, 250 and 300) were tested to determine which NTrees values would provide the best accuracy of classification. The accuracy of the RF classification has increased when using 100 Ntrees, after which further additional increases did not enhance the achieved accuracy. Table 3.8 shows the random forest classification validation results applied with a different number of trees.

Table 3.8. Random forest classification overall accuracy and kappa coefficient validation results when applying different trees numbers.

Number of Trees	Overall Accuracy	Kappa Coefficient
10	0.935	0.919
50	0.955	0.943
100	0.965	0.956
150	0.965	0.956
200	0.965	0.956
250	0.965	0.956
300	0.965	0.956

The RF confusion matrix showed near perfect agreement between the validation datasets and the classification results of all the classes. However, this agreement is only valid for the validation datasets and in order to achieve more robust validation, more validation sample datasets must be collected and well distributed, covering a larger area of the study region. Table 3.9 illustrates the confusion matrices generated to validate the accuracy of RF classification.

Table 3.9. RF Classification confusion matrices obtained from a different number of trees in Random Forest.

RF Number of Trees						
10	50	100	150	200	250	300
Confusion Matrices						
[37,0,0,0,3]	[39,0,0,0,1]	[40,0,0,0,0]	[40,0,0,0,0]	[40,0,0,0,0]	[40,0,0,0,0]	[40,0,0,0,0]
[0,39,0,0,1]	[0,40,0,0,0]	[0,40,0,0,0]	[0,40,0,0,0]	[0,40,0,0,0]	[0,40,0,0,0]	[0,40,0,0,0]
[0,0,39,1,0]	[0,0,39,1,0]	[0,0,39,1,0]	[0,0,39,1,0]	[0,0,39,1,0]	[0,0,39,1,0]	[0,0,39,1,0]
[1,2,0,37,0]	[0,1,0,39,0]	[0,1,0,39,0]	[0,1,0,39,0]	[0,1,0,39,0]	[0,1,0,39,0]	[0,1,0,39,0]
[1,0,1,3,35]	[1,0,1,4,34]	[1,0,0,4,35]	[1,0,0,4,35]	[1,0,0,4,35]	[1,0,0,4,35]	[1,0,0,4,35]

On the other hand, several classification trials were performed to determine the impact of using different cost parameter values on the SVM classification accuracy. The linear kernel was applied on the support vector machine which is a basic simple kernel with one dimensional structure. Table 3.10 shows the overall accuracy and kappa coefficient validation results obtained from applying different cost parameter values to the SVM classifier. Table 3.11 shows the confusion matrices of the SVM using different cost (C) parameter values.

Table 3.10. Support vector machine overall accuracy and kappa coefficient validation results obtained by applying different cost parameter values.

C Parameter Value	Overall Accuracy	Kappa Coefficient
0.2	0.96	0.95
0.5	0.935	0.9188
1	0.945	0.931
2	0.935	0.91875
3	0.915	0.89375
4	0.935	0.91875
5	0.935	0.91875

Table 3.11. SVM classification confusion matrices obtained using different cost (C) parameter values.

Cost Parameter Values						
0.2	0.5	1	2	3	4	5
Confusion Matrices						
[40,0,0,0,0]	[38,0,0,0,2]	[38,0,0,0,2]	[38,0,0,0,2]	[37,0,0,0,3]	[37,0,0,0,3]	[38,0,0,0,2]
[0,40,0,0,0]	[0,40,0,0,0]	[0,40,0,0,0]	[0,40,0,0,0]	[0,40,0,0,0]	[0,40,0,0,0]	[0,40,0,0,0]
[0,0,39,1,0]	[0,0,39,1,0]	[0,0,39,1,0]	[0,0,39,1,0]	[0,0,39,1,0]	[0,0,38,1,1]	[0,0,39,1,0]
[0,2,0,37,1]	[0,2,0,37,1]	[0,2,0,37,1]	[0,1,1,35,3]	[0,2,0,36,2]	[0,2,0,37,1]	[0,1,0,37,2]
[1,0,1,2,36]	[1,0,5,1,33]	[1,0,0,4,35]	[1,0,1,3,35]	[1,0,7,1,31]	[1,0,0,4,35]	[1,0,0,6,33]

Although having low values of the C parameter increases the margin of the hyperplane, which would allow for more classification to be formed and leads to misclassification (Yang, 2011), it is observed that the SVM classifier achieved higher classification accuracy when using small cost parameter values (i.e. 0.2). This can be related to the overlapping in the training samples of land cover classes in the study area. However, there is no defined value for the C parameter that achieves the lowest misclassification results, it depends mainly on the training dataset. Selecting a kernel type to be used with the support vector machine would need more investigation to determine the optimal kernel and parameters that provide the best accuracy of classification.

Also, the overall accuracy and kappa coefficient have been computed for all the classified images using both the random forest and support vector machine. Figure 3.14 shows the overall classification accuracy and the kappa coefficient for the random forest and the support vector machine for all classified images.

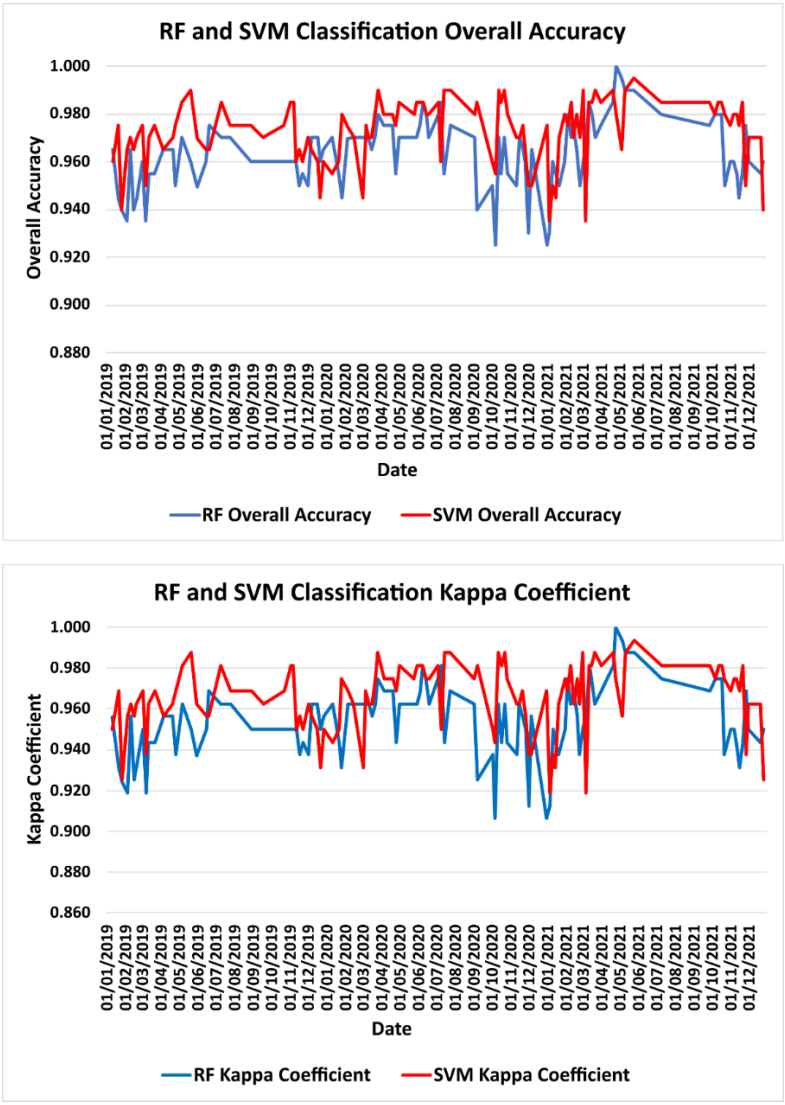

Figure 3.14. Image classification overall accuracy and kappa coefficient for both RF and SVM.

The validation comparison results applied on all the time series images demonstrated that both random forest and support vector machine achieved high accuracy of classification when applying a cost parameter of 0.2 for SVM and with a number of trees of 100 for the random forest. Figure 3.15 and Figure 3.16 show several land cover classification maps generated using random forest and support vector machine, respectively.

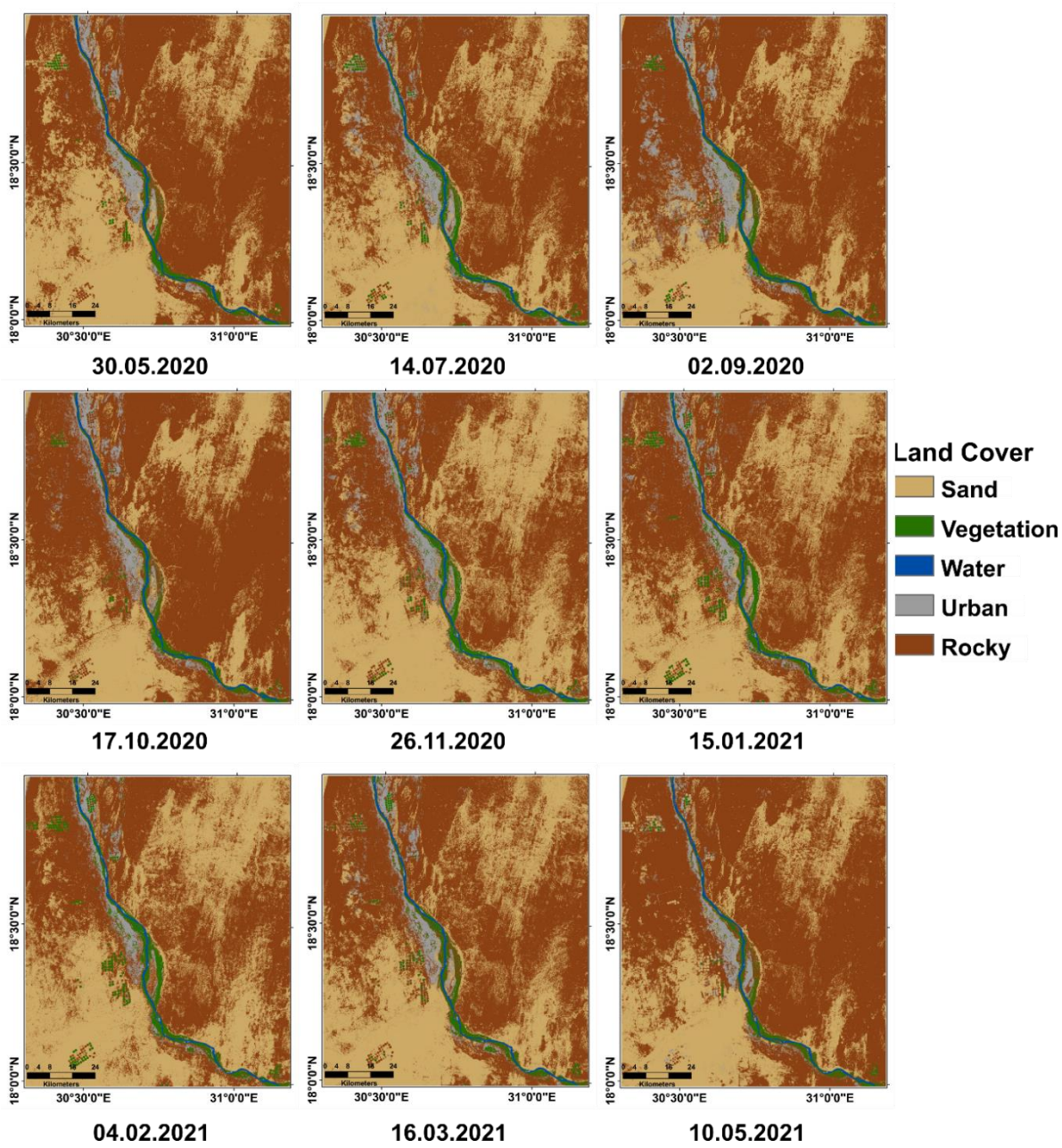

Figure 3.15. Selected land cover classification maps generated using Random Forest classifier.

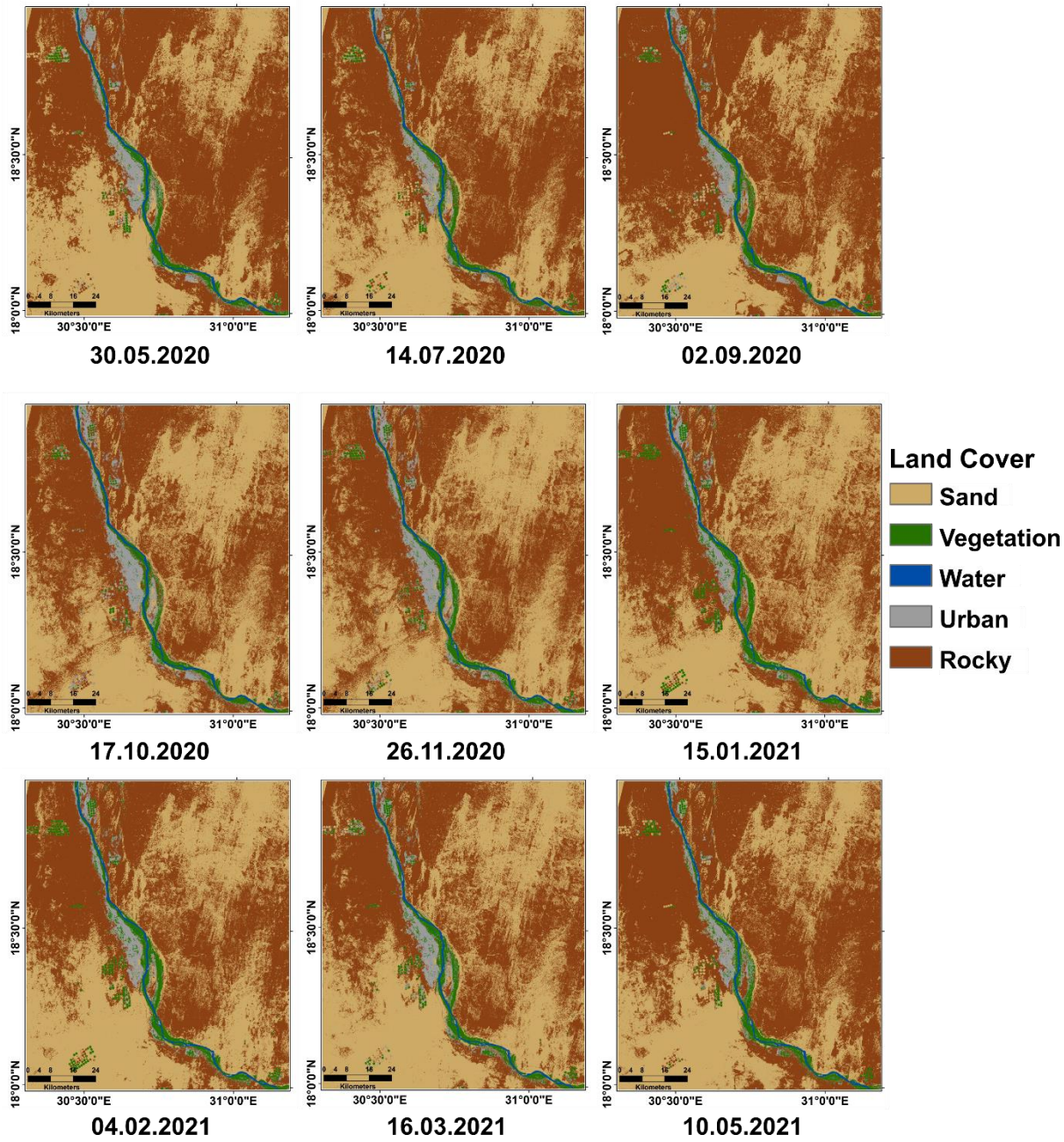

Figure 3.16. Selected land cover classification maps generated using Support Vector Machine classifier.

We can clearly see from the classification maps that the dominant land cover types are the rocky and sand classes which cover most of the study area. The urban and vegetation areas are mainly distributed along the riverbanks as the River Nile is the main source of water for irrigation and domestic use. There are some agricultural projects a few kilometres from the banks where canals are connected to the Nile for irrigation.

The pixel's area summation for each class was computed from the image classification results to detect the time series area changes for each land cover class over the study period. Figure 3.17 illustrates the time series of land cover classification area changes using the random forest and support vector machine classifiers.

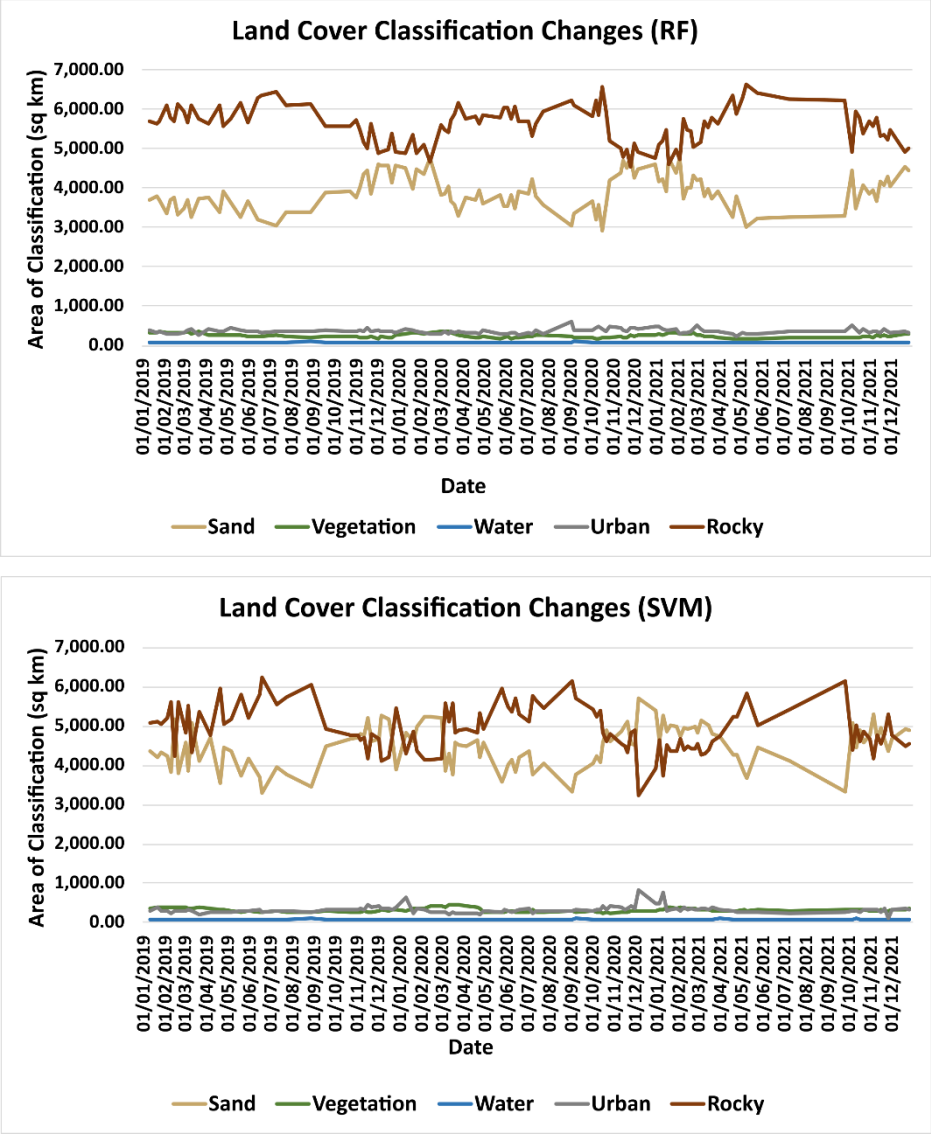

Figure 3.17. Time series of land cover classification area changes using RF and SVM.

It can be clearly seen that the rocky and sand classes cover larger areas compared to the other classes, with the rocky class having an area ranging between the 4500-6500 km^2 for RF and 3200-6200 km^2 for SVM, while the sand class areas range between 3000-4800 km^2 for RF and 3300-5700 km^2 for SVM. On the other hand, the vegetation and urban classes have an area ranging between 150-350 km^2 and 250-600 km^2 for RF and 230-450 km^2 and 110-850 km^2 for SVM, respectively, while the water class has the lowest land cover area ranging between 70-110 km^2 for RF and 80-105 km^2 for SVM, Figure 3.18.

The vegetation class areas increase during the growing season (November-March) and decrease during the rainfall and seed sowing season (June to September), Figure 3.18. The water areas see slight changes due to the water level variation between the autumn and summer seasons, and the presence of some islands in the middle of the river channel as a result of sediment deposition and a drop in water levels during the summer season, which slightly increases the water land cover area.

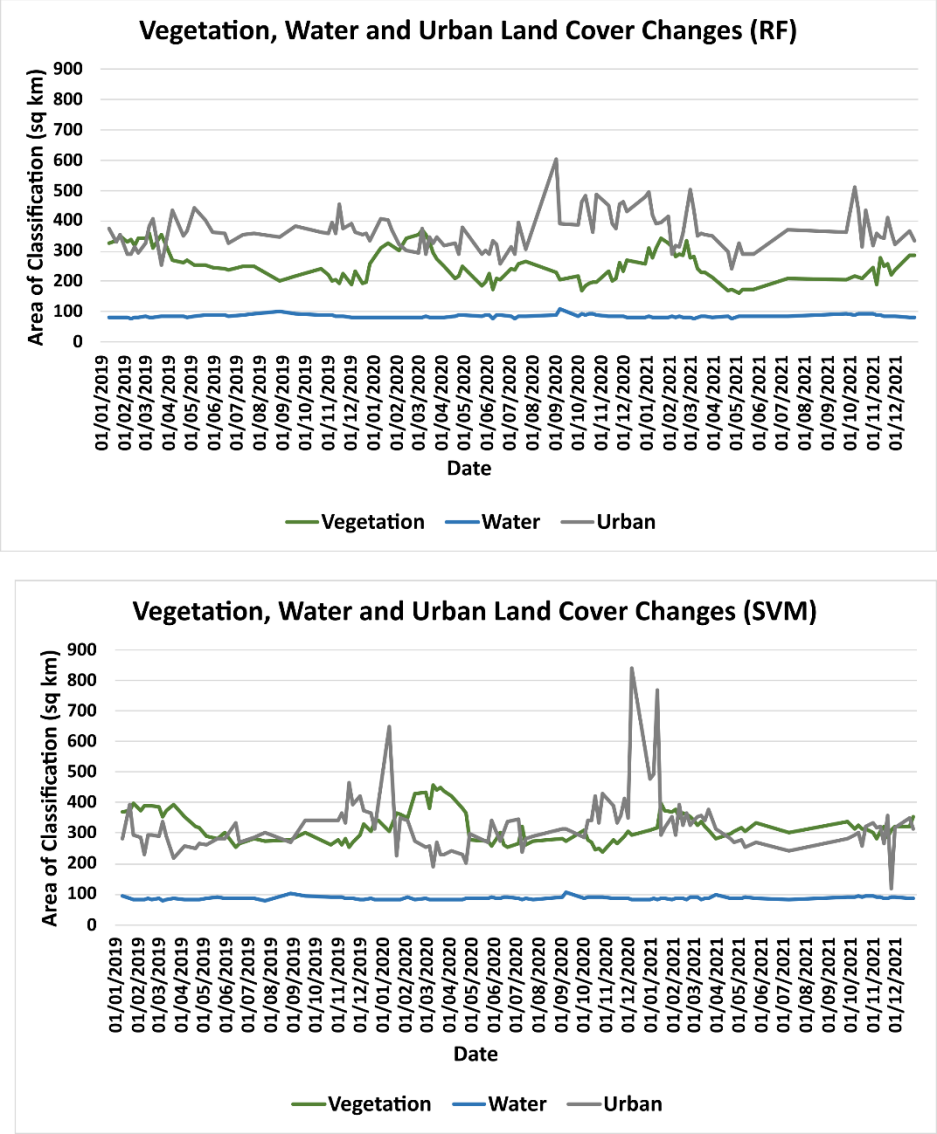

Figure 3.18. Time series of vegetation, water and urban classes area changes using RF and SVM.

The sand classification results show a pattern of significant area changes during the study period, Figure 3.19. The sandy areas were observed to increase during the period between September to February, ranging between 4000-4800 km^2 for RF and 4500-5200 km^2 for SVM, while the area decreased during the period between March to August, with an area ranging between 3300-4200 km^2 for RF and 3300-4600 km^2 for SVM.

These class area changes can be related to the changes in the wind's behaviour. It has been reported that in Northern Sudan, near Goled city, the wind has an average wind speed ranging between 4m/s to 6m/s with maximum gusts ranging between 14m/s and 19m/s, while it changes its dominant blowing direction from north north west all year to blow from the south/southwest during the autumn season (Munro et al. 2012). This change in wind behaviour results in changes to the dynamic area coverage of the dunes.

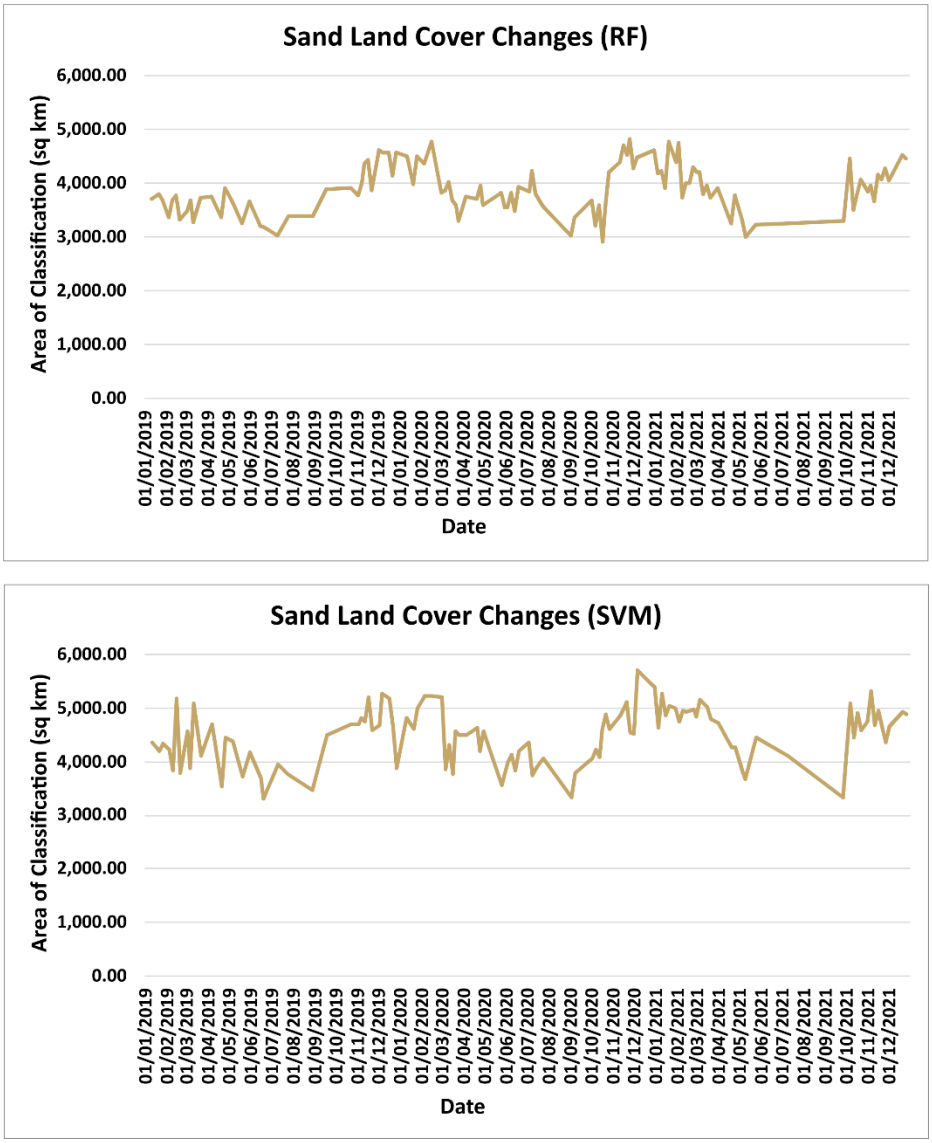

Figure 3.19. Time series of sand class area changes using RF and SVM.

There is a significant correlation between the increase in the sand class area and the decrease in the rocky class area. The Pearson coefficient between the two classes, computed from the RF classification results, shows a high negative correlation of (-0.987), which means that any increase in the sand class area would mean a significant decrease in the rocky class area (Table 3.12). This is also clearly seen in the classification maps, Figure 3.15. This correlation is mainly due to the fact that the simple movement of the dunes is to the surrounding bare lands. In addition, there is a negative correlation of (-0.352) between the sand class and water class, due to the variation in the water level near the riverbanks.

A negative correlation is observed between the water class and the vegetation class of -0.480 as the vegetation areas on the riverbanks are overwhelmed with water during the flood season, while it increases during the summer when it is utilized for cropping.

Table 3.12. Computed Pearson coefficient for correlation assessment between land cover classes for the RF classification results.

Class	Vegetation	Water	Urban	Rocky
Sand	0.183	-0.352	0.183	-0.987
Vegetation	-	-0.480	-0.077	-0.272
Water	-0.480	-	0.171	0.356
Urban	-0.077	0.171	-	-0.291

The overlap between the training sample classes leads to misclassification. For instance, the interchangeable variation of the seasonality in the vegetation areas results in misclassifying some vegetation areas into rocky bare lands during the drying season or also occurring between the urban class and the rocky class where both classes have significantly close reflectance responses as the urban areas are built on a bare land which is part of the rocky class. The latter was clearly observed in the confusion matrices, with rocky areas being classified as urban. Figure 3.20 shows a scatterplot of the reflectance of the training samples of the five land cover classes applied on image 11 January 2019.

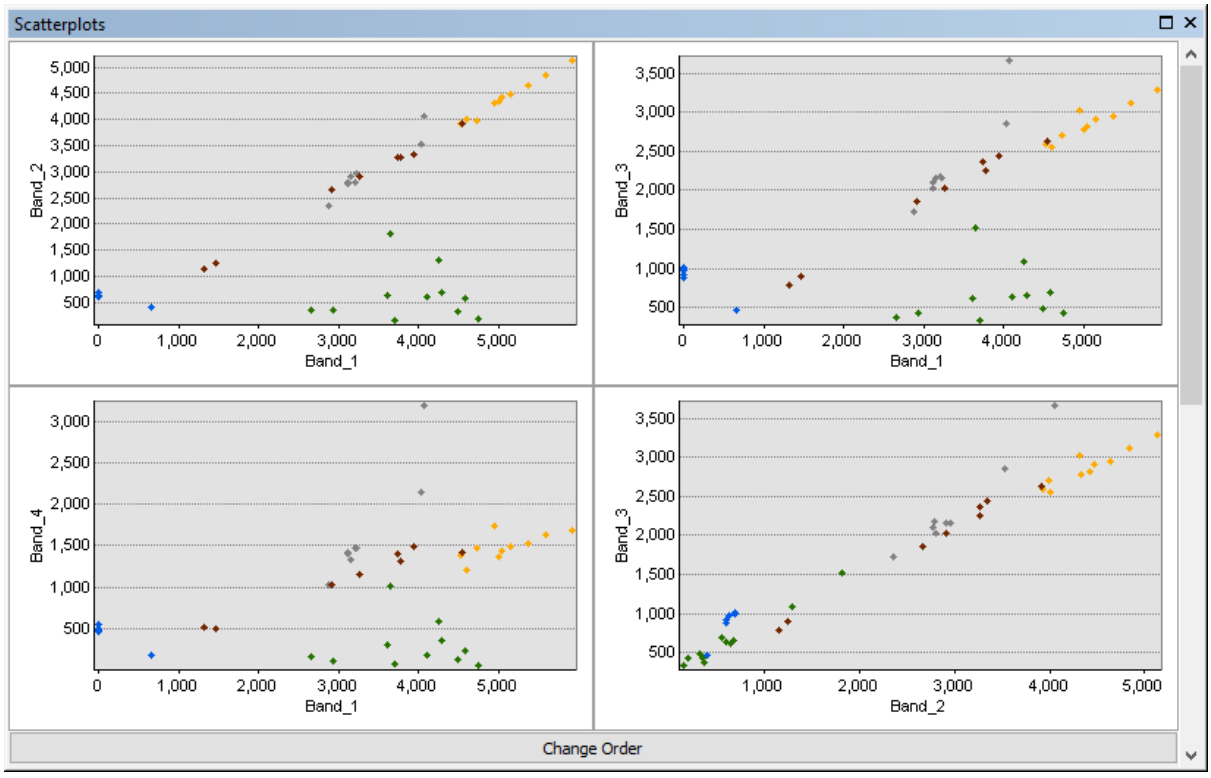

Figure 3.20. A scatterplot of reflectance of the training samples for the five land cover classes.

3.3.2 Individual Dune Movement Detection

The individual dune detection SET tool has been used to detect the displacement and direction of individual dunes. Firstly, the tool was tested on an individual dune that was digitized from two historical high-resolution images in Google Earth, with these two archived images having been collected in November 2011 and December 2012. The digitized dune features were then converted into dune points that represent the boundary of the dunes, after which the displacement and direction of movement were calculated using SET in ArcGIS, Figure 3.21.

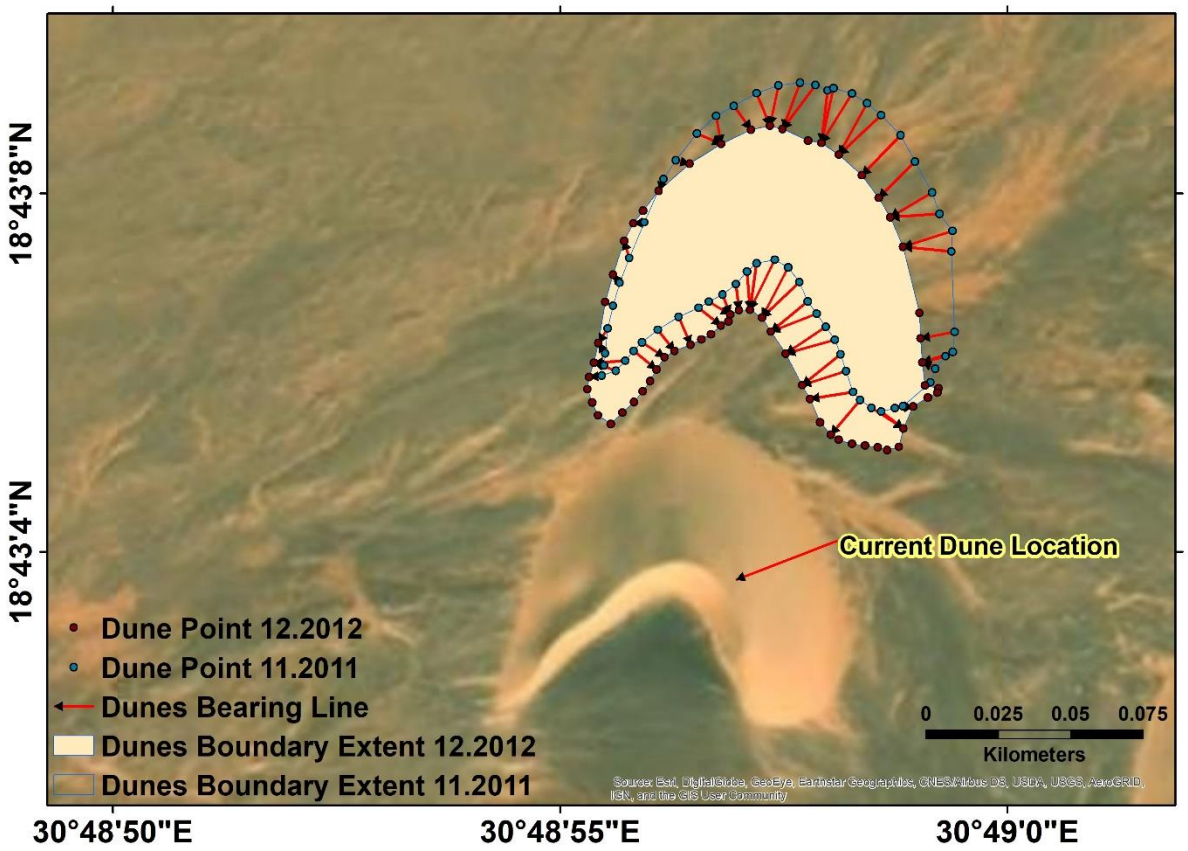

Figure 3.21. Detected individual dune movement between November 2011 and December 2012 using SET applied dunes extracted from high resolution images.

The tool detected a significant movement between November 2011 to December 2012 with an average displacement of 15 metres and a dominant direction of movement to the southwest on the eastern side of the dune, while it detected an average displacement of 7 metres with a dominant direction of movement to the southeast in the west side of the dune. The location of the dune has shifted more than 125 metres toward the southwest between 2011 and 2022, i.e. the current location of the dune. Table 3.13 illustrates the displacement and direction of the detected sand dune movement between November 2011 and December 2012.

Table 3.13. The displacement and direction of the detected sand dune movement between November 2011 and December 2012.

FID	ORIG_X	ORIG_Y	Near_FID	Near Distance	Near X	Near Y	Near Angle	Azimuth
0	30.81574	18.71855	49	8.184	30.81581	18.71851	122.428	302.428
1	30.81571	18.71853	51	9.544	30.81578	18.71848	129.555	309.555
2	30.81565	18.71851	54	10.387	30.81568	18.71842	157.512	337.512
3	30.81558	18.71847	55	9.020	30.81563	18.71840	142.503	322.503
4	30.81553	18.71843	56	9.000	30.81560	18.71838	124.814	304.814
5	30.81551	18.71840	57	9.833	30.81558	18.71834	131.127	311.127
6	30.81548	18.71837	5	10.252	30.81538	18.71836	-93.855	86.145
7	30.81545	18.71834	5	7.674	30.81538	18.71836	-69.121	110.879
8	30.81541	18.71832	4	4.184	30.81537	18.71832	-95.329	84.671
9	30.81541	18.71835	5	3.434	30.81538	18.71836	-74.572	105.428
10	30.81542	18.71839	6	4.202	30.81540	18.71842	-32.130	147.870
11	30.81543	18.71847	6	5.823	30.81540	18.71842	-148.025	31.975
12	30.81544	18.71854	7	2.910	30.81542	18.71855	-61.803	118.197
13	30.81546	18.71861	8	3.547	30.81544	18.71864	-36.688	143.312
14	30.81549	18.71869	9	6.172	30.81548	18.71874	-15.658	164.342
15	30.81554	18.71880	10	3.642	30.81551	18.71880	-95.208	84.792
16	30.81560	18.71893	12	4.248	30.81558	18.71890	-158.849	21.151
17	30.81564	18.71899	13	4.591	30.81568	18.71898	105.235	285.235
18	30.81570	18.71907	14	8.671	30.81578	18.71904	114.262	294.262
19	30.81576	18.71913	14	9.747	30.81578	18.71904	169.884	349.884
20	30.81582	18.71916	15	9.853	30.81587	18.71909	145.339	325.339
21	30.81589	18.71920	16	11.973	30.81593	18.71910	158.543	338.543
22	30.81596	18.71922	16	14.159	30.81593	18.71910	-168.556	11.444
23	30.81602	18.71923	17	16.909	30.81597	18.71909	-160.348	19.652
24	30.81607	18.71923	17	18.555	30.81597	18.71909	-144.530	35.470
25	30.81611	18.71921	19	18.122	30.81609	18.71904	-173.712	6.288
26	30.81613	18.71922	19	19.289	30.81609	18.71904	-168.259	11.741
27	30.81618	18.71920	19	19.651	30.81609	18.71904	-149.671	30.329
28	30.81623	18.71917	20	19.883	30.81614	18.71901	-152.320	27.680
29	30.81627	18.71913	20	19.373	30.81614	18.71901	-134.390	45.610

FID	ORIG_X	ORIG_Y	Near_FID	Near Distance	Near X	Near Y	Near Angle	Azimuth
30	30.81634	18.71907	21	18.837	30.81621	18.71894	-137.349	42.651
31	30.81638	18.71899	22	17.216	30.81627	18.71887	-136.247	43.753
32	30.81643	18.71889	23	16.066	30.81630	18.71881	-121.662	58.338
33	30.81645	18.71883	23	16.053	30.81630	18.71881	-94.065	85.935
34	30.81650	18.71877	24	16.980	30.81634	18.71872	-108.481	71.519
35	30.81649	18.71871	24	15.916	30.81634	18.71872	-84.020	95.980
36	30.81650	18.71846	26	11.324	30.81640	18.71844	-101.603	78.397
37	30.81650	18.71840	27	10.743	30.81640	18.71836	-110.181	69.819
38	30.81647	18.71838	27	7.998	30.81640	18.71836	-105.832	74.168
39	30.81644	18.71835	27	4.815	30.81640	18.71836	-64.882	115.118
40	30.81643	18.71830	28	2.007	30.81641	18.71829	-119.464	60.536
41	30.81634	18.71823	32	3.301	30.81637	18.71823	93.737	273.737
42	30.81632	18.71822	32	6.001	30.81637	18.71823	84.599	264.599
43	30.81627	18.71821	33	9.365	30.81634	18.71816	128.814	308.814
44	30.81624	18.71822	33	12.629	30.81634	18.71816	124.040	304.040
45	30.81621	18.71825	40	15.262	30.81612	18.71814	-141.170	38.830
46	30.81619	18.71827	42	14.272	30.81605	18.71825	-99.563	80.437
47	30.81617	18.71834	43	15.248	30.81603	18.71829	-108.794	71.206
48	30.81615	18.71839	43	16.559	30.81603	18.71829	-130.177	49.823
49	30.81613	18.71843	44	16.779	30.81598	18.71839	-106.609	73.391
50	30.81610	18.71848	44	16.057	30.81598	18.71839	-125.185	54.815
51	30.81607	18.71851	45	16.124	30.81593	18.71846	-112.106	67.894
52	30.81605	18.71855	45	15.948	30.81593	18.71846	-130.702	49.298
53	30.81602	18.71861	46	17.235	30.81590	18.71850	-134.819	45.181
54	30.81599	18.71866	46	19.196	30.81590	18.71850	-153.599	26.401
55	30.81594	18.71868	47	18.998	30.81587	18.71853	-154.859	25.141
56	30.81589	18.71867	47	16.202	30.81587	18.71853	-172.231	7.769
57	30.81586	18.71865	47	13.217	30.81587	18.71853	175.968	355.968
58	30.81582	18.71861	48	8.972	30.81583	18.71853	173.143	353.143
59	30.81578	18.71858	49	7.322	30.81581	18.71851	160.615	340.615
60	30.81574	18.71855	49	8.184	30.81581	18.71851	122.428	302.428

The same process was then applied to detect the movement of a group of selected dunes generated from two sequential classified images collected on the 30 of May and the 09 of July 2020. The selected dunes were converted into polygons without smoothing the cell edges of polygons to conform to the exact shape of the extracted classified dunes, Figure 3.22.

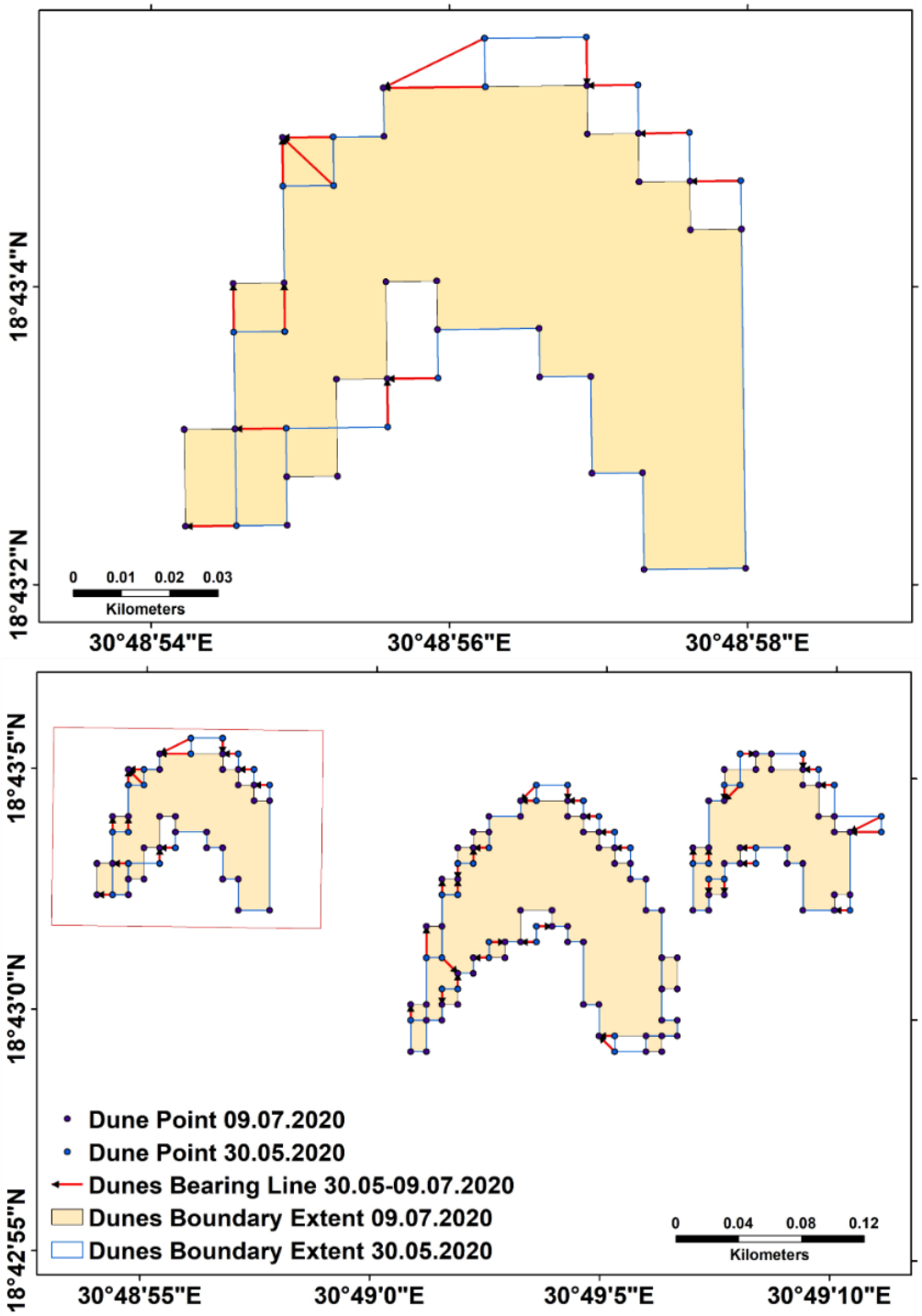

Figure 3.22. A displacement map of a collection of dunes near the city of Goled detected using SET, showing an average displacement of 10m with a detected movement in a southwest dominant direction.

The results show an average displacement of 10 metres and a dominant movement direction to the west/southwest. It is also observed that the lowest detected displacement is related to the resolution of the used satellite images (i.e. Sentinel 2 with 10 m spatial resolution), Table 3.14. This indicates that the spatial resolution of the images plays a significant role in the measured displacement detected using SET.

It can be clearly seen that the tool can distinguish the displacement between the dunes. However, due to the complexity of the generated dunes from the classification, different points are linked and assigned with incorrect points in the second image. This tool showed that detecting the deformation of individual dunes could be provided from moderate images, however, the higher the resolution of the images, the better the footprints of the individual dunes will get, which consequently would result in increasing the detecting capabilities of the SET technique.

The detected movement of the individual dunes using SET has been assessed by visually inspecting and measuring the dunes on the two corresponding images, providing similar average displacement.

In general, the tool performed well in detecting the dune movement. The tool showed good competency with the simple movement in a non-complex dune field, and for individual dunes with smoothed edges, barchan dunes. However, it is observed that all the points in the primary dune point location were assigned to the nearest dune point in the secondary location of the dune, though some points were assigned to the same point in the secondary dune location, which has resulted in some gaps in the displacement calculation.

The individual dune detection SET tool requires more development for the computation of the displacement and direction of movement. This can be achieved by fixing the mixed point issue and restricting the distance radius search based on pervious knowledge of the expected movement between corresponding points. As the 'Near analysis' tool works on providing the distance and proximity information between the primary dune point and the closest point on the secondary dune, multiple points in the primary dune are mapped to one point in the secondary point. This could be resolved by restricting the connection to only one point on each dune points dataset.

Table 3.14. The displacement and direction of the detected sand dune movement between May 30 and July 7 of 2020.

FID	ORIG_X	ORIG_Y	Near_FID	Near Distance	Near X	Near Y	Near Angle	Azimuth
0	30.81610775	18.71725245	0	0	30.81610775	18.71725245	0	0
1	30.81591818	18.71725023	1	0	30.81591818	18.71725023	0	0
2	30.81591586	18.71743086	2	0	30.81591586	18.71743086	0	0
3	30.81582108	18.71742976	3	0	30.81582108	18.71742976	0	0
4	30.81581876	18.71761038	4	0	30.81581876	18.71761038	0	0
5	30.81572398	18.71760928	5	0	30.81572398	18.71760928	0	0
6	30.81572282	18.71769959	6	0	30.81572282	18.71769959	0	0
7	30.81553325	18.71769738	7	0	30.81553325	18.71769738	0	0
8	30.81553441	18.71760707	10	9.997	30.81543962	18.71760596	-90.701	89.29868575
9	30.81543962	18.71760596	10	0	30.81543962	18.71760596	0	0
10	30.81544078	18.71751565	10	9.997	30.81543962	18.71760596	-0.701	179.2986573
11	30.81525122	18.71751344	17	9.997	30.81515643	18.71751233	-90.701	89.29859813
12	30.81525354	18.71733281	14	0	30.81525354	18.71733281	0	0
13	30.81515875	18.7173317	15	9.997	30.81506397	18.7173306	-90.701	89.29857499
14	30.81515411	18.71769296	18	9.997	30.81515295	18.71778327	-0.701	179.2985588
15	30.8152489	18.71769406	19	9.997	30.81524774	18.71778438	-0.701	179.2985892
16	30.81524542	18.717965	20	9.997	30.81524425	18.71805532	-0.701	179.2985783
17	30.8153402	18.71796611	20	14.139	30.81524425	18.71805532	-45.701	134.2986087
18	30.81533904	18.71805642	20	9.997	30.81524425	18.71805532	-90.701	89.29860674
19	30.81543382	18.71805753	21	0	30.81543382	18.71805753	0	0
20	30.81543266	18.71814784	22	0	30.81543266	18.71814784	0	0
21	30.81562223	18.71815005	22	19.995	30.81543266	18.71814784	-90.701	89.29869435
22	30.81562107	18.71824037	22	22.355	30.81543266	18.71814784	-117.266	62.73364118
23	30.81581064	18.71824258	23	9.997	30.8158118	18.71815227	179.299	359.2987532
24	30.8158118	18.71815227	23	0	30.8158118	18.71815227	0	0
25	30.81590658	18.71815337	23	9.997	30.8158118	18.71815227	-90.701	89.29878561
26	30.81590774	18.71806306	25	0	30.81590774	18.71806306	0	0
27	30.81600253	18.71806416	25	9.997	30.81590774	18.71806306	-90.701	89.29881966
28	30.81600369	18.71797385	27	0	30.81600369	18.71797385	0	0
29	30.81609847	18.71797495	27	9.997	30.81600369	18.71797385	-90.701	89.29885371

Many experiments have been carried out to detect the rate of sand dune movement. For instance, (Abou El-Magd et al. 2013) used optical satellite images and GIS to trace the border of the dunes and measure the spatial extension of the sand dune movement in Egypt. SET has the advantage of automatically tracking the extent of the dunes to detect their movement. Moreover, it detects the movement of the dunes on multiple edge points, which will ensure detecting the variation in displacement within the same dune.

Also, (Dong, 2015) has developed an automated dune migration estimation tool (PSTP) using LiDAR time series data, to automatically extract dune slip faces and compute the shift rate generated from two DTMs on different dates. This tool has worked quite well in detecting the migration rate and direction of the dunes. A future study is recommended to compare the capabilities of both the PSTP and SET in the detection of sand dune movement.

3.4 Conclusion

This chapter investigated the use of optical satellite images and machine learning for detecting the movement of sand dunes using a framework that utilizes image processing and geospatial analysis tools. The time series changes of the land cover classification have been computed to detect the area changes over time; this was conducted using machine learning classifiers applied in Google earth engine. A comparison between the random forest and support vector machine algorithms was carried out to identify the optimum classification method for this study. Both classifiers demonstrated superior capabilities in providing high accuracy of classification. This method identified areas at significant risk of being overwhelmed by sand.

Rocky and sand classes cover larger areas compared to the other classes with the rocky class having an area ranging between the 4500-6500 km^2 for RF and 3200-6200 km^2 for SVM, while the sand class area ranges between 3000-4800 km^2 for RF and 3300-5700 km^2 for SVM. On the other hand, the vegetation and urban classes have an area ranging between 150-350 km^2 and 250-600 km^2 for RF and 230-450 km^2 and 110-850 km^2 for SVM, respectively, while the water class has the lowest land cover area ranging between 70-110 km^2 for RF and 80-105 km^2 for SVM. The classification results showed that the sand cover displays a pattern of significant area changes, with an area increase during the period between September to February ranging between 4000-4800 km^2 for RF and for 4500-5200 km^2 SVM, and an area decrease during the period between March to August with an area ranging between 3300-4200 km^2 for RF and 3300-4600 km^2 for SVM. There is a significant correlation between the increase in the sand class area and the decrease in the rocky class area.

The validation comparison results applied on all the time series images demonstrated that both random forest and support vector machine achieved high accuracy of classification when applying a cost parameter of 0.2 for SVM and with a number of trees of 100 for the random forest.

The SET individual dune detection tool worked more efficiently with the dunes extracted from high-resolution images when it faced some challenges with detecting the movement of dunes generated from moderate resolution images due to the complex representation of the dunes. Also, the detected displacement of the dunes depends highly on the spatial resolution of the classified images. This means that higher resolution images can allow for the detection of small movements, that can occur daily and even in a shorter time period.

Although the optical images provided an understanding of the horizontal movement of sand dunes, sand dunes move on the vertical component as well and this needs to be investigated further in future research; this is reported later in the thesis.

Using optical images to detect vertical movement needs a lot of work specifically in the generation of digital terrain models (DTMs). However, alternative techniques such as the InSAR technique might be suitable to detect the vertical displacement of the dunes; this requires a thorough investigation that includes simultaneous land surveys to collect ground truth data to validate the movement detected by InSAR.

4 CHAPTER 4: THE USES OF SAR OFFSET TRACKING FOR DETECTING THE MOVEMENT OF SAND DUNES: SUDAN CASE STUDY

4.1 Background

Synthetic Aperture Radar (SAR) data captured from satellite sensors are widely used for earth observation (Zhou et al. 2009), where they have been applied for monitoring the changes in forests canopy (Balzter et al. 2007), detecting land subsidence (Tosi et al. 2015), modelling the deformation of earthquakes (Massonnet and Feigl, 1998), volcanoes (Pedersen and Sigmundsson, 2006), landslides (Zhou et al. 2009, Cai et al. 2017) and floods (Refice et al. 2014). SAR data have also been used for modelling sand dunes, where several case studies were conducted using the interferometric synthetic aperture radar (InSAR) technique for mapping desert dunes (Blumberg, 1998), in particular for the estimation of the volume (Maghsoudia et al. 2013) and height (Chang et al. 2011) of dunes. Additionally, coherence maps generated by InSAR are used to analyse the dynamics of sand dune movement (Havivi et al. 2018). However, the InSAR technique struggles to measure rapid dune motions due to the coherence loss between repeat SAR acquisitions.

In this study, the SAR offset tracking technique was investigated for detecting the movement of sand dunes. This technique determines the offset between pixels of the same area that appear in two different SAR images. The accuracy of offset tracking depends on the pixel size of the SAR images (Cai et al. 2017), and it is about 1/30th of the image pixel size for both range and azimuth directions (Casu et al. 2011), which results from errors in the co-registration of the two images (Riveros et al. 2013). In the case of Sentinel 1, this is 0.3 m. The main advantage of using offset tracking over Interferometric SAR (InSAR) is that it performs better at estimating large displacements beyond the maximum detectable InSAR deformation (Pepe and Calò, 2017), and also where coherence is low (Strozzi et al. 2002), while avoiding the error-prone unwrapping step used in InSAR for the generation of velocity maps (Riveros et al. 2013). Finally, offset tracking can detect the movement in both range and azimuth directions which can be used to compute the horizontal displacement vectors (Riveros et al. 2013). Offset tracking techniques have been applied widely for studying glacier motion in Monacobreen (Strozzi et al. 2002) and Argentina (Riveros et al. 2013), for the estimation of landslides (Wang and Jónsson, 2015, Wang et al. 2015, Cai et al. 2017), and the deformation monitoring of earthquakes (Wang et al. 2015, Wang and Jónsson, 2015), coal mines (Ou et al. 2018) and volcanoes (Casu et al. 2011).

Pixel offset was used before for the detection of dune motion on Mars applied on optical images (Ayoub et al. 2014); however, this is the first study that applies offset tracking on SAR images for detecting terrestrial sand dune movement.

4.2 Study Area

Sand movement is one of the main environmental phenomena in Sudan that threatens livelihoods and rural communities, where sand overwhelms built-up areas, agricultural fields, and irrigation canals (Munro et al. 2012, LATIF and ELHAG, el Moghraby et al. 1987). Moreover, it affects the River Nile by shaping its banks (Munro et al. 2012, Eljack et al. 2010).

Northern Sudan is the most affected region by sand dune movement in Sudan (Munro et al. 2012). Epigraphic evidence found in the temple of Taharqo at the Kawa archaeological site in Northern Sudan records an inscription of Irike-Amanote, a Kushite King of Meroe, showing the clearing of sand from the processional way in the second half of the 5th century BC (Munro et al. 2012). This implies that sand movement is an ancient environmental phenomenon in Sudan. More recently, this issue has been exacerbated by the increasing aridity and spread of the Sahara Desert due to climate change (Thomas and Nigam, 2018).

The region of interest for this study covers an area of approximately 75 km x 75 km in Northern Sudan within the Nubian Desert (Figure 4.1), where sand dunes are the dominant type of land cover. Three distinct dune fields within the study area were investigated for dune motions. Dune field 1 is in a built-up area near houses on the east bank of the River Nile at Goled city. In this area, locals use vegetation, such as *Prosopis juliflora* (mesquite) and *acacia mellifera* (kitr), to stabilize sand from overwhelming their crops and houses (Munro et al. 2012). Dune field 2 is a field with a dominant land cover of sand dunes where individual dunes can be identified from the rest of the land cover, which consists of barren land and small rocks, in addition to a mountainous area on the eastern side. The dunes have approximate dimensions of 120 metres wide, 150 metres long and 20 metres high. Dune field 3 lies in a mountainous area with small mountains to the east and south (Figure 4.2).

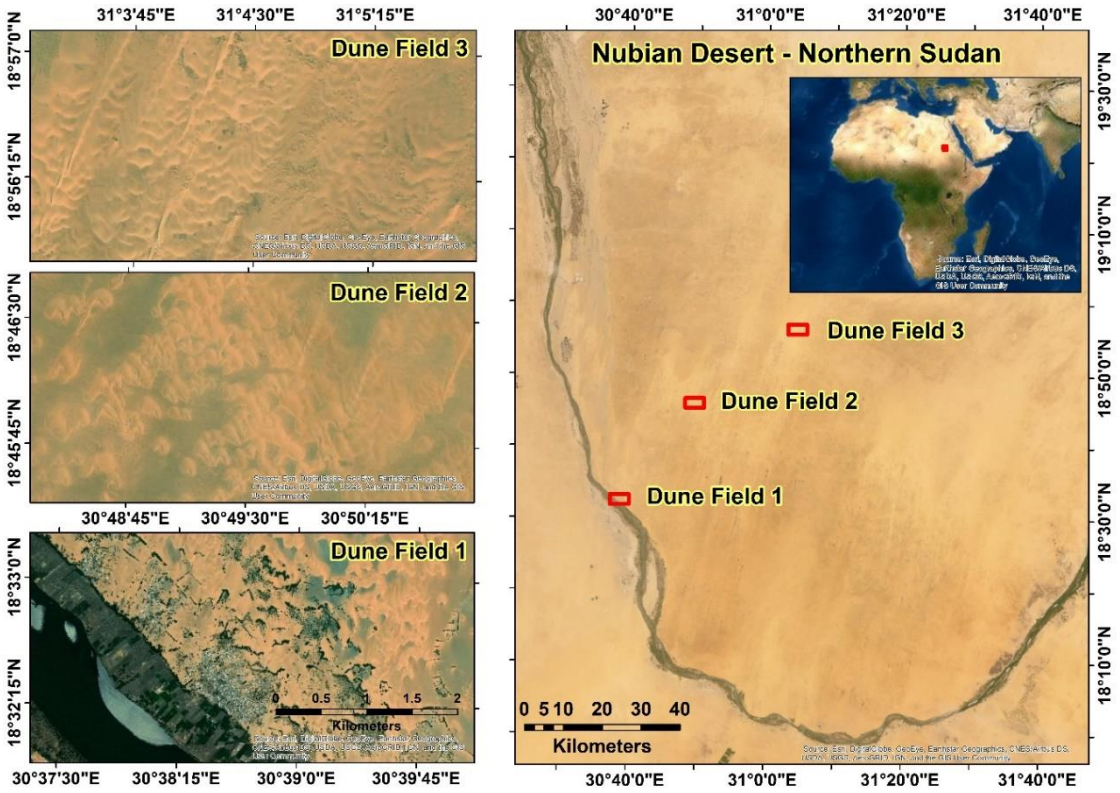

Figure 4.1. Study area in the Nubian Desert, Northern Sudan, with the three dune fields of interest; Dune field 1 is affected by vegetation, Dune fields 2 and 3 both have no vegetation. (Background image © Sources: Esri, DigitalGlobe, GeoEye, i-cubed, USDA FSA, US.)

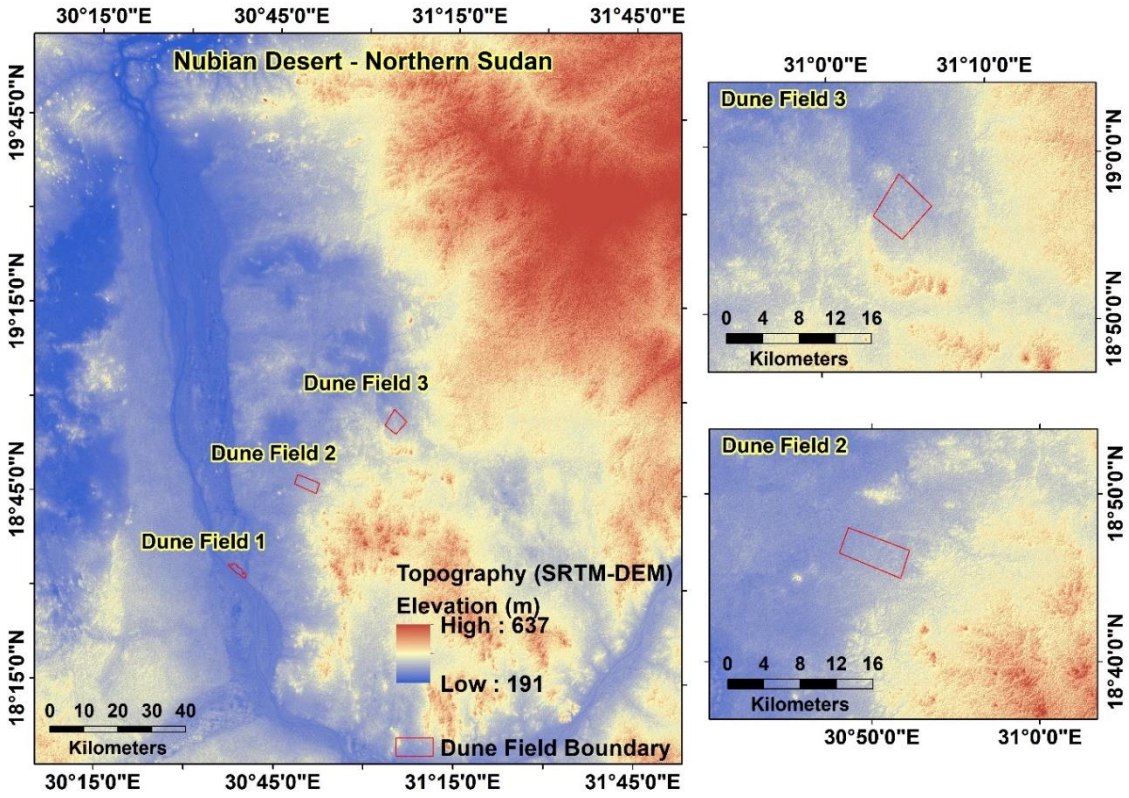

Figure 4.2. The topography of the study area.

4.3 Data and Methods

4.3.1 Data

4.3.1.1 SAR images

Ten Sentinel-1 Level-1 Ground Range Detected (GRD) VV/VH polarised SAR images were used for offset tracking to determine the displacement of sand dunes in the study area for a period of four months, encompassing a large sand storm that hit Northern Sudan on the 12th of August 2017 (NASA, 2017). The GRD images have pixel spacing of 10 x 10 m and are combined to form nine pairs for the dates between the 4th of June and the 14th of October 2017 (Table 4.1). The frequency of the Sentinel-1 acquisitions is 12 days at this latitude. GRD images were used instead of single look complex (SLC) data as the pixel offset technique available in the Sentinel Application Platform (SNAP) works on GRD products and only requires the amplitude information and not the phase. Additionally, the GRD products are already projected to the ground range using an Earth ellipsoid model, which reduces the processing time.

Table 4.1. Image pairs used to generate displacement maps for the study area.

Image Pairs	Primary Image	Secondary Image
Image Pair 1	4 June 2017	16 June 2017
Image Pair 2	16 June 2017	10 July 2017
Image Pair 3	10 July 2017	22 July 2017
Image Pair 4	22 July 2017	3 August 2017
Image Pair 5	3 August 2017	15 August 2017
Image Pair 6	15 August 2017	8 September 2017
Image Pair 7	8 September 2017	20 September 2017
Image Pair 8	20 September 2017	2 October 2017
Image Pair 9	2 October 2017	14 October 2017

4.3.1.2 Wind data

The European Centre for Medium-Range Weather Forecast (ECMWF) provides vector wind data for the globe (Dee et al. 2011, C3S, 2017). ERA5 is the fifth generation of ECMWF reanalysis data generated by the Copernicus Climate Change Service, modelled using archived data from 1950 onwards. This is calculated using a climate–atmosphere model and data assimilation system named Integrated Forecasting system-based 4D-Var, which provides hourly estimates of atmospheric quantities (Hoffmann et al. 2019). For this study, the U (east) and V (north) wind components, in the units of m s^{-1}, were used from the ERA5 model provided on an hourly basis at a height of 10 metres above the surface at 0.25° grid resolution. The wind data resolution is coarse compared to the individual dunes within a dune field. It is assumed that most of the sand motion was caused by winds near the surface of the sand. U and V wind components were combined to compute the horizontal wind speed and wind direction for the period between June-October 2017 (Figure 4.3).

It should be noted that the ERA5 data is a reanalysis product and does not take into account the local high-resolution topography and potential vegetation, trees, etc. (Hoffmann et al. 2019), which have a significant impact on the local wind speed and direction, and the thus on the movement of the dunes.

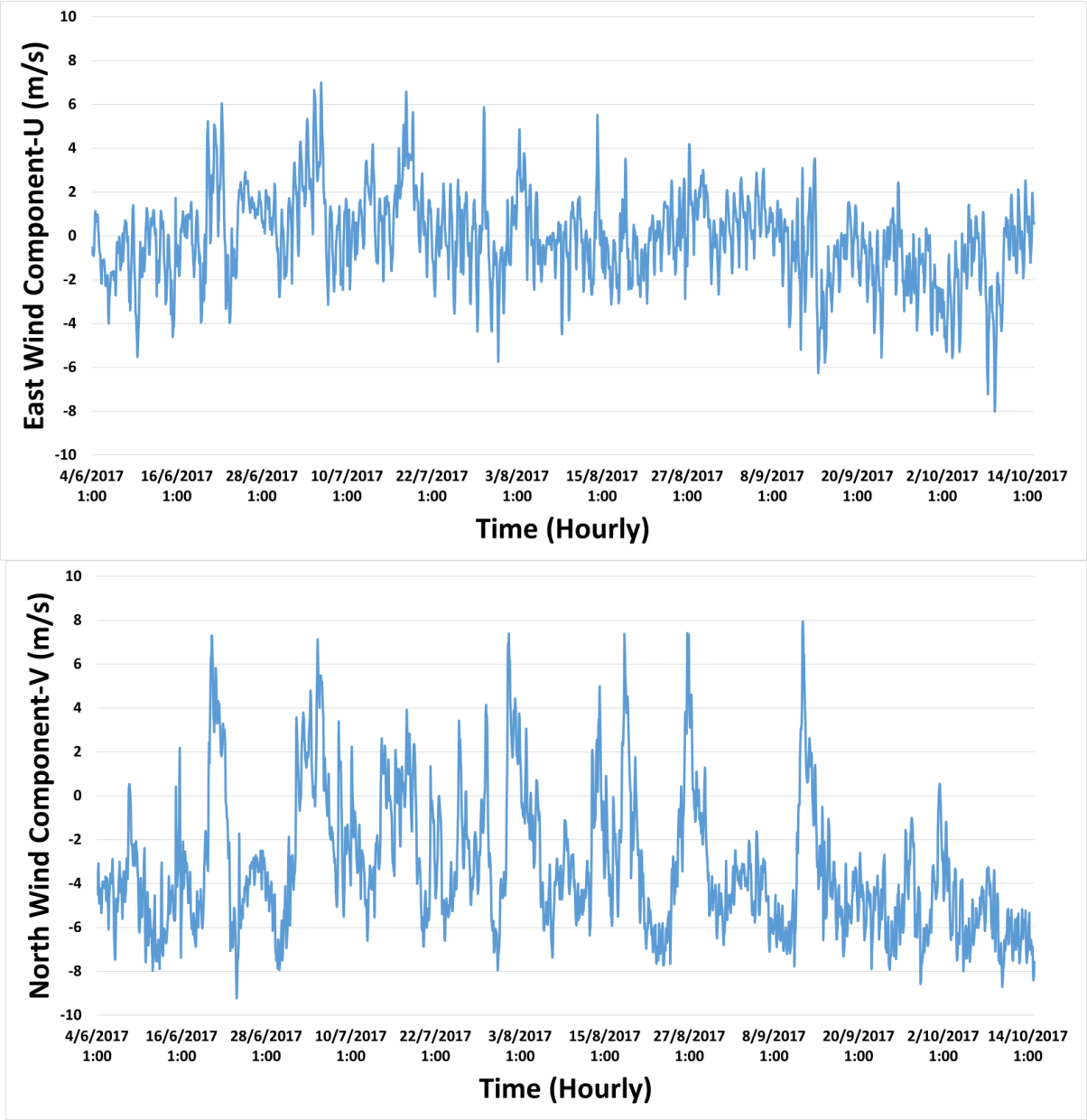

Figure 4.3. East and north wind components between the 4th of June and the 14th of October 2017.

During the study period, the U wind component varied between east and west but predominantly blew from the east, while the V component mostly blew from the south with considerable variation in the degree of motion from the north.

4.3.2 SAR Pixel Offset Method

Sentinel-1 GRD images were processed using the Sentinel Application Platform (SNAP) provided by the European Space Agency (ESA) and available at http://step.esa.int. This toolbox provides a package of tools for SAR imagery processing, including pixel offset tracking. The Sentinel-1 GRD data first need to undergo a pre-processing step before pixel offset tracking can be applied. First precise orbit files that contain the information on the location of the satellite at the time of acquiring the SAR images were used to co-register each individual pair and align the pixels between the secondary image and the primary image to within a few tenths of a pixel in range and thousandths of a pixel in azimuth. To reduce processing time a crop around the study region was taken from the co-registered dataset. Offset tracking was implemented in several sub-steps. First, secondary ground control points (GCPs) that correspond to the user specified GCP grid on the primary image were computed using normalized cross-correlation. Then, the offset and the movement velocity between the primary and secondary GCPs positions were computed. The computed velocities of points were compared to the maximum velocity, with the latter defined based on previous studies in the same study area where the observed sand drift rate was 4.53 m^3 per linear metre width per year, observed by sand traps (Munro et al. 2012); therefore, a maximum velocity of 5 m/day was used to ensure all the movement of the dunes was observed on a short temporal period (days). Points with larger values were considered outliers. This varies depending on the specified user parameters. A local average was applied to valid GCPs. Figure 4.4 illustrates the steps of generating velocity maps using SNAP. Table 4.2 shows the offset tracking parameters used to generate the velocity maps.

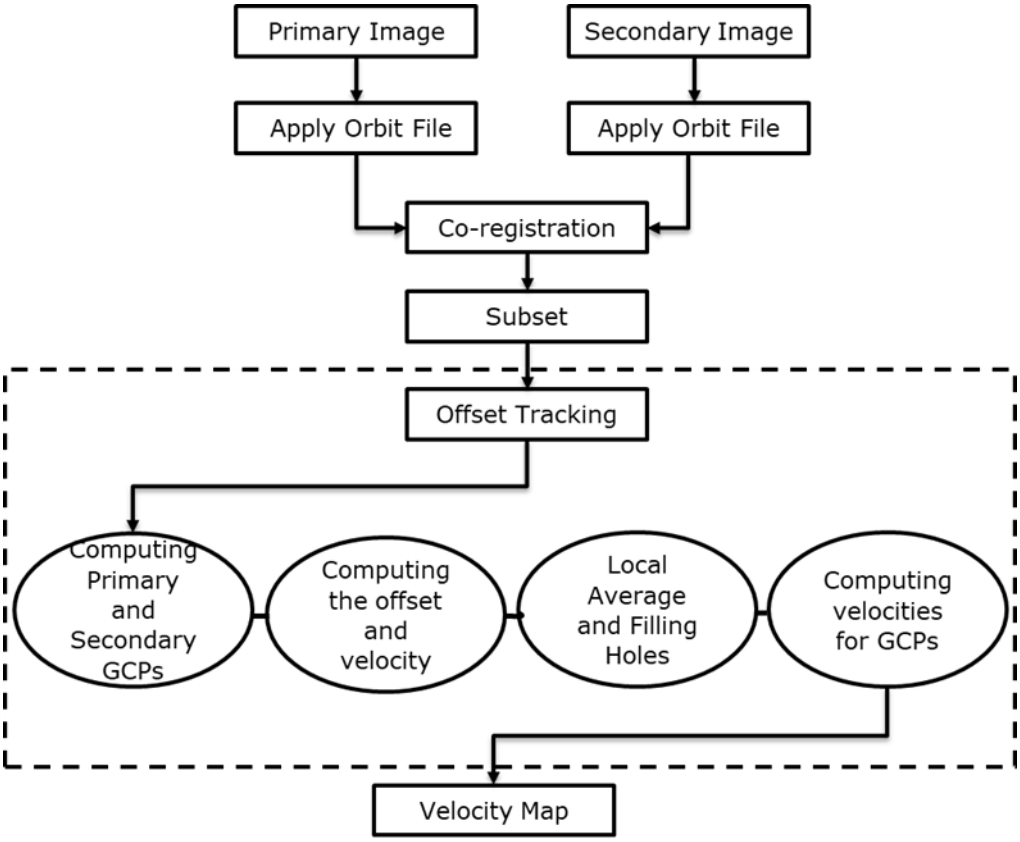

Figure 4.4. The steps of generating velocity maps using SNAP.

Table 4.2. Offset tracking parameters.

Parameter	Values
Grid Range and Azimuth Spacing (in meters)	400 × 400
Total GCP Points	31648
Registration Window Width and Height	128 × 128
Cross-Correlation Threshold	0.1
Average Box Size	5
Max Velocity (m/d)	5.0
Radius for Hole Filling	4

A file that contains vector points of the grid GCPs velocities was also generated after applying offset tracking. This file contains the GCP's coordinates, displacement, velocity, heading (direction of movement), azimuth shift and slant range shift. These parameters were used to characterise the movement of the dunes.

A sequence of displacement vector maps was generated for the study area to study the movement of the dunes and relate this movement to influencing factors. By daisy chaining the image pairs, the estimate displacement time series for each pixel was computed.

Since buildings are generally not built on moving sand dunes, it is assumed that points over built-up areas remain stable and are not displaced by the wind. This allowed a threshold of motion to be defined, representing a 'stable' displacement threshold. Any displacements beyond this level can be attributed to wind-driven motion.

Therefore, pixels over buildings were selected and the mean displacement and standard deviation for each image pair were calculated (Table 4.3). The average displacement (0.62±0.46 m) for the studied period was used to distinguish between small and large displacements of sand dunes. Figure 4.5 illustrates part of the built-up areas and GCPs that fall within them.

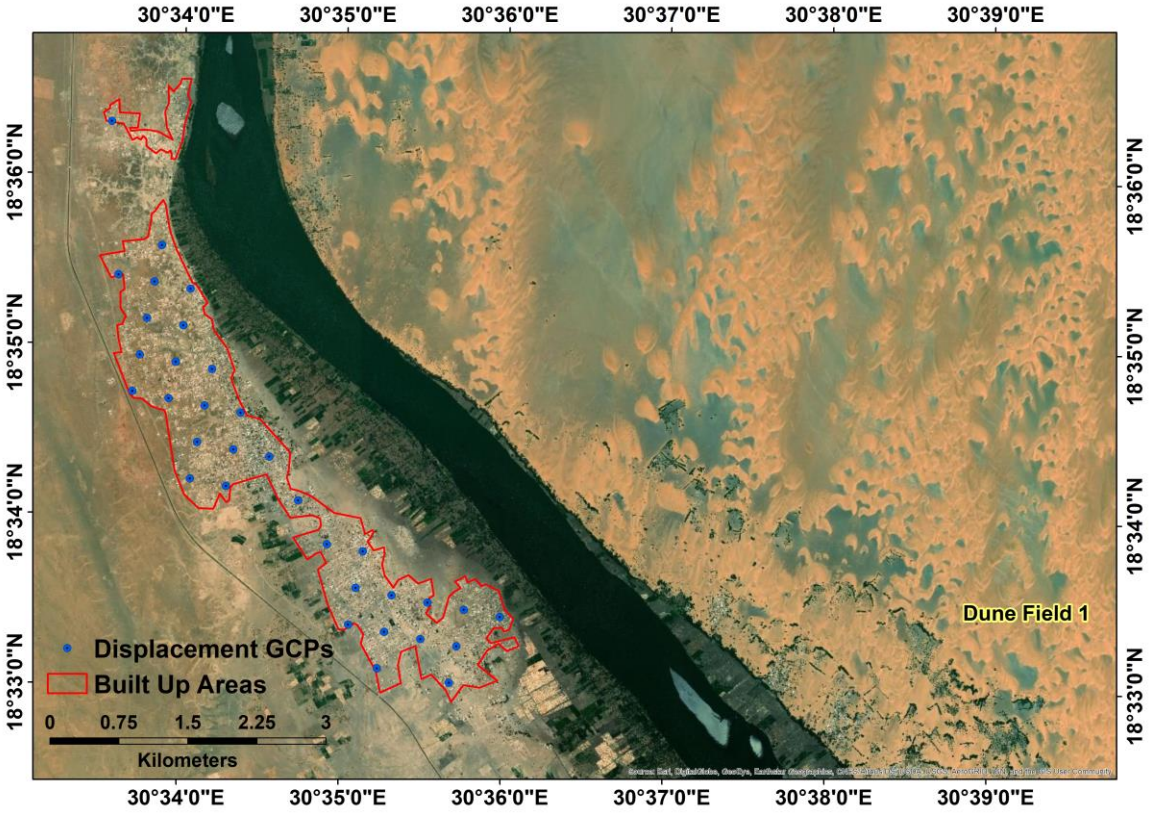

Figure 4.5. Displacement GCPs that fall within built-up areas with an average displacement of 0.62 m.

4.4 Results

4.4.1 Displacement of Sand Dunes

On average, the measured dune displacement in each of the nine offset image pairs was about 0.7 m, 2.4 m and 2.6 m in dune fields 1, 2 and 3, respectively (Figure S 2), where the three dune fields contained, respectively, 52, 49 and 81 dune points. However, there is considerable variation between the images. In a single offset image, the average dune displacement varies between 0.4-1 m in dune field 1, 1.3-3.5 m in dune field 2, and 1.8-3.8 m in dune field 3. Since offset images were created using consecutive SAR dates, we can temporally combine the offsets from each pair into a displacement time series. The east and north displacements for every GCP in each dune field were averaged (Figure S 3) to give the spatially averaged displacement time series for each dune field (Figure 4.6). The cumulative east displacement over the four months study period was 1.8 m, -1.1 m and 4.8 m for dune fields 1, 2 and 3, respectively, while the cumulative north displacement was 0.7 m, 2.9 m and 4.2 m (Figure 4.6).

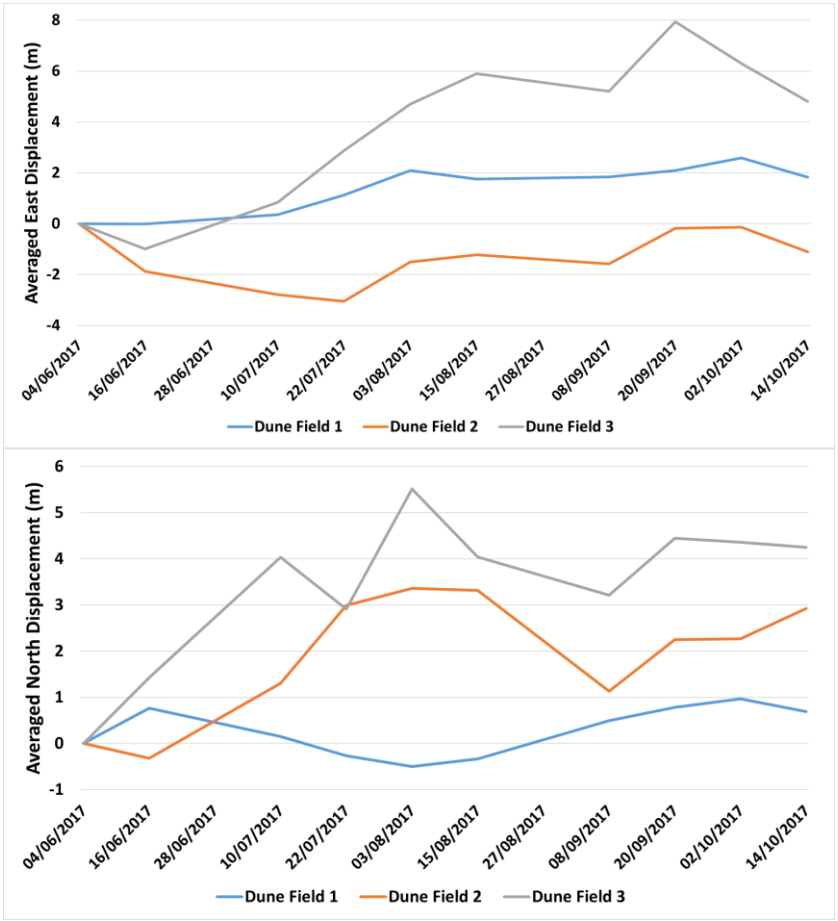

Figure 4.6. Spatially averaged east and north displacement time series with respect to the first SAR acquisition date (4th June 2017) for dune fields 1, 2 and 3.

The 0.62 ± 0.46 m threshold used to determine the movement of the dunes was proved to be reliable, as the GCPs in the built-up area are stable (Table 4.3).

Table 4.3. Displacements of the stable built-up areas.

Date	Minimum Displacement (m)	Maximum Displacement (m)	Mean Displacement (m)	Standard Deviation (m)
4-16 June 2017	0.34	0.88	0.64	0.15
16 June-10 July 2017	0.32	0.98	0.64	0.20
10-22 July 2017	0.52	0.82	0.68	0.08
22 July 3 August 2017	0.73	1.20	0.94	0.13
3-15 August 2017	0.04	0.80	0.35	0.18
15 August-8 Sep 2017	0.23	0.89	0.54	0.18
8-20 September 2017	0.45	0.77	0.61	0.10
20 September-2 Oct 2017	0.20	0.60	0.37	0.10
2-14 October 2017	0.51	1.11	0.82	0.21

4.4.2 Impact of Wind Speed and Direction on Sand Dune Movement

Wind is the main factor in the movement of sand dunes in deserts (C3S, 2017). In Sudan during the Autumn season (July–October), the wind tends to blow from the south (Munro et al. 2012). The azimuth of the dominant wind blowing direction for dune fields 1, 2 and 3 during the studied period was 181, 185 and 187 degrees, with an average wind speed of 4.6 m/s, 4.84 m/s and 4.84 m/s, respectively. The southerly wind (Figure 4.7) resulted in an average displacement of 0.7 m in dune field 1 and 2.6 m in dune field 3, where both dune fields had a dominant movement to the north-east with an azimuth of 56°, while dune field 2 had an average displacement of 2.4 m to the north, with an azimuth of 346° (Figure S 4).

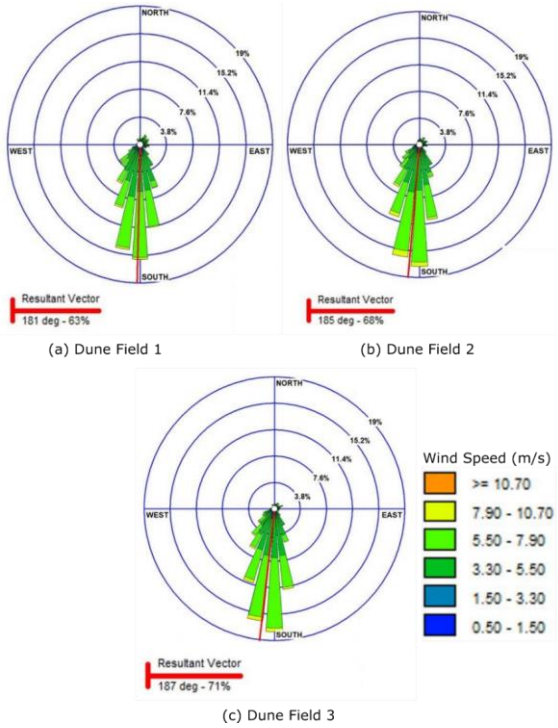

Figure 4.7. Wind rose maps of blowing wind for (a) dune field 1, (b) dune field 2, and (c) dune field 3.

The variation in wind components during the Autumn season resulted in drifting sand dunes in different directions. The sand dunes in dune field 1 moved in a consistent direction, and this was due to the impact of vegetation in controlling the movement (Figure 4.8), while the sand dunes in dune field 2 were divided into two groups according to their motion, which was probably a result of the mountainous topography near the dune field (Figure 4.9). Dune field 3 had mostly consistent sand movement affected by its mountainous topography (Figure 4.10). This opposite directional movement of the dunes in dune fields 2 and 3 might also be due to measurement uncertainty.

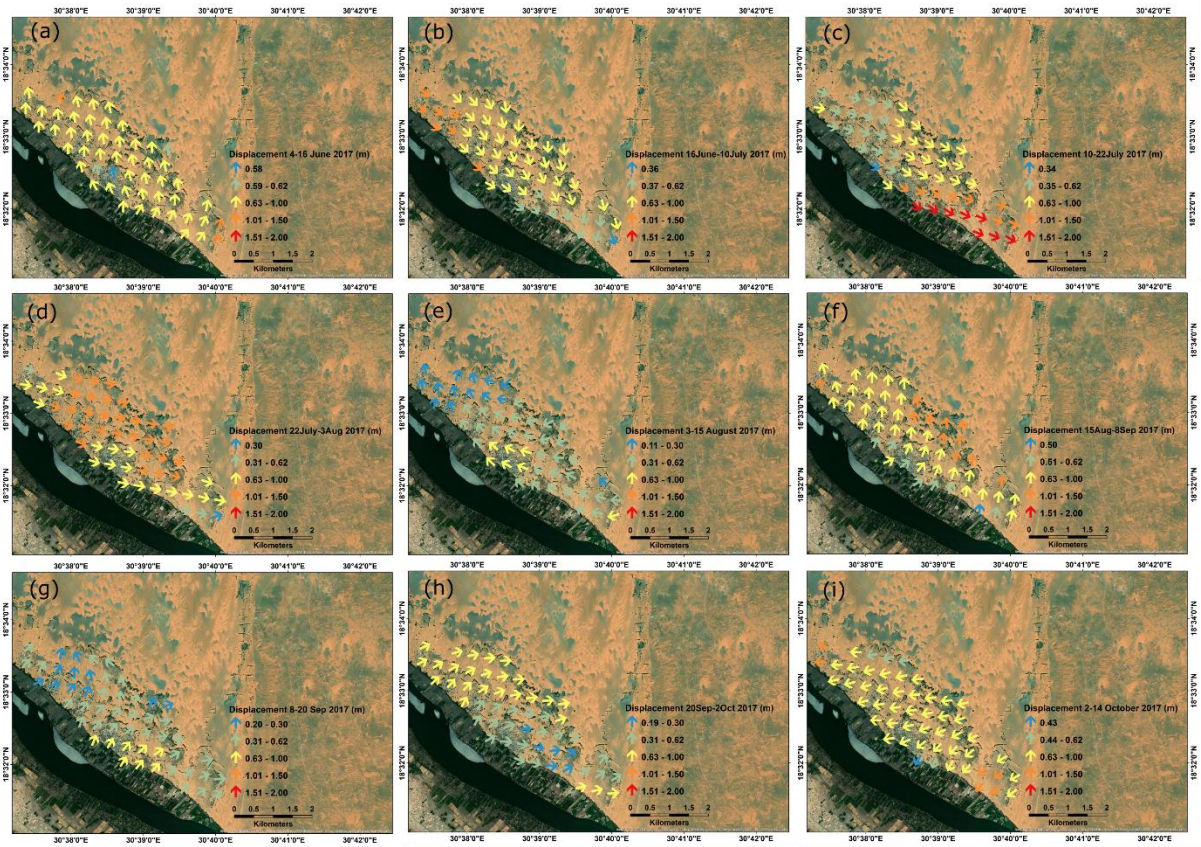

Figure 4.8. Displacement maps of dune field 1 for each pair of the SAR images. (a) Displacement map between 4th and 16th of June 2017, (b) Displacement map between 16th of June and 10th of July 2017, (c) Displacement map between 10th and 22nd of July 2017, (d) Displacement map between 22nd of July and 3rd of August 2017, (e) Displacement Map between 3rd and 15th of August 2017, (f) Displacement map between 15th August and 8th of Sep 2017, (g) Displacement map between 8th and 20th of September 2017, (h) Displacement map between 20th of September and 2nd of Oct 2017, (i) Displacement map between 2nd and 14th of October 2017.

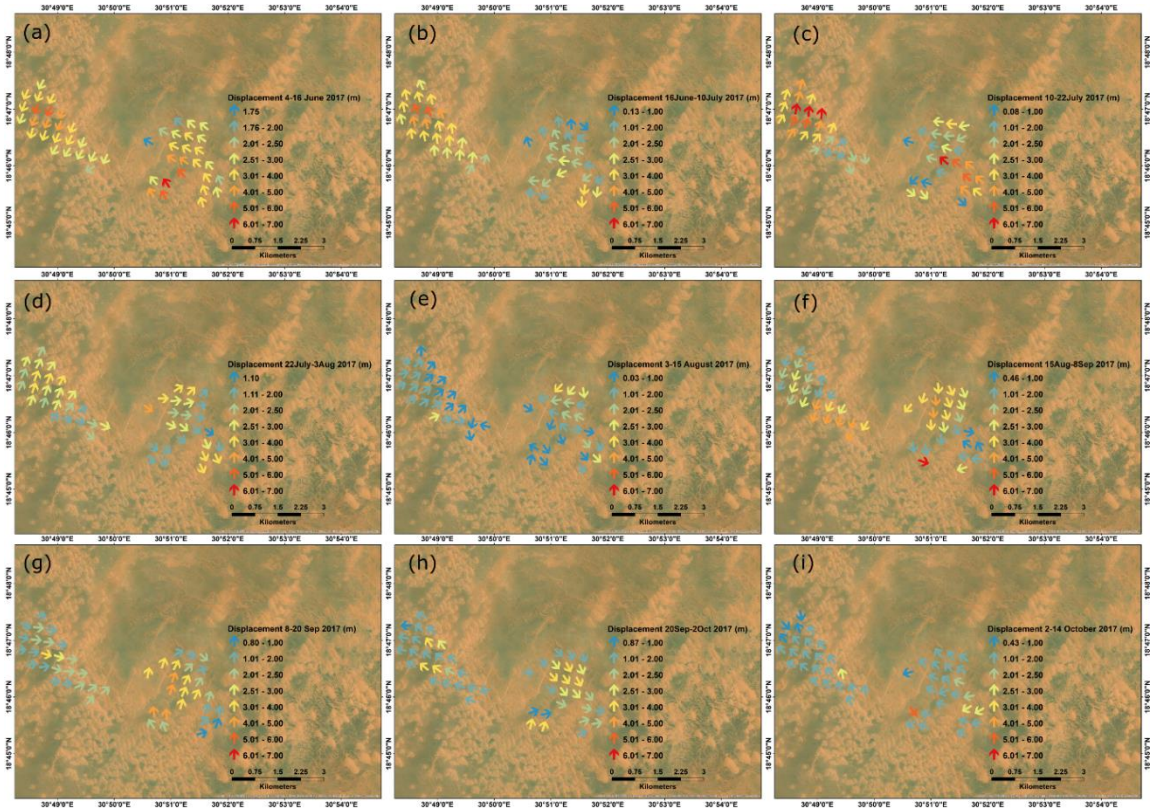

Figure 4.9. Displacement maps of dune field 2 for each pair of the SAR images. (a-i) are the sequence of displacement maps between the 4th of June to the 14th of October 2017.

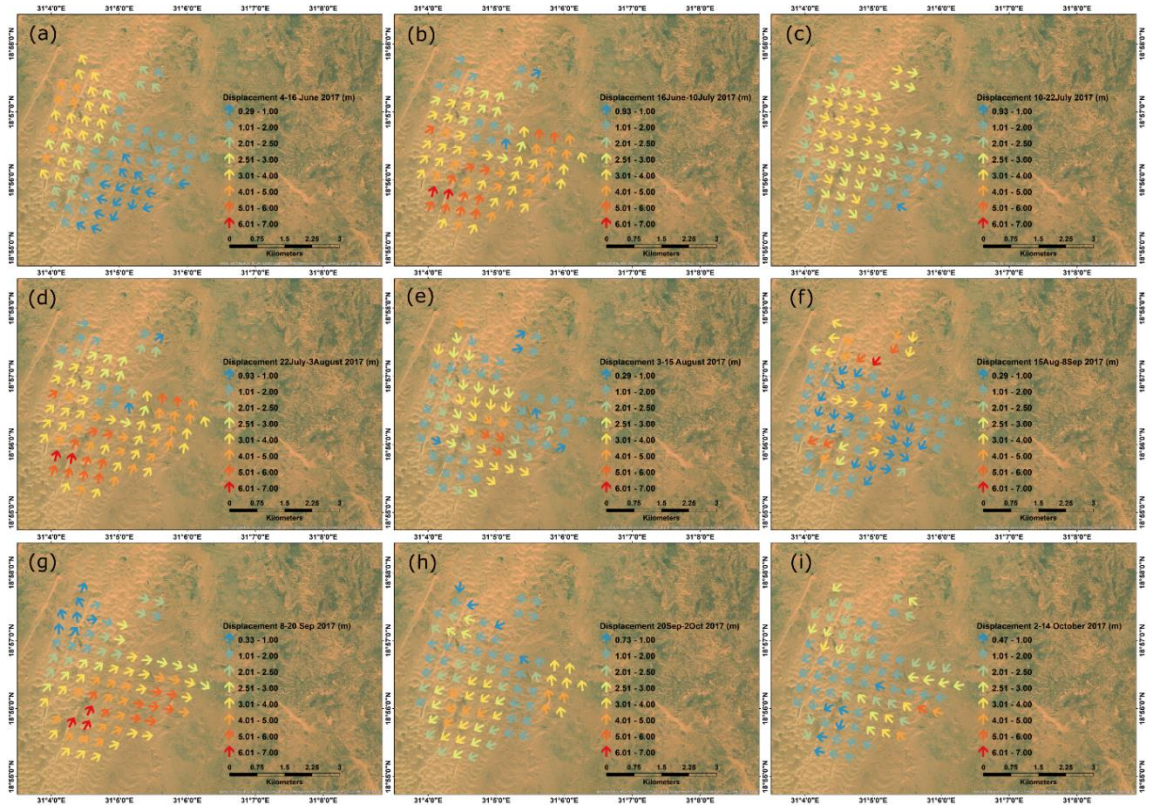

Figure 4.10. Displacement maps of dune field 3 for each pair of the SAR images. (a-i) are the sequence of displacement maps between the 4th of June to the 14th of October 2017.

4.4.3 Impact of Vegetation

A comparison was carried out to further determine the impact of vegetation cover on the movement of sand by considering the differences between the displacements of randomly selected dune points in the vegetated dune field 1 and the displacements of dune points in non-vegetated dune fields 2 and 3 (Figure 4.11). Large displacements were observed in the non-vegetated dune fields 2 and 3 with an average displacement of 2.4 and 2.6 m, respectively, compared to the average displacement of stable areas of 0.6m, which is similar to the stability threshold of 0.62 ± 0.46 m determined for the built-up areas. Dunes in the vegetated dune field have a small average displacement of 0.7m, similar to the stable area. This clearly shows the impact of vegetation in slowing down the movement of sand. This supports Munro et al's (2012) recommendation of using vegetation for stabilizing dunes in agricultural and built-up areas in Sudan.

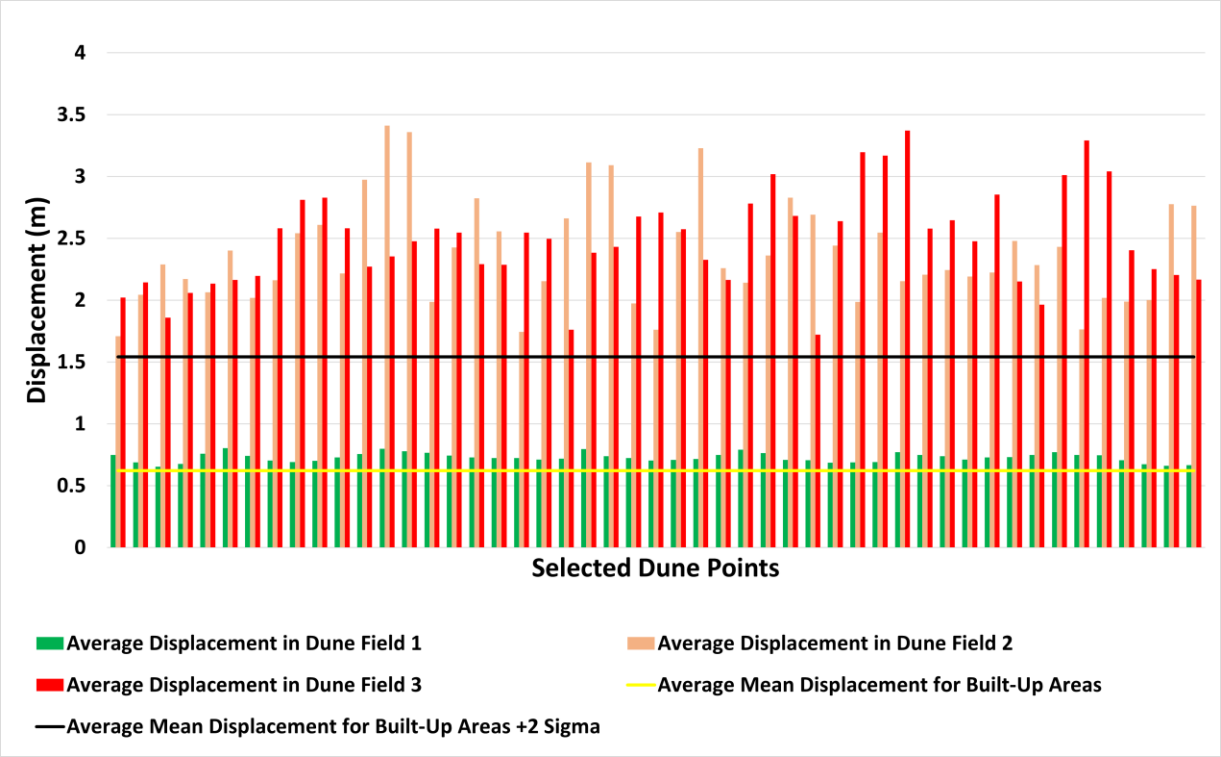

Figure 4.11. Average displacement of dune fields 1,2 and 3 for randomly selected points compared to the stable zone of the built-up areas.

4.5 Discussion

4.5.1 Analysis of Dune Displacement

Wind blew mostly from the south, pushing the sand towards the north, which is in the opposite direction of its normal movement during the Spring and Summer seasons, i.e. to the south (Munro et al. 2012). In this section, a discussion is made to reflect on some cases of the displacements of dune fields 1, 2 and 3 under normal and gusty wind conditions to show the impact of the variation in the influencing factors on the dune displacements.

The first case is under a normal wind condition, just before the start of the autumn season in Sudan, in the period between the 4th to the 16th of June 2017 with a wind blowing dominantly from the south with an average wind speed of 4.9 m/s. This resulted in an average displacement of 0.8 m, 3.5 m and 1.9 m for dune fields 1, 2 and 3, respectively (Figure S 2). Dune field 1 had a movement direction towards the north north-east (Figure 4.8a) which reflects the impact of the dominant wind direction. The movement in dune field 2 had two dominant movement directions (Figure 4.9a); the east side of the dune field near the borders with the mountain had resulted in a diverted movement to the north-west, while the west side of the dune field moved in an opposite direction, to the south-west. This is most likely due to the impact of topography (Figure 4.2) forming a local counter-clockwise wind vortex, where the western arm of the vortex has probably generated a local wind motion towards the south. These types of localised wind phenomenon are not included in the more regional ERA5 wind models, and it requires ground observation. Dune field 3 has mountains on its south and east sides (Figure 4.2). This had an impact on its movement, which can be clearly seen in the diverted motion with a dominant component towards the north-west (Figure 4.10a).

The second case shows the displacement of the dunes in the period between the 8th to the 20th of September with a wind blowing dominantly from the south with an average speed of 4.9 m/s. However, a northerly gusty wind with an average wind speed of 7.6 m/s occurred on the 12th of September. This resulted in an averaged displacement of 0.4 m, 2.4 m and 3.4 m for dune fields 1, 2 and 3, respectively (Figure S 2). Dune field 1 had a movement direction towards the north-east (Figure 4.8g), which reflects the impact of the dominant wind direction but also shows the vegetation cover's impact in stabilising the movement of the dunes and potentially preventing the impact of the easterly wind. Whereas the movement in dune field 2 had two dominant movement directions (Figure 4.9g); the east side group of dune points moved to the north while the west side group of the dune points moved to the east.

This is most likely due to both the impact of the northerly gusty wind on the 12th of September and the impact of the strong westerly wind component, which exceeded the speed of 5.5 m/s during the period between the 8th to the 20th of September (Figure 4.3). Regarding dune field 3, the dune points had a displacement to the north-east (Figure 4.10g) affected by the northerly gusty wind on the 12th of September and the impact of the westerly wind component during the period between the 8th and the 20th of September.

The third case is the displacement of the dunes in dune field 1 between the 16th of June and the 10th of July to the south-east, even though the dominant wind direction for the period between the 16th of June and the 28th of June was blowing from the south. Two north-easterly gusty winds occurred between the 20th to the 22nd of June and between the 4th and the 5th of July, which exceeded 9.5 m/s wind speed and resulted in this movement (Figure 4.8b). It has to be mentioned here that the time interval between the two available SAR images for this offset image is 24 days, a larger temporal interval compared to the 12 days for the rest of the pairs. The north cumulative displacement continued moving south, reaching the maximum southward displacement in the period between the 22nd of July and the 3rd of August 2017 due to the occurrence of several northerly/north-easterly gusty winds. Afterwards, the dunes started to move gradually to the north (Figure S 3a).

In general, the displacement time series for dune field 1 (Figure 4.6) show a larger cumulative displacement in the east compared to the northern component and this is due to the impact of the wall of trees in diverting the movement of the dunes parallel to its orientation. Dune field 2 had a larger movement in the north component, while dune field 3 had the largest movement among the three dune fields in both east and north components.

A correlation analysis was carried out to identify the relationship between the displacement of the dunes in the eastward and northward directions and the wind east (U) and north (V) components by computing the Pearson correlation coefficient for dune fields 1, 2 and 3. In general, most of the correlations are positive, which shows that wind direction directly affects sand motion, apart from in dune field 1, which could be due to the impact of the tree line. Dune field 2 has a poor correlation in the east, probably because of the two vortexes seen in the measurements caused by local topography, which are not picked up by the coarse wind measurements. The correlations are not perfect, because of the variability of the wind gusts and the timing difference between wind and dune measurements, Table 4.4, Figure S 5.

Table 4.4. Pearson correlation analysis between the average east displacement and U wind and between average north displacement and V wind for dune fields 1,2 and 3.

Dune Field	Pearson Correlation Coefficient (r)	
	E	N
Dune Field 1	0.42	−0.36
Dune Field 2	0.02	0.30
Dune Field 3	0.62	0.30

4.5.2 Reflection on Other Studies

Other studies have shown a clear correlation between the movement of sand dunes and the impact of wind, vegetation cover and topography. Munro et al. 2012 and Abuzid 2009, found that sand moves interchangeably in different directions and that during the Autumn season sand drifts to the north as a result of the southerly wind (Munro et al. 2012, Abuzied, 2009). This study showed several variations in the direction of dune movement during the Autumn season; however, most of the displacement computed in this study showed a dominant movement to the north-east for dune fields 1 and 3, and a movement to the north for dune field 2 (Figure S 4). This movement coincides with the dominant direction of the wind in the autumn season (southerly wind). Munro et al. 2012, showed similar sand drifting during the same season (Munro et al. 2012). However, they also reported some southerly sand drifting cases that can also be clearly seen in this present study, as a result of the occurrence of several gusty wind episodes blowing from the north.

The impact of vegetation cover on sand dune motion has been reported in many studies, where it reduces the wind speed blowing over the sand dunes (Kok et al. 2012). Vegetation cover has been used to control the movement of dunes in deserts (Munro et al. 2012, Berte, 2010) and coastal areas and beaches (Koja, 2012, Durán and Moore, 2013). Salih et al. 2017 stated that any increase in the vegetation cover results in more stability of the sand motion (Salih et al. 2017).

Additionally, Thomas and Tsoar 1990 stated that vegetation has a significant role in slowing down the movement of dunes and that sand dunes which migrate actively are less vegetated than those that migrate slowly (Lancaster, 1995). Baoli and Tom 2015 conducted research on mapping sand dunes from satellite images; however, they excluded dune fields with the presence of vegetation cover, as they claimed that it was difficult to interpret the behaviour of the dunes due to the uncertainty resulting from vegetation (Liu and Coulthard, 2015). However, in this research, the comparison between the vegetated dune field 1 with the non-vegetated dune fields 2 and 3 clearly showed the impact of vegetation cover in stabilizing the movement of the dunes. Additionally, it affected the dune points to the edge of the barrier wall of trees more in dune field 1, where most of the dunes were deviated in parallel, which visibly shows the impact of the vegetation.

Other studies have reflected on the impact of topography on the movement of the dunes (Kok et al. 2012). Suliman 2012 showed in his study on sand dune movement in the north-west coastal region of Libya that the topography is the most important factor in shaping the dunes, while the sand particles are diverted due to the mountainous topography (Koja, 2012), which is also seen clearly in this study.

As the detected movement by SAR offset tracking is the horizontal sand dune movement, this raises an interesting question that should be firmly answered as to how to detect the impact of vertical sand dune motion and what the correlation is between the horizontal and vertical movement of sand dunes. Answering this will require further work and necessitate the generation of high-resolution digital elevation models.

4.5.3 Limitations

The SAR pixel offset technique requires ground truth data to validate its accuracy more reliably. However, some limitations can be highlighted here for the images and wind data.

An important limitation to the use of SAR data to monitor sand dune motion in Sudan is the revisit frequency of the Sentinel-1 constellation. This can be minimised by only using image pairs that have the smallest temporal (≤24 days) and spatial baselines (≤16m). However, large displacements that occur within the satellite revisit time can still cause decorrelation and registration errors. The acquisition frequency for Sentinel-1 over Sudan is 12 days, which is not good enough to detect the impact of individual wind storms as the significantly gusty winds tend to occur during shorter periods (a few days at most) in the Autumn season (Munro et al. 2012) (Figure 4.3). This technique might work better for detecting coastal sand movement in Europe, where the temporal coverage of Sentinel-1 images is higher (every 6 days) compared to Sudan and Africa in general.

One way to overcome this is by using high temporal resolution images acquired by other sensors (e.g. TerraSAR-X, RadarSat-2 satellites…etc) (Fallourd et al. 2011).

The ERA5 modelled wind data does not take into account the local high-resolution topography and trees, where its impact was seen in the different dune movement behaviours in the three dune fields. This is a limitation of the ERA5 data. However, in this study, the DEM used for the analysis provided an understanding of the topography and its impact on diverting the movement of sand. The impact of rocky surfaces was reported by Bagnold in 1941 (Munro et al. 2012), as in dune fields 2 and 3, where it resulted in higher saltation and led to a larger movement, which reflects the impact of topography. Ground recording weather stations would be the optimum solution to have accurate measurements of the wind data.

4.5.4 Regional Impact

Over the whole study period, large movements were detected in other areas that contain sand dunes, which indicates that sand moves fast with an average velocity ranging between 0.15 and 0.32 m/day, which was used to identify the most vulnerable areas of sand movement in the region (Figure 4.12). Some agricultural projects, villages and parts of the roads are affected by this large movement of sand. Therefore, the SAR offset tracking technique can provide a risk mapping technique, identifying the areas exposed to high degrees of sand drift.

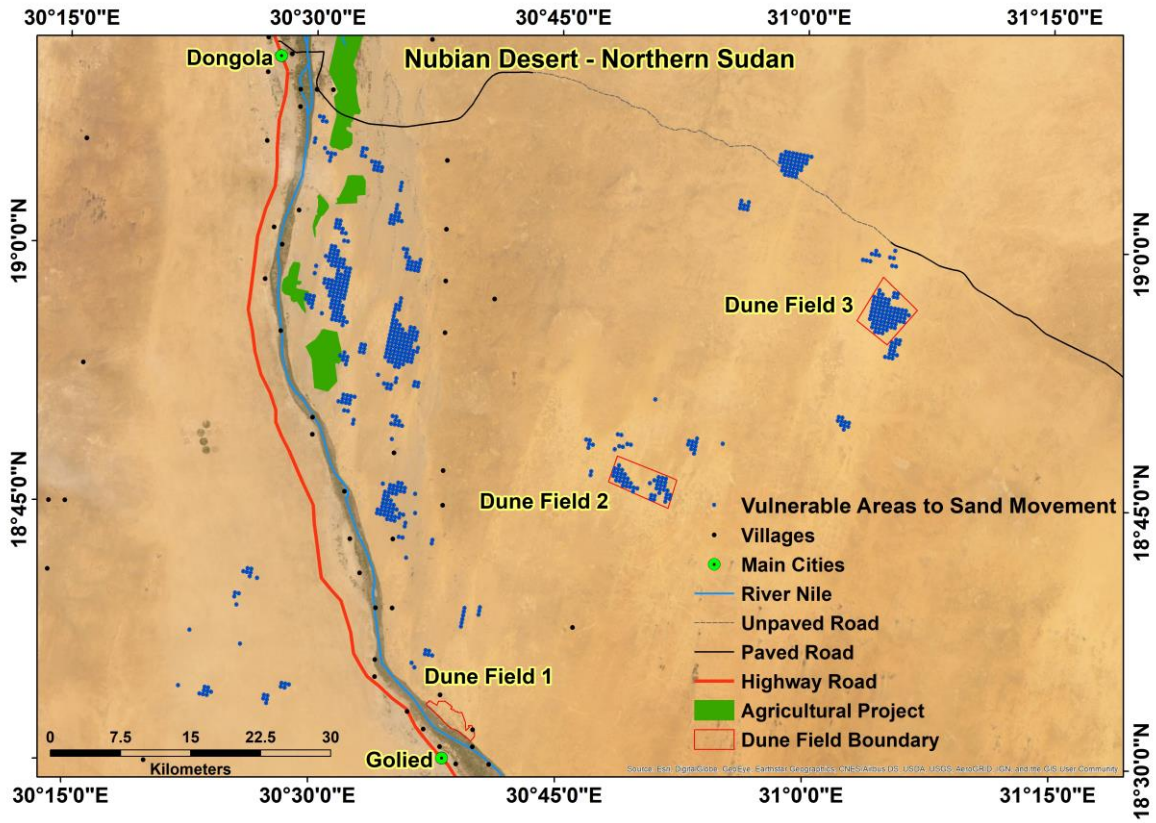

Figure 4.12. Vulnerable areas to sand movement.

4.6 Conclusion

This is the first application of SAR offset tracking in detecting the movement of terrestrial sand dunes. In this study, the impacts of the influencing factors (wind speed/direction, vegetation and topography) on the dune movement were investigated. The cumulative east displacement over the four months study period was 1.8 m, -1.1 m and 4.8 m for dune fields 1, 2 and 3, respectively, while the cumulative north displacement was 0.7 m, 2.9 m and 4.2 m. It was found that vegetation significantly slows down the movement of the dunes, with high displacements being observed in the non-vegetated dune fields 2 and 3, with an average displacement of 2.4 m and 2.6 m, respectively, over a study period of four months (4th of June to 14th of October 2017), compared to the average displacement of stable areas of 0.62 m. The vegetated dune field 1 had a small average displacement of 0.7 m, similar to the stable areas. The pixel offset results showed a positive correlation between the wind speed/direction and the dune movement. This impact of the wind cannot be separated from the impact of vegetation cover and topography; however, the impact of vegetation can be clearly observed when comparing the vegetated dune field 1 and the non-vegetated dune fields 2 and 3, while the impact of mountainous topography can be observed in dune field 2 and 3, diverting the direction of the movement, mainly near the edges of the mountains.

To achieve a better understanding of the movement of sand dunes, high temporal resolution imagery is required in order to detect the small movements that tend to happen on a daily basis. Additionally, the land cover characteristics of the dune field have a significant impact on the movement of the dunes; therefore, having high-resolution accurate DEMs will ensure a better understanding of the impact of topography and vegetation cover on the sand dune movement.

This study identified areas with large sand dune movements that can be considered for further investigations and field works. The SAR offset tracking technique can play an important role in detecting and modelling sand movement by enabling highly detailed monitoring of the sand dune fields. It can also support planning regional projects to combat desertification and sand movement.

5 CHAPTER 5: MONITORING COASTAL DUNES USING AIRBORNE LIDAR DTMS: FORMBY CASE STUDY

This chapter is based on two published articles that investigated monitoring sand dunes in coastal areas. The first article concerns a field survey of Formby coastal dunes where terrestrial laser scanner (TLS) and Global navigation satellite system (GNSS) instruments were used (Mahmoud, 2021). The second article investigated the activity of Formby sand dunes using multi-temporal Airborne LiDAR DTMs (Mahmoud et al. 2021).

This chapter addresses the third objective of the research, with a developed framework that uses multi-temporal Airborne LiDAR DTMs for monitoring the dynamic activity of sand dunes, determining how much sand volume has been lost or deposited in the Formby dune system as well as determining the rate of change in the elevation of the dunes. In addition, it demonstrates a practical investigation of the capabilities of land surveying techniques in sand dune monitoring.

5.1 Background

Different measuring techniques have been used to detect the dynamics of coastal dunes. This has involved the use of Airborne and terrestrial LiDAR techniques, in addition to GNSS techniques. Airborne LiDAR or laser scanning is an active remote sensing technique used to model the surface of the earth (Wehr and Lohr, 1999, Juha Hyyppä, 2009, Jaboyedoff et al. 2012, Gallay, 2013, Maltamo et al. 2014, Okyay et al. 2019). Airborne LiDAR system is based on a GNSS receiver and inertial measuring unit (IMU) for the determination of the point's position and a laser system which emits and receives the transmitted and backscattered light pluses for the point's reading (Wehr and Lohr, 1999). It maps the earth's surface and provides a very dense and accurate three dimension spatial data set generated over a short period of time (Woolard and Colby, 2002). Airborne LiDAR data have been used widely for monitoring coastal changes: sediment volumetric changes (Meridith et al. 1999), shorelines (Stockdonf et al. 2002, Caudle et al. 2019), coast morphology (Saye et al. 2005, Middleton et al. 2013, Grünthal et al. 2014, Julge et al. 2014, Le Mauff et al. 2018), and vegetation growth on coastal dunes (Frati et al. 2021). The more traditional land surveying techniques (GNSS and terrestrial laser scanner) can be time consuming when surveying large areas, given the rough terrains of the coastal dunes. This limits both the coverage and the frequency of such observations. Airborne LiDAR has the advantage of covering large areas in a very short time, whilst also maintaining good accuracy of the spatial representation of the dunes. Repeated survey acquisitions can be applied for change detection analysis and used to study the morpho-dynamics of the dunes. However, this generates associated challenges in managing, analysing and interpreting large data sets from repeated surveys (Okyay et al. 2019).

Coastal sand dunes can be found in most climatic environments (Pye and Tsoar, 2008). In England and Wales, coastal sand dunes cover an area of about 200 km^2 over 112 different sites (Pye et al. 2007). The largest in England is at Formby, along the Sefton coast (Esteves et al. 2012). Many studies have been undertaken to understand the coastal changes at Formby, investigating the impact of changes in sea water and tidal levels (Gresswell, 1937, Pye and Blott, 2008, Pye and Blott, 2016) and storms (Pye and Neal, 1994, Pye and Blott, 2008, Dissanayake et al. 2015, Pye and Blott, 2016), and determining the morpho-dynamic and volumetric changes of the coast (Nordstrom et al. 1990, Pye and Neal, 1994, Woolard and Colby, 2002, Lymbery et al. 2007, Karunarathna et al. 2018). The dune system at Formby is predicted to have been established between 1400 AD and 1600 AD (Sefton Metropolitan Borough Council, 2016). Historical data suggests that Formby coast has experienced several accretions and erosion episodes over the years (Pye and Blott, 2016), where the coast has seen significant erosion around 1906 due to a decrease in the rate of sand supply (Gresswell, 1937) and also, between 1977 and 1994, due to the combined impact of the westerly winds and strong storms (Pye and Neal, 1994). In 1994, high tides and strong winds resulted in the erosion of seaward facing frontal dunes (Pye and Neal, 1994). Such weather conditions continue to erode the coastlines of Formby and shift the sand dunes inland at a rate of 4 meters every year, mostly observed over the last decade (Trust, Gresswell, 1937, Trust, 2015).

With rising global temperatures and sea levels expected to lead to stronger storms (Zhang et al. 2004a), coastal erosion and flooding are expected to occur more frequently. Moreover, climate change forecasts predict that the next 50 to 100 years will see an increase in temperature and precipitation and a slight decrease in wind speed in Wales and northwest England, which could lead to the replacement of dune areas with fixed dune grassland and scrub, endangering the existence of rare species (Pye et al. 2014). Therefore, there is a strong need to understand the dynamic behaviour of the dunes on these coasts and how much sand volume is lost or gained to the dune system over time. In this case study, we investigate the activity of sand dunes at Formby coast by using a time series of high-resolution LiDAR digital terrain models over a period of 21 years. We establish how much sand volume has been lost or deposited in the dune system during this time period as well as determine the rate of change in elevation of sand dunes at Formby.

5.2 Study Area

The Formby site is owned by the National Trust and it is part of the Sefton coast that covers an area of approximately 20 km^2 (Pye et al. 2007). It consists of an evolving sandy beach and an inland dune field with frontal, semi-fixed and fixed dunes.

In this research, an area of about 1.3 km^2 has been investigated with a coastline that stretches for about 5 km. The Formby site contains one of the largest and most rapidly evolving sand dune systems in England (Trust, 2015). The height of the inland dunes ranges from 6m to 28m above mean sea level, while the height of the beach ranges from 2.7m to 6m. This information is derived from the elevation data of the latest available LiDAR DTM acquired in 2020. The study area has been divided into 5 zones A, B, C, D and E, which have an area of 0.16 km^2, 0.22 km^2, 0.11 km^2, 0.48 km^2 and 0.33 km^2 respectively. This division was based on location along the coast, geomorphological characteristics and presence/absence of vegetation (Figure 5.1). Zone B, D and E have a significant presence of vegetation. Zone A consists of a narrow dune system while zone C has a deep dune system extending up and over Victoria Road.

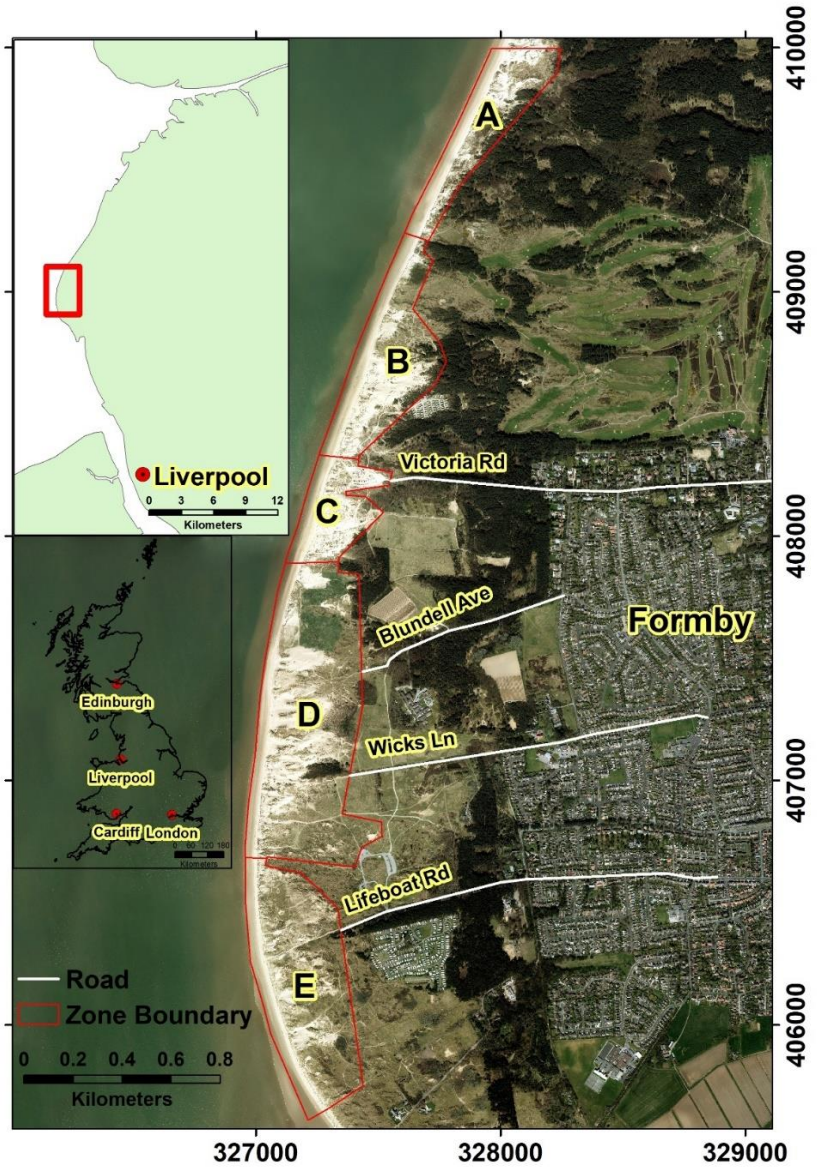

Figure 5.1. The Formby coast study area, showing the five zone divisions A, B, C, D and E. (Background image and GB Boundary layer © EDINA Digimap Ordnance Survey Service, projected to the OSGB 1936 British National grid coordinate system).

5.3 TLS and GNSS Fieldwork Observations

For the investigation of the capabilities of land surveying techniques in monitoring sand dunes, fieldwork took place on the 10th and 11th of December 2020 and involved three persons to cover an area of 240m x 460m of zone C in the study area (Figure 5.1). The instruments used in this survey were a Lecia Viva GS 10 GNSS unit, used for the collection of GNSS observations on the dunes, in addition to a Leica RTC360 terrestrial laser scanner. This TLS has a measuring rate of up to 2 million points per second and an advanced High Dynamic Range (HDR) imaging system for coloured 3D point clouds. The highest resolution on the TLS (i.e. a resolution of 3 mm every 10m) was applied with a double pass option, to exclude any moving objects (e.g. passing people) from the scans.

Optimum locations to set up the GNSS base station and the TLS targets were determined in the field. Eight targets for the laser scanner were set-up on the top surface of the dunes in locations that are visible to the TLS, with A1, A2, A3, A4, B1, B2, B3, and B4 as the TLS targets locations on the first and second day of acquisition, respectively. Table 5.1 illustrates the coordinates of TLS targets locations, projected to the OSGB 1936 British National grid coordinate system.

Table 5.1. TLS targets location coordinates.

Day 1				Day 2			
TLS Id	Easting (m)	Northing (m)	Ortho. Height (m)	TLS Id	Easting (m)	Northing (m)	Ortho. Height (m)
A1	327368.43	408141.83	19.60	B1	327289.29	408152.00	10.05
A2	327353.63	408138.21	21.87	B2	327288.86	408158.71	9.88
A3	327343.99	408141.49	20.88	B3	327287.63	408167.29	9.87
A4	327340.85	408150.86	19.63	B4	327288.43	408174.62	9.89

These target locations were used in the post processing step to register the TLS scans and link them together in the Cyclone software. The GNSS and TLS surveys were carried out simultaneously. A GNSS base station was set up in a clear location on top of the dunes. This base station is needed to receive the corrections for the GNSS real-time kinematic (RTK)-rover observations. The GNSS was configured to the double difference static observation technique to collect the base station data, which collected location data every second for about 5 hours (the survey time period on each day). After a couple of TLS scans, the GNSS was fixed over the TLS targets to observe its location using the RTK-static method with 5 minutes of observations spent on each location to ensure better accuracy of positioning. Figure 5.2 illustrates the location of the GNSS base stations and the TLS targets set-ups in the study area.

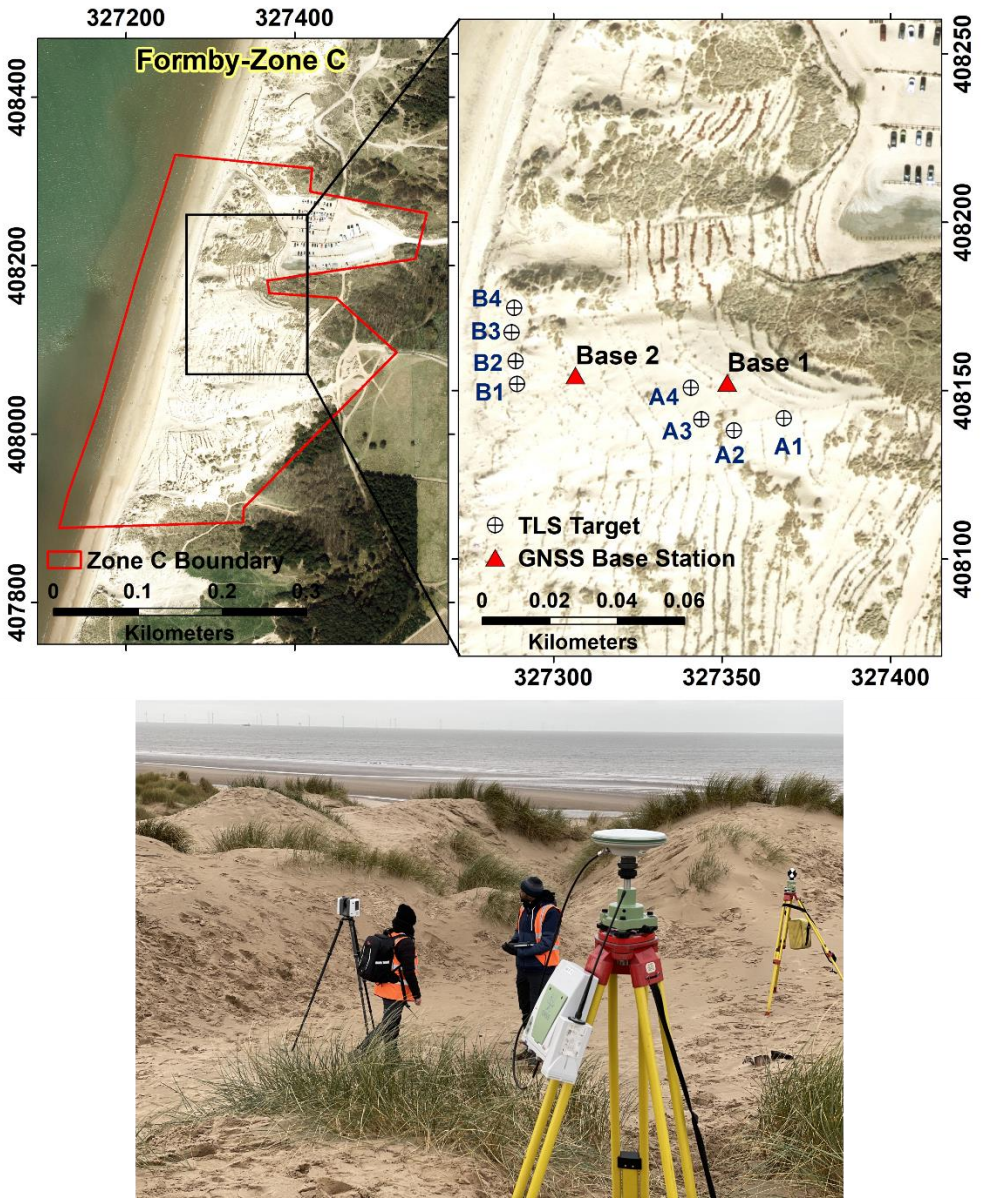

Figure 5.2. GNSS base station and TLS targets set up in the study area.

The scanning work continued to cover other areas. Since the terrain of the surveyed sand dunes is quite bumpy, it was decided to perform the following TLS scans relying only on the targetless field registration method imbedded in the TLS, based on the Visual Inertial System (VIS) technology. This can quickly link the continuous scans together without the need for targets, based on five cameras built into the TLS to track the movement of the scanner in relation to prior scans. In addition, extra objects were used to help in the alignment of the scans, such as the GNSS storing boxes, fences and signposts (Figure 5.3). As the TLS targets are in the north part of zone C, the scanner set-ups on the beach and middle/south sides of zone C did not use them, due to being not in the visible range of the scanner. About 30 TLS scans were carried out each day.

(a)

(b)

(c)

Figure 5.3. Extra objects used for the alignment of the TLS scans, (a) GNSS boxes used to link TLS scans in the middle of zone C (b) a signpost and GNSS box used on the beach (c) fences used in the south part of zone C.

Simultaneously, the GNSS RTK-rover was used to survey the dunes and the parallel area of the beach. The GNSS was set up to the RTK-Rover mode with a 5-second observation time and 1 observation per second with a threshold of 5mm. 177 points were collected on the first day and 354 points on the second day. The GNSS observation points were collected on the dunes in the best way to reflect the rough terrain of the dunes, while on the beach the points were collected every 15m with an interval of 20m between the observation lines. Figure 5.4 shows the collection of RTK data on the frontal dunes in the north part of the study area.

Figure 5.4. Collection of RTK GNSS data on the frontal dunes of the north part of the study area at Formby.

The same observation strategy was followed on the second day, however, this time the work started from the beach shoreline parallel to the dune area. Scanning the dunes down from the beach gave a different angle of the dunes, which provides the height of the dunes, (i.e. up to 20m) but most importantly shows the area that is most vulnerable to coastal erosion (Figure 5.5, a). It was observed that the sea water was very close to the dunes roughly about 40-50 metres away in the early morning (08:40 AM – low tide at the time of the visit), while it retreated back around mid-day (high tide) creating a shore coast that stretches for about 250-300m (Figure 5.5, b).

(a)

(b)

Figure 5.5. Formby beach and the frontal dunes, (a) a side view of the frontal dunes, (b) sea water receding from the frontal dunes up for about 250-300 m.

The Leica infinity software was used for post processing of the GNSS data. The base station positions' raw data for days one and two were referenced to the six nearest highly accurate network ordnance survey (OS) base stations near Formby at Blackpool (BLAP), Giggleswick (GIGG), Manchester (MANR), Daresbury (DARE), St Asaph (ASAP) and Crewe (CREW), (Figure 5.6). Table 5.2 illustrates the location coordinates of the OS and GNSS receiver base stations.

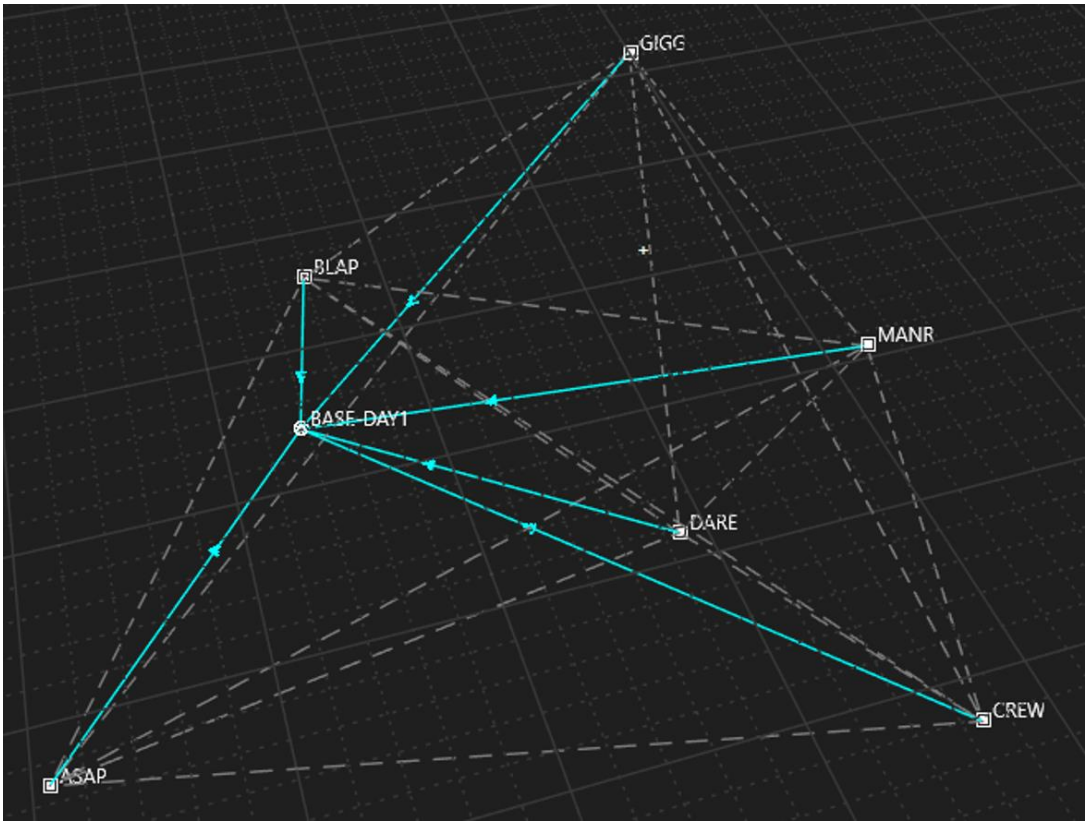

Figure 5.6. Formby base station post processed to the nearest Ordnance Survey base stations.

Table 5.2. OS base stations and GNSS receiver coordinates.

Station Id	Easting (m)	Northing (m)	Ortho. Height (m)
GNSS-base-day1	327351.53	408152.33	21.07
GNSS-base-day2	327306.56	408154.49	18.47
ASAP	301344.51	373724.04	49.65
BLAP	331891.99	431672.40	13.72
CREW	373692.42	355503.07	68.72
DARE	357455.83	383290.43	36.78
GIGG	379890.35	464481.97	232.47
MANR	384509.69	401675.93	79.11

The RINEX files that contain the precise coordinates and data of these OS base stations were downloaded, https://www.ordnancesurvey.co.uk/gps/os-net-rinex-data/, and imported into the Leica infinity software to correct the base station (Base1, Base2) at Formby. Once the base station location was corrected; the RTK-rover observations were simultaneously corrected based on that.

The accuracy of the base stations is down to 1 cm while the accuracy of the RTK-rover observations ranges between 1-2 cm, due to the time spent on each observation (i.e. hours on the base station and a few seconds on the RTK-rover observations).

The point cloud processing software Cyclone was used to process the point cloud data collected by the TLS. Standard metrics of the Cyclone software were used, which involves a maximum error of 0.015m and a minimum overlap of 20% between the linked set-ups selected to restrict the results. Links between set-ups have been created to stitch the point cloud data together. Also, links between no consecutive set-ups were made in the north part where the TLS targets are visible. Many small bundles were created due to the significant challenge for the software to link all the scans together at once.

The TLS results show that the north part of zone C has higher quality and less bundle error within the determined threshold compared to the middle, south and beach areas of zone C. This is because the TLS targets are located in the north part of zone C and are visible to the scanner in the north side set-ups. Figure 5.7 shows a plan view of the study area point clouds after linking the TLS scans.

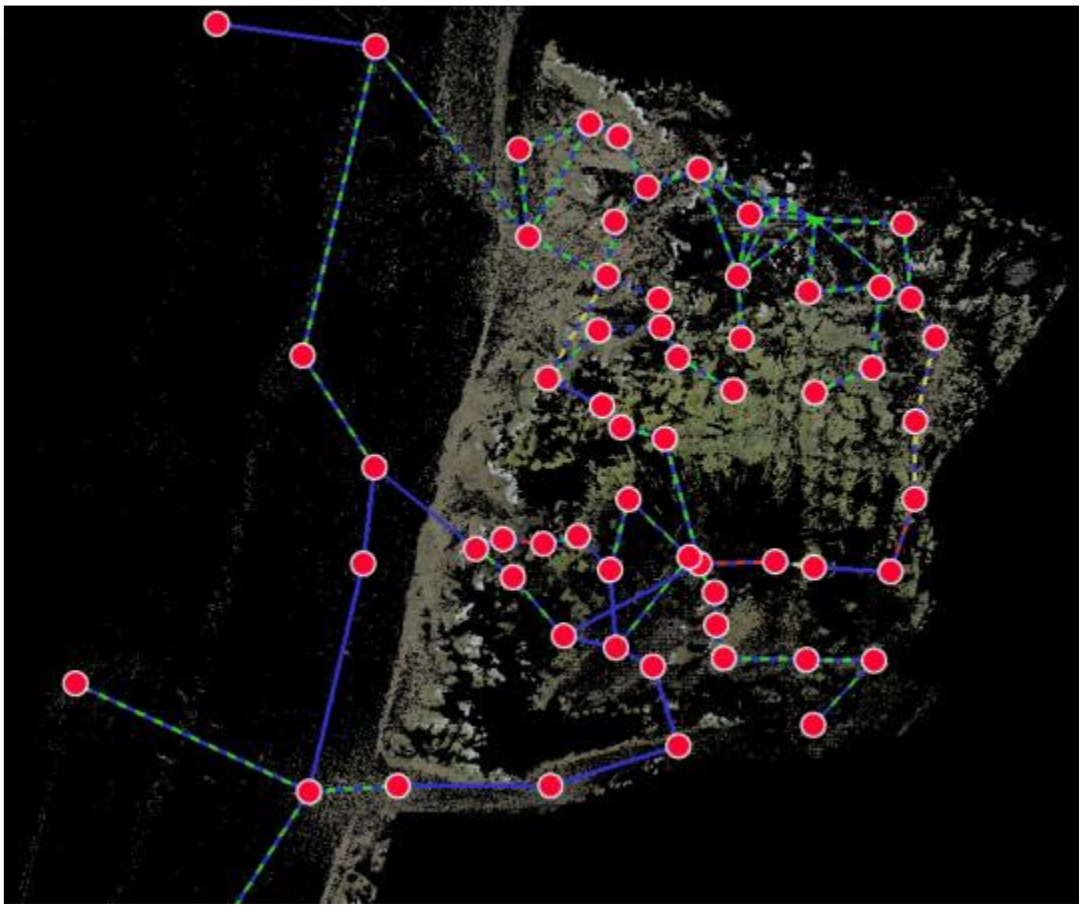

Figure 5.7. A plan view of the study area point clouds after linking the TLS scans.

The GNSS RTK observations collected in the two days amounted to 531 points. These GNSS data show that the dunes in zone C have elevations ranging between 6-20m. It can be seen that more GNSS data were collected on the beach outside of the zone C boundary, as the beach stretched when the sea water receded during the afternoon. Figure 5.8 shows the GNSS RTK collected data and an interpolated elevation model using the inverse distance weighted (IDW) interpolation method.

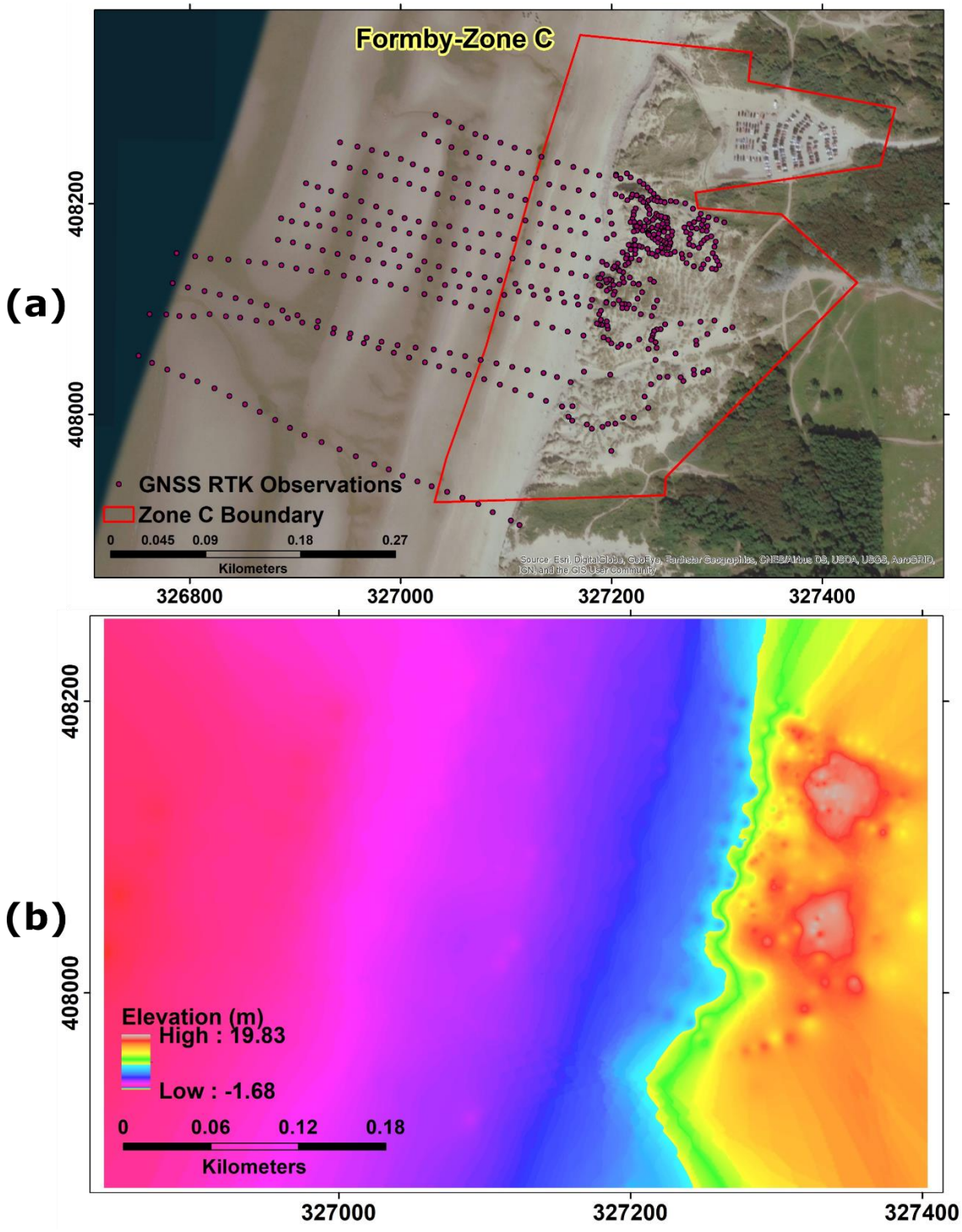

Figure 5.8. GNSS RTK observations, (a) distribution of the collected GNSS RTK observations, and (b) interpolation of the GNSS RTK data.

This field study demonstrated that there are many challenges when observing sand dunes using GNSS and TLS. For instance, the homogenous terrain of the dunes has restricted the VIS technology for connecting the different set-ups together. In areas where there are distinct features the VIS can be relied on significantly, however, in such cases as sand dunes where there are many similarities between features this technology is less capable. The result of that is seen in the blue link lines in the post processing stage, (Figure 5.7), where the software could not recognize the connection between the overlapped set-ups and had to force the clouds to make a match to link the scans. This has been the case especially in the middle and south part of zone C where the TLS targets are not visible to the scanner, in addition to these areas being significantly vegetated. The setups on the beach area also faced a similar challenge, with the TLS targets not being in the visible range of the scanner.

Moreover, the limitation in the survey time has restricted the optimum way of conducting this study and that should ideally have included more targets visible to each new TLS set-up; this is needed to achieve better accuracy of the registration of the TLS. This process is time consuming and can be difficult with the rough terrain of the dunes. In addition, the location of the targets would require more time to be observed using the GNSS to determine their exact location.

Different techniques that are more dynamic and can cope with the dune motion are recommended to be used to overcome the challenges faced by the TLS and GNSS. This includes the use of handheld terrestrial laser scanners, drones and other remote sensing techniques. However, this would also come with its challenges, and it would affect the high accuracy that can be achieved from the two terrestrial techniques.

5.4 Airborne LiDAR DTM Analysis

5.4.1 Data

A way to overcome the limitations of land surveying techniques in sand dunes monitoring is to use the airborne LiDAR technique. In this study, the airborne LiDAR digital terrain models (DTMs) acquired by the Environmental Agency and available at https://environment.data.gov.uk/, were used with a vertical accuracy of better than +/- 15cm (Agnecy) and horizontal accuracy of +/- 40cm (Agency). The accuracy of the LiDAR data was validated by ground truth points with a vertical accuracy of +/- 0.03m. The LiDAR surveys were undertaken in the winter months (Agency). All the available LiDAR DTMs that covered the study area between 1999 and 2020 have been used. The used data are projected to the OSGB 1936 British National grid coordinate system. Table 5.3 illustrates the LiDAR DTMs and their coverage of the study area.

Table 5.3. Formby LiDAR DTMs.

Date of Acquisition	Spatial Resolution	Vertical Accuracy	Coverage
1999	2m	0.15m	Whole study area
2000	2m	0.15m	Only Zone A, B and C
2001	2m	0.15m	Only Zone A and, partially, Zone B
2002	2m	0.15m	Only Zone A, B and part of Zone C
2008	25cm	0.15m	Whole study area
2010	1m	0.15m	Whole study area
2013	1m	0.15m	Whole study area
2014	2m	0.15m	Whole study area
2016	1m	0.10m	Whole study area
2017	1m	0.10m	Whole study area
2018	1m	0.10m	Whole study area
2020	1m	0.15m	Whole study area

5.4.2 Methodology

Conservation and monitoring projects are carried out by the local authorities at Formby. This involves the use of observation technologies, historical maps and aerial imagery to improve the analysis and predictions of the coastal changes (Lymbery et al. 2007). On the ground, the establishment of brushwood fences and beach grass planting to the North of Lifeboat Road, and wooden fences north of Victoria Road and Freshfield are applied to nurture the dune accumulation process (Nordstrom et al. 1990). In the UK, the removal of vegetation bushes on dunes is suggested in order to make the dune more hospitable for biodiverse natural habitats (Pye et al. 2007). All these measures have an impact on the dynamics of the dunes, and there is a strong need to take into consideration comprehensive assessments.

The study area was segmented into beach and dunes by manually digitizing the inflection points in the boundary between the beach and the dunes. This allows a much more detailed comparison of the dynamics of the coastal dunes at Formby to be drawn.

A framework has been developed for monitoring the dune changes from time series DTMs at all scales: it is based on dune point elevation changes, cross sectional profiles, longitudinal profiles, as well as deposition/erosion and volumetric changes for dune field elevations. It aims to investigate the activity of sand dunes at Formby coast based on raster and vector analysis. To understand the actual changes in Formby dunes the actual elevation values of the DTMs were used. R and GIS software (QGIS and ArcGIS) were used to analyse the LiDAR data.

The framework shown in Figure 5.9 consists of two main steps: (1) raster analysis which includes DTM difference analysis, rate of change and regression analysis, deposition and erosion analysis; and (2) volumetric analysis, an automated process for vector analysis which involves carrying out elevation profile and time series analysis.

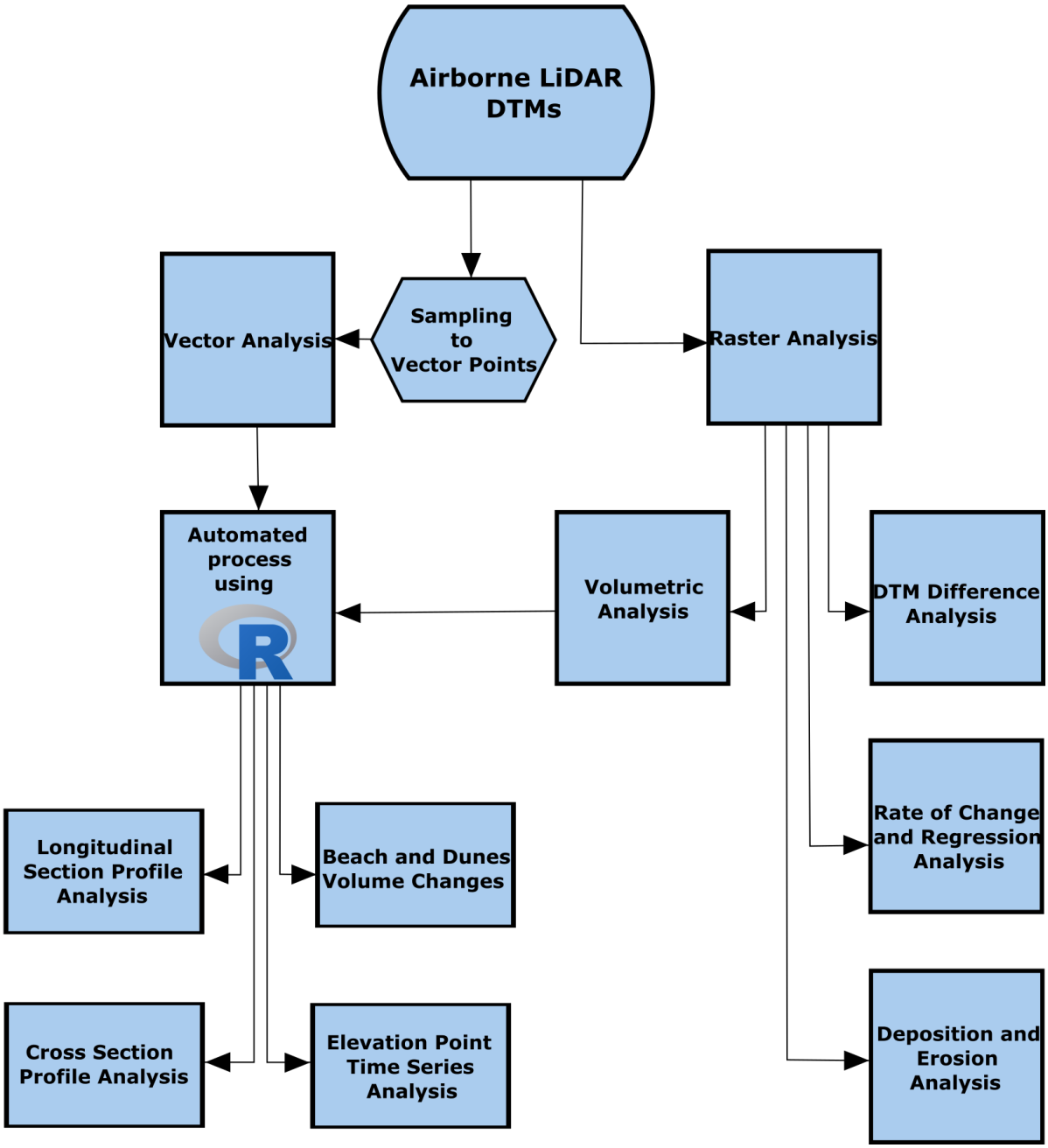

Figure 5.9. A framework for LiDAR DTM Analysis.

A preliminary step for the raster analysis consists of cropping the DTMs to the study area using the 'extract by mask' tool in ArcGIS and then calculating the DTM of difference (DoD) between a primary DTM (i.e. 1999) and a secondary DTM (i.e. one from 2008-2020) using the raster calculator tool. DTMs of 2000, 2001 and 2002 are excluded from all the raster analysis steps due to the variation in the area they cover. The DTMs were also resampled to 2 m spatial resolution using the bilinear interpolation method, to ensure that the raster analysis was executed consistently. The bilinear method calculates the new pixel value by computing a weighted distance average of the four nearest input pixel centres (Samadi et al. 2014).

A linear regression analysis was conducted to determine the rate of change in the elevation of the dune points at Formby and to assess the dynamics of the dunes in each zone in the study area. The rate of change and regression analysis was computed using the 'curve fit' tool, which is an ArcMap extension developed by Upper Midwest Environmental Sciences Center (UMESC), to perform a linear regression analysis on the resampled LiDAR DTMs. The curve fit tool is a computationally intense process, which works on the pixel level of the provided DTMs to produce a velocity map showing the rate of change in elevation for each pixel within the study area. This provides a statistical reference for the dynamic dune elevation changes at Formby, determining the deposition and erosion rate of change of the beach and dunes.

To compute the volumes of the study area each year, the 'raster surface volume' tool was used in QGIS. The volume is calculated above the mean sea level. The result of this step is presented as bar charts drawn in R to show the beach and dune volume changes over the years. This was followed by another volumetric analysis using the spatial analysis 'cut and fill' tool in ArcGIS to calculate the volume erosion and deposition changes. The tool calculates the volume changes between corresponding areas in the prior DTM (i.e. 1999) and the post DTM inputs (i.e. 2008-2020). The result is a raster with its values showing the areas of erosion and deposition in the study area.

For the vector analysis, 237 east-west profiles were used with a north-south interval of 20m between every cross section and a sample point every 1m along each cross section. These cross sections stretch over the beach and inland areas in a perpendicular direction to the shoreline. They provide information about the orientation and slope changes of the dunes. An initial step of the vector analysis requires converting the raster DTMs into points in ArcGIS using the 'extract multi values to points' tool. This tool assigns all the corresponding values from all the DTM inputs to the cross-section vector points' shapefiles. This process resulted in 67,400 points on all cross sections. The average length of the cross-sections is 185m, 243m, 257m, 398m and 332 in zones A, B, C, D and E respectively.

The longitudinal sections provide another view that reflects the south to north movement of the dunes due to longshore sand drifts. Two longitudinal section profiles were presented to show the impact of the waves and winds in changing the beach, and the south-north movement of the dunes. It also illustrated the variation in elevation along the whole beach and dunes, which provided a way of comparing the dynamics of the dunes in each zone.

An elevation point time series analysis is drawn from the cross section vector data points. This analysis is separate from the regression results, which show the rate of elevation change in each pixel. The elevation point time series analysis is another way of displaying the changes in elevation for a single point of interest. Such a type of analysis is suitable for any time series application. It has been used here to illustrate the changes in elevation for individual points along the beach and dunes at Formby.

Finally, an automated process has been developed using R to perform the elevation profile and time series analysis. The code analysed 237 cross sections profiles, longitudinal section profiles and elevation points by generating line charts that illustrate the changes in elevation over the study period, providing a detailed interpretation of Formby dune dynamics.

5.4.3 Results

5.4.3.1 DTM of difference (DoD)

In this section, an analysis using the available DTMs at Formby was carried out to understand the horizontal and vertical changes in the dunes that occurred during the 21 years study period. The DTM of difference results shows the elevation changes in the study area varied between a maximum height decrease of 18m and a maximum increase of 15m (Figure 5.10). Progressively increasing erosion is observed in the frontal dunes of zones B, C, and D, in addition to the north part of zone A, with an average elevation difference raging from -11m to -6m (Figure 5.10). Areas to the east of these frontal dunes have seen significant deposition, while the frontal dunes of zone E have seen similar deposition with an average elevation difference ranging between 2m and 5m. Inland semi-fixed dunes with vegetation presence had minimal elevation differences ranging between -0.2m and 0.3m. The beach area of zone E has had a slight elevation increase with an elevation difference ranging between 0.05m and 0.5m. Figure 5.10 shows the DTM of difference maps computed between each year's DTM and the primary DTM from 1999.

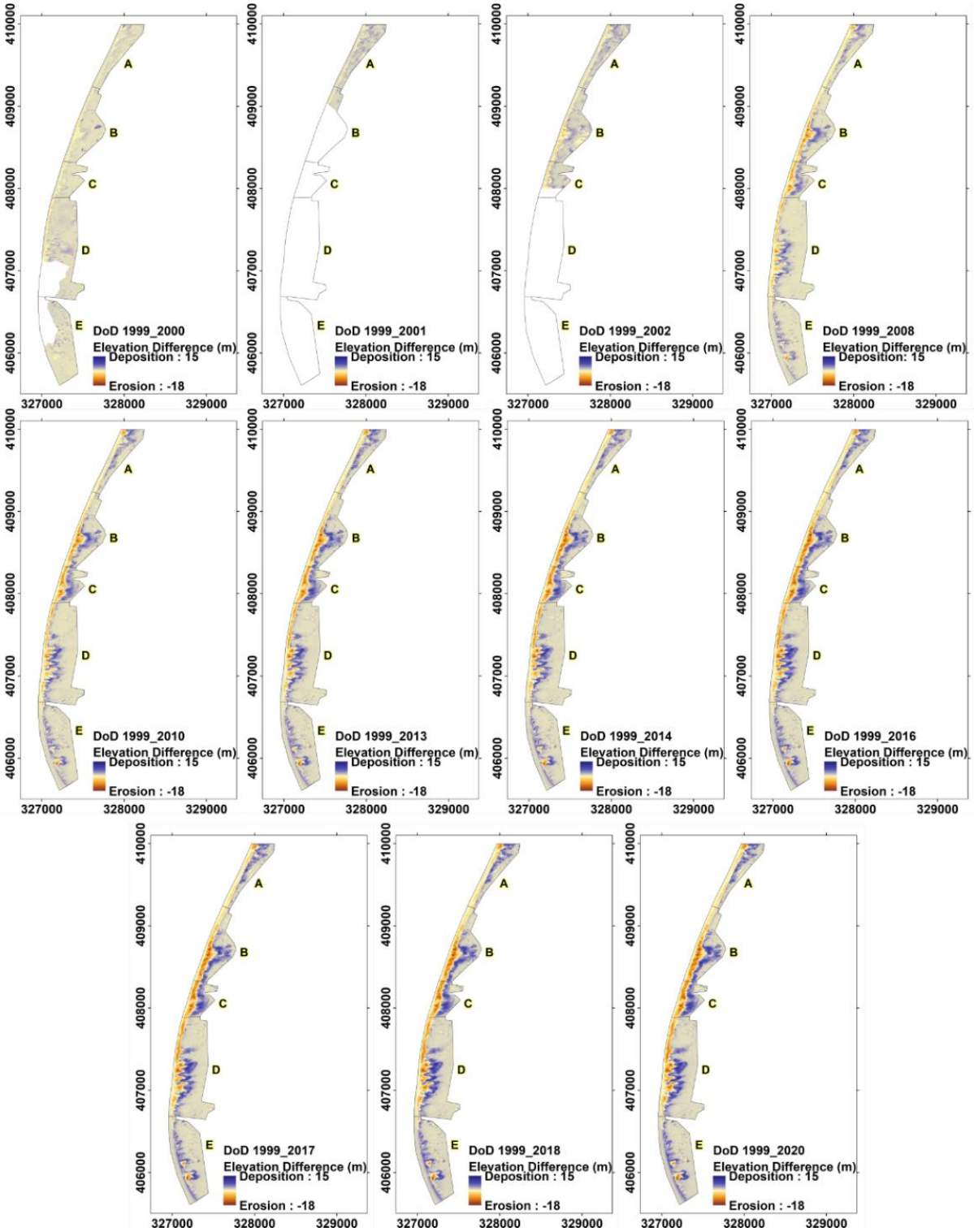

Figure 5.10. Formby elevation difference maps. It shows the vertical changes of the dunes that occur between each year's DTM and the primary DTM of 1999. DTMs of 2000, 2001 and 2002 do not cover the whole study area. Progressively increasing erosion is observed in the frontal dunes of zones B, C, and D, in addition to the north part of zone A. Areas to the east of these frontal dunes have seen significant deposition, while also the frontal dunes of zone E have seen similar deposition.

To see detailed year-by-year changes, the DTM difference analysis was carried out on a sequential basis. Figure S *6*-S 10 show the difference maps for each zone. The high erosion of the frontal dunes in zones A, B, C and D in 2014 was a result of the particularly strong storms that hit the Formby coast in the winter between December 2013 and February 2014 (Pye and Blott, 2016). In general, an elevation increase is observed in inland dune areas which are due to the eastward migration of beach sand. Areas with a strong presence of vegetation remain unchanged, due to the impact of vegetation on stabilizing sand dunes (Trust, 2015). The results from the linear regression analysis computed between 1999 and 2020 illustrate the rate of elevation changes ranging between -0.78 to 0.02 m/year and -0.92 to 0.73 m/year for the beach and the dunes respectively (Figure 5.11).

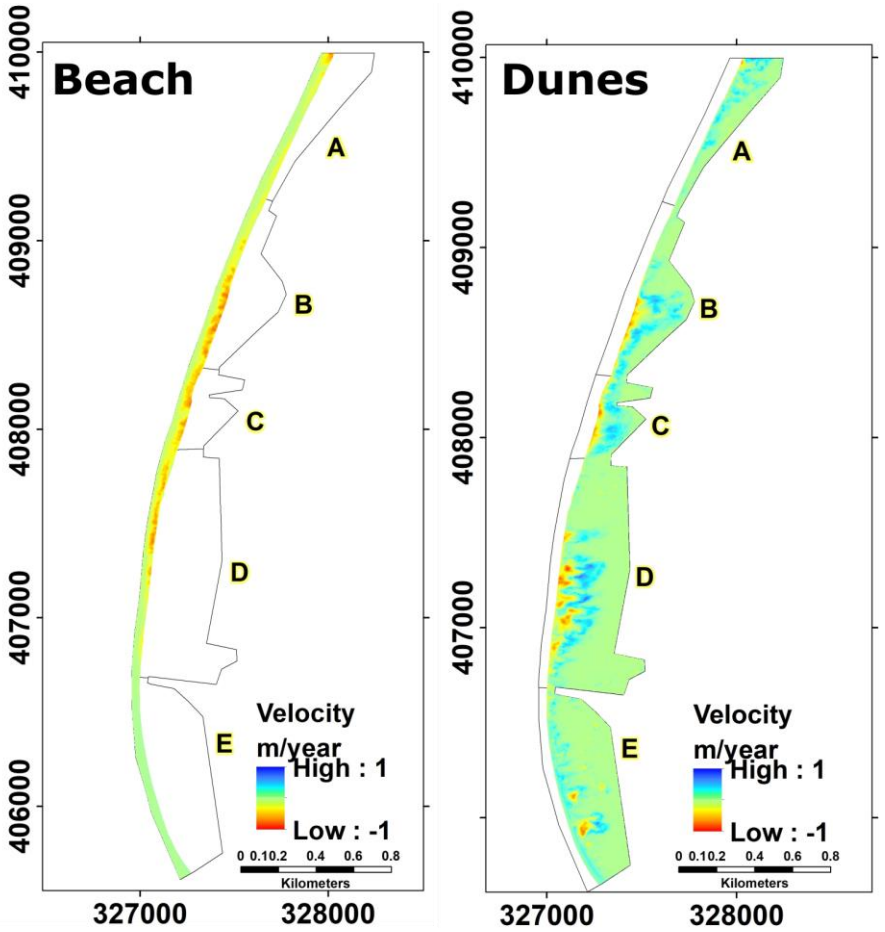

Figure 5.11. The rate of elevation changes in the beach and dune areas. Blue colours represent the rate of elevation increase while red represents rates of elevation decrease, i.e. loss of material. Loss of material on the beach is balanced by increase in inland dunes.

The rate of elevation changes shows a significant loss in most of the beach areas and some parts of the frontal dunes, especially in zone B, C, and D. It also illustrates sand deposition in the inner dunes, represented by high rates of elevation increase. The beach in zone E has a slight increase in elevation, ranging between 0.01m to 0.08 m/year in most of its parts. Areas with the presence of vegetation in all zones, but mostly more towards inland zones, generally remain unchanged.

5.4.3.2 Volumetric analysis

The raster surface volume tool in QGIS was used to calculate the volume above mean sea level. It is assumed that the subsurface of all of the study area at Formby is sand that has developed over the years into dunes in some parts. Figure 5.12 illustrates the volume changes in the beach and dunes of Formby over the 21 years of measurement.

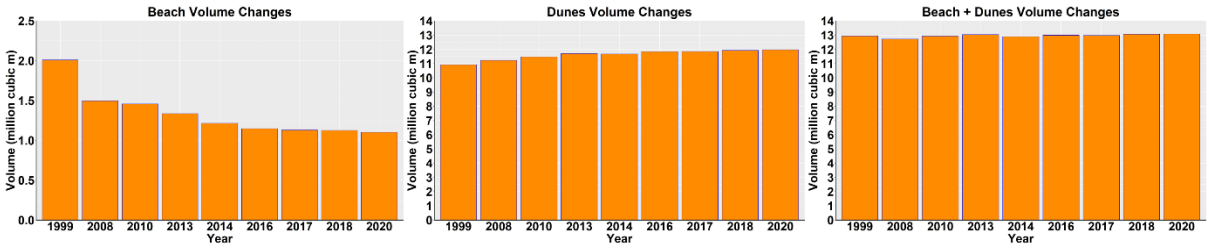

Figure 5.12. Volume changes in the beach and dune areas, with a sand volume loss on the beach and an increase in the volume of the dunes. It also shows that the volume of the entire dune system of Formby has remained unchanged.

Overall, Formby beach has had a significant volume loss of about 907,000 m^3 in 21 years; about 500,000 m^3 were lost between 1999 and 2008, in addition to more than 160,000 m^3 lost between 2008 and 2013, and 120,000 m^3 were lost between 2013 and 2014. Since then, the beach has gradually continued losing sand with about 110,000 m^3 lost between 2014 and 2020.

During the same period, Formby dunes saw a volume increase of about 1,049,000 m^3 over the 21 years. About 306,000 m^3 were deposited in the dunes between 1999 and 2008, and about 475,000 m^3 were deposited between 2008 and 2013. A sand volume loss of about 32,000 m^3 occurred between 2013 and 2014, and this is due to the stormy winter of 2013-2014, after which the dunes continued to grow again gradually gaining sand with about 300,000 m^3 gained between 2014 and 2020.

The total volume of the entire dune system of Formby (beach + dunes) has seen a very slight increase of about 130,000 m^3 over the 21 years.

5.4.3.3 Deposition and erosion analysis

The deposition and erosion analysis provides a detailed map view of the spatial distribution of volume changes that occurred in the beach and dune areas over the study period. The results (Figure 5.13) show that the beach areas in zone E had an increase in sand volume due to sand deposition. This started occurring from 2010 onwards, while the rest of the beach areas were losing sand. The erosion of the beach shows that any volume of sand lost from the beach is generally not being recovered, which means site managers must undertake careful conservation work.

Generally, we can see that the dune areas in all zones have had sand deposition (Figure 5.14). The vegetated dune areas also had sand deposition, even though this deposition is considerably lower. It also gives an indication that sand is moving inland. This emphasizes the outcome from the volumetric analysis (Figure 5.12), with the beach losing sand while the dunes are gaining. Areas classified as "unchanged" were not observed in either the beach or the dune's deposition/erosion maps. This indicates that Formby site dune system is constantly evolving.

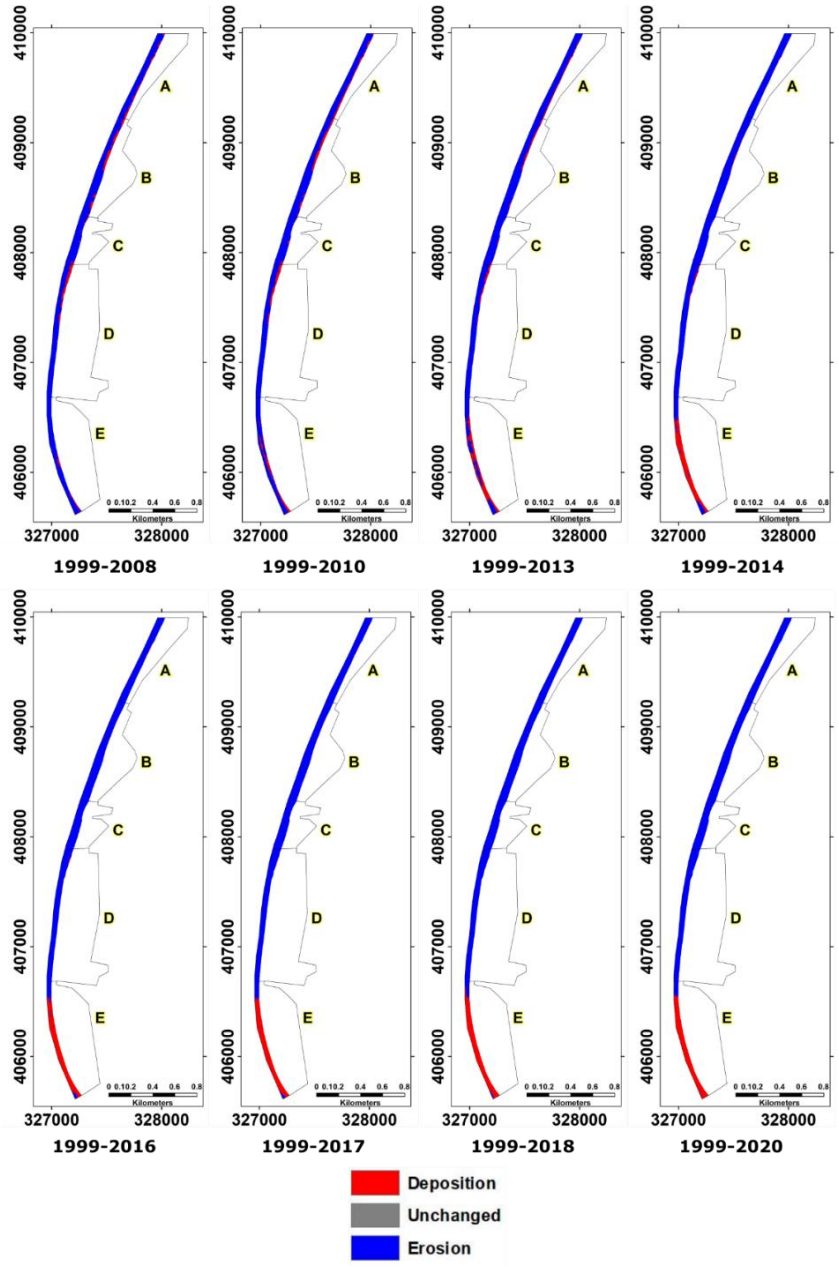

Figure 5.13. Deposition and erosion maps for the beach. It shows the volumetric changes and areas of deposition and erosion in the beach of Formby. Zone E has had an increase in sand volume due to sand deposition. This started occurring from 2010 onwards, while the rest of the beach areas were losing sand. The erosion of the beach shows that any volume of sand lost from the beach is generally not being recovered with an increased flux of sand into the coastal system.

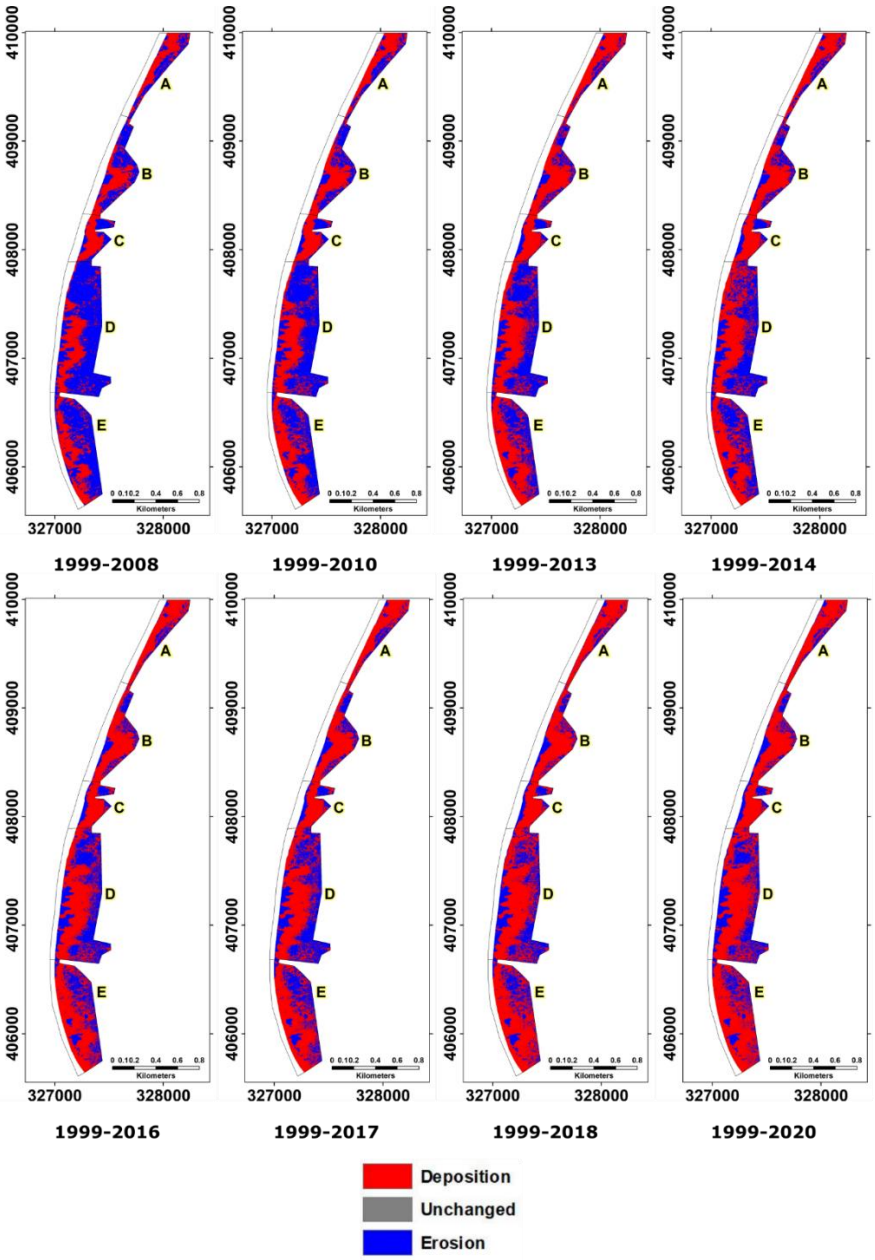

Figure 5.14. Dunes Deposition and Erosion Maps. It shows the volumetric changes and areas of deposition and erosion in the dunes of Formby. The dune areas in all zones are seeing sand deposition yearly.

5.4.3.4 Elevation profile analysis

The beach longitudinal profile is located at a distance of 25m inland from the shoreline, while the longitudinal profile over the dunes is located 100m from the shoreline. Both profiles contain an elevation point measurement every 20m along the profile. The beach longitudinal profile shows that there has been a significant change in the beach elevation, with most of the change occurring between 1999 and 2008, with subsidence of 11m, 6m, 8m and 9m, from zone A, zone B, zone C and zone D respectively (Figure 5.15). While it has seen a decrease of about 0.5m between 2008 and 2020. The elevation along zone E increased by about 0.5m in 21 years.

The longitudinal profile over the dunes shows significant changes in the elevation of the inner dunes (Figure 5.15). The irregularity of the dunes' longitudinal elevation profile illustrates the dune's topographical complexity. Generally, the dunes in zone A have increased by about 4m. Dunes in zones B, D and the more southerly parts of E tend to have higher elevations ranging from 18m to 25m. The dunes in the south part of zone C have the lowest height ranging from 8m to 10m and these dunes are seeing significant erosion and deposition in the north part with elevation differences of about 6m, while the dunes in the south part of zone C have had a slight increase in elevation of about 2m.

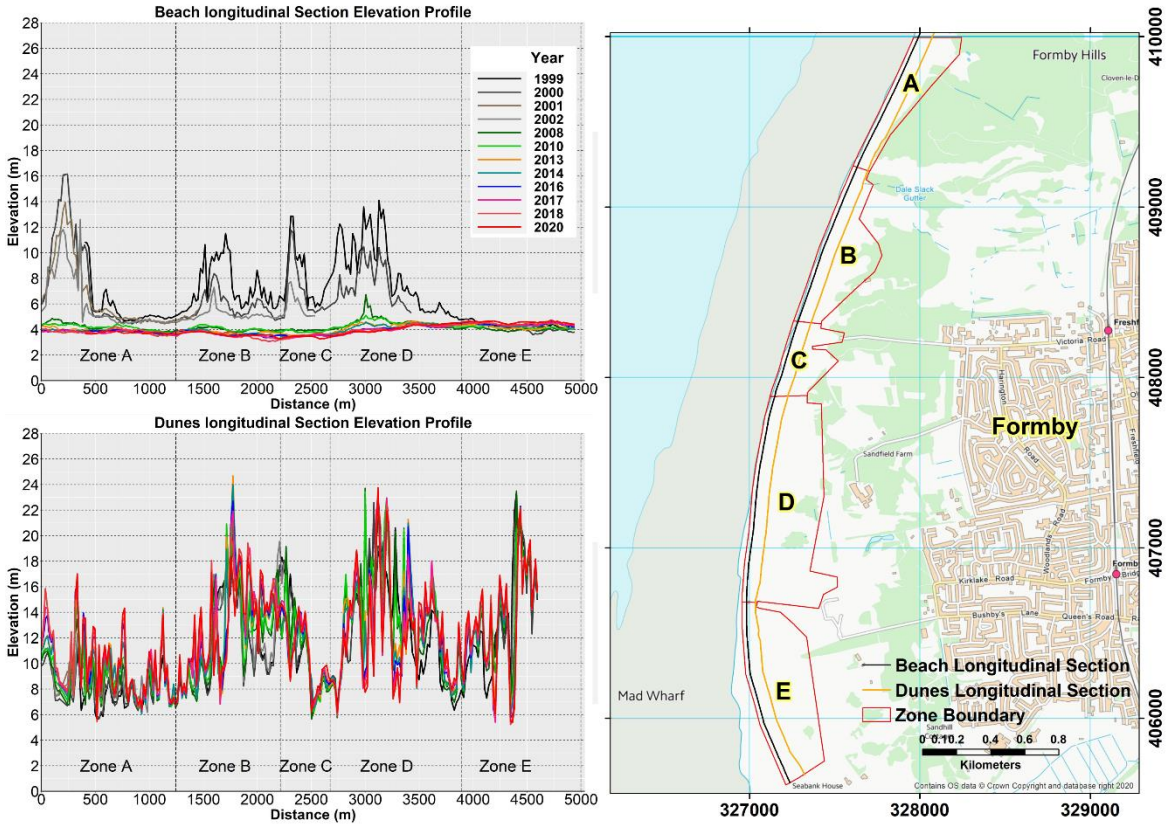

Figure 5.15. Beach and Dunes Longitudinal Elevation Profiles. The black line on the map figure shows the location of the beach longitudinal profile. The orange line shows the location of the profile over the dunes. Most of the elevation changes on the beach longitudinal profile occurred between 1999 and 2008. The irregularity of the dune's longitudinal elevation profile illustrates the dune's topographical complexity.

The cross-section profiles, which run perpendicular to the coastline, reveal information about the horizontal and vertical movement of the dunes. Figure 5.16 shows selected cross sections to reflect the elevation changes along cross sections CS23, CS95, CS120, CS159 and CS200 in zones A, B, C, D and E respectively.

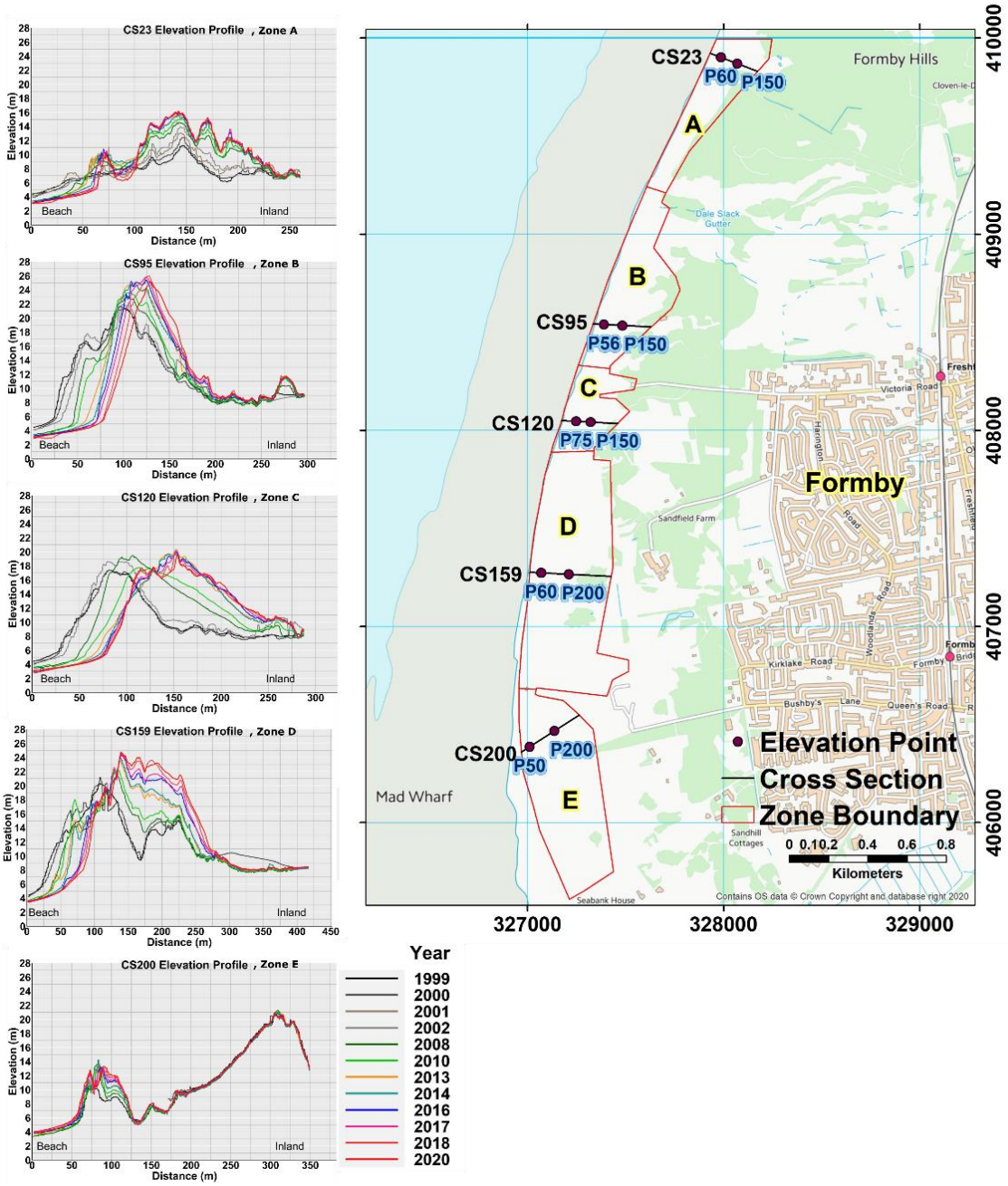

Figure 5.16. Selected Cross Section Profiles and elevation points from Zone A, B, C, D and E. The black lines on the map figure show the location of the cross section profiles. The coloured lines in each profile represent the DTM acquisition from different years.

The dune profile changes over time show the horizontal migration of the frontal dunes during the measurement period (1999-2020). In zones A, B, C and D the dunes migrated about 50m inland, while the frontal dunes in zone E migrated about 10m in the opposite direction towards the sea (Figure 5.16). We can also see from CS23 in (Figure 5.16) that the dunes had an elevation increase of 5m between 1999 and 2020 in zone A, while dunes in CS159 had an increase of about 12m in zone D. The elevation of the inner dunes in Zone E remained unchanged while the frontal dunes had an increase of about 5m. This is particularly the case in all the vegetated parts of CS23, CS95, CS159, and CS200.

Selected points are presented here (Figure 5.17 - P60,P150/CS23, P56,P150/CS95, P75,P150/CS120, P60,P200/CS159 and P50,P200/CS200 that represent the elevation changes of points on the beach and the dunes from cross sections CS23, CS95, CS120, CS159 and CS200 in zone A, B, C, D and E, respectively. The elevation time series of these selected points reflect the elevation changes for individual points on the beach and the dunes at Formby over the study period.

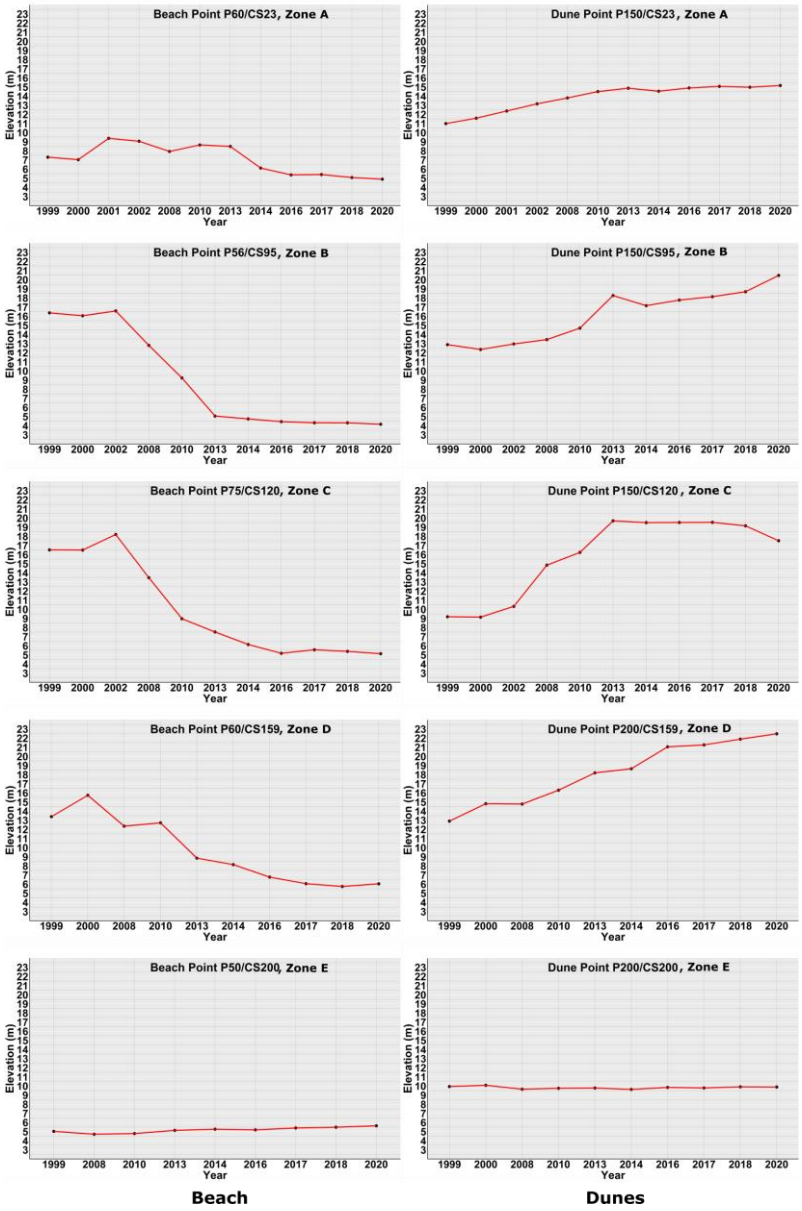

Figure 5.17. Selected elevation points profiles from zone A, B, C, D and E on the beach and the dunes. It shows the elevation time series changes of individual points over the study period.

We can see that there is a significant elevation decrease in the points on the beach, while there is an increase in the elevation of the points on the inland dunes; this applies to zone A, B, C, and D. In zone E, the elevation of points on both the beach and the dunes are slightly increasing.

5.4.4 Discussion

The analysis carried out in this study from the DTM of differences, the volumetric and elevation profile analysis provides a view of the dynamics of the dunes at Formby. It can be interpreted from the cross-section profiles that the frontal dunes face significant horizontal movement compared to inner dunes, this is because frontal dunes are affected more directly by waves and winds (Wolf et al. 2011). Interpreting the horizontal movement of the inner dunes in a complex dune field is difficult, as all the inner dunes are one joined unit; nevertheless, the vertical elevation changes can be easily seen and interpreted. The horizontal decrease of the frontal dunes lines is inversely related to the height of the dunes (Pye and Tsoar, 2008).

From profile CS120 in zone C (Figure 5.16) it can be clearly seen that the frontal dunes have shifted eastwards by about 50m during the 21 years observation period. This is due to the impact of the westerly wind blowing from the sea (Gresswell, 1937), which has resulted in this eastward erosion and deposition; this is also seen in CS95 in zone B. This horizontal movement is associated with about 4m height increase of the dunes which suggests there is a link between the horizontal movement and the height of the dunes. This vertical increase in the elevations of the dunes could be due to the vegetation impact limiting the eastwards migration of the dunes and acting as a barrier that forces the dunes to grow vertically.

The longitudinal section profiles (Figure 5.15) demonstrate that the Formby beach in zones A, B, C and D generally lost a large volume of sand between 1999 and 2008, with minimum and maximum elevations ranging between 4m and 16m. This significant material loss alerted the authorities in Formby to take action, and they introduced some conservation measures, from planting trees to stabilize sand dunes to building fences to trap sand and control its movement (Sefton Metropolitan Borough Council, 2016). Also, paths were built to manage access to the dunes and to prevent any erosion that could be caused by visitors.

The volume loss in the beach area and the volume gain in the dunes (Figure 5.12) indicate that those two processes are linked; the loss of sand volume from the beach results in an increase in sand volume in the dunes. The volume of the whole dune system of Formby (beach + dunes) has had an increase of about 130,000 +/- 280,000 m^3 over the 21 years, which means the total volume of sand in the Formby dune system remained unchanged within the bounds of the uncertainty. Therefore, it is interpreted that all the volumetric changes were due to sand redistribution within the dune system, with erosion from the beach and outer dunes being balanced by deposition in the inner dune areas.

Determining the coastline is considered difficult due to the dynamics of sea water and tides. For example, at high tide the shoreline of Formby extends only for 40-50 metres from the frontal dunes, while at low tide the sea water recedes up to 250-300 meters from the frontal dunes. Figure 5.18 shows the effect of low tides on sea water motion at Formby coast. The impact of the predominant waves and blowing wind from the west and northwest at Formby coast (Wolf et al. 2011); has resulted in forming these eastwardly frontal dunes. We can see from the cross section profile analysis (Figure 5.16) the recession of the frontal dunes and the extension of the beach by about 50m in zone A, B, C and D.

Figure 5.18. The effect of low tides on sea water motion at Formby coast. Around midday during the visit, the sea water receded by up to 250-300 meters from the frontal dunes (view taken from the top of the frontal dunes on the Formby coast).

Previous studies showed that the shorelines have shrunk significantly in the last decade and erosion of seaward facing frontal dunes occurred due to the westerly winds and strong storms (Pye and Neal, 1994). It is found that the highest rate of frontal dune recession is in zone B and C as a result of the 2013-2014 Winter storms (Figure 5.16). This has also been reported by (Pye and Blott, 2016) with a net recession over the Winter period of about 12m, and with a maximum dune toe recession of 20m (Karunarathna et al. 2018). Erosion of the frontal dunes near Victoria Road was reported in the early 1900s.

This erosion has continued to the present day occurring in the areas surrounding the Lifeboat Road up to Fisherman's Path and the Freshfield/Ainsdale boundary (Sefton Metropolitan Borough Council, 2016). The same erosion is continuing in zone B, C and D (Figure 5.13). Figure S *11* illustrates further selected cross sections (CS15, CS40, CS55), (CS65, CS88, CS100), (CS110, CS117, CS125), (CS135, CS155, CS185), (CS195, CS215, CS235) from zone A, B, C, D, and E, respectively, that reflect the profiles changes of the beach and dunes between 1999 and 2020 in the north, middle and south sections of each zone. CS15 shows a significant dune toe recession in the frontal dunes of about 50m in the north section of zone A between 1999 and 2020. This is also seen in the north sections (CS65, CS110, CS135) and the middle sections from zone B, C, and D, and also from the south sections (CS100, CS125) from zone B and C. CS215 in the middle section of zone E shows a build-up of new dunes with a height increase of about 7m, while the old frontal dunes shift eastwards by about 50m. CS195 and CS235 on the north and south sections of zone E show 10m-20m seaward extension on its frontal dunes.

Although the longitudinal section profile does not represent the elevation changes in the whole study area, but only on the route selected, it reveals valuable information about the height differences in each zone and the changes that occurred over time. The beach longitudinal profile showed that there have been large changes in the beach elevation with a decrease of 12m, 8m, 9m and 10m between 1999 and 2008 in zones A, B, C, and D (Figure 5.15). The longitudinal profile over the dunes (Figure 5.15) showed that dunes in zones B, D and the more southerly parts of zone E tend to have higher elevations, and this pattern appears to be stable over time. This could be due to the presence of vegetation in these zones acting as a barrier, stabilizing the eastwards horizontal movement of the deposited sand and contributing to the vertical growth of the dunes.

Coastal sand dune erosion tends to occur during winter, with a loss in sand volume, while accretion occurs during the summer period which to some extent balances the sand loss during winter (Pye and Blott, 2016). This interpretation of the relationship between the beach and the dunes can be supported by analysing previous historic data (e.g. aerial imagery, field observation...etc.) to look for similar dune behaviour. Moreover, coastal sand dune monitoring campaigns must be undertaken at least twice a year, during the winter and summer periods, to fully understand the dynamic of the dunes over different weather conditions.

5.5 Conclusion

Coastal dunes are a primary natural flood defence in coastal risk management. The use of land surveying techniques is effective for monitoring small sand dune areas and provides high accuracy data, however, this field study demonstrated that there are many challenges when observing sand dunes using GNSS and TLS. The main limitation is that the data collection process is time consuming. Furthermore, the homogenous terrain of the dunes has restricted the VIS technology to link the different TLS set-ups.

The airborne LiDAR study analysed unique LiDAR DTM time series data collected over the Formby coast. The findings show that the Formby coast dune system is highly dynamic with the redistribution of sand within the system. It has been found that the rate of elevation change for the beach and dunes was between -0.79 to 0.08 m/year and -0.91to 0.73 m/year respectively during the 1999-2020 measurement period. The beach and the frontal dunes experienced erosion, but this was balanced by sand accumulation in the inner dunes. Areas with the presence of vegetation remained largely unchanged due to the impact of vegetation in stabilizing the movement of the dunes.

Formby beach has seen a significant volume loss of about 907,000 m^3 in 21 years' time, while the dunes have seen a volume increase of about 1,049,000 m^3 over a period of 21 years. The volume of the entire dune system of Formby (beach + dunes) remained broadly unchanged, which indicates that all the volumetric changes happened due to sand redistribution within the system, with erosion in the beach and frontal dunes compensated by deposition in the inner dune areas. The DTM time series revealed that the Formby beach, marked by the frontal edge of the dunes, migrated about 50m inland during the measurement period.

Further investigation into the dune activity at nearby coastal sites is recommended to fully understand the dynamic links between dune fields on the northwest coast of England. This provides important information for local site managers and planners to preserve the local environment, plan interventions and minimize the risks to local infrastructure.

6 GENERAL DISCUSSION- A REFLECTION ON THE USES OF REMOTE SENSING TECHNIQUES FOR SAND DUNE MONITORING

6.1 Background

In this chapter, InSAR and COSI-Corr, another couple of techniques for monitoring sand dunes were briefly discussed. This was followed by a discussion, reflecting on the capabilities of the remote sensing techniques that have been used in this research. In addition, a developed strategy for monitoring sand dunes has been introduced.

6.2 Sand Dunes Monitoring using DInSAR

Monitoring the displacement of sand dunes is a challenging task, especially when it comes to detecting the vertical movement of the dunes for a continuous period of time. Following on from the use of LiDAR and GNSS to detect such movement in Chapter 5, in this chapter the differential interferometric synthetic aperture radar technique has been investigated to detect the horizontal and vertical movement of the dunes by processing a pair of Sentinel-1 single look complex (SLC) SAR images acquired on the 4th and the 16th of June 2017. These images were captured by Sentinel-1B mission in a descending flight direction and an interferometric wide swath (IW) beam mode and a vertical-vertical (VV) and vertical-horizontal VH polarization. The InSAR processing was conducted using ESA SNAP toolbox to detect the displacement in dune areas near Goled city in Northern Sudan, see Figure 3.4, in chapter 3.

The initial step for InSAR processing in SNAP is to split the Sentinel-1 multi-swath product using Sentinel-1 TOPSAR split tool to select the subswath, bursts and polarization required for the study area. The sub-swath IW3 with 9 bursts and VV polarization was selected. Then, the precise orbit files were applied to provide accurate location of the satellite and velocity information. The precise orbit files are made available a few days or weeks after the generation of the image products (Ferretti et al. 2007). These precise orbit files refine the orbit state vectors provided in the initial metadata of the image product.

The split Sentinel-1 SLC were then co-registered using the precise orbits of the two images and a digital elevation model corresponding to the pixels on the two images of the same ground target. The co-registered stack was then used to generate the interferogram between the two images, to distinguish the interferometric phase surface deformation in the study area, in addition to providing the coherence amplitude image that reveals areas with high and low coherence, which indicates the characteristics of the land cover features.

The topographic phase was then estimated and subtracted from the interferogram, followed by a step of phase noise removal using Goldstein phase filtering to reduce the residues and assist and enhance the phase unwrapping accuracy. The phase unwrapping is a major step to recover the unambiguous phase data from a 2-D array of phase corresponding to the interferometric phase to the topographic height and remove phase ambiguity. The phase unwrapping was applied using a plugin in SNAP called SNAPHU, https://step.esa.int/main/snap-supported-plugins/snaphu/. Then the phase interferogram is used to compute the displacement map. This displacement is provided in the line of sight (LOS) of the satellite; therefore, it was converted into vertical displacement using the following equation:

Vertical displacement = (Wavelength * UPI) / (-4 * PI * cos(rad(incident angle))).

The wavelength of Sentinel-1 sensor is 0.056 metres, the incident angle was averaged to 47 for the whole sub-swath and UPI is the unwrapped phase interferogram in radians.

A geometric correction step has lastly been performed using range doppler terrain correction to reform the interferogram, coherence and displacement into ground coordinates. Figure 6.1 illustrates the processing steps for generating phase displacement maps using InSAR in SNAP.

Figure 6.1. DInSAR deformation processing using SNAP

Figure 6.2 show the DInSAR results between 4 and 16 June 2017, phase interferogram, the coherence map and the unwrapped phase image.

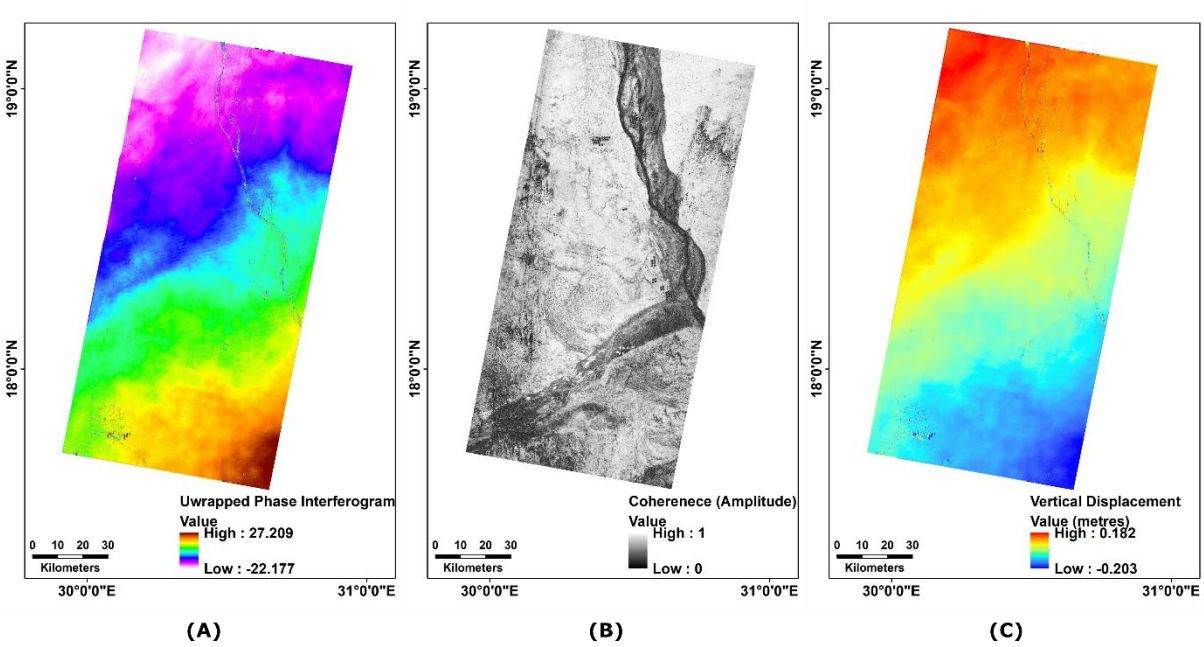

Figure 6.2. The study area DInSAR results between 4th and 16 June 2017. (A) Unwrapped phase interferogram, (B) Coherence map, (c) the vertical displacement.

The phase interferogram result indicates the level of deformation seen during the study period. It shows that areas with vegetation, water and sand dunes have seen significant changes due to the characteristics of these features in comparison to the urban and bare land areas. This also appears on the coherence map, where low coherence is seen in water surface, agricultural fields and sand dunes areas, where they appear as black patches suggesting significant changes. Urban areas and bare lands tend to appear as white patches as they remain stable. The computed phase displacement shows a vertical displacement ranging between 0.18 and -0.20 metres, which is considered to be significant given the short period of the measurement. This implies that InSAR can detect the changes in sand dunes over the period in question.

The coherence map revealed an interesting land feature, a valley in the south-west of the study area, known as Wadi Hower. Wadi Hower was the largest tributary of the river Nile that used to flow from Chad in the West to meet the River Nile near Old Dongola city in Northern Sudan. Decades ago, this Wadi was severely affected by desertification and was overwhelmed by sand to become extinct (Pachur and Kröpelin, 1987). Figure 6.3 shows a topographic map of Wadi Hower produced by (Pachur and Kröpelin, 1987) showing barchan sand dunes surrounding its banks.

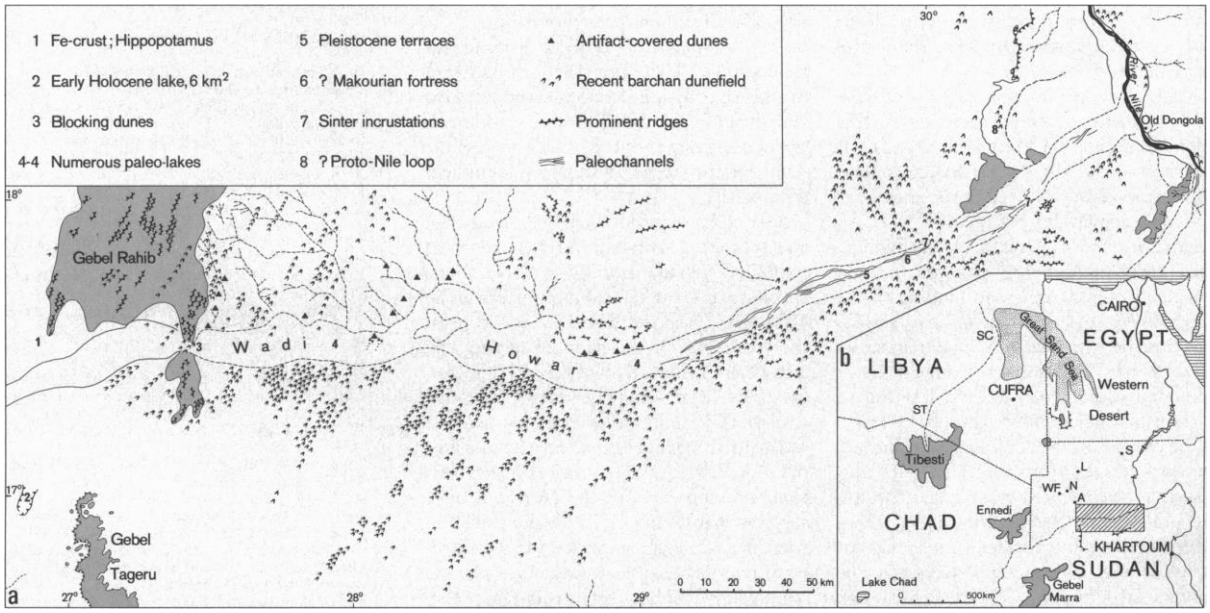

Figure 6.3. Topographic map of Wadi Hower in Northern Sudan.

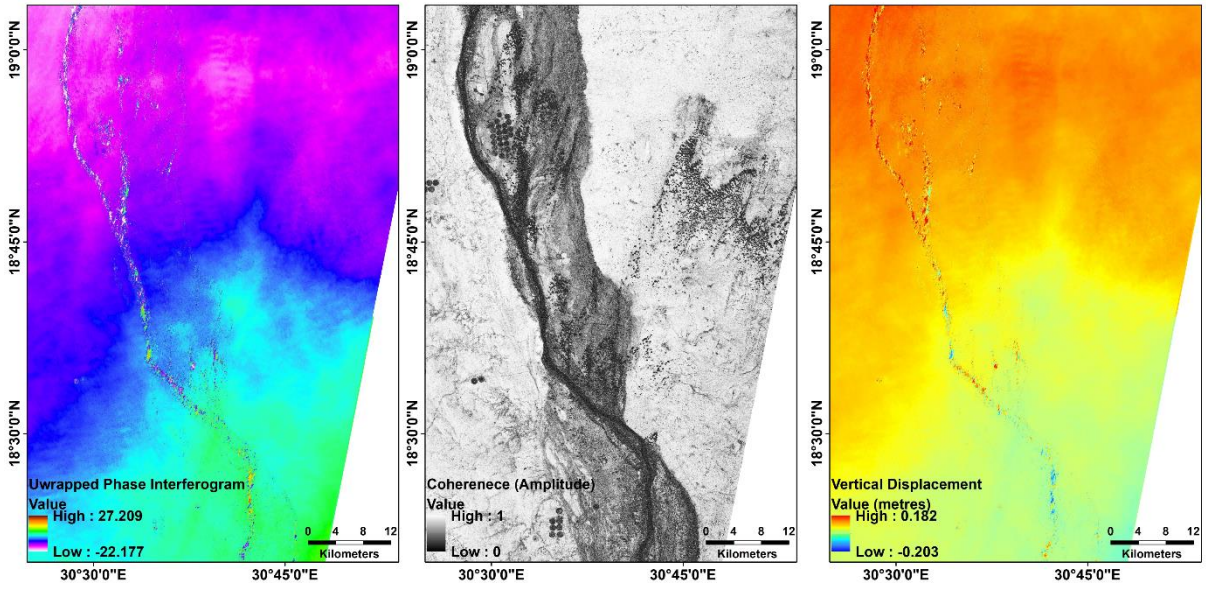

Figure 6.4. DInSAR results for Goled city.

From Figure 6.4, we can observe that, in dune fields with low vegetation presence, the vertical displacement was found to be less than in the dune fields with high vegetated presence; fields located mostly near the river banks. This is the opposite of what was detected using SAR pixel tracking where the horizontal movement of dune fields in the non-vegetated dune fields was found to be larger compared to the horizontal movement of vegetated dune fields, see section 4.4.3 in chapter 4. Accordingly, the presence of vegetation reduces the horizontal movement of the dunes, however, on the other hand it will contribute to the vertical growth of the dunes as vegetation works as a barrier that slows the speed of sand movement but consequently increases accumulation and thus the height of the dunes. Therefore, it can be concluded that there is a correlation between the horizontal and vertical movements of the dunes. This claim must be further investigated and validated using ground truth data to accurately measure the horizontal and vertical movement of the dunes in dune fields with different geomorphological characteristics.

Detecting the vertical displacement of the dunes using only a pair of SAR images has some limitations. This is mainly because of the decorrelation between the primary and secondary images due to phenological changes in vegetation or rapidly changing land features, such as water and dunes (Braun, 2021). Therefore, reducing the temporal baseline of the pair might increase the precision of the detected dune displacement. This movement could happen on a daily basis and that means if the time interval is quite large (e.g. a year or months) then the resultant interferograms will tend to be ambiguous. This requires more investigations, associated with ground data collection for validation.

Future InSAR research work should investigate the capabilities of different SAR sensors, different polarizations, space resolutions, orbit configurations and acquisition modes. Also, it should investigate the capabilities of different radar images (e.g. P, L, X bands) in distinguishing the activity of the dunes. In addition, automated time series InSAR processing tools should be developed.

6.3 Reflection on the Sand Monitoring Techniques used in this Research

The aim of this research focused on investigating the use of different remote sensing techniques for monitoring the movement of sand dunes. It also investigated the limitations of conventional measuring techniques such as sand traps and land surveying techniques.

This section summarizes the capabilities and limitations of each technique addressing several key points: (1) the acquired data; (2) the coverage and spatial distribution of the used technique, which provides a good indicator of the suitability and feasibility of the technique for detecting sand dune movement in large areas; (3) the sand monitoring results, illustrating the changes in sand dunes; (4) the achieved accuracy; and (5) the limitation and complexity of implementation of each technique for detecting sand dune movement.

Conventional techniques provide vital information about sand dunes, such as the sand particles size, which can be detected by sand traps, in addition to highly accurate ground truth data collected by GNSS, total station and levels that can be used for validating the monitoring results detected by the remote sensing techniques. However, these conventional techniques have significant limitations related to time consuming data collection processes and the complexity of monitoring large inaccessible sand areas. Additionally, they only provide an approximation of the dune movement, as the data are collected for discrete dune locations. Moreover, with few repeated surveys, conventional techniques are limited to detecting the movement that occurs within days or hours due to the rapid movement of the sand dunes. This can be overcome by applying time series analysis using remote sensing techniques, providing continuous observations of the dunes over periods of years.

The multi-temporal optical satellite framework (SET) is used to detect the land cover classification changes that relate to the horizontal, areal changes of sand dunes, in addition to determining the displacement and direction of movement of individual dunes. The achieved accuracy depends on the accuracy of the image classification results, which depends mainly on the samples used to train the classifier and the spatial resolution of the optical images. This technique is suitable for detecting sand dune movement over large areas. It also identifies areas at significant risk of sand encroachment. The cloud coverage in optical images represents the main challenge for this technique, as it leads to land cover miss-classification, which will affect the detected areal changes of sand.

The SAR pixel offset technique showed high competency in detecting the horizontal sand dune movement. The advantage of this technique is that it can be valuable in areas with a high presence of cloud, where optical remote sensing techniques fail to provide accurate analysis of the dune changes. As for the previous technique, pixel offset can only detect horizontal dune movement. However, it can detect the displacement of the dunes in the range and azimuth directions, which can be used to compute the direction of the dune movement.

Multi-temporal Airborne LiDAR DTMs were used to monitor the dynamic changes of the dunes. This technique demonstrated high capability in monitoring sand dunes both horizontally and vertically. This technique provides rates of horizontal and vertical dune motion in addition to the volumetric changes of the dunes. The achieved accuracy depends on the DTM accuracy, which depends on the accuracy of the GNSS positioning technique used. The limitation of this technique is that it relies on expensive, repeated airborne flights.

InSAR can detect the vertical movement of the dunes, however, the main limitation of this technique is due to the decorrelation and low coherence of the sand reflectance as a result of the rapid movement of the dunes. Table 6.1 illustrates a summarization of the capabilities and limitations of all of the used sand dune monitoring techniques.

Table 6.1. Capabilities and limitations of sand monitoring techniques.

Technique/Assessing Factor	Acquired Data	Coverage and spatial distribution	Sand Monitoring results	Achieved Accuracy	Limitations/Complexity of Processing
Sand Traps	• It collects sand particles providing information on the grain size impact, and the rate of horizontal or vertical movement and its direction.	• Low efficiency in covering large inaccessible areas, especially in desert areas.	• Approximate estimated rate of movement, and direction of sand movement.	• Low accuracy due to the approximate detection of sand movement due to the limited number of installed traps.	• Requires ground surveys. • Installing sand traps require experience and knowledge of the direction and wind behaviour. • Does not measure accurately the impact of other factors such as vegetation and topography. • Only provides the final approximation of the dune movement in discrete locations and does not detect the movement of the dunes in the whole study area.
GNSS	• Provides discrete dune points collected as 3D coordinate data.	• Low efficiency in covering large areas. • GNSS signal might face some interference losses in mountainous and heavily vegetated dune fields.	• Discrete data dune points. It requires repeated surveys to detect the movement of the dunes.	• High accurate collected dune points can be used to validate the remote sensing techniques' results.	• Requires ground surveys. • Data collection is time consuming and requires a large workforce, especially in desert areas, which is not feasible.

Technique/Assessing Factor	Acquired Data	Coverage and spatial distribution	Sand Monitoring results	Achieved Accuracy	Limitations/Complexity of Processing
Terrestrial LiDAR	• Provides dense 3D points cloud data of the dunes. • Provides intensity data that shows the reflectance of the surface which can be used to distinguish the activity of the dunes.	• Highly dense collected dune points are provided as millions of point clouds. • Determined by the distance of the scanner from dune features, the closer to the scanner the more points collected.	• Can be used to generate DTMs for the dunes. However, detecting the movement of the dunes requires repeated surveys.	• High accurate collected dune points can be used to validate the remote sensing techniques' results.	• Requires ground surveys. • Simple set-up for the scanner, however moving the TSL is hard due to the complex terrain of the dunes. • The homogenous terrain of the dunes restricts the VIS technology for linking up different TLS set-ups and scans. • To achieve better accuracy in the registration of TLS scans, more time must be allowed to observe the TLS targets using the GNSS, which will make the technique time consuming. • Post processing is complicated.
Optical Images (SET)	• Time series sand cover changes maps. • Multi-temporal image acquisition depends on the satellite mission.	• Large spatial coverage~ (300kmX300km) but depends on the satellite altitude. • Image mosaicking would allow for covering a large region of interest.	• Time series horizontal sand cover changes. • Detection of displacement and direction of individual dunes.	• Achieved accuracy depends on the accuracy of the classification results which depends mainly on the training samples and the spatial resolution of the images.	• No ground surveys are required. • Requires high performance computing capabilities. • Clouds present a challenge for image classification and detecting the changes in sand land cover.

Technique/Assessing Factor	Acquired Data	Coverage and spatial distribution	Sand Monitoring results	Achieved Accuracy	Limitations/Complexity of Processing
SAR Pixel offset	• Time series sand dune displacement maps. • Multi-temporal image acquisition depends on the satellite mission.	• Large spatial coverage~ (300kmX300km) but depends on the satellite altitude. • Image mosaicking would allow for covering a large region of interest.	• Detect the horizontal movement in the range and azimuth directions. • Provide the rate of sand dune horizontal changes. • Performs better at estimating large displacements beyond the maximum detectable deformation.	• Achieved accuracy depends on the pixel size of the SAR images, it is about 1/30th of the image pixel size.	• No ground surveys are required. • Requires experience and preprocessing to ensure the detected dune movement results are accurate.
InSAR	• Time series sand dune displacement maps. • Multi-temporal image acquisition depends on the satellite mission.	• Large spatial coverage~ (300kmX300km) but can vary with the satellite altitude.	• Detect the vertical displacement of dunes. • Coherence images can be processed with a further technique as the optical images for horizontal change detection.	• Achieved accuracy requires more investigations that involve ground data collection and validation.	• No ground surveys are required. • Detected displacement has some limitations due to the low coherence of the sand reflectance due to the rapid movement of the dunes. • Detecting the horizontal displacement requires processing ascending and descending images which further complicates the processing.

Technique/Assessing Factor	Acquired Data	Coverage and spatial distribution	Sand Monitoring results	Achieved Accuracy	Limitations/Complexity of Processing
Airborne LiDAR	• Multi-temporal sand dune DTMs.	• Depends on the altitude of the aircraft with coverage of a few kilometres square.	• Provide the rate of horizontal and vertical changes. • Computations of sand volumetric changes.	• Achieved accuracy depends on the DTM accuracy which depends on the used GNSS positioning technique.	• No ground surveys are required, however for high accuracy of LiDAR data, ground GNSS base stations are required for providing accurate locations of the aircraft. • The post processing and generation of LiDAR DTMs could be complex in vegetated dune fields, especially in coastal areas.

6.4 Developed Strategy for Monitoring Sand Dunes

This section presents a developed strategy for monitoring sand dune movement at different dune scales from an individual dune to a complex dune field. The strategy provides a defined approach that can be applied for monitoring sand dune movement in desert or coastal areas utilizing remote sensing techniques, to ensure consistent time series analysis for the detection of small and large sand dune movement that can occur on a daily, monthly and annual basis.

A strategic monitoring plan for sand dunes movement must follow three main implementation stages: (1) the detection of sand dunes using different surveying techniques, measuring the changes and movement of the dunes; (2) a monitoring stage, where time series analysis is applied to distinguish patterns in the dune movement, in addition to identifying the impact of the sand movement influencing factors (i.e. wind, vegetation, topography, …etc.) and their relationship to the sand movement behaviour; and (3), a prediction stage of sand movement, based on previously detected dune behaviour and the influencing factors from the monitoring results. Figure 6.5 illustrates the implementation stages of a strategic plan for monitoring sand dune movement.

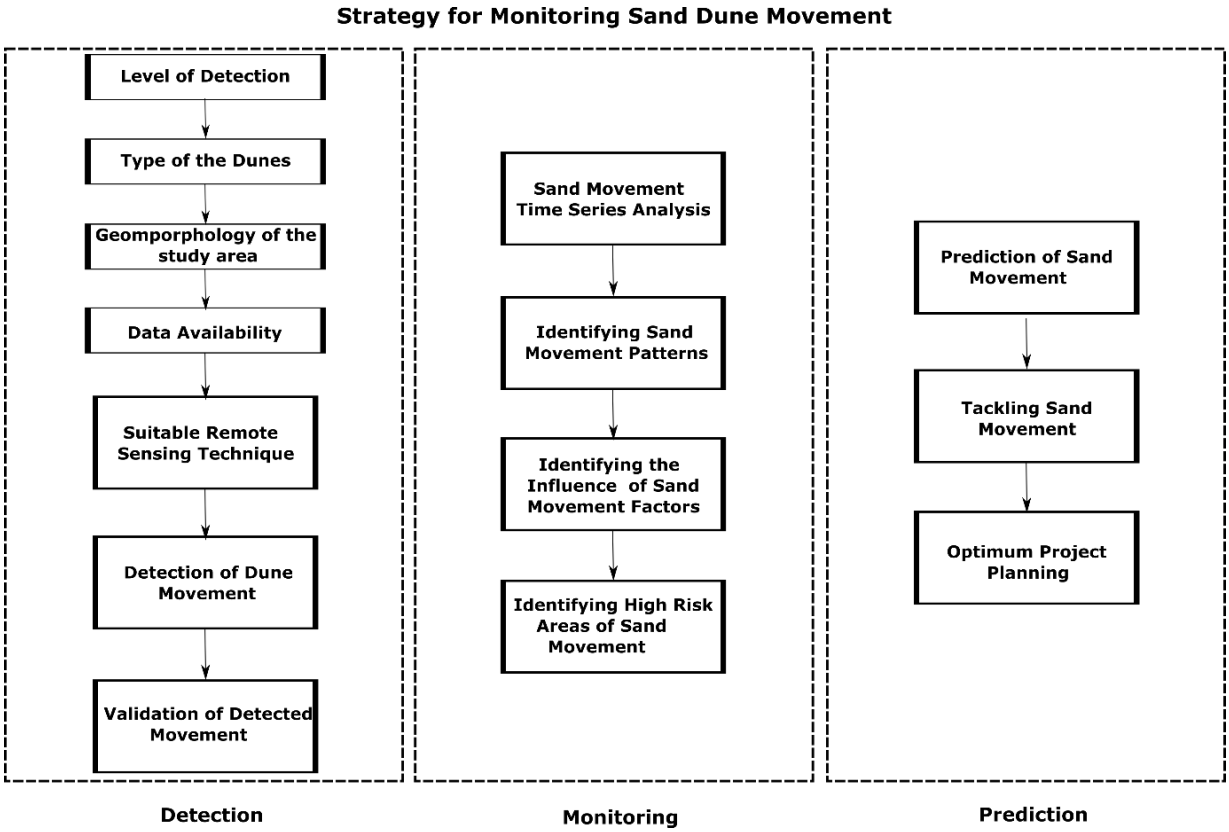

Figure 6.5. Strategy for monitoring sand dune movement.

The detection stage of sand dune movement utilizes remote sensing techniques to measure the movement of the dunes. Selecting a suitable remote sensing technique or type of data can vary from one study area to another, depending on the level of detection required, the type of the dunes, the geomorphology of the study area and the data availability.

The level of detection is identified based on the required dune detection scale, varying from individual dunes, dune fields, and regional sand movement to dust storms. In addition, different dune types (e.g. barchans dunes, linear dunes, sand sheets...etc.) would require optimizing different techniques for monitoring. The geomorphology of the study area and the landforms has a significant impact on determining the type of data (e.g. optical images, Radar, DTMs…etc.) to be used in the detection stage. The data availability is a key factor in the monitoring process, as it can limit the choices of techniques or the level of temporal and spatial detection of the dunes, which will have an impact on the accuracy of the predicted dune movement.

The detection of sand dune movement would provide statistical information on the rate of change, horizontal sand expansion, vertical dune changes and dune volumetric changes. The validation of this detected movement is quite an important step to determine the accuracy of the technique and precision of the detected movement. This can be achieved by using land surveying techniques, planned to detect sand dune movement, to provide accurate ground movement coordinated with the detection of the dunes using remote sensing techniques.

The monitoring stage involves applying time series analysis from the detection stage to identify patterns in the movement of the dunes over the study period. In this regard, the continuity of the remote sensing data provides consistent monitoring results of the dune movement behaviour. This is associated with defining the impact of the influencing factors on the dune movement activity. This provides measurable knowledge of the dynamic of the dunes in the region of interest, in addition to identifying and mapping areas with a high risk of sand encroachment.

The prediction of sand movement is an important factor in controlling the impact of sand movement, as understanding the dune movement behaviour and the impact of dune movement factors, it will allow for best practice of stabilizing sand dunes using variable techniques and that would consequently lead to optimized planning for habitational and environmental projects. In addition, the prediction of sand movement would significantly affect the socio-economic behaviour of local residents, especially in areas where sand is greatly overwhelming houses and agricultural crops.

A practical implementation of this strategy was followed in the case studies of this research to monitor sand dunes in desert and coastal areas. These case studies focused only on the implementation of the detection and monitoring stages. The prediction stage will be developed as an extension of this research.

This strategic plan is a key element for practical investigations for monitoring sand dune movement, and for the dune management restoration and stabilization projects. It can be applied for monitoring sand movement in both desert and coastal areas. The practicality of this strategy relies mainly on the high capability of the remote sensing techniques in providing a consistent measurement of the dunes and its competence in monitoring inaccessible dune fields.

7 CONCLUSION

Sand dune movement is considered one of the major environmental issues in arid and semi-arid regions threatening livelihood and rural communities. It also contributes to the degradation of land causing poverty and food insecurity. On the other hand, coastal dunes play an important role in coastal erosion risk management, where they act as a dynamic natural sea defence, in addition to providing habitats that enrich coastal biodiversity and adding resilience to the ecosystem. Sand movement can be experienced on different scales: individual dune movement, dune field changes or in a form of dust storms.

The aim of this research was to investigate the capabilities of various remote sensing techniques (i.e. optical multi-spectral satellite sensors, SAR techniques, airborne LiDAR) for detecting and monitoring sand dunes movement and its impact on urban areas, crop fields, water bodies, archaeological sites and determining the most vulnerable areas to sand dunes encroachment. In addition, it was designed to study the impact of the influencing factors that control the movement of the dunes, such as wind speed/direction, vegetation, topography and sand supply.

This research highlighted the capabilities of the remote sensing techniques in addition to defining the limitations of using the more traditional land surveying techniques for monitoring sand dunes. Based on that analysis, a strategy has been developed for monitoring sand dune movement. This strategy consists of three main implementation stages: (1) the detection of sand dunes using different surveying techniques measuring the changes and movement of the dunes; (2) a monitoring stage, where time series analysis is applied to distinguish patterns in the dune movement in addition to identifying the impact of the sand movement influencing factors (i.e. wind, vegetation, topography, …etc.) and its relationship to the sand movement behaviour; and (3), a prediction stage of sand movement based on previously detected dune behaviour and the influencing factors from the monitoring results.

An optimum strategy for monitoring sand dunes must address both the horizontal and vertical movement of the dunes. This can be achieved by using multi-temporal Airborne LiDAR data sets. However, this technique is expensive and has some challenges in the post processing stage. Moreover, it does not address the areal land cover changes of sand dunes, which can be detected easily by optical remote sensing techniques. On the contrary, the SAR techniques - pixel offset and DInSAR - can distinguish the displacement of the dunes in the horizontal and vertical components, respectively, in addition to detecting the direction of movement of the dunes.

Therefore, selecting the optimum remote sensing technique for sand dune monitoring, varies from one study area to another, depending on the level of detection required, the type of the dunes, the geomorphology of the study area and the data availability. For instance, the availability of Airborne LiDAR datasets is limited in developing countries which makes the other remote sensing techniques a more suitable option for monitoring sand movement.

The rapid development of SAR and optical data, and their processing, will have a huge impact on the development of advanced techniques for monitoring sand dunes. Moreover, the emergence of cloud-based computing services will allow for real time data processing. This can be adapted by local authorities, using remote sensing techniques in their monitoring and preservation projects on sand dunes. However, this requires developing platforms that provide real time analysis based on remote sensing data sets, with a simple implementation process, so that non-expert users can easily run the processing, to understand the behaviour of the dunes in their dune system.

The techniques developed in this research have applications beyond monitoring sand dunes such as land cover change detection and monitoring landslides and mines. The SAR pixel offset technique is recommended for monitoring land morphology in areas where high decorrelation, low coherence, is expected such as in glacial areas, where it can estimate large displacements.

The following sections provide a summary of each remote sensing technique used in this research to monitor the movement of sand dunes.

7.1 Optical Satellite Images

The first objective of the research has been addressed with a developed automated framework (SET) that uses Google Earth Engine and machine learning classifiers applied on multi-temporal Sentinel 2 L2A satellite images has been developed to detect the changes in the area of sand dunes, in addition to computing the displacement and direction of movement for individual sand dunes. Two machine learning classifiers were used in this study, the random forest and the support vector machine to monitor the horizontal movement of sand dunes in Northern Sudan between December 2018 to December 2021.

The validation comparison results demonstrated that both random forest and support vector machine achieved high accuracy of classification when applying a cost parameter of 0.2 for SVM and with a number of trees of 100 for the random forest.

The classification results showed that the rocky and sand classes are the dominant land cover types in the study area, with the rocky class covering an area ranging between the 4500-6500 km^2 for RF and 3200-6200 km^2 for SVM, while the sand class area ranged between 3000-4800 km^2 for RF and 3300-5700 km^2 for SVM. On the other hand, the vegetation and urban classes had an area ranging between 150-350 km^2 and 250-600 km^2 for RF and 230-450 km^2 and 110-850 km^2 for SVM, respectively, while the water class had the lowest land cover area ranging between 70-110 km^2 for RF and 80-105 km^2 for SVM. The classification results showed that the sand cover displayed a pattern of significant area changes, with an area increase during the period between September to February ranging between 4000-4800 km^2 for RF and for 4500-5200 km^2 SVM, and an area decrease during the period between March to August with an area ranging between 3300-4200 km^2 for RF and 3300-4600 km^2 for SVM. There is a significant correlation between the increase in the area of the sand class and the decrease in the rocky class area.

On the other hand, the individual dune detection tool was applied to detect the individual dune movement in Northern Sudan, near Goled city. The tool detected a significant movement for an individual dune digitized from two high resolution images in November 2011 and December 2012 where it showed an average displacement of 15 metres and a dominant movement direction to the southwest on the eastern side of the dune, while it detected an average displacement of 7 metres with a dominant movement direction to the southeast in the west side of the dune. The location of the dune has shifted in the southwest direction by more than 125 metres between 2011 and 2022, the current location of the dune. The movement of the same dune was detected using SET from two sequential classified images on the 30 of May and the 09 of July 2020. The results showed an average displacement of 10 metres and a dominant movement direction to the west/southwest. It is also observed that the lowest detected displacement is related to the lower resolution of the satellite images used (i.e. Sentinel 2 with 10 m spatial resolution).

The tool distinguished the displacement of the dunes; however, due to the complexity of the generated dunes from the classification, different points are linked and assigned with incorrect points in the second image. This tool showed that detecting the deformation of individual dunes could be provided from moderate images, but the higher resolution the images, the better the footprints of the individual dunes, which consequently would result in increasing the detecting capabilities of the technique (SET). The detected movement of the individual dunes was assessed by visually inspecting and measuring the dunes on the two corresponding images, providing similarly average displacement.

7.2 SAR Offset Tracking

Another remote sensing technique was used to detect the horizontal movement of the dunes in the Northern's Sudan study area, namely SAR offset tracking. This addressed the second objective of the research, investigating the capabilities of the SAR Offset Tracking technique for detecting horizontal sand dune movement. This is the first application of SAR offset tracking in detecting the movement of sand dunes. This technique determines the offset between pixels of the same area that appear in two different SAR images. The accuracy of offset tracking depends on the pixel size of the SAR images, and it is about 1/30th of the image pixel size for both range and azimuth directions, which results from errors in the co-registration of the two images.

Ten Sentinel-1 Level-1 Ground Range Detected (GRD) VV/VH polarised SAR images were used for offset tracking to determine the displacement of sand dunes in the study area for a period of four months. Three distinct dune fields within the study area were investigated for dune motion with a vegetated dune field (dune field 1) and two non-vegetated dune fields (dune field 2, dune field 3) used to distinguish the impact of vegetation on the movement of the dunes in addition to the other influencing factors (i.e. wind speed/direction and topography).

A time series of displacement vector maps were generated by daisy chaining the image pairs to estimate the displacement time series for all pixels in the dune fields. The cumulative east displacement over the study period was 1.8 m, -1.1 m and 4.8 m for dune fields 1, 2 and 3, respectively, while the cumulative north displacement was 0.7 m, 2.9 m and 4.2 m.

The wind behaviour had a significant impact on the movement of the dunes. Dune fields 1, 2 and 3 had a dominant wind blowing direction of 181, 185 and 187 degrees, with an average wind speed of 4.6 m/s, 4.84 m/s and 4.84 m/s, respectively. This southerly wind resulted in an average displacement of 0.7 m in dune field 1 and 2.7 m in dune field 3 with a dominant movement to the north-east and an azimuth of 56°, while dune field 2 had an average displacement of 2.5 m to the north, with an azimuth of 346°.

The displacement time series for dune field 1 showed larger movement in the east cumulative displacement compared to the northern component and this is due to the impact of the wall of trees in diverting the movement of the dunes parallel to its orientation. Dune field 2 had a larger movement in the north component, while dune field 3 had the largest movement among the three dune fields in both east and north components.

This technique showed high competency in detecting the horizontal sand dune movement, with the advantage of detecting the displacement of the dunes in the range and azimuth directions, which can be used to compute the direction of the dune movement. It also identified areas with large sand dune movement that can be considered for further investigations.

7.3 Airborne LiDAR DTMs

The third case study investigated the use of Airborne LiDAR data to monitor the dynamics of Formby coastal sand dunes in Northwest England over a period of 21 years between 1999 and 2020. This addresses the third objective of the research with a developed framework for monitoring the dune changes from time series of high-resolution DTMs at all scales: dune point elevation changes, cross sectional profiles, and longitudinal profiles were produced, as well as deposition/erosion and volumetric changes for dune field. The study aimed to investigate the activity of the sand dunes at Formby coast by carrying out a series of raster and vector analysis.

It has been found that the rate of elevation change for the beach and dunes was between -0.79 to 0.08 m/year and -0.91to 0.73 m/year respectively during the measurement period, indicating that the beach and the frontal dunes experienced erosion, while sand accumulation was observed in the inner dunes. Areas with presence of vegetation remained largely unchanged, emphasizing the impact of vegetation in stabilizing the movement of the dunes.

Formby beach has seen significant volume loss of about 907,000 m^3 in 21 years' time, while the dunes' volume increased by about 1,049,000 m^3. The volume of the entire dune system of Formby (beach + dunes) remained broadly unchanged, which indicates that all the volumetric changes happened due to sand redistribution within the dune system, with erosion in the beach and frontal dunes compensated by deposition in the inner dune areas. The DTM time series revealed that the Formby beach, marked by the frontal edge of the dunes, migrated horizontally by about 50m inland during the measurement period. In addition, it showed Formby coast dune system to be a highly dynamic system with active redistribution of sand within the system.

This technique demonstrated high capability in monitoring sand dunes both horizontally and vertically, providing rates of horizontal and vertical dune motion in addition to the volumetric changes of the dunes.

7.4 DInSAR

The fourth objective of the research was to investigate the capabilities of Differential Interferometric Synthetic Aperture Radar (DInSAR) for detecting the vertical deformation of sand dunes. A pair of Sentinel-1 single look complex (SLC) SAR images acquired on the 4th and the 16th of June 2017 were processed to detect the displacement of the dunes near Goled city in Northern Sudan.

The phase interferogram results gave an indication of the level of deformation seen during the study period. Areas with vegetation, water and sand dunes have seen significant changes due to the characteristics of these features in comparison to the urban and bare land areas. This also appeared on the coherence map, where low coherence was seen in water surface, agricultural fields and sand dune areas, where they appeared as black patches suggesting significant changes. Urban areas and bare lands were observed as white patches as they remained stable. The computed phase displacement showed a vertical displacement ranging between 0.18 and -0.20 metres, which is considered to be significant given the short period of the measurement. This implies that InSAR can detect the changes in sand dunes over the period in question.

Detecting the vertical displacement of the dunes using only a pair of SAR images has some limitations. This is mainly because of the decorrelation between the primary and secondary images due to phenological changes in vegetation or rapidly changing land features, such as water and dunes. Therefore, reducing the temporal baseline of the pair might increase the precision of the detected dune displacement. This requires more investigations, associated with ground data collection for validation.

7.5 Findings and Challenges

7.5.1 Findings

1. This research identified significant limitations of the conventional techniques, such as sand traps and land surveying techniques, related to time consuming data collection process and the complexity of monitoring large inaccessible sand areas.
2. The classification time series analysis of multi-temporal optical satellite images provided a comprehensive detection observation of the areal changes of sand dunes. This technique can be used as a preliminary step for investigating the activity of sand dunes in large study areas.
3. The individual dune detection tool (SET) performed very well in detecting individual dune movement. The tool showed good competency with simple movement in non-complex dune fields with smoothed edges and separated dunes. However, it is observed that all the points in the primary dune point location were assigned to the nearest dune point in the secondary location of the dune, though some points were

assigned to the same point in the secondary dune location, which has resulted in some gaps in the displacement calculation.

4. From the sand encroachment tool experiments, it can be understood that using higher spatial resolution images would result in better land cover classification, distinguishing between the different land cover types, which will have a significant impact on precisely measuring the changes of sand dunes over a certain period.
5. SAR offset tracking computes the two components of the dune displacement in the azimuth and range directions allowing the detection of the direction of dune displacement. These results can be used to establish a relationship between the movement of the dunes and the influencing factors.
6. Multi-temporal Airborne LiDAR DTMs demonstrated high capability in monitoring sand dunes both horizontally and vertically, providing the rate of horizontal and vertical dunes in addition to the volumetric changes of the dunes.
7. Sand movement can occur on daily basis and even over a few hours, therefore high temporal resolution data must be used to ensure an accurate monitoring process.
8. Sand movement can be observed both horizontally and vertically. However, there is a limited understanding of the vertical movement of the dunes, with most researchers focusing their work only on studying the horizontal movement of the dunes. This can be linked to the limited availability of multi-temporal elevation data in most desert regions.
9. Determining the impact of each influencing factor on dune movement requires a consistent monitoring process associated with accurately measuring the dynamic behaviour of each influencing factor.
10. The variation in wind components during different weather seasons results in drifting sand dunes in different directions.
11. Vegetation is considered to be an effective stabiliser of dune movement. Areas with vegetation have a slower rate of horizontal dune movement, however, on the other hand, vegetation contributes to accumulation and hence the vertical growth of the dunes.
12. Topography has a significant impact on diverting and shaping sand dunes.
13. The remote sensing time series analysis provides risk maps that identify areas exposed to high degrees of sand drifting. This is considered an important input for decision making, supporting the planning of local and regional projects.
14. Some researchers mix the desertification and sand movement phenomena when interpreting the advancement of the desert. The two phenomena are distinctive, though both contribute to the expansion of the desert.

7.5.2 Challenges

1. One of the common challenges when monitoring sand dunes using remote sensing techniques is the limited availability of topographical maps needed for validation, especially in desert areas.
2. Digital terrain models are the optimum type of data for monitoring sand dune movement as both the horizontal and vertical motion of the dunes can be detected. However, the limited availability of these data poses a major challenge.
3. Generating digital surface models of sand dunes using optical imagery to understand the vertical movement of the dunes is a real challenge.
4. Generating digital elevation models for active sand dunes using InSAR could be a challenge due to the rapid changes of the dunes.
5. The collection of training samples for image classification is also a challenge, especially in remote access areas.
6. The individual dune detection SET tool requires more development for the computation of the displacement and direction of movement. This can be achieved by fixing the mixed point issue and restricting the distance radius search based on pervious knowledge of the expected movement between corresponding points. The Near tool works on providing the distance and proximity information between the primary dune point and the closest point on the secondary dune, which results in multiple points in the primary dune to one point in the secondary point. This could be resolved by restricting the connection to only one point on each dune point dataset.
7. Interpreting the horizontal movement of the inner dunes in a connected complex dune field is difficult as all the inner dunes are one joined unit; nevertheless, the vertical elevation changes can be easily seen and interpreted.
8. For accurate prediction of the dune movement, the impact of the influencing factors must be clearly distinguished, and this is not an easy task.
9. Distinguishing the impact of sand grain size from remote sensing data requires a thorough investigation.

7.6 Future work and Recommendations

1. Develop an automated integrated method based on SAR offset tracking time series for the detection of horizontal sand movement integrated with DInSAR time series to detect the vertical sand dune movement.
2. Carry out comparative research to investigate the use of SAR and optical pixel offset to monitor the horizontal sand dune movement using e.g. COSI-Corr and SNAP.

3. Investigate different types of SAR images (i.e. P, L, X microwave bands) and different modes (i.e. impact of different polarization, impact of incidence angle) to optimize the best suitable technique for monitoring sand dune changes.
4. Investigate the use of historical aerial photographs and drone imagery to monitor the movement of sand dunes. This type of data can be valuable in providing a high level of detail about the dunes and allows the generation of digital terrain models that can be utilized to assess and map the geomorphological changes of the dunes.
5. Carry out geomorphological analysis to understand the dynamics of the dunes in remote inaccessible desert areas, in the Sahara or Rub Elkhali. This can contribute to supporting the regional mega projects in northern Africa, distinguishing areas vulnerable to sand movement and therefore supporting optimum planning for the success of reforestation projects in the region.
6. Assess projects to determine the impact of sand movement on river channels, irrigational canals, crop fields and archaeological sites.
7. Carry out investigations on other dune fields with different dune characteristics and geomorphology (e.g. Namibia dunes, Rub Elkhali dunes, etc.).
8. With the latest advancement in remote sensing and cloud computing services, there is a great opportunity to develop time series analysis geospatial tools that can provide real time and accurate observations of the movement of the dunes. This can allow also for the development of geoprocessing tools used to update the sand sea map of the world.

APPENDICES

University of Nottingham
UK | CHINA | MALAYSIA

British Geological Survey
Expert | Impartial | Innovative

The Uses of Remote Sensing for Modelling Sand Movement in Sudan

PhD Student: Ahmed Mahmoud, Supervisors: Prof. Stuart Marsh, Dr. Martin Smith, Dr. Panistmuls Pasimluls

Background

- Sand movement is a global environmental phenomenon that is threating livelihood and rural communities.
- There are several factors that contribute to the movement of sand such as the grain size and sorting characteristics of the dune which influence the size and the spacing of the dunes. In addition, the topography and the vegetation cover where vegetation stabilize the movement of sand, but most importantly the wind behaviour (wind speed and direction).
- Sudan is highly affected by sand movement and also considered a dust source as it is part of the Saharan Desert.

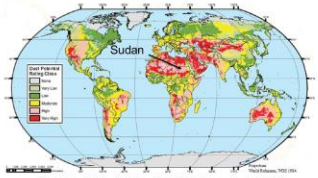

Global Dust Potential Map (DFT, 2013; Shepard et al., 2016)


Sand Encroachment in the ancient Cemetery of Meroe, Sudan


Sand Encroachment Displaced Entire Communities in the River Nile state, Northern Sudan (UNEP, 2016)

Detecting sand movement has been always a challenge as sand moves quite rapidly. Moreover, desert areas are very large to be covered effectively using terrestrial techniques (i.e. GNSS, total stations and levels) or sand traps which were the main methods that were used in the field to measure the transport rates of sand by capturing the blown sand grains by wind in traps.

Leica Terrestrial Surveying Equipment (a) GNSS, (b) Total Station and (c) Level

Sand Traps: (d) Horizontal trap (Munro et al., 2012); (e) Vertical Trap (Sherman et al., 2014)

However, due to the advance of the remote sensing techniques and the wide use of the satellite and aerial imagery the latter techniques can be used to replace the terrestrial ones and ensure better understanding and larger coverage of the movement of sand.

Aim of the Research

This research investigates the use of different remote sensing techniques (i.e. DInSAR, SAR offset tracking, image classification of optical satellite and aerial imagery) in detecting the movement of sand dunes over time; by monitoring the changes of sand mass and measuring the magnitude and direction of movement for individual dunes. Moreover, it investigates the impact of the sand movement influencing factors on the rate of movement.

DInSAR for Detecting Movement of Sand

- The differential interferometric synthetic aperture radar (DInSAR) uses two SAR images acquired over the same area taken slightly from different sensor positions or on different dates to distinguish the changes of the earth terrain.
- SAR images are considered very useful for the purpose of dunes mapping, volumetric estimation and monitoring desert height changes.

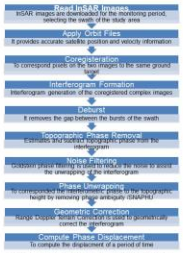

DInSAR Phase Displacement Steps in SNAP Software

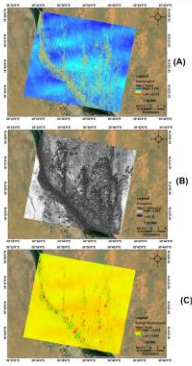

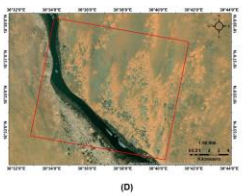

DInSAR Results between 12 to 24 of November 2016 (A) Interferogram, (B) Coherence Map, (C) Vertical Displacement, (D) Dune Field ;Study Area

SAR Offset Tracking

The application of SAR offset tracking in monitoring the movement of sand dunes is a novel use technique that works on monitoring the changes of a certain phenomenon

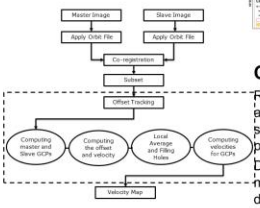

Work Flow for SAR Offset Tracking

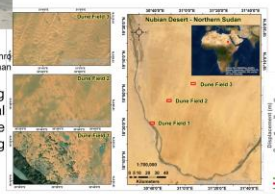

Nubian Desert Dune Fields, Dune Field 1: Presence of Vegetation; Dune Fields 2,3: Absence of Vegetation (Images source is ESRI)

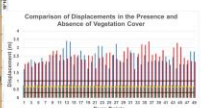

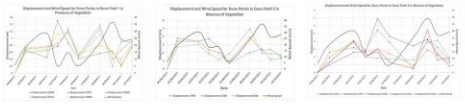

Sand Encroachment Tool (SET)

The sand encroachment tool has been developed in the model builder of ArcGIS software. It integrates remote sensing with GIS in order to monitor the changes of sand mass over a period of time and also to detect the displacement and direction of movement of individual dunes.

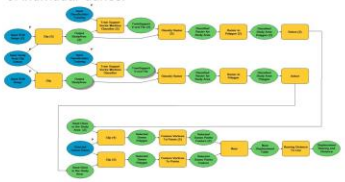
SET Framework for the Detection of Sand Dunes Movement

This tool works perfectly with higher resolution images as dunes boundaries can be clearly identified. However, when applying it on images of moderate or lower spatial resolution it results in assigning incorrect displacement bearings lines.

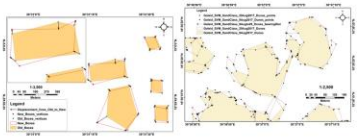

Conclusion

Remote sensing technique can be used as an alternative methods for monitoring and modelling sand movement with better representation and more precision for the volumetric calculations.

DInSAR is a good technique for understanding the movement in the vertical component of the sand dune, while SAR offset tracking can be really useful for the detection of the horizontal changes and by combining the results from both techniques will results understanding the movement of dunes on both components.

SAR offset tracking can be applied for a long period which gives the opportunity of applying times series analysis that support building of a detection model to predict the movement rates of dunes taking into consideration the impact of all movement influencing factors.

SET is an automated frame work that is quite significant for detecting the movement of individual dunes, therefore it is a vital tool for monitoring the movement of individual dunes which means providing broader understanding of dune movement on multiscale.

Note that the validation of all these techniques for modelling the movement of sand dunes requires field work using terrestrial techniques and for which it will take place in April.

Nottingham Geospatial Institute
Faculty of Engineering Research Showcase May 2020

Figure S 1. Second year poster competition, Engineering research showcase May 2020.

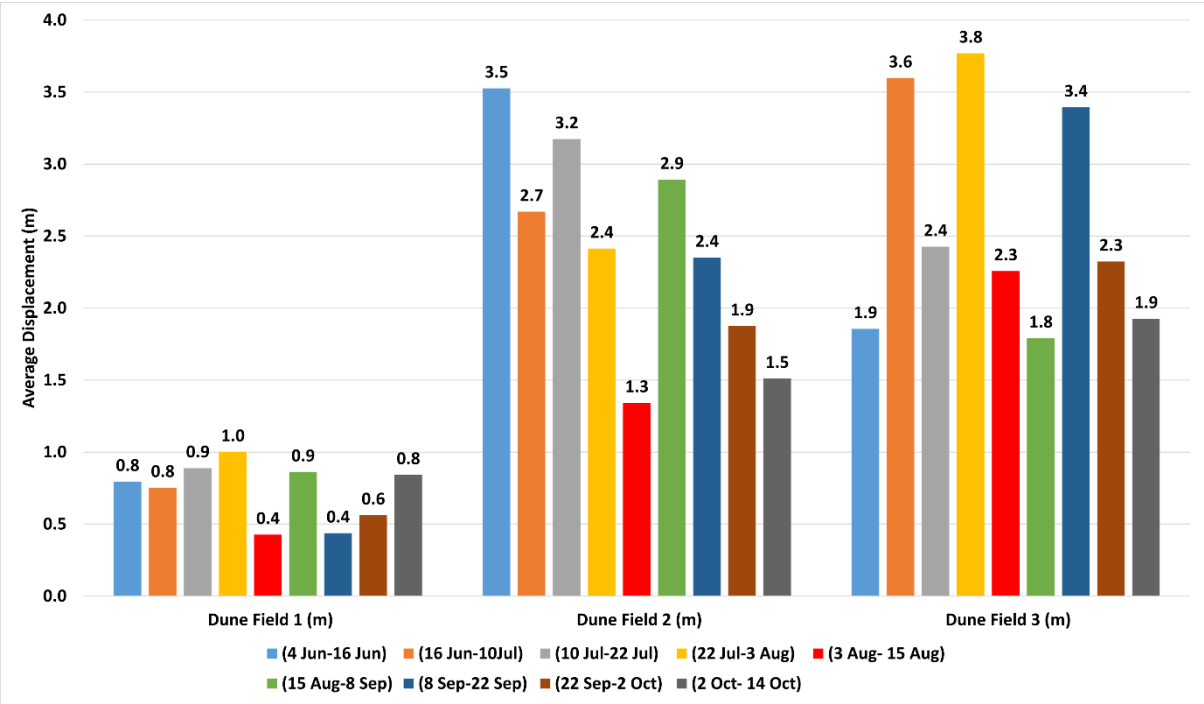

Figure S 2. Average displacement for Dune Fields 1,2 and 3 over the study period (four month) for each offset image.

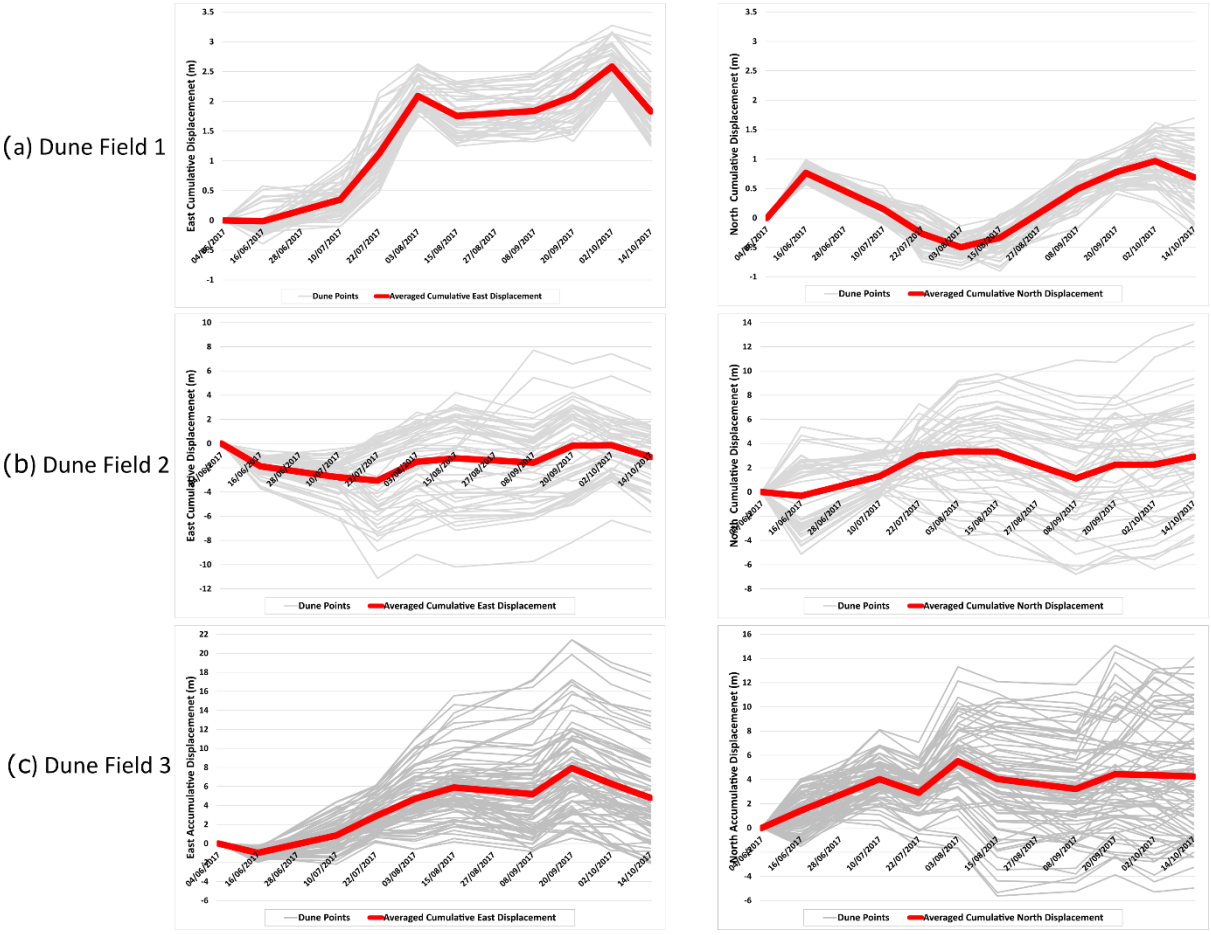

Figure S 3. East and North cumulative displacement plots for each dune field, SAR offset tracking case study.

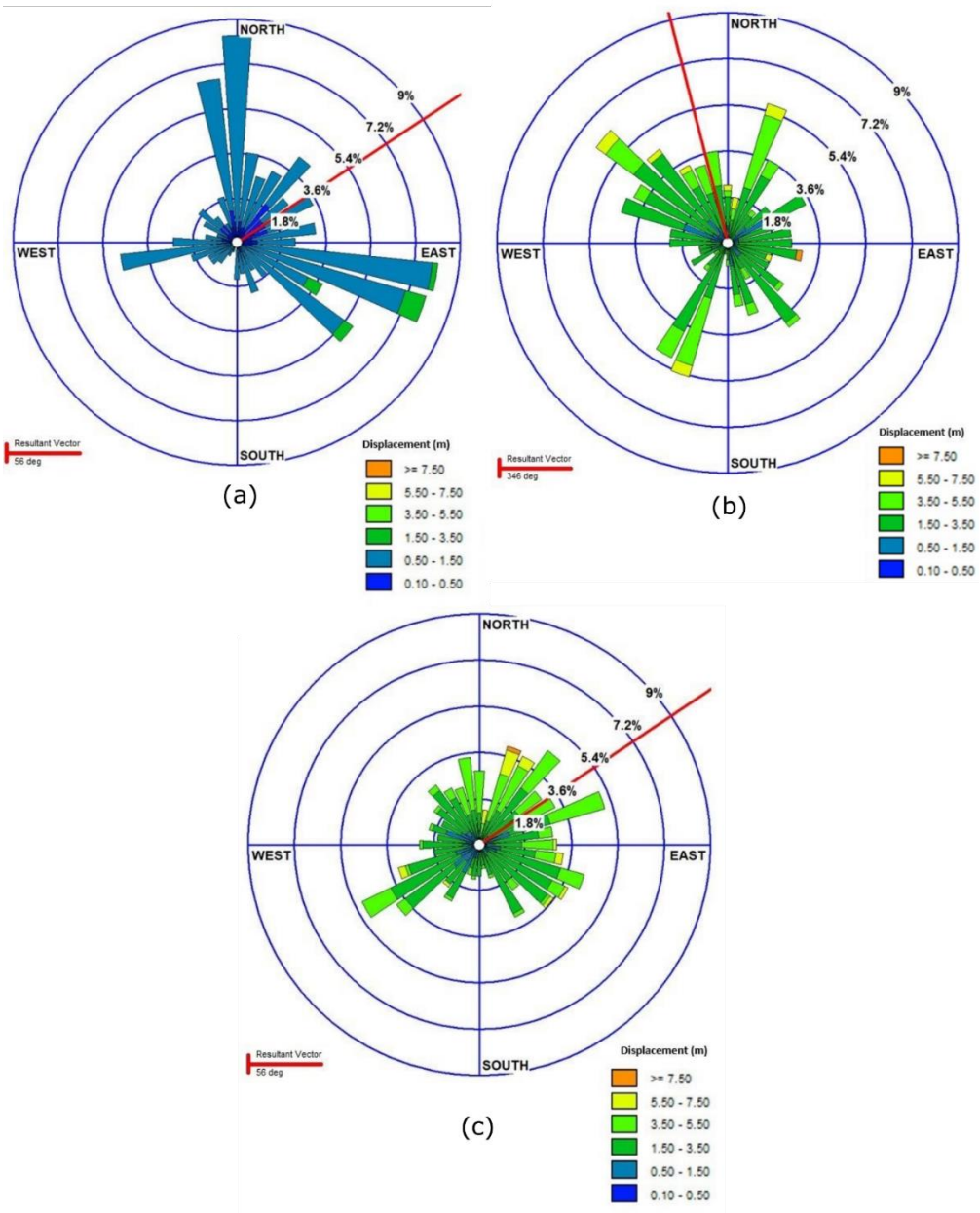

Figure S 4. Displacements Rose for dune fields 1,2 and 3 for the period between 4th June and 14th October 2017, SAR offset tracking case study.

(a) Dune Field 1

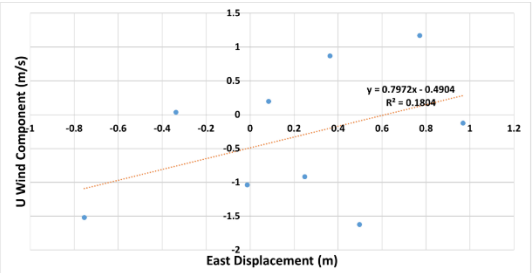

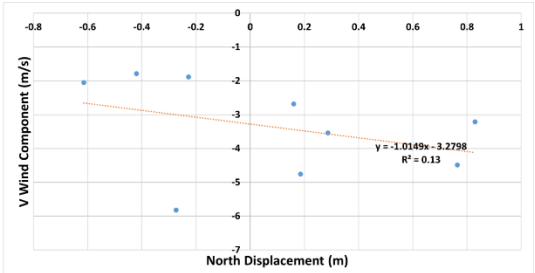

(b) Dune Field 2

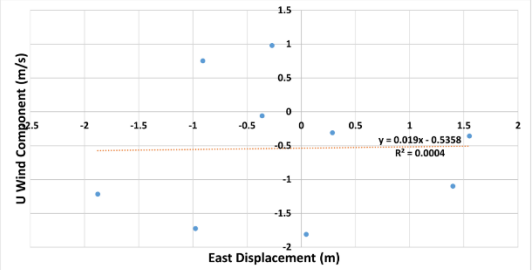

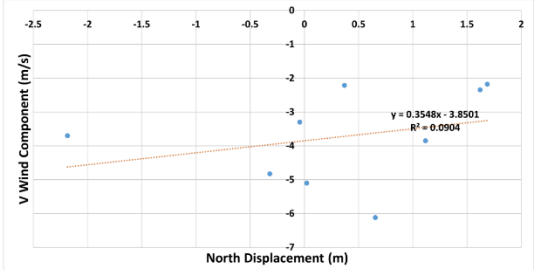

(c) Dune Field 3

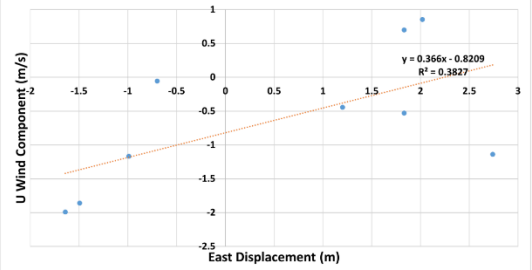

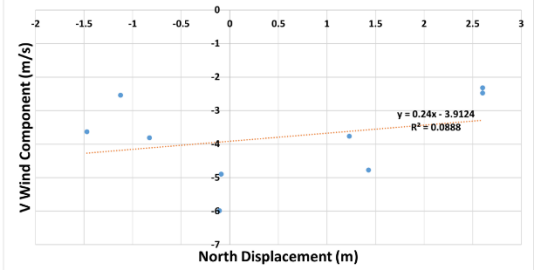

Figure S 5. Pearson Correlation Analysis for the average East and North displacement compared to the average U and V wind, SAR offset tracking case study.

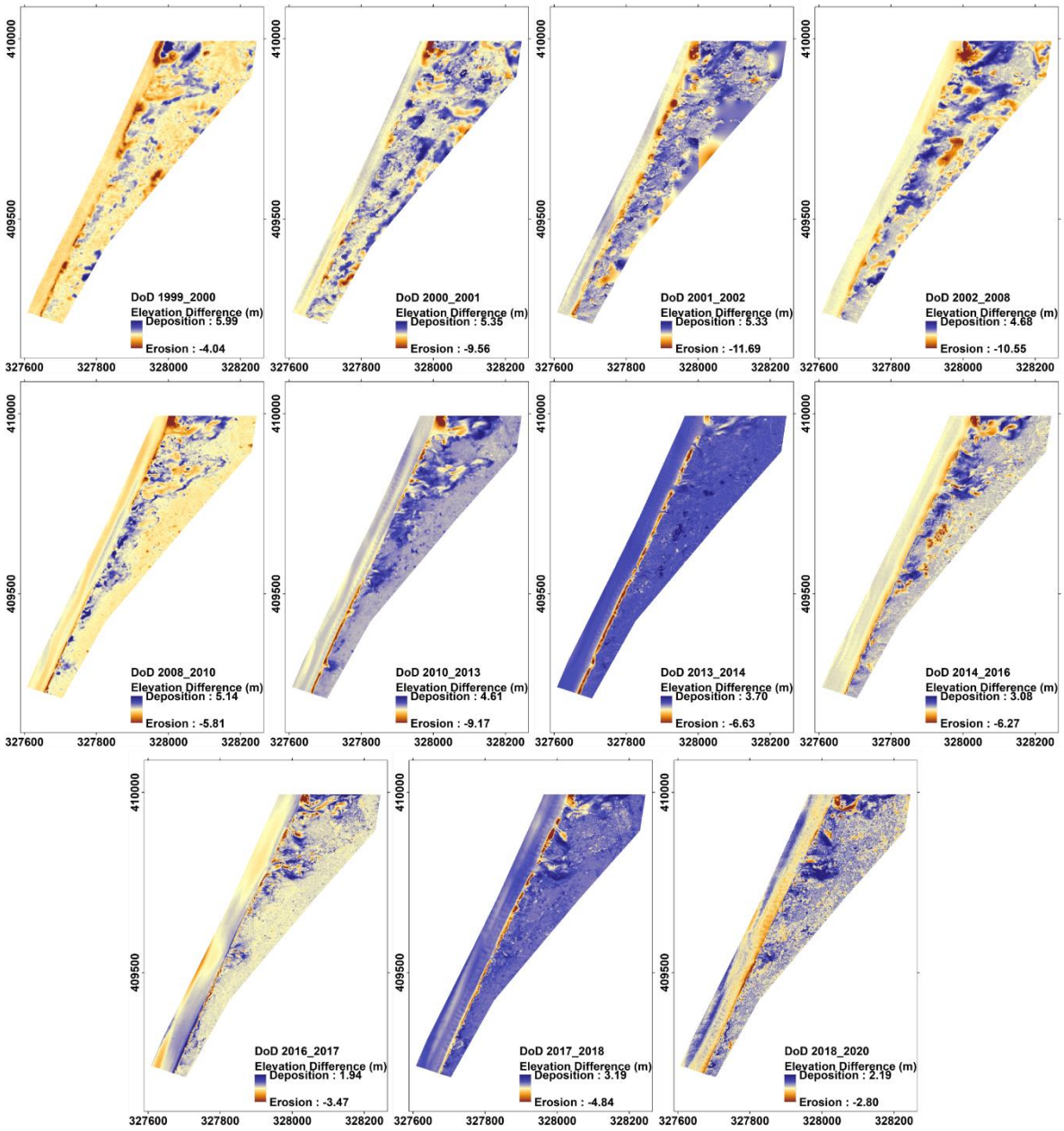

Figure S 6. Zone A DTM of Difference (DoD) Maps, Formby case study.

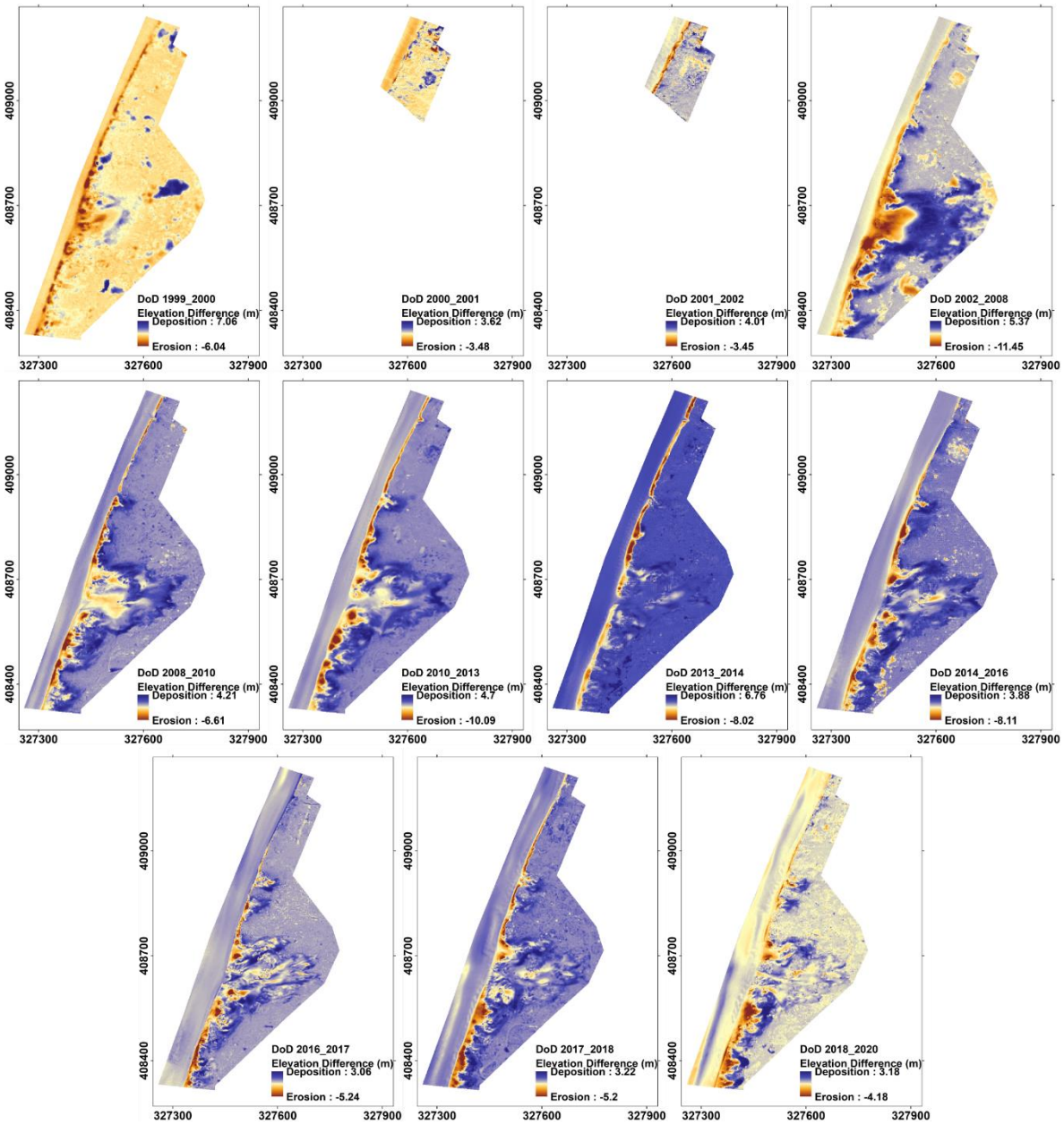

Figure S 7. Zone B DTM of Difference (DoD) Maps, Formby case study.

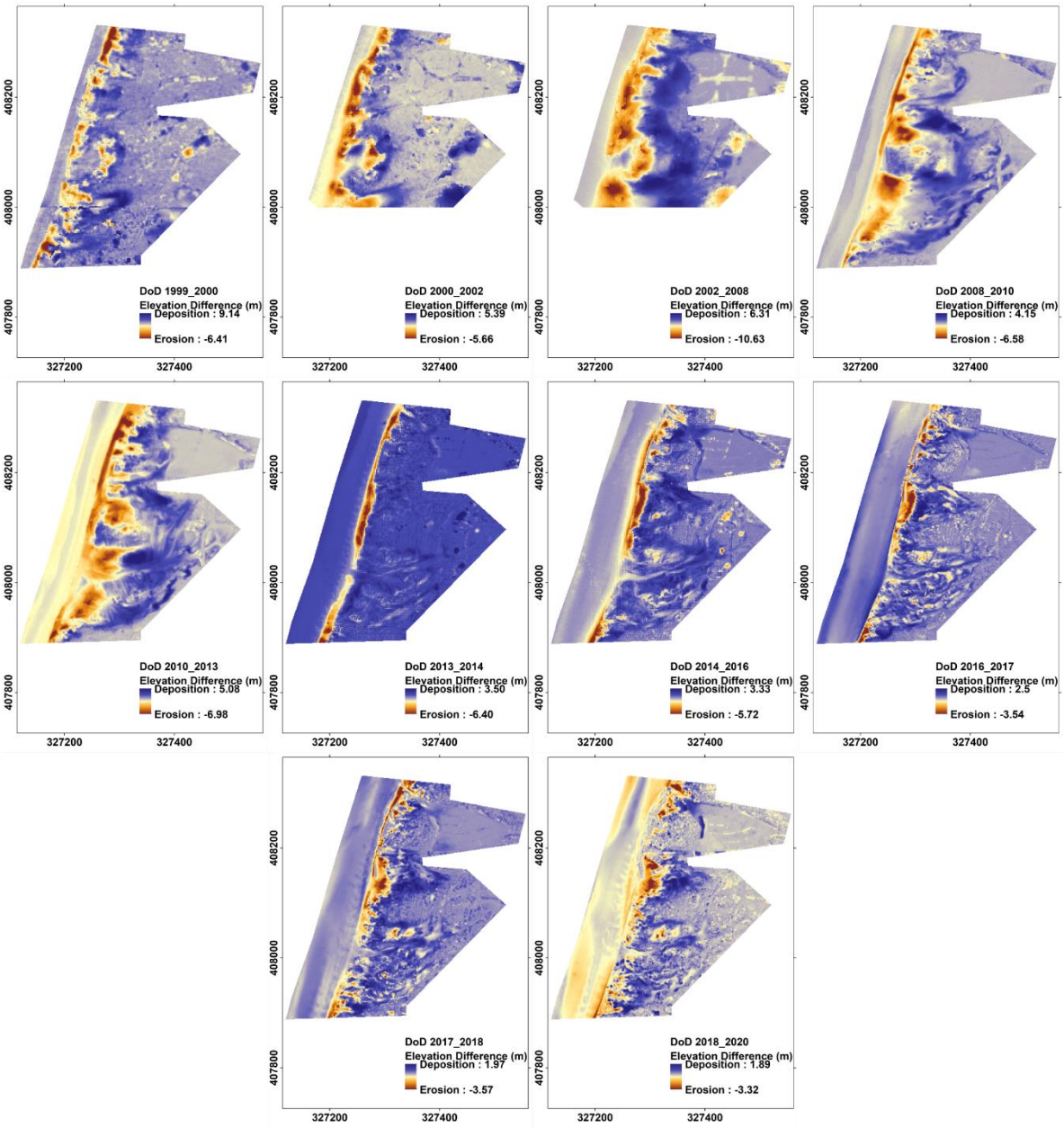

Figure S 8. Zone C DTM of Difference (DoD) Maps, Formby case study.

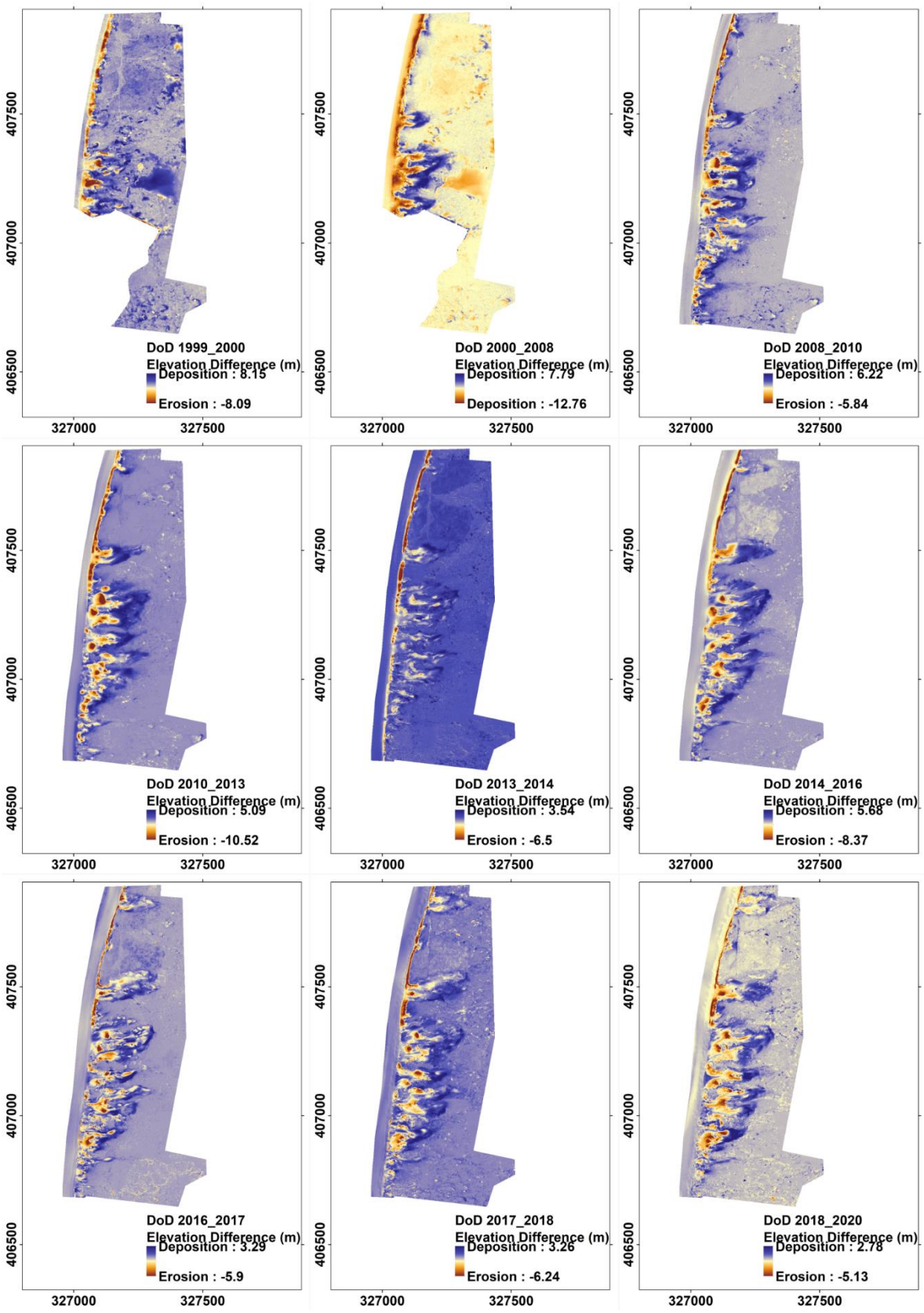

Figure S 9. Zone D DTM of Difference (DoD) Maps, Formby case study.

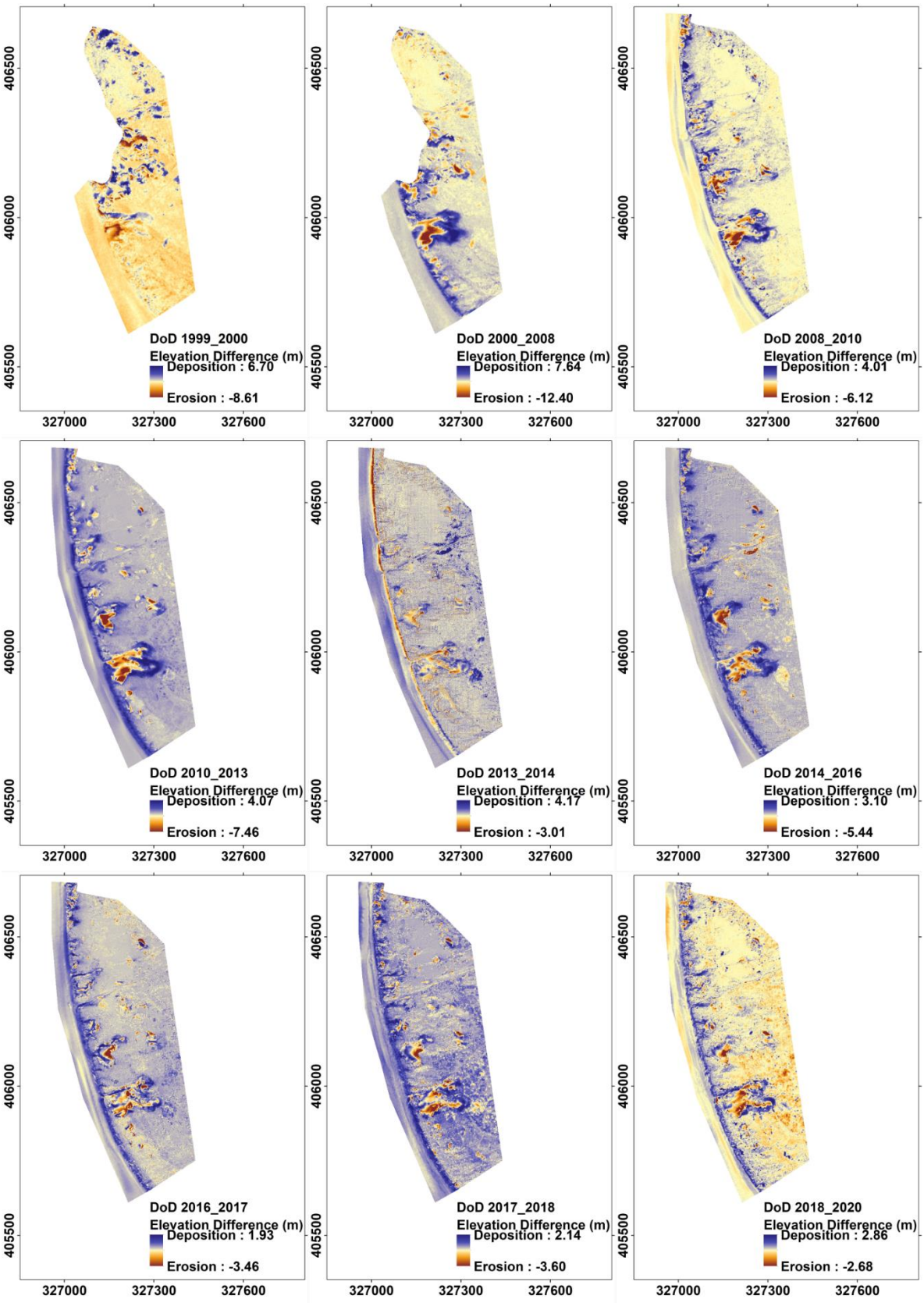

Figure S 10. Zone E DTM of Difference (DoD) Maps, Formby case study.

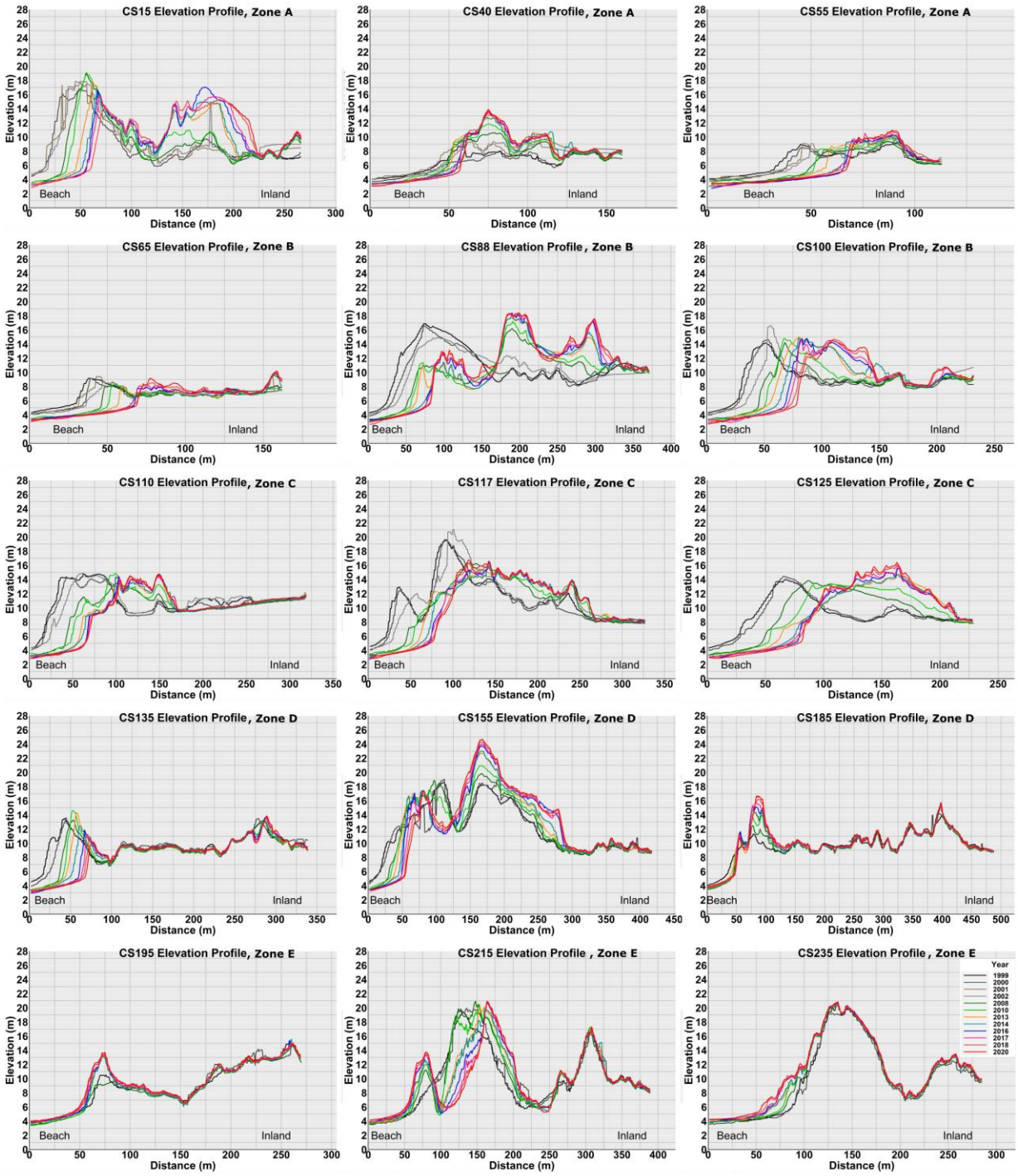

Figure S 11. Selected cross sections (CS15, CS40, CS55), (CS65, CS88, CS100), (CS110, CS117, CS125), (CS135, CS155, CS185), (CS195, CS215, CS235) from zone A, B, C, D, and E, respectively, that reflect the profiles changes of the beach and dunes between 1999 and 2020 in the north, middle and south sections of each zone. Formby case study.

Multitemporal image classification code written with JavaScript in Google Earth Engine to automate sand movement time series analysis processing using machine learning in chapter 3:

```
////////////////////////////////////////////////////////////////////////////
// Define the study area
////////////////////////////////////////////////////////////////////////////
var Study_Area = ee.FeatureCollection('projects/ee-
ahmedmahmoud/assets/shapefiles/Study_Area');
Study_Area = Study_Area.geometry();
Map.centerObject(Study_Area);
Map.addLayer(Study_Area, {color: 'yellow'}, 'Study_Area');
////////////////////////////////////////////////////////////////////////////
//Collect the Sentinel 2 Multi spectral instrument L2A images between
December 2018 to December 2021
////////////////////////////////////////////////////////////////////////////
var SenImageCollection = ee.ImageCollection("COPERNICUS/S2_SR")
                    .filterBounds(rio)
                    .filterDate('2018-12-01', '2021-12-31')
                    .select('B[1-8]')
                    .filter(ee.Filter.lt('CLOUDY_PIXEL_PERCENTAGE',1))
                    .map(function(image){return image.clip(Study_Area)});
print('SenImageCollection', SenImageCollection);
////////////////////////////////////////////////////////////////////////////
// Image Visualizing
////////////////////////////////////////////////////////////////////////////
// Visualzation of a single image
var listOfimages = SenImageCollection.toList(SenImageCollection.size());
Map.addLayer(ee.Image(listOfimages.get(0)), {bands: ['B8', 'B3', 'B2'],
min: 0, max: 3000});
Map.addLayer(ee.Image(listOfimages.get(70)), {bands: ['B8', 'B3', 'B2'],
min: 0, max: 3000});
Map.addLayer(ee.Image(listOfimages.get(100)), {bands: ['B8', 'B3', 'B2'],
min: 0, max: 3000});
// Visualization of all the images
var listOfimages = SenImageCollection.toList(SenImageCollection.size());
var len = listOfimages.size();
len.evaluate(function(l) {
  for (var i=0; i < l; i++) {
    var image = ee.Image(listOfimages.get(i));
    Map.addLayer(image, {bands: ['B4', 'B3', 'B2'], min: 0.0, max: 0.3},
'image-'+i.toString());
  }
});
////////////////////////////////////////////////////////////////////////////
// Get the list of the image acquisition dates
////////////////////////////////////////////////////////////////////////////
var ImageDates = SenImageCollection.map(function(image){
    return ee.Feature(null, {'date': image.date().format('YYYY-MM-dd'),
'id': image.id()});
})
.distinct('date')
.aggregate_array('date');
print ('ImageDates', ImageDates);
////////////////////////////////////////////////////////////////////////////
// Statistics of the cloud pixel percentage in the image collection
////////////////////////////////////////////////////////////////////////////
var CloudCoverageStats =
SenImageCollection.aggregate_stats('CLOUDY_PIXEL_PERCENTAGE');
print('Cloud Coverage stats:', CloudCoverageStats);
////////////////////////////////////////////////////////////////////////////
```

```
// Visualization parameters for the calssification legend
//////////////////////////////////////////////////////////////////////////////
var class_vis = {min:0, max: 4,
palette:['F7B83F', '146E04', '071AC7', 'A0A0A5','AB6106']};
//////////////////////////////////////////////////////////////////////////////
//////////////////////////
// Create RGB visualization images to use as animation frames.
var rgbVis = SenImageCollection.map(function(image) {
  return image.visualize(class_vis);
});
// Define GIF visualization parameters.
var gifParams = {
  'region': Study_Area,
  'dimensions': 300,
  'crs': 'EPSG:32636',
  'framesPerSecond': 5
};
// Render the GIF animation in the console.
print(ui.Thumbnail(rgbVis, gifParams));
//////////////////////////////////////////////////////////////////////////////
// Merged the training samples into one feature collection
//////////////////////////////////////////////////////////////////////////////
var training_samples = SandClass_points.merge(VegetationClass_points)
                      .merge(WaterClass_points)
                      .merge(UrbanClass_points).merge(RockyClass_points);
print('training samples dataset', training_samples);
var testsamples = SandClass_testpoints
                  .merge(VegetationClass_testpoints)
                  .merge(WaterClass_testpoints)
                  .merge(UrbanClass_testpoints)
                  .merge(RockyClass_testpoints);
print('test samples dataset', testsamples);
//////////////////////////////////////////////////////////////////////////////
//Train the Random Forest classifier and classify the image collection
//////////////////////////////////////////////////////////////////////////////
var bands = ['B2', 'B3', 'B4', 'B8'];
function RFclassification(image){
  var classification_training_samples =
image.select(bands).sampleRegions({collection:training_samples,
    properties: ['landcover'],
    scale: 10
});
var RFtrained_classifier =
ee.Classifier.smileRandomForest(100).train(classification_training_samples,
'landcover', bands);
var RFclassified_image =
image.select(bands).classify(RFtrained_classifier);
return RFclassified_image;
}
var RFclassified_imageCollection =
SenImageCollection.map(RFclassification);
print('RFclassified_imageCollection', RFclassified_imageCollection);
var RFclassified_imageCollectionlist =
RFclassified_imageCollection.toList(RFclassified_imageCollection.size());
print('RFclassified_imageCollectionlist',
RFclassified_imageCollectionlist);
Map.centerObject(Study_Area, 8);
Map.addLayer(ee.Image(RFclassified_imageCollectionlist.get(58)), class_vis
, 'classification0');
//////////////////////////////////////////////////////////////////////////////
```

```
// Calculate the area for each land cover class from all classification
images
// Plot a chart to show the time series for area changes in each class
//////////////////////////////////////////////////////////////////////////
var RFClassareas = RFclassified_imageCollectionlist.map(areaByClass);
print('RFClassareas', RFClassareas);
var chart = ui.Chart.feature.byFeature(RFClassareas)
  .setChartType('LineChart')
  .setOptions(({
    hAxis: {
      title: 'Date', titleTextStyle: {italic: false, bold: true}},
    vAxis: {
      title: 'Area of Classification (sq km)', titleTextStyle: {italic:
false, bold: true}
    },
    colors:['AB6106', 'A0A0A5', '071AC7', 'F7B83F', '146E04']
    }));
print(chart);
// This part of the code (how-to-automate-calculating-area) has been
modified after (Daniel Wiell, 2020)
// https://gis.stackexchange.com/users/154371/daniel-wiell?tab=profile
// https://code.earthengine.google.com/d20512d31f5d46d5d9302000ce86bc28
// https://gis.stackexchange.com/questions/361464/google-earth-engine-how-
to-automate-calculating-area-for-each-class-for-each-im/361486#361486
function areaByClass(image) {
  var classNames = ee.List(['Sand', 'Vegetation', 'Water', 'Urban',
'Rocky']);
  var groups = ee.Image.pixelArea().addBands(image)
    .reduceRegion({
      reducer: ee.Reducer.sum().group({
        groupField: 1, groupName: 'Class_id'}),
      geometry: Study_Area,
      scale: 10,
      bestEffort: true}).get('groups');
  var areaByClass = ee.Dictionary(
    ee.List(groups).map(function (AreaDic) {
    var AreaDic = ee.Dictionary(AreaDic)
      return [
        classNames.get(AreaDic.getNumber('Class_id')),
        AreaDic.getNumber('sum').divide(1e6) // square km
      ];
      }).flatten());
    return ee.Feature(null, areaByClass)
  }
//////////////////////////////////////////////////////////////////////////
// Create RGB visualization classification images to use as animation
frames
//////////////////////////////////////////////////////////////////////////
var rgbVis2 = RFclassified_imageCollection.map(function(RFclassified_image)
{
  return RFclassified_image.visualize(class_vis);
});
// Define GIF visualization parameters.
var gifParams2 = {
  'region': Study_Area,
  'dimensions': 300,
  'crs': 'EPSG:32636',
  'framesPerSecond': 1
};
// Print the GIF URL to the console.
print(rgbVis2.getVideoThumbURL(gifParams2));
```

```
// Render the GIF animation in the console.
// print(ui.Thumbnail(rgbVis, gifParams));
// Define arguments for the getFilmstripThumbURL function parameters.
var filmArgs = {
  dimensions: 128,
  region: Study_Area,
  crs: 'EPSG:32636'
  };
// Print a URL that will produce a filmstrip when accessed.
print(rgbVis2.getFilmstripThumbURL(filmArgs));
//////////////////////////////////////////////////////////////////////
//Train the RF classifier using the test samples and RF classified results
for accuracy validation
// Compute confusion matrix and kappa coefficient to assess the accuracy of
RF classifier
// and validate the classification results using the test samples
// This part of the code is written to validate the classified images
individually
//////////////////////////////////////////////////////////////////////
var RFvalidation_test_samples =
(ee.Image(RFclassified_imageCollectionlist.get(110))).sampleRegions({
  collection: testsamples,
  properties: ['landcover'],
  scale: 10
});
var RFvalidation_classifier =
ee.Classifier.smileRandomForest(100).train(RFvalidation_test_samples,
'landcover');
var RFvalidation_image =
(ee.Image(RFclassified_imageCollectionlist.get(110))).classify(RFvalidation
_classifier);
print('RF valdiation dataset', RFvalidation_test_samples);
var RFtestaccuracy =
RFvalidation_test_samples.errorMatrix('landcover','classification');
print('RFvalidation error matrix:', RFtestaccuracy);
print('RFvalidation overall accuracy:', RFtestaccuracy.accuracy());
//Export the RF confusion error matrix
var RFconfusionmatrix20211231 = ee.Feature(null,
{matrix:RFtestaccuracy.array()});
Export.table.toDrive({
  collection: ee.FeatureCollection(RFconfusionmatrix20211231),
  description: 'RFconfusionmatrix20211231',
  fileFormat: 'CSV'
});
// Compute the kappa coefficient for RF classification
var RFkappa = RFtestaccuracy.kappa();
print('RFkappa', RFkappa);
//////////////////////////////////////////////////////////////
// Export classification maps
//////////////////////////////////////////////////////////////
Export.image.toDrive({
  image: ee.Image(RFclassified_imageCollectionlist.get(57)),
  description: 'ClassifiedImage14072020',
  folder: 'GEE_Exports',
  region: Study_Area,
  scale: 10,
  maxPixels: 1e12
});
//////////////////////////////////////////////////////////////////////
// Export the training samples and test validation datasets
//////////////////////////////////////////////////////////////////////
```

```
Export.table.toDrive({
  collection: training_samples,
  description: 'training_samples',
  fileFormat: 'shp'
});
// Export the test samples and test validation data
Export.table.toDrive({
  collection: testsamples,
  description: 'testsamples',
  fileFormat: 'shp'
});
////////////////////////////////////////////////////////////////////////////
////////////////////////////////////////////////////////////////////////////
// Classification using the Support Vector Machine
////////////////////////////////////////////////////////////////////////////
////////////////////////////////////////////////////////////////////////////
function classification(image){
  var classification_training_samples =
image.select(bands).sampleRegions({collection:training_samples,
    properties: ['landcover'],
    scale: 10
});
var SVMtrained_classifier = ee.Classifier.libsvm({
    kernelType: 'LINEAR',
    gamma: null,
    cost: 0.2
}).train(classification_training_samples, 'landcover', bands);
var SVMclassified_image =
image.select(bands).classify(SVMtrained_classifier);
return SVMclassified_image;
}
var SVMclassified_imageCollection = SenImageCollection.map(classification);
print('SVMclassified_imageCollection', SVMclassified_imageCollection);
var SVMclassified_imageCollectionlist =
SVMclassified_imageCollection.toList(SVMclassified_imageCollection.size());
print('SVMclassified_imageCollectionlist',
SVMclassified_imageCollectionlist);
Map.centerObject(Study_Area, 8);
Map.addLayer(ee.Image(SVMclassified_imageCollectionlist.get(11)), class_vis
, 'classification11');
Map.addLayer(ee.Image(SVMclassified_imageCollectionlist.get(18)), class_vis
, 'classification18');
Map.addLayer(ee.Image(SVMclassified_imageCollectionlist.get(40)), class_vis
, 'classification40');
Map.addLayer(ee.Image(SVMclassified_imageCollectionlist.get(46)), class_vis
, 'classification46');
Map.addLayer(ee.Image(SVMclassified_imageCollectionlist.get(60)), class_vis
, 'classification60');
////////////////////////////////////////////////////////////////////////////
// Calculate the area for each land cover class from all classification
images
// The output here is a list table that contains the areas sum for each
class from all the classification images
// In addition to a line chart that shows the changes over time
////////////////////////////////////////////////////////////////////////////
function classAreaSum(SVMclassified_image){
var imagecalssesarea =
ee.Image.pixelArea().addBands(SVMclassified_image).reduceRegion({
  reducer:ee.Reducer.sum().group({
    groupField:1,
    groupName:'Class_id'}),
```

```
    geometry: Study_Area,
    scale: 10,
    bestEffort: true});
  return imagecalssesarea;
}
var Areaclassified_imagelist =
SVMclassified_imageCollectionlist.map(classAreaSum);
print('Area Table in sq.m', Areaclassified_imagelist);
// Plot a chart to show the time series of area changes in each class
var Classareas = SVMclassified_imageCollectionlist.map(areaByClass);
print('Classareas', Classareas);
var chart = ui.Chart.feature.byFeature(Classareas)
  .setChartType('LineChart')
  .setOptions(({
    hAxis: {
      title: 'Date', titleTextStyle: {italic: false, bold: true}},
    vAxis: {
      title: 'Area of Classification (sq km)', titleTextStyle: {italic:
false, bold: true}
    },
    colors:['AB6106', 'A0A0A5', '071AC7', 'F7B83F', '146E04']
    }));
print(chart);
function areaByClass(image) {
  var classNames = ee.List(['Sand', 'Vegetation', 'Water', 'Urban',
'Rocky']);
  var groups = ee.Image.pixelArea().addBands(image)
    .reduceRegion({
      reducer: ee.Reducer.sum().group({
        groupField: 1, groupName: 'Class_id'}),
      geometry: Study_Area,
      scale: 10,
      bestEffort: true}).get('groups');
  var areaByClass = ee.Dictionary(
    ee.List(groups).map(function (AreaDic) {
    var AreaDic = ee.Dictionary(AreaDic)
      return [
        classNames.get(AreaDic.getNumber('Class_id')),
        AreaDic.getNumber('sum').divide(1e6) // square km
      ];
      }).flatten());
    return ee.Feature(null, areaByClass)
  }
Export.table.toDrive({
  collection: Classareas,
  description: 'Classareas',
  fileFormat: 'CSV'
});
////////////////////////////////////////////////////////////
// Create RGB visualization images to use as animation frames
////////////////////////////////////////////////////////////
var rgbVis =
SVMclassified_imageCollection.map(function(SVMclassified_image) {
  return SVMclassified_image.visualize(class_vis);
});
// Define GIF visualization parameters.
var gifParams = {
  'region': Study_Area,
  'dimensions': 300,
  'crs': 'EPSG:32636',
  'framesPerSecond': 1
```

```
};
// Print the GIF URL to the console.
print(rgbVis.getVideoThumbURL(gifParams));
// Render the GIF animation in the console.
// print(ui.Thumbnail(rgbVis, gifParams));
// Define arguments for the getFilmstripThumbURL function parameters.
var filmArgs = {
  dimensions: 128,
  region: Study_Area,
  crs: 'EPSG:32636'
  };
// Print a URL that will produce a filmstrip when accessed.
print(rgbVis.getFilmstripThumbURL(filmArgs));
//////////////////////////////////////////////////////////
// Export.table.toDrive({
//   collection: AreasSumClassified,
//   description: 'AreasSumClassified',
//   fileFormat: 'CSV'
// });
//////////////////////////////////////////////////////////////////////////
// Compute confusion matrix and kappa coefficient to assess the accuracy of
SVM classifier
// and validate the SVM classification results using test samples
//////////////////////////////////////////////////////////////////////////
var SVMvalidation_test_samples =
(ee.Image(SVMclassified_imageCollectionlist.get(0))).sampleRegions({
  collection: testsamples,
  properties: ['landcover'],
  scale: 10
});
//Classify the test samples based on the SVM classified results to check
the classification accuracy
var SVMvalidation_classifier = ee.Classifier.libsvm({
    kernelType: 'LINEAR',
    gamma: null,
    cost: 0.2
}).train(SVMvalidation_test_samples, 'landcover');
var SVMvalidation_image =
(ee.Image(SVMclassified_imageCollectionlist.get(0))).classify(SVMvalidation
_classifier);
print('SVM validation dataset', SVMvalidation_test_samples);
var SVMtestaccuracy =
SVMvalidation_test_samples.errorMatrix('landcover','classification');
print('SVMvalidation error matrix:', SVMtestaccuracy);
print('SVMvalidation overall accuracy:', SVMtestaccuracy.accuracy());
//Export the SVM confusion error matrix
var SVMconfusionmatrix20211231 = ee.Feature(null,
{matrix:SVMtestaccuracy.array()});
Export.table.toDrive({
  collection: ee.FeatureCollection(SVMconfusionmatrix20211231),
  description: 'SVMconfusionmatrix20211231',
  fileFormat: 'CSV'
});
// Compute the kappa for the SVM classification
var SVMkappa = SVMtestaccuracy.kappa();
print('SVMkappa', SVMkappa);
//////////////////////////////////////////////////
// Calculate image differencing between two dates
//////////////////////////////////////////////////
var image1 = (ee.Image(listOfimages.get(19)).select(['B8']));
var image2 = (ee.Image(listOfimages.get(38)).select(['B8']));
```

```
var imageDiff = image1.subtract(image2);
print('imageDiff', imageDiff);
Map.addLayer(imageDiff, {min: 0, max: 3000});
////////////////////////////////////////////////////////////
// Export SVM classification maps
////////////////////////////////////////////////////////////
Export.image.toDrive({
  image: ee.Image(SVMclassified_imageCollectionlist.get(93)),
  description: 'SVMClassifiedImage10052021',
  folder: 'GEE_Exports',
  region: Study_Area,
  scale: 10,
  maxPixels: 1e12
});
// ////////////////////////////////////////////////////////////
// // Export image differencing maps
////////////////////////////////////////////////////////////
Export.image.toDrive({
  image: imageDiff,
  description: 'ImageDiff10072019_15022019',
  folder: 'GEE_Exports',
  region: Study_Area,
  scale: 10,
  maxPixels: 1e12
});
////////////////////////////////////////////////////
// // Export an image from the image collection
////////////////////////////////////////////////////
Export.image.toDrive({
  image: (ee.Image(listOfimages.get(56)).select(['B8','B4','B3','B2'])),
  description: 'Image09072020',
  folder: 'GEE_Exports',
  region: Study_Area,
  scale: 10,
  maxPixels: 1e12
});
////////////////////////////////////////////////////////////////////////////
// Create RGB visualization for the image collection
////////////////////////////////////////////////////////////////////////////
var rgbVis3 = SenImageCollection.map(function(image){
    return image.visualize(class_vis);
});
// Define GIF visualization parameters.
var gifParams3 = {
  'region': Study_Area,
  'dimensions': 300,
  'crs': 'EPSG:32636',
  'framesPerSecond': 1
};
// Print the GIF URL to the console.
// print(rgbVis3.getVideoThumbURL(gifParams3));
// Render the GIF animation in the console.
print(ui.Thumbnail(rgbVis3, gifParams3));
// Define arguments for the getFilmstripThumbURL function parameters.
var filmArgs = {
  dimensions: 128,
  region: Study_Area,
  crs: 'EPSG:32636'
  };
// // Print a URL that will produce a filmstrip when accessed.
// print(rgbVis3.getFilmstripThumbURL(filmArgs));
```

REFERENCES

ABDELAZIZ BOUTEFLIKA, CHERIF RAHMANI, CRISTINA NARBONA, JACQUES DIOUF, HAMA ARBA DIALLO & MUTEPFA, F. 2016. deserts and Drylands. Our Planet, The magazine of the United Nations Environment Programme (UNEP), 17 No 1.

ABDELRAHIM ELHAG, D. ZOMRAWI, N. & KHIDIR, S. 2019. Analysis of Sand Dunes Accumulation using Remote Sensing and GIS.

ABOU EL-MAGD, I. HASSAN, O. & ARAFAT, S. 2013. Quantification of sand dune movements in the south western part of Egypt, using remotely sensed data and GIS. Journal of Geographic Information System, 2013.

ABUZIED, H. 2009. Mapping and assessment of wind erosion in central Northern State, Sudan. Unpublished PhD thesis, Desertification and Desert Cultivation Studies Institute, University of Khartoum.

AFRASINEI, G. M. MELIS, M. T. ARRAS, C. PISTIS, M. BUTTAU, C. & GHIGLIERI, G. 2018. Spatiotemporal and spectral analysis of sand encroachment dynamics in southern Tunisia. European Journal of Remote Sensing, 51**,** 352-374.

AGENCY, E. National LIDAR Programme [Online]. Environment Agency. Available: https://data.gov.uk/dataset/f0db0249-f17b-4036-9e65-309148c97ce4/national-lidar-programme [Accessed 17 August 2021].

AGHABABAEIAN, H. OSTADTAGHIZADEH, A. ARDALAN, A. ASGARY, A. AKBARY, M. YEKANINEJAD, M. S. & STEPHENS, C. 2021. Global health impacts of dust storms: A systematic review. Environmental Health Insights, 15**,** 11786302211018390.

AGNECY, E. LIDAR Ground Truth Surveys [Online]. Environment Agnecy. Available: https://environment.data.gov.uk/dataset/16b4d492-0c0d-410b-9732-65eebcc3d9f9 [Accessed 17 August 2021].

AHMADY-BIRGANI, H. MCQUEEN, K. G. MOEINADDINI, M. & NASERI, H. 2017. Sand dune encroachment and desertification processes of the Rigboland Sand Sea, Central Iran. Scientific reports, 7**,** 1-10.

AL-GHAMDI, K. & HERMAS, E. 2015. Assessment of dune migration hazards against landuse northwest Al-lith City, Saudi Arabia, using multi-temporal satellite imagery. Arabian Journal of Geosciences, 8**,** 11007-11018.

AL-MUTIRY, M. HERMAS, E. AL-GHAMDI, K. & AL-AWAJI, H. 2016. Estimation of dune migration rates north Riyadh City, KSA, using SPOT 4 panchromatic images. Journal of African Earth Sciences, 124**,** 258-269.

ALBALAWI, E. K. & KUMAR, L. 2013. Using remote sensing technology to detect, model and map desertification: A review. Journal of Food, Agriculture & Environment, 11**,** 791-797.

ALBARAKAT, R. & LAKSHMI, V. 2019. Monitoring dust storms in Iraq using satellite data. Sensors, 19**,** 3687.

ALGHAMDI, A. A. & AL-KAHTANI, N. S. 2005. Sand control measures and sand drift fences. Journal of performance of constructed facilities, 19**,** 295-299.

AMANI, M. KAKOOEI, M. MOGHIMI, A. GHORBANIAN, A. RANJGAR, B. MAHDAVI, S. DAVIDSON, A. FISETTE, T. ROLLIN, P. & BRISCO, B. 2020. Application of google earth engine cloud computing platform, sentinel imagery, and neural networks for crop mapping in canada. Remote Sensing, 12**,** 3561.

ARÉVALO, P. BULLOCK, E. L. WOODCOCK, C. E. & OLOFSSON, P. 2020. A suite of tools for continuous land change monitoring in google earth engine. Front. Clim, 2**,** 576740.

AVOUAC, J.-P. AYOUB, F. LEPRINCE, S. KONCA, O. & HELMBERGER, D. V. 2006. The 2005, Mw 7.6 Kashmir earthquake: Sub-pixel correlation of ASTER images and seismic waveforms analysis. Earth and Planetary Science Letters, 249**,** 514-528.

AYDDA, A. ALTHUWAYNEE, O. & POKHAREL, B. An easy method for barchan dunes automatic extraction from multispectral satellite data. IOP Conference Series: Earth and Environmental Science, 2020. IOP Publishing, 012015.

AYOUB, F. AVOUAC, J.-P. NEWMAN, C. RICHARDSON, M. LUCAS, A. LEPRINCE, S. & BRIDGES, N. 2014. Threshold for sand mobility on Mars calibrated from seasonal variations of sand flux. Nature communications, 5**,** 1-8.

AYOUB, F. LEPRINCE, S. & AVOUAC, J.-P. 2017. User's guide to COSI-CORR co-registration of optically sensed images and correlation. California Institute of Technology: Pasadena, CA, USA.
BAAS, A. C. 2004. Evaluation of saltation flux impact responders (Safires) for measuring instantaneous aeolian sand transport intensity. Geomorphology, 59**,** 99-118.
BADDOCK, M. C. NIELD, J. M. & WIGGS, G. F. 2018. Early-stage aeolian protodunes: Bedform development and sand transport dynamics. Earth Surface Processes and Landforms, 43**,** 339-346.
BAGNOLD, R. A. 1941. The physics of blown sand and desert dunes, Great Britain, METHUEN & CO. LTD. LONDON.
BAIRD, T. BRISTOW, C. & VERMEESCH, P. 2019. Measuring Sand Dune Migration Rates with COSI-Corr and Landsat: Opportunities and Challenges. Remote Sensing, 11**,** 2423.
BAITIS, E. KOCUREK, G. SMITH, V. MOHRIG, D. EWING, R. C. & PEYRET, A.-P. 2014. Definition and origin of the dune-field pattern at White Sands, New Mexico. Aeolian Research, 15**,** 269-287.
BALZTER, H. 2001. Forest mapping and monitoring with interferometric synthetic aperture radar (InSAR). Progress in physical geography, 25**,** 159-177.
BALZTER, H. ROWLAND, C. S. & SAICH, P. 2007. Forest canopy height and carbon estimation at Monks Wood National Nature Reserve, UK, using dual-wavelength SAR interferometry. Remote Sensing of Environment, 108**,** 224-239.
BARBARELLA, M. FIANI, M. & ZOLLO, C. 2017. Assessment of DEM derived from very high-resolution stereo satellite imagery for geomorphometric analysis. European Journal of Remote Sensing, 50**,** 534-549.
BELGIU, M. & DRĂGUŢ, L. 2016. Random forest in remote sensing: A review of applications and future directions. ISPRS journal of photogrammetry and remote sensing, 114**,** 24-31.
BERTE, C. J. 2010. Fighting sand encroachment: lessons from Mauritania, Food and Agriculture Organization of the United Nations (FAO).
BLUMBERG, D. G. 1998. Remote sensing of desert dune forms by polarimetric synthetic aperture radar (SAR). Remote Sensing of Environment, 65**,** 204-216.
BOLOORANI, A. D. NABAVI, S. O. BAHRAMI, H. A. MIRZAPOUR, F. KAVOSI, M. ABASI, E. & AZIZI, R. 2014. Investigation of dust storms entering Western Iran using remotely sensed data and synoptic analysis. Journal of Environmental Health Science and Engineering, 12**,** 1-12.
BRAUN, A. 2021. Retrieval of digital elevation models from Sentinel-1 radar data–open applications, techniques, and limitations. Open Geosciences, 13**,** 532-569.
BREIMAN, L. 2001. Random forests. Machine learning, 45**,** 5-32.
BRIDGES, N. AYOUB, F. AVOUAC, J. LEPRINCE, S. LUCAS, A. & MATTSON, S. 2012. Earth-like sand fluxes on Mars. Nature, 485**,** 339.
BRITTON, B. 2016. Climate change could render Sudan 'uninhabitable' [Online]. CNN. Available: https://edition.cnn.com/2016/12/07/africa/sudan-climate-change/index.html [Accessed 08.03 2022].
BUTT, M. J. & MASHAT, A. S. 2018. MODIS satellite data evaluation for sand and dust storm monitoring in Saudi Arabia. International Journal of Remote Sensing, 39**,** 8627-8645.
C3S, C. C. C. S. 2017. ERA5: Fifth generation of ECMWF atmospheric reanalyses of the global climate. Copernicus Climate Change Service Climate Data Store (CDS).
CAI, J. WANG, C. MAO, X. & WANG, Q. 2017. An adaptive offset tracking method with SAR images for landslide displacement monitoring. Remote Sensing, 9**,** 830.
CASU, F. MANCONI, A. PEPE, A. & LANARI, R. 2011. Deformation time-series generation in areas characterized by large displacement dynamics: The SAR amplitude pixel-offset SBAS technique. IEEE Transactions on Geoscience and Remote Sensing, 49**,** 2752-2763.
CAUDLE, T. L. PAINE, J. G. ANDREWS, J. R. & SAYLAM, K. 2019. Beach, Dune, and Nearshore Analysis of Southern Texas Gulf Coast Using Chiroptera LIDAR and Imaging System. Journal of Coastal Research, 35**,** 251-268.

CHANG, X. GUO, J. & WANG, X. 2011. Detecting the amount of eroded and deposited sand using DInSAR. Terr. Atmos. Ocean. Sci. 22, 187, 194.
CHANG, Y. HOU, K. LI, X. ZHANG, Y. & CHEN, P. Review of land use and land cover change research progress. IOP Conference Series: Earth and Environmental Science, 2018. IOP Publishing, 012087.
CHEN, S. EUGENE, M. & ALAN, G. 2017. UAV Data for Coastal Dune Mapping. "Environmental Engineering" 10th International Conference Vilnius Gediminas Technical University.
CHEN, Y. ZHANG, G. DING, X. & LI, Z. 2000. Monitoring earth surface deformations with InSAR technology: principles and some critical issues. Journal of Geospatial Engineering, 2**,** 3-22.
CORBÍ, H. RIQUELME, A. MEGÍAS-BAÑOS, C. & ABELLAN, A. 2018. 3-D morphological change analysis of a beach with seagrass berm using a terrestrial laser scanner. ISPRS International Journal of Geo-Information, 7**,** 234.
COURRECH DU PONT, S. NARTEAU, C. & GAO, X. 2014. Two modes for dune orientation. Geology, 42**,** 743-746.
DAVIDSON-ARNOTT, R. BAUER, B. WALKER, I. HESP, P. OLLERHEAD, J. & DELGADO-FERNANDEZ, I. 2009. Instantaneous and mean aeolian sediment transport rate on beaches: an intercomparison of measurements from two sensor types. Journal of Coastal Research**,** 297-301.
DEE, D. P. UPPALA, S. M. SIMMONS, A. BERRISFORD, P. POLI, P. KOBAYASHI, S. ANDRAE, U. BALMASEDA, M. BALSAMO, G. & BAUER, D. P. 2011. The ERA-Interim reanalysis: Configuration and performance of the data assimilation system. Quarterly Journal of the royal meteorological society, 137**,** 553-597.
DEL VALLE, H. F. ROSTAGNO, C. M. CORONATO, F. R. BOUZA, P. J. & BLANCO, P. D. 2008. Sand dune activity in north-eastern Patagonia. Journal of Arid Environments, 72**,** 411-422.
DELGADO BLASCO, J. M. CHINI, M. VERSTRAETEN, G. & HANSSEN, R. F. 2020. Sand dune dynamics exploiting a fully automatic method using satellite SAR data. Remote Sensing, 12**,** 3993.
DEUTSCHER, J. PERKO, R. GUTJAHR, K. HIRSCHMUGL, M. & SCHARDT, M. 2013. Mapping tropical rainforest canopy disturbances in 3D by COSMO-SkyMed spotlight InSAR-stereo data to detect areas of forest degradation. Remote sensing, 5**,** 648-663.
DISSANAYAKE, P. BROWN, J. & KARUNARATHNA, H. 2015. Impacts of storm chronology on the morphological changes of the Formby beach and dune system, UK. Natural Hazards and Earth System Sciences, 15**,** 1533-1543.
DONG, P. 2015. Automated measurement of sand dune migration using multi-temporal lidar data and GIS. International Journal of Remote Sensing, 36**,** 5426-5447.
DONG, P. XIA, J. ZHONG, R. ZHAO, Z. & TAN, S. 2021. A New Method for Automated Measurement of Sand Dune Migration Based on Multi-Temporal LiDAR-Derived Digital Elevation Models. Remote Sensing, 13**,** 3084.
DORNBUSCH, U. 2010. Ground survey methods for mixed sand and gravel beaches in intertidal environments: a comparison. Journal of Coastal Research, 26**,** 451-464.
DURÁN, O. & HERRMANN, H. J. 2006. Vegetation against dune mobility. Physical review letters, 97**,** 188001.
DURÁN, O. & MOORE, L. J. 2013. Vegetation controls on the maximum size of coastal dunes. Proceedings of the National Academy of Sciences, 110**,** 17217-17222.
DURÁN, O. SCHWÄMMLE, V. LIND, P. G. & HERRMANN, H. J. 2011. Size distribution and structure of Barchan dune fields. Nonlinear Processes in Geophysics, 18**,** 455-467.
ED CHAVES, M. CA PICOLI, M. & D SANCHES, I. 2020. Recent applications of Landsat 8/OLI and Sentinel-2/MSI for land use and land cover mapping: A systematic review. Remote Sensing, 12**,** 3062.
EL-ASKARY, H. KAFATOS, M. & HEGAZY, M. Environmental monitoring of dust storms over the Nile Delta, Egypt using MODIS satellite data. Proceedings Of Third International Symposium Remote Sensing of Urban Areas, Istanbul, Turkey, 2002. 452.

EL-HADIDY, S. M. 2020. Monitoring shoreline changes and aeolian sand encroachment, Nasser Lake, Egypt, using remote sensing and GIS techniques. Arabian Journal of Geosciences, 13**,** 1-14.
EL-OSSTA, E. QAHWAJI, R. & IPSON, S. S. 2013. Detection of dust storms using MODIS reflective and emissive bands. IEEE Journal of Selected Topics in Applied Earth Observations and Remote Sensing, 6**,** 2480-2485.
EL HAJJ, M. BÉGUÉ, A. GUILLAUME, S. & MARTINÉ, J.-F. 2009. Integrating SPOT-5 time series, crop growth modeling and expert knowledge for monitoring agricultural practices—The case of sugarcane harvest on Reunion Island. Remote Sensing of Environment, 113**,** 2052-2061.
EL MOGHRABY, A. I. ALI, O. & EL SEED, M. T. 1987. Desertification in western Sudan and strategies for rehabilitation. Environmental conservation, 14**,** 227-231.
ELJACK, E. CSAPLOVICS, E. & ADAM, H. September 14-16, 2010. Mapping and assessment of sand encroachment on the Nile River northern Sudan, by means of remote Sensing and GIS. Conference on International Research on Food Security, Natural Resource Management and Rural Development. ETH Zurich, 2010.
ELLIS, J. T. MORRISON, R. F. & PRIEST, B. H. 2009. Detecting impacts of sand grains with a microphone system in field conditions. Geomorphology, 105**,** 87-94.
ELS, A. 2017. Tracking sand dune movements using multi-temporal remote sensing imagery: a case study of central Sahara (Libyan Fazzan/Ubari Sand Sea). University of the Witwatersrand.
ENGEL, M. MAY, S. M. SCHEFFERS, A. SQUIRE, P. PINT, A. KELLETAT, D. & BRÜCKNER, H. 2015. Prograded foredunes of Western Australia's macro-tidal coast – implications for Holocene sea-level change and high-energy wave impacts. Earth Surface Processes and Landforms, 40**,** 726-740.
ESTEVES, L. S. BROWN, J. M. WILLIAMS, J. J. & LYMBERY, G. 2012. Quantifying thresholds for significant dune erosion along the Sefton Coast, Northwest England. Geomorphology, 143**,** 52-61.
ETTRITCH, G. BUNTING, P. JONES, G. & HARDY, A. 2018. Monitoring the coastal zone using earth observation: application of linear spectral unmixing to coastal dune systems in Wales. Remote Sensing in Ecology and Conservation, 4**,** 303-319.
FALLOURD, R. HARANT, O. TROUVÉ, E. NICOLAS, J.-M. GAY, M. WALPERSDORF, A. MUGNIER, J.-L. SERAFINI, J. ROSU, D. & BOMBRUN, L. 2011. Monitoring temperate glacier displacement by multi-temporal TerraSAR-X images and continuous GPS measurements. IEEE Journal of Selected Topics in Applied Earth Observations and Remote Sensing, 4**,** 372-386.
FAN, H. DENG, K. JU, C. ZHU, C. & XUE, J. 2011. Land subsidence monitoring by D-InSAR technique. Mining Science and Technology (China), 21**,** 869-872.
FENG, X. QU, J. FAN, Q. TAN, L. & AN, Z. 2019. Characteristics of Desertification and Short-Term Effectiveness of Differing Treatments on Shifting Sand Dune Stabilization in an Alpine Rangeland. International journal of environmental research and public health, 16**,** 4968.
FERNANDEZ-CASCALES, L. LUCAS, A. RODRIGUEZ, S. GAO, X. SPIGA, A. & NARTEAU, C. 2018. First quantification of relationship between dune orientation and sediment availability, Olympia Undae, Mars. Earth and Planetary Science Letters, 489**,** 241-250.
FERRETTI, A. MONTI-GUARNIERI, A. PRATI, C. & ROCCA, F. 2007. InSAR processing: a practical approach. InSAR Principles: Guidelines for SAR Interferometry Processing and Interpretation, ser. ESA TM. ESA.
FRATI, G. LAUNEAU, P. ROBIN, M. GIRAUD, M. JUIGNER, M. DEBAINE, F. & MICHON, C. 2021. Coastal Sand Dunes Monitoring by Low Vegetation Cover Classification and Digital Elevation Model Improvement Using Synchronized Hyperspectral and Full-Waveform LiDAR Remote Sensing. Remote Sensing, 13**,** 29.
GALLAY, M. 2013. Direct acquisition of data: airborne laser scanning. Geomorphological Techniques. British Society for Geomorphology.

GAO, X. NARTEAU, C. & ROZIER, O. 2015a. Development and steady states of transverse dunes: A numerical analysis of dune pattern coarsening and giant dunes. Journal of Geophysical Research: Earth Surface, 120**,** 2200-2219.
GAO, X. NARTEAU, C. ROZIER, O. & DU PONT, S. C. 2015b. Phase diagrams of dune shape and orientation depending on sand availability. Scientific reports, 5**,** 1-12.
GENZANO, N. PERGOLA, N. & MARCHESE, F. 2020. A Google Earth Engine tool to investigate, map and monitor volcanic thermal anomalies at global scale by means of mid-high spatial resolution satellite data. Remote Sensing, 12**,** 3232.
GHADIRY, M. SHALABY, A. & KOCH, B. 2012. A new GIS-based model for automated extraction of Sand Dune encroachment case study: Dakhla Oases, western desert of Egypt. The Egyptian Journal of Remote Sensing and Space Science, 15**,** 53-65.
GOMES, V. C. QUEIROZ, G. R. & FERREIRA, K. R. 2020. An overview of platforms for big earth observation data management and analysis. Remote Sensing, 12**,** 1253.
GÓMEZ-CHOVA, L. TUIA, D. MOSER, G. & CAMPS-VALLS, G. 2015. Multimodal classification of remote sensing images: A review and future directions. Proceedings of the IEEE, 103**,** 1560-1584.
GÓMEZ, D. SALVADOR, P. SANZ, J. CASANOVA, C. & CASANOVA, J. 2018. Detecting Areas Vulnerable to Sand Encroachment Using Remote Sensing and GIS Techniques in Nouakchott, Mauritania. Remote Sensing, 10**,** 1541.
GOOSSENS, D. OFFER, Z. & LONDON, G. 2000. Wind tunnel and field calibration of five aeolian sand traps. Geomorphology, 35**,** 233-252.
GORELICK, N. HANCHER, M. DIXON, M. ILYUSHCHENKO, S. THAU, D. & MOORE, R. 2017. Google Earth Engine: Planetary-scale geospatial analysis for everyone. Remote sensing of Environment, 202**,** 18-27.
GOUDIE, A. & SEELY, M. 2011. World heritage desert landscapes: potential priorities for the recognition of desert landscapes and geomorphological sites on the World Heritage List. Gland: International Union for Conservation of Nature (IUCN).
GRESSWELL, R. K. 1937. The geomorphology of the south-west Lancashire coast-line. The Geographical Journal, 90**,** 335-349.
GRÜNTHAL, E. GRUNO, A. & ELLMANN, A. Monitoring of coastal processes by using airborne laser scanning data. Environmental Engineering. Proceedings of the International Conference on Environmental Engineering. ICEE, 2014. Vilnius Gediminas Technical University, Department of Construction Economics …, 1.
HADEEL, A. JABBAR, M. T. & CHEN, X. 2010. Application of remote sensing and GIS in the study of environmental sensitivity to desertification: a case study in Basrah Province, southern part of Iraq. Applied Geomatics, 2**,** 101-112.
HAVIVI, S. AMIR, D. SCHVARTZMAN, I. AUGUST, Y. MAMAN, S. ROTMAN, S. R. & BLUMBERG, D. G. 2018. Mapping dune dynamics by InSAR coherence. Earth Surface Processes and Landforms, 43**,** 1229-1240.
HAYES, D. J. & SADER, S. A. 2001. Comparison of change-detection techniques for monitoring tropical forest clearing and vegetation regrowth in a time series. Photogrammetric engineering and remote sensing, 67**,** 1067-1075.
HERMAS, E. LEPRINCE, S. & EL-MAGD, I. A. 2012. Retrieving sand dune movements using sub-pixel correlation of multi-temporal optical remote sensing imagery, northwest Sinai Peninsula, Egypt. Remote sensing of environment, 121**,** 51-60.
HERSEN, P. 2005. Flow effects on the morphology and dynamics of aeolian and subaqueous barchan dunes. Journal of Geophysical Research: Earth Surface, 110.
HERTLING, U. & LUBKE, R. 1999. Use of Ammophila arenaria for dune stabilization in South Africa and its current distribution—perceptions and problems. Environmental Management, 24**,** 467-482.
HERVÁS, J. BARREDO, J. I. ROSIN, P. L. PASUTO, A. MANTOVANI, F. & SILVANO, S. 2003. Monitoring landslides from optical remotely sensed imagery: the case history of Tessina landslide, Italy. Geomorphology, 54**,** 63-75.
HIGGINBOTTOM, T. P. & SYMEONAKIS, E. 2014. Assessing land degradation and desertification using vegetation index data: Current frameworks and future directions. Remote Sensing, 6**,** 9552-9575.

HILTON, M. NICKLING, B. WAKES, S. SHERMAN, D. KONLECHNER, T. JERMY, M. & GEOGHEGAN, P. 2017. An efficient, self-orienting, vertical-array, sand trap. Aeolian Research, 25**,** 11-21.
HOFFMANN, L. GÜNTHER, G. LI, D. STEIN, O. WU, X. GRIESSBACH, S. HENG, Y. KONOPKA, P. MÜLLER, R. & VOGEL, B. 2019. From ERA-Interim to ERA5: the considerable impact of ECMWF's next-generation reanalysis on Lagrangian transport simulations. Atmospheric Chemistry and Physics, 19**,** 3097-3124.
HOUBORG, R. FISHER, J. B. & SKIDMORE, A. K. 2015. Advances in remote sensing of vegetation function and traits. Elsevier.
HU, Z. GAO, X. LEI, J. & ZHOU, N. 2021. Geomorphology of aeolian dunes in the western Sahara Desert. Geomorphology, 392**,** 107916.
HUANG, C. DAVIS, L. & TOWNSHEND, J. 2002. An assessment of support vector machines for land cover classification. International Journal of remote sensing, 23**,** 725-749.
HUANG, H. CHEN, Y. CLINTON, N. WANG, J. WANG, X. LIU, C. GONG, P. YANG, J. BAI, Y. & ZHENG, Y. 2017. Mapping major land cover dynamics in Beijing using all Landsat images in Google Earth Engine. Remote Sensing of Environment, 202**,** 166-176.
HUGENHOLTZ, C. H. LEVIN, N. BARCHYN, T. E. & BADDOCK, M. C. 2012. Remote sensing and spatial analysis of aeolian sand dunes: A review and outlook. Earth-science reviews, 111**,** 319-334.
HUGGETT, R. 2007. Fundamentals of geomorphology, Routledge.
HUNTER, R. E. RICHMOND, B. M. & RHO ALPHA, T. 1983. Storm-controlled oblique dunes of the Oregon coast. Geological Society of America Bulletin, 94**,** 1450-1465.
ISHIHARA, M. & TADONO, T. 2017. Land cover changes induced by the great east Japan earthquake in 2011. Scientific reports, 7**,** 1-7.
JABOYEDOFF, M. OPPIKOFER, T. ABELLÁN, A. DERRON, M.-H. LOYE, A. METZGER, R. & PEDRAZZINI, A. 2012. Use of LIDAR in landslide investigations: a review. Natural hazards, 61**,** 5-28.
JACKSON, D. 1996. A new, instantaneous aeolian sand trap design for field use. Sedimentology, 43**,** 791-796.
JOHANSEN, K. PHINN, S. & TAYLOR, M. 2015. Mapping woody vegetation clearing in Queensland, Australia from Landsat imagery using the Google Earth Engine. Remote Sensing Applications: Society and Environment, 1**,** 36-49.
JUHA HYYPPÄ, W. W. MARKUS HOLLAUS & HANNU HYYPPÄ 2009. Airborne Laser Scanning. The SAGE handbook of remote sensing. Sage Publications.
JULGE, K. EELSALU, M. GRÜNTHAL, E. TALVIK, S. ELLMANN, A. SOOMERE, T. & TÕNISSON, H. Combining airborne and terrestrial laser scanning to monitor coastal processes. 2014 IEEE/OES Baltic International Symposium (BALTIC), 2014. IEEE, 1-10.
KADAVI, P. R. & LEE, C.-W. 2018. Land cover classification analysis of volcanic island in Aleutian Arc using an artificial neural network (ANN) and a support vector machine (SVM) from Landsat imagery. Geosciences Journal, 22**,** 653-665.
KARAKANI, E. G. MALEKIAN, A. GHOLAMI, S. & LIU, J. 2021. Spatiotemporal monitoring and change detection of vegetation cover for drought management in the Middle East. Theoretical and Applied Climatology, 144**,** 299-315.
KARUNARATHNA, H. BROWN, J. CHATZIRODOU, A. DISSANAYAKE, P. & WISSE, P. 2018. Multi-timescale morphological modelling of a dune-fronted sandy beach. Coastal Engineering, 136**,** 161-171.
KHAN, R. & GILANI, H. 2021. Global drought monitoring with big geospatial datasets using Google Earth Engine. Environmental Science and Pollution Research, 28**,** 17244-17264.
KHARAZMI, R. TAVILI, A. RAHDARI, M. R. CHABAN, L. PANIDI, E. & RODRIGO-COMINO, J. 2018. Monitoring and assessment of seasonal land cover changes using remote sensing: a 30-year (1987–2016) case study of Hamoun Wetland, Iran. Environmental monitoring and assessment, 190**,** 1-23.

KIM, J.-W. LU, Z. LEE, H. SHUM, C. SWARZENSKI, C. M. DOYLE, T. W. & BAEK, S.-H. 2009. Integrated analysis of PALSAR/Radarsat-1 InSAR and ENVISAT altimeter data for mapping of absolute water level changes in Louisiana wetlands. Remote Sensing of Environment, 113**,** 2356-2365.
KIM, J. DORJSUREN, M. CHOI, Y. & PUREVJAV, G. 2020. Reconstructed aeolian surface erosion in southern Mongolia by multi-temporal InSAR phase coherence analyses. Frontiers in Earth Science**,** 458.
KING, E. CONLEY, D. MASSELINK, G. LEONARDI, N. MCCARROLL, R. & SCOTT, T. 2019. The impact of waves and tides on residual sand transport on a sediment-poor, energetic, and macrotidal continental shelf. Journal of Geophysical Research: Oceans, 124**,** 4974-5002.
KLEMAS, V. 2015. Remote sensing of floods and flood-prone areas: an overview. Journal of Coastal Research, 31**,** 1005-1013.
KOJA, S. F. 2012. Sand dune movement and its impact on human activities in the North Western coast region of Libya. An analysis of the sediment characteristics of sand dunes, and their movement using satellite images, and the effects of encroachment on farms assessed by a questionnaire survey. University of Bradford.
KOK, J. F. PARTELI, E. J. MICHAELS, T. I. & KARAM, D. B. 2012. The physics of wind-blown sand and dust. Reports on progress in Physics, 75**,** 106901.
KOREN, I. KAUFMAN, Y. J. WASHINGTON, R. TODD, M. C. RUDICH, Y. MARTINS, J. V. & ROSENFELD, D. 2006. The Bodélé depression: a single spot in the Sahara that provides most of the mineral dust to the Amazon forest. Environmental Research Letters, 1**,** 014005.
KRAUS, K. & PFEIFER, N. 1998. Determination of terrain models in wooded areas with airborne laser scanner data. ISPRS Journal of Photogrammetry and remote Sensing, 53**,** 193-203.
ŁABUZ, T. A. 2016. A review of field methods to survey coastal dunes—experience based on research from South Baltic coast. Journal of Coastal Conservation, 20**,** 175-190.
LAM, D. K. REMMEL, T. K. & DREZNER, T. D. 2011. Tracking desertification in California using remote sensing: A sand dune encroachment approach. Remote Sensing, 3**,** 1-13.
LAN, P. T. SON, T. S. GUNASEKARA, K. NHAN, N. T. & HIEN, L. P. 2013. Application of Remote Sensing and GIS technology for monitoring coastal changes in estuary area of the Red river system, Vietnam. Journal of the Korean Society of Surveying, Geodesy, Photogrammetry and Cartography, 31**,** 529-538.
LANCASTER, N. 1995. Geomorphology of desert dunes, Routledge.
LANDIS, J. R. & KOCH, G. G. 1977. The measurement of observer agreement for categorical data. biometrics**,** 159-174.
LANGNER, A. MIETTINEN, J. & SIEGERT, F. 2007. Land cover change 2002–2005 in Borneo and the role of fire derived from MODIS imagery. Global Change Biology, 13**,** 2329-2340.
LATIF, M. A. A. & ELHAG, M. M. 2015. Combating Desertification in Sudan. In: EFE, P. D. R. (ed.) Environment and Ecology at the Beginning of 21st Century. First ed.: ST. KLIMENT OHRIDSKI UNIVERSITY PRESS.
LE MAUFF, B. JUIGNER, M. BA, A. ROBIN, M. LAUNEAU, P. & FATTAL, P. 2018. Coastal monitoring solutions of the geomorphological response of beach-dune systems using multi-temporal LiDAR datasets (Vendée coast, France). Geomorphology, 304**,** 121-140.
LEENDERS, J. VAN BOXEL, J. & STERK, G. 2005. Wind forces and related saltation transport. Geomorphology, 71**,** 357-372.
LEPRINCE, S. BARBOT, S. AYOUB, F. & AVOUAC, J.-P. 2007. Automatic and precise orthorectification, coregistration, and subpixel correlation of satellite images, application to ground deformation measurements. IEEE Transactions on Geoscience and Remote Sensing, 45**,** 1529-1558.
LEPRINCE, S. BERTHIER, E. AYOUB, F. DELACOURT, C. & AVOUAC, J. P. 2008. Monitoring earth surface dynamics with optical imagery. Eos, Transactions American Geophysical Union, 89**,** 1-2.

LEVIN, N. & BEN-DOR, E. 2004. Monitoring sand dune stabilization along the coastal dunes of Ashdod-Nizanim, Israel, 1945–1999. Journal of arid Environments, 58**,** 335-355.
LI, X. GE, L. DONG, Y. & CHANG, H.-C. Estimating the greatest dust storm in eastern Australia with MODIS satellite images. 2010 IEEE International Geoscience and Remote Sensing Symposium, 2010. IEEE, 1039-1042.
LILLESAND, T. KIEFER, R. W. & CHIPMAN, J. 2015. Remote sensing and image interpretation, John Wiley & Sons.
LIN, L. HAO, Z. POST, C. J. MIKHAILOVA, E. A. YU, K. YANG, L. & LIU, J. 2020. Monitoring land cover change on a rapidly urbanizing island using google earth engine. Applied Sciences, 10**,** 7336.
LIU, B. & COULTHARD, T. J. 2015. Mapping the interactions between rivers and sand dunes: implications for fluvial and aeolian geomorphology. Geomorphology, 231**,** 246-257.
LIU, C.-C. SHIEH, M.-C. KE, M.-S. & WANG, K.-H. 2018. Flood prevention and emergency response system powered by google earth engine. Remote sensing, 10**,** 1283.
LIVINGSTONE, I. WIGGS, G. F. & WEAVER, C. M. 2007. Geomorphology of desert sand dunes: A review of recent progress. Earth-science reviews, 80**,** 239-257.
LOUIS, J. DEBAECKER, V. PFLUG, B. MAIN-KNORN, M. BIENIARZ, J. MUELLER-WILM, U. CADAU, E. & GASCON, F. Sentinel-2 Sen2Cor: L2A processor for users. Proceedings Living Planet Symposium 2016, 2016. Spacebooks Online, 1-8.
LU, D. MAUSEL, P. BRONDIZIO, E. & MORAN, E. 2004. Change detection techniques. International journal of remote sensing, 25**,** 2365-2401.
LU, D. & WENG, Q. 2007. A survey of image classification methods and techniques for improving classification performance. International journal of Remote sensing, 28**,** 823-870.
LÜ, P. NARTEAU, C. DONG, Z. ROZIER, O. & COURRECH DU PONT, S. 2017. Unravelling raked linear dunes to explain the coexistence of bedforms in complex dunefields. Nature communications, 8**,** 1-9.
LUBKE, R. & HERTLING, U. 2001. The role of European marram grass in dune stabilization and succession near Cape Agulhas, South Africa. Journal of Coastal Conservation, 7**,** 171-182.
LUCAS, A. RODRIGUEZ, S. NARTEAU, C. CHARNAY, B. DU PONT, S. C. TOKANO, T. GARCIA, A. THIRIET, M. HAYES, A. G. & LORENZ, R. D. 2014. Growth mechanisms and dune orientation on Titan. Geophysical Research Letters, 41**,** 6093-6100.
LUIJENDIJK, A. HAGENAARS, G. RANASINGHE, R. BAART, F. DONCHYTS, G. & AARNINKHOF, S. 2018. The state of the world's beaches. Scientific reports, 8**,** 1-11.
LYMBERY, G. WISSE, P. & NEWTON, M. 2007. Report on coastal erosion predictions for Formby Point, Formby, Merseyside. Sefton Council. 33p.
MAGHSOUDIA, M. HAJIZADEHB, A. NEZAMMAHALLEHB, M. SEYEDREZAIC, H. JALALID, A. & MAHZOUNE, M. 2013. Interferometric synthetic aperture radar (InSAR) technology and geomorphology interpretation. ISPRS-International Archives of the Photogrammetry, Remote Sensing and Spatial Information Sciences**,** 253-256.
MAHMOUD, A. M. A. 2021. A Field Survey of Formby Coastal Dunes using TLS and GNSS. SENSED. the RSPSoc Newsletter.
MAHMOUD, A. M. A. HUSSAIN, E. NOVELLINO, A. PSIMOULIS, P. & MARSH, S. 2021. Monitoring the dynamics of Formby sand dunes using airborne LiDAR DTMs. Remote Sensing, 13**,** 4665.
MALTAMO, M. NÆSSET, E. & VAUHKONEN, J. 2014. Forestry applications of airborne laser scanning. Concepts and case studies. Manag For Ecosys, 27**,** 2014.
MANZONI, M. MOLINARI, M. E. & MONTI-GUARNIERI, A. 2021. Multitemporal InSAR Coherence Analysis and Methods for Sand Mitigation. Remote Sensing, 13**,** 1362.
MAS, J. F. 1999. Monitoring land-cover changes: a comparison of change detection techniques. International journal of remote sensing, 20**,** 139-152.
MASSONNET, D. & FEIGL, K. L. 1998. Radar interferometry and its application to changes in the Earth's surface. Reviews of geophysics, 36**,** 441-500.

MATEO-GARCIA, G. VEITCH-MICHAELIS, J. SMITH, L. OPREA, S. V. SCHUMANN, G. GAL, Y. BAYDIN, A. G. & BACKES, D. 2021. Towards global flood mapping onboard low cost satellites with machine learning. Scientific reports, 11**,** 1-12.
MATHER, P. M. & KOCH, M. 2011. Computer processing of remotely-sensed images: an introduction, John Wiley & Sons.
MAXWELL, A. E. WARNER, T. A. & GUILLÉN, L. A. 2021. Accuracy assessment in convolutional neural network-based deep learning remote sensing studies—part 1: Literature review. Remote Sensing, 13**,** 2450.
MCEWEN, A. S. ELIASON, E. M. BERGSTROM, J. W. BRIDGES, N. T. HANSEN, C. J. DELAMERE, W. A. GRANT, J. A. GULICK, V. C. HERKENHOFF, K. E. & KESZTHELYI, L. 2007. Mars reconnaissance orbiter's high resolution imaging science experiment (HiRISE). Journal of Geophysical Research: Planets, 112.
MERIDITH, A. W. ESLINGER, D. L. & AURIN, D. 1999. An evaluation of hurricane-induced erosion along the North Carolina coast using airborne LIDAR surveys, Coastal Services Center.
MIDDLETON, J. COOKE, C. KEARNEY, E. MUMFORD, P. MOLE, M. NIPPARD, G. RIZOS, C. SPLINTER, K. & TURNER, I. 2013. Resolution and accuracy of an airborne scanning laser system for beach surveys. Journal of Atmospheric and Oceanic Technology, 30**,** 2452-2464.
MIDEKISA, A. HOLL, F. SAVORY, D. J. ANDRADE-PACHECO, R. GETHING, P. W. BENNETT, A. & STURROCK, H. J. 2017. Mapping land cover change over continental Africa using Landsat and Google Earth Engine cloud computing. PloS one, 12**,** e0184926.
MILLER, S. D. 2003. A consolidated technique for enhancing desert dust storms with MODIS. Geophysical Research Letters, 30.
MONTREUIL, A. L. BULLARD, J. E. CHANDLER, J. H. & MILLETT, J. 2013. Decadal and seasonal development of embryo dunes on an accreting macrotidal beach: North Lincolnshire, UK. Earth Surface Processes and Landforms, 38**,** 1851-1868.
MORTON, R. A. LEACH, M. P. PAINE, J. G. & CARDOZA, M. A. 1993. Monitoring beach changes using GPS surveying techniques. Journal of Coastal Research**,** 702-720.
MOUNTRAKIS, G. IM, J. & OGOLE, C. 2011. Support vector machines in remote sensing: A review. ISPRS Journal of Photogrammetry and Remote Sensing, 66**,** 247-259.
MUNRO, R. IBRAHIM, M. A. M. ABUZIED, H. & EL-HASSAN, B. 2012. Aeolian sand landforms in parts of the Sudan and Nubia. Origins and impacts on past and present land use. Sudan & Nubia, 16**,** 140-154.
MURCHIE, S. ARVIDSON, R. BEDINI, P. BEISSER, K. BIBRING, J. P. BISHOP, J. BOLDT, J. CAVENDER, P. CHOO, T. & CLANCY, R. 2007. Compact reconnaissance imaging spectrometer for Mars (CRISM) on Mars reconnaissance orbiter (MRO). Journal of Geophysical Research: Planets, 112.
NASA. 2017. Dust storm over Sudan and the Red Sea [Online]. NASA. Available: <https://modis.gsfc.nasa.gov/gallery/individual.php?db_date=2017-08-17> [Accessed].
NASHASHIBI, A. Y. SARABANDI, K. AL-ZAID, F. A. & ALHUMAIDI, S. 2011. Characterization of radar backscatter response of sand-covered surfaces at millimeter-wave frequencies. IEEE transactions on geoscience and remote sensing, 50**,** 2345-2354.
NASIR, S. IQBAL, I. A. ALI, Z. & SHAHZAD, A. Accuracy assessment of digital elevation model generated from pleiades tri stereo-pair. 2015 7th international conference on recent advances in space technologies (RAST), 2015. IEEE, 193-197.
NAVARRO-PONS, M. MUÑOZ-PEREZ, J. J. ROMAN-SIERRA, J. RUIZ-CAÑAVATE, A. & GOMEZ-PINA, G. 2015. Characterization of wind-blown sediment transport with height in a highly mobile dune (SW Spain).
NECSOIU, M. LEPRINCE, S. HOOPER, D. M. DINWIDDIE, C. L. MCGINNIS, R. N. & WALTER, G. R. 2009. Monitoring migration rates of an active subarctic dune field using optical imagery. Remote Sensing of Environment, 113**,** 2441-2447.
NORDSTROM, K. F. PSUTY, N. & CARTER, B. 1990. Coastal dunes: form and process, Wiley.

NURI, A. A. F. HAMID, A. A. EL ABBAS DOKA, M. A. & SALIH, E. M. 2016. Assessment of Vegetation Cover Degradation Using Remote Sensing and GIS Techniques along Sudanese Red Sea Coast (Suakin to Ashad). Journal of Geography and Geology, 8**,** 55.

OKYAY, U. TELLING, J. GLENNIE, C. L. & DIETRICH, W. E. 2019. Airborne lidar change detection: An overview of Earth sciences applications. Earth-Science Reviews, 198**,** 102929.

OPOLOT, E. 2013. Application of remote sensing and geographical information systems in flood management: a review. Research journal of applied sciences engineering and technology, 6**,** 1884-1894.

OSMANOĞLU, B. SUNAR, F. WDOWINSKI, S. & CABRAL-CANO, E. 2016. Time series analysis of InSAR data: Methods and trends. ISPRS Journal of Photogrammetry and Remote Sensing, 115**,** 90-102.

OU, D. TAN, K. DU, Q. CHEN, Y. & DING, J. 2018. Decision Fusion of D-InSAR and Pixel Offset Tracking for Coal Mining Deformation Monitoring. Remote Sensing, 10**,** 1055.

PACHUR, H.-J. & KRÖPELIN, S. 1987. Wadi Howar: Paleoclimatic evidence from an extinct river system in the southeastern Sahara. Science, 237**,** 298-300.

PAL, M. 2005. Random forest classifier for remote sensing classification. International journal of remote sensing, 26**,** 217-222.

PEDERSEN, R. & SIGMUNDSSON, F. 2006. Temporal development of the 1999 intrusive episode in the Eyjafjallajökull volcano, Iceland, derived from InSAR images. Bulletin of Volcanology, 68**,** 377-393.

PEPE, A. & CALÒ, F. 2017. A review of interferometric synthetic aperture RADAR (InSAR) multi-track approaches for the retrieval of Earth's surface displacements. Applied Sciences, 7**,** 1264.

PETTORELLI, N. VIK, J. O. MYSTERUD, A. GAILLARD, J.-M. TUCKER, C. J. & STENSETH, N. C. 2005. Using the satellite-derived NDVI to assess ecological responses to environmental change. Trends in ecology & evolution, 20**,** 503-510.

PHIRI, D. SIMWANDA, M. SALEKIN, S. NYIRENDA, V. R. MURAYAMA, Y. & RANAGALAGE, M. 2020. Sentinel-2 data for land cover/use mapping: a review. Remote Sensing, 12**,** 2291.

PING, L. NARTEAU, C. DONG, Z. ZHANG, Z. & COURRECH DU PONT, S. 2014. Emergence of oblique dunes in a landscape-scale experiment. Nature Geoscience, 7**,** 99-103.

POTTER, C. & WEIGAND, J. 2016. Analysis of desert sand dune migration patterns from Landsat image time series for the Southern California desert. J. Remote Sens. GIS, 5**,** 1-8.

PRADHAN, B. MONEIR, A. A. A. & JENA, R. 2018. Sand dune risk assessment in Sabha region, Libya using Landsat 8, MODIS, and Google Earth Engine images. Geomatics, Natural Hazards and Risk, 9**,** 1280-1305.

PROVOOST, S. JONES, M. L. M. & EDMONDSON, S. E. 2011. Changes in landscape and vegetation of coastal dunes in northwest Europe: a review. Journal of Coastal Conservation, 15**,** 207-226.

PYE, K. & BLOTT, S. 2008. Decadal-scale variation in dune erosion and accretion rates: an investigation of the significance of changing storm tide frequency and magnitude on the Sefton coast, UK. Geomorphology, 102**,** 652-666.

PYE, K. BLOTT, S. & HOWE, M. 2014. Coastal dune stabilization in Wales and requirements for rejuvenation. Journal of coastal conservation, 18**,** 27-54.

PYE, K. & BLOTT, S. J. 2016. Assessment of beach and dune erosion and accretion using LiDAR: Impact of the stormy 2013–14 winter and longer term trends on the Sefton Coast, UK. Geomorphology, 266**,** 146-167.

PYE, K. & NEAL, A. 1994. Coastal dune erosion at Formby Point, north Merseyside, England: causes and mechanisms. Marine Geology, 119**,** 39-56.

PYE, K. SAYE, S. & BLOTT, S. 2007. Sand dune processes and management for flood and coastal defence Part 1: Project overview and recommendations. Joint Defra/EA Flood and Coastal Erosion RiskManagement R&D Programme.

PYE, K. & TSOAR, H. 2008. Aeolian sand and sand dunes, Springer Science & Business Media.

PYE, K. & TSOAR, H. 2009. Aeolian sand and sand dunes, Springer
QU, J. J. HAO, X. KAFATOS, M. & WANG, L. 2006. Asian dust storm monitoring combining Terra and Aqua MODIS SRB measurements. IEEE Geoscience and remote sensing letters, 3**,** 484-486.
RASMUSSEN, K. R. & MIKKELSEN, H. E. 1998. On the efficiency of vertical array aeolian field traps. Sedimentology, 45**,** 789-800.
RATNAYAKE, R. 2004. Remote sensing and GIS application for monitoring forest management operations. University of Nottingham.
REFICE, A. CAPOLONGO, D. PASQUARIELLO, G. D'ADDABBO, A. BOVENGA, F. NUTRICATO, R. LOVERGINE, F. P. & PIETRANERA, L. 2014. SAR and InSAR for flood monitoring: Examples with COSMO-SkyMed data. IEEE Journal of Selected Topics in Applied Earth Observations and Remote Sensing, 7**,** 2711-2722.
REGASA, M. S. NONES, M. & ADEBA, D. 2021. A Review on Land Use and Land Cover Change in Ethiopian Basins. Land, 10**,** 585.
REITZ, M. D. JEROLMACK, D. J. EWING, R. C. & MARTIN, R. L. 2010. Barchan-parabolic dune pattern transition from vegetation stability threshold. Geophysical Research Letters, 37.
RIVEROS, N. C. EUILLADES, L. D. EUILLADES, P. A. MOREIRAS, S. M. & BALBARANI, S. 2013. Offset tracking procedure applied to high resolution SAR data on Viedma Glacier, Patagonian Andes, Argentina.
SALIH, A. A. GANAWA, E.-T. & ELMAHL, A. A. 2017. Spectral mixture analysis (SMA) and change vector analysis (CVA) methods for monitoring and mapping land degradation/desertification in arid and semiarid areas (Sudan), using Landsat imagery. The Egyptian Journal of Remote Sensing and Space Science, 20**,** S21-S29.
SAM, L. GAHLOT, N. & PRUSTY, B. 2015. Estimation of dune celerity and sand flux in part of West Rajasthan, Gadra area of the Thar Desert using temporal remote sensing data. Arabian Journal of Geosciences, 8**,** 4.
SAMADI, M. BOLOORANI, A. D. ALAVIPANAH, S. K. MOHAMADI, H. & NAJAFI, M. S. 2014. Global dust Detection Index (GDDI); a new remotely sensed methodology for dust storms detection. Journal of environmental health science and engineering, 12**,** 1-14.
SAYE, S. VAN DER WAL, D. PYE, K. & BLOTT, S. 2005. Beach–dune morphological relationships and erosion/accretion: an investigation at five sites in England and Wales using LIDAR data. Geomorphology, 72**,** 128-155.
SAZIB, N. MLADENOVA, I. & BOLTEN, J. 2018. Leveraging the Google Earth Engine for drought assessment using global soil moisture data. Remote sensing, 10**,** 1265.
SCHEIDT, S. P. & LANCASTER, N. 2013. The application of COSI-Corr to determine dune system dynamics in the southern Namib Desert using ASTER data. Earth Surface Processes and Landforms, 38**,** 1004-1019.
SEELY, M. 2012. Namib sand sea world heritage nomination. Namibia National Committee for World Heritage, Windhoek, Namibia.
SEFTON METROPOLITAN BOROUGH COUNCIL, F. C. E. R. M. T. 2016. SEFTON AND WEST LANCASHIRE Annual Local Monitoring Report 2015.
SENTINEL, E. 2015. User Handbook. ESA Standard Document, 64.
SHAHRAIYNI, H. T. KARIMI, K. NOKHANDAN, M. H. & MOGHADAS, N. H. 2015. Monitoring of dust storm and estimation of aerosol concentration in the Middle East using remotely sensed images. Arabian Journal of Geosciences, 8**,** 2095-2110.
SHAKER, A. YAN, W. WONG, M. EL-ASHMAWY, N. & HADDAD, B. 2008. Flood hazard assessment using panchromatic satellite imagery. The International Archives of the Photogrammetry Remote Sensing and Spatial Information Sciences. Vol. XXXVII.
SHELESTOV, A. LAVRENIUK, M. KUSSUL, N. NOVIKOV, A. & SKAKUN, S. 2017. Exploring Google Earth Engine platform for big data processing: Classification of multi-temporal satellite imagery for crop mapping. frontiers in Earth Science, 5**,** 17.
SHEPHERD, G. TERRADELLAS, E. BAKLANOV, A. KANG, U. SPRIGG, W. NICKOVIC, S. BOLOORANI, A. D. AL-DOUSARI, A. BASART, S. & BENEDETTI, A. 2016. Global assessment of sand and dust storms.

SHERMAN, D. SWANN, C. & BARRON, J. 2014. A high-efficiency, low-cost aeolian sand trap. Aeolian Research, 13**,** 31-34.
SHERMAN, D. J. JACKSON, D. W. NAMIKAS, S. L. & WANG, J. 1998. Wind-blown sand on beaches: an evaluation of models. Geomorphology, 22**,** 113-133.
SHEYKHMOUSA, M. MAHDIANPARI, M. GHANBARI, H. MOHAMMADIMANESH, F. GHAMISI, P. & HOMAYOUNI, S. 2020. Support vector machine versus random forest for remote sensing image classification: A meta-analysis and systematic review. IEEE Journal of Selected Topics in Applied Earth Observations and Remote Sensing, 13**,** 6308-6325.
SILVESTRO, S. FENTON, L. VAZ, D. BRIDGES, N. & ORI, G. 2010. Ripple migration and dune activity on Mars: Evidence for dynamic wind processes. Geophysical Research Letters, 37.
SINGH, A. 1989. Review article digital change detection techniques using remotely-sensed data. International journal of remote sensing, 10**,** 989-1003.
SINHA, S. JEGANATHAN, C. SHARMA, L. & NATHAWAT, M. 2015. A review of radar remote sensing for biomass estimation. International Journal of Environmental Science and Technology, 12**,** 1779-1792.
SOLAZZO, D. SANKEY, J. B. SANKEY, T. T. & MUNSON, S. M. 2018. Mapping and measuring aeolian sand dunes with photogrammetry and LiDAR from unmanned aerial vehicles (UAV) and multispectral satellite imagery on the Paria Plateau, AZ, USA. Geomorphology, 319**,** 174-185.
SONG, Y. CHEN, C. XU, W. ZHENG, H. BAO, A. LEI, J. LUO, G. CHEN, X. ZHANG, R. & TAN, Z. 2020. Mapping the temporal and spatial changes in crescent dunes using an interferometric synthetic aperture radar temporal decorrelation model. Aeolian Research, 46**,** 100616.
STOCKDONF, H. F. SALLENGER JR, A. H. LIST, J. H. & HOLMAN, R. A. 2002. Estimation of shoreline position and change using airborne topographic lidar data. Journal of Coastal Research**,** 502-513.
STOCKTON, P. & GILLETTE, D. 1990. Field measurement of the sheltering effect of vegetation on erodible land surfaces. Land Degradation & Development, 2**,** 77-85.
STOUT, J. & ZOBECK, T. 1997. Intermittent saltation. Sedimentology, 44**,** 959-970.
STROZZI, T. LUCKMAN, A. MURRAY, T. WEGMULLER, U. & WERNER, C. L. 2002. Glacier motion estimation using SAR offset-tracking procedures. IEEE Transactions on Geoscience and Remote Sensing, 40**,** 2384-2391.
SURESH, D. & YARRAKULA, K. 2020. InSAR based deformation mapping of earthquake using Sentinel 1A imagery. Geocarto International, 35**,** 559-568.
TANTIANUPARP, P. SHI, X. ZHANG, L. BALZ, T. & LIAO, M. 2013. Characterization of landslide deformations in three gorges area using multiple InSAR data stacks. Remote Sensing, 5**,** 2704-2719.
TEMPFLI, K. HUURNEMAN, G. BAKKER, W. JANSSEN, L. L. FERINGA, W. GIESKE, A. GRABMAIER, K. HECKER, C. HORN, J. & KERLE, N. Principles of remote sensing: an introductory textbook. 2009. ITC.
TEREFENKO, P. PAPROTNY, D. GIZA, A. MORALES-NÁPOLES, O. KUBICKI, A. & WALCZAKIEWICZ, S. 2019. Monitoring cliff erosion with LiDAR surveys and bayesian network-based data analysis. Remote Sensing, 11**,** 843.
THOMAS, N. & NIGAM, S. 2018. Twentieth-century climate change over Africa: Seasonal hydroclimate trends and sahara desert expansion. Journal of Climate, 31**,** 3349-3370.
THOMAS, V. FINCH, D. MCCAUGHEY, J. NOLAND, T. RICH, L. & TREITZ, P. 2006. Spatial modelling of the fraction of photosynthetically active radiation absorbed by a boreal mixedwood forest using a lidar–hyperspectral approach. Agricultural and Forest Meteorology, 140**,** 287-307.
TOSI, L. STROZZI, T. DA LIO, C. & TEATINI, P. Regional and local land subsidence at the Venice coastland by TerraSAR-X PSI. NISOLS 2015 (Ninth Symposium on Land Subsidence), 2015. Copernicus Publications.

TOUTIN, T. & CHENG, P. 2002. Comparison of automated digital elevation model extraction results using along-track ASTER and across track SPOT stereo images. Optical engineering, 41**,** 2102-2106.
TRUST, N. Shifting Shores at Formby [Online]. Available: https://www.nationaltrust.org.uk/formby/features/shifting-shores-at-formby [Accessed 2021].
TRUST, N. 2015. Shifting shores: Playing our part at the coast [Online]. Available: https://nt.global.ssl.fastly.net/documents/shifting-shores-report-2015.pdf [Accessed 17 August 2021].
TSOAR, H. 2001. Types of aeolian sand dunes and their formation. Geomorphological fluid mechanics. Springer.
TÜRK, T. 2018. Determination of mass movements in slow-motion landslides by the Cosi-Corr method. Geomatics, Natural Hazards and Risk, 9**,** 325-336.
VAN DE GRAAFF, J. 1986. Probabilistic design of dunes; an example from the Netherlands. Coastal Engineering, 9**,** 479-500.
VAN DER MEULEN, F. & VAN DER MAAREL, E. 1989. Coastal defence alternatives and nature development perspectives.
VERMEESCH, P. & DRAKE, N. 2008. Remotely sensed dune celerity and sand flux measurements of the world's fastest barchans (Bodélé, Chad). Geophysical Research Letters, 35.
VERMEESCH, P. FENTON, C. KOBER, F. WIGGS, G. BRISTOW, C. S. & XU, S. 2010. Sand residence times of one million years in the Namib Sand Sea from cosmogenic nuclides. Nature Geoscience, 3**,** 862-865.
VERMEESCH, P. & LEPRINCE, S. 2012. A 45-year time series of dune mobility indicating constant windiness over the central Sahara. Geophysical Research Letters, 39.
VOS, K. SPLINTER, K. D. HARLEY, M. D. SIMMONS, J. A. & TURNER, I. L. 2019. CoastSat: A Google Earth Engine-enabled Python toolkit to extract shorelines from publicly available satellite imagery. Environmental Modelling & Software, 122**,** 104528.
WANG, J. X. 2015. Mapping the global dust storm records: Review of dust data sources in supporting modeling/climate study. Current Pollution Reports, 1**,** 82-94.
WANG, P. & KRAUS, N. C. 1999. Horizontal water trap for measurement of aeolian sand transport. Earth surface processes and landforms, 24**,** 65-70.
WANG, T. & JÓNSSON, S. 2015. Improved SAR amplitude image offset measurements for deriving three-dimensional coseismic displacements. IEEE Journal of Selected Topics in Applied Earth Observations and Remote Sensing, 8**,** 3271-3278.
WANG, T. WEI, S. & JÓNSSON, S. 2015. Coseismic displacements from SAR image offsets between different satellite sensors: Application to the 2001 Bhuj (India) earthquake. Geophysical Research Letters, 42**,** 7022-7030.
WEHR, A. & LOHR, U. 1999. Airborne laser scanning—an introduction and overview. ISPRS Journal of photogrammetry and remote sensing, 54**,** 68-82.
WIGGS, G. ATHERTON, R. & BAIRD, A. 2004. Thresholds of aeolian sand transport: establishing suitable values. Sedimentology, 51**,** 95-108.
WIGGS, G. F. THOMAS, D. S. BULLARD, J. E. & LIVINGSTONE, I. 1995. Dune mobility and vegetation cover in the southwest Kalahari Desert. Earth surface processes and landforms, 20**,** 515-529.
WILLIS, K. S. 2015. Remote sensing change detection for ecological monitoring in United States protected areas. Biological Conservation, 182**,** 233-242.
WINKLER, K. FUCHS, R. ROUNSEVELL, M. & HEROLD, M. 2021. Global land use changes are four times greater than previously estimated. Nature communications, 12**,** 1-10.
WOLF, J. BROWN, J. M. & HOWARTH, M. J. 2011. The wave climate of Liverpool Bay—observations and modelling. Ocean Dynamics, 61**,** 639-655.
WOOLARD, J. W. & COLBY, J. D. 2002. Spatial characterization, resolution, and volumetric change of coastal dunes using airborne LIDAR: Cape Hatteras, North Carolina. Geomorphology, 48**,** 269-287.

XIONG, L. WANG, G. BAO, Y. ZHOU, X. WANG, K. LIU, H. SUN, X. & ZHAO, R. 2019. A rapid terrestrial laser scanning method for coastal erosion studies: A case study at Freeport, Texas, USA. Sensors, 19**,** 3252.
XU, Z. MASON, J. A. & LU, H. 2015. Vegetated dune morphodynamics during recent stabilization of the Mu Us dune field, north-central China. Geomorphology, 228**,** 486-503.
YANG, X. 2011. Parameterizing support vector machines for land cover classification. Photogrammetric Engineering & Remote Sensing, 77**,** 27-37.
YENGOH, G. T. DENT, D. OLSSON, L. TENGBERG, A. E. & TUCKER III, C. J. 2015. Use of the Normalized Difference Vegetation Index (NDVI) to assess Land degradation at multiple scales: current status, future trends, and practical considerations, Springer.
ZHANG, K. DOUGLAS, B. C. & LEATHERMAN, S. P. 2004a. Global warming and coastal erosion. Climatic change, 64**,** 41-58.
ZHANG, T.-H. ZHAO, H.-L. LI, S.-G. LI, F.-R. SHIRATO, Y. OHKURO, T. & TANIYAMA, I. 2004b. A comparison of different measures for stabilizing moving sand dunes in the Horqin Sandy Land of Inner Mongolia, China. Journal of Arid Environments, 58**,** 203-214.
ZHANG, Z. XU, C.-Y. EL-TAHIR, M. E.-H. CAO, J. & SINGH, V. 2012. Spatial and temporal variation of precipitation in Sudan and their possible causes during 1948–2005. Stochastic environmental research and risk assessment, 26**,** 429-441.
ZHOU, X. CHANG, N.-B. & LI, S. 2009. Applications of SAR interferometry in earth and environmental science research. Sensors, 9**,** 1876-1912.
ZHU, B.-Q. ZHANG, J.-X. & SUN, C. 2021. Physiochemical characteristics, provenance, and dynamics of sand dunes in the arid Hexi Corridor. Frontiers in Earth Science**,** 726.
ZSAMBOKY, M. FERNÁNDEZ-BILBAO, A. SMITH, D. KNIGHT, J. & ALLAN, J. 2011. Impacts of climate change on disadvantaged UK coastal communities. Joseph Rowntree Foundation.
ZUREK, R. W. & SMREKAR, S. E. 2007. An overview of the Mars Reconnaissance Orbiter (MRO) science mission. Journal of Geophysical Research: Planets, 112.
ZURQANI, H. A. POST, C. J. MIKHAILOVA, E. A. SCHLAUTMAN, M. A. & SHARP, J. L. 2018. Geospatial analysis of land use change in the Savannah River Basin using Google Earth Engine. International journal of applied earth observation and geoinformation, 69**,** 175-185.